Dark signalling and code division multiple access in an optical fibre LAN with a bus topology

Thesis

Abstract

This thesis describes an optical fibre network that uses a bus topology and Code Division Multiple Access (CDMA). Various potential configurations are analysed and compared and it is shown that a serious limitation of optical CDMA schemes using incoherent correlators is the effect of optical beating due to the presence of multiple incoherent optical signals at the receiver photodiode. The network proposed and analysed in this thesis avoids beating between multiple optical fields because it only uses a single, shared, optical source. It does this through the SLIM (Single Light-source with In-line Modulation) configuration in which there is a continuously-operating light source at the head-end of a folded bus, and modulators at the nodes to impose signals on the optical field in the form of pulses of darkness which propagate along the otherwise continuously bright bus. Optical CDMA can use optical-fibre delay-line correlators as matched filters, and these may be operated either coherently or incoherently. Coherent operation is significantly more complex than incoherent operation, but incoherent correlators introduce further beating even in a SLIM network. A new design of optical delay-line correlator, the hybrid correlator, is therefore proposed, analysed and demonstrated. It is shown to eliminate beating. A model of a complete network predicts that a SLIM bus using optical CDMA with hybrid correlators can be operated at TeraBaud rates with the number of simultaneous users limited by multiple access interference (MAI), determined only by the combinatorics of the code set.

The Open University

Faculty of Technology

Dark signalling and code division multiple access in an optical fibre LAN with a bus topology

David Alan Chapman

Doctor of Philosophy

October 2002

Supervisors: Professor J. Monk and Professor P. A. Davies

Acknowledgements

I am indebted to many people: my supervisors, Professors John Monk and Phil Davies; everyone at the Open University who has generously helped me directly or indirectly; and members of the Photonics Research Group at the University of Kent for accommodating me in the summer of 1997.

I would also like to acknowledge the support of my parents, and special thanks goes to my wife, Joy, and my children, Alex and Vincent, for their loyal support over the nine years since I started this work.

Contents

List of Figures

List of Tables

Chapter 1

Introduction

The data rates required of local area networks have been rising. This trend can be seen in the successive standards in the Ethernet family, starting at 2.94 Mbits/s in the original experiment of Metcalfe [8], through the successive issues of the IEEE 802.3 standard [9]: 10 Mbits/s in 1980, 100 Mbits/s (Fast Ethernet) in 1995, 1 Gbit/s (Gigabit Ethernet) in 1998 and 10 Gbits/s (10 Gigabit Ethernet [10]) in 2002.

Although technologies have so far kept pace with the requirements of LANs, in doing so they have lost some of the merits of the early LANs. The original Ethernet used a bus topology, on to which additional nodes could be simply added. This made for simple wiring in the form of a single coaxial copper cable that could be tapped to create a new node and allowed straightforward expansion and contraction of the network dimensions. To be able to transmit the higher data rates over useful distances, however, multiple sets of twisted-pair cables are used and the topology is changed from a bus to a star [11]. This leads to a substantial increase in the wiring needed. Furthermore the CSMA/CD protocol used by Ethernet becomes inefficient at higher data rates, and to overcome this inefficiency the highest-performance networks use full-duplex communication to each node and switching at hubs, leading to the more complex 'switched Ethernet'.

Optical fibre is used to replace the multiple twisted pairs in higher speed Ethernet, but the fibre is used only as a point-to-point transmission medium. The network performance is constrained by the electronic processing at each end, and the star topology with electronic switching at the hub remains. Other LAN and MAN standards designed specifically for use with fibre, such as FDDI and DQDB [12], still rely on electronics at each node, and are therefore constrained by the limitations of electronic signal processing and do not fully exploit the capacity of optical fibre.

To regain the simplicity and flexibility that is desired of LANs, and to accommodate ever increasing data rates, new techniques are needed that allow the optical capacity of fibre to be exploited directly. The work reported in this thesis is an investigation into one such technique that delivers the flexibility of the original Ethernet while exploiting the capacity of fibre.

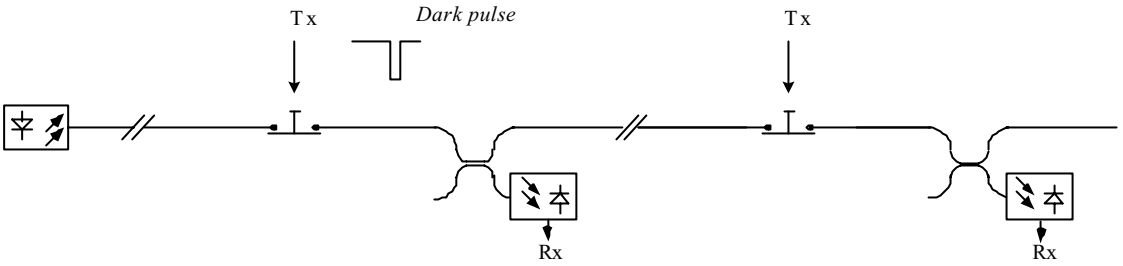

Figure 1.1: 'Dark-signalling' in an optical fibre bus.

The technique proposed arose from an original idea of the author and co-worker (Dr. D. A. Gorham) first proposed at an IEE colloquium in 1991 [13]. The underlying concept is that of the dark-signalling optical fibre bus, shown in Figure 1.1. Signalling uses the SLIM (Single Light source with In-line Modulation) configuration in which a single light source operates continuously at one end of the bus (the head-end), and terminals signal by interrupting the light path with in-line intensity modulators so that pulses of darkness propagate down the otherwise continuously bright fibre.

The bus topology vastly simplifies the cabling compared to a star topology, saving space in cable ducts as well as simplifying planning and provisioning. As with original Ethernet, new nodes can be added without reconfiguration. Channel sharing through optical CDMA uses all-optical processing so that network capacity is not constrained by the speed of electronics. The problems of optical beating, which have severely limited previous proposals for CDMA in optical networks, are avoided through a new design of optical correlator and the use of only a single light source in a SLIM bus. Unlike the CSMA/CD protocol, furthermore, channel sharing through CDMA does not inherently limit the allowed physical separation of nodes on a shared medium so that the proposed network may run as a WAN as readily as a LAN. Near-far effects that are sometimes a problem of CDMA are not significant in this proposal because of the dark signalling. Calculations have shown that a single SLIM bus can have hundreds of attached nodes, each with a unique physical-layer address, and that two hundred or more of them can be using the medium simultaneously.

1.1 The work of this Ph.D. and the structure of the thesis

Figure 1.2 shows a hierarchy of topics for study of the dark signalling bus within the context of optical fibre communications, with the main focus of the work reported in this thesis highlighted in red. The current status of research and development of these topics has been reviewed and is described in the later sections of this chapter.

Past work on optical CDMA has been examined in detail and is reviewed, classified, and its relevance to the SLIM bus assessed. This is reported in **Chapter 2.**

One of the most important sources of noise in many optical networks – and which

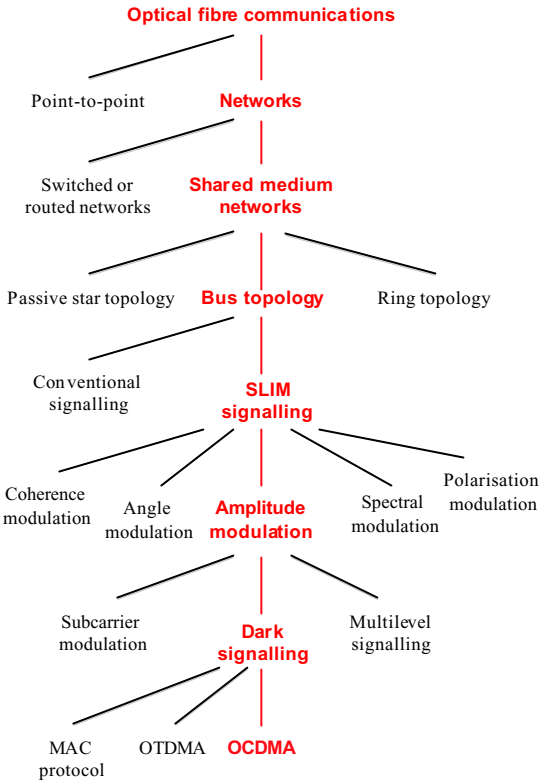

Figure 1.2: Map contextualizing the work of this thesis

has been overlooked in many proposals – arises from the beating between multiple optical carriers incident upon a photodiode. Even if there is only a single optical source (as in the SLIM bus), multiple paths can result in beating. Models of optical beating have been developed for the work of this thesis and are described in **Chapter 3**.

The power budgets of passive and amplified optical busses and stars have been analysed and the results are presented in **Chapter 4**. Chapter 4 also reports on the development of a model of the evolution of signal and noise power in both conventional and SLIM busses, as well as a numerical implementation of the model using *Mathematica*. The results show that the SLIM bus overcomes the problem of unsuppressed noise from EDFAs.

The merits and limitations of three different designs of optical correlator for use with CDMA in a SLIM bus have been investigated theoretically and experimentally, including a new design, the *hybrid correlator*, which has emerged from the work of this thesis. The theoretical comparison, including the effects of optical beating, is presented in **Chapter 5**. It is shown that there are aspects of the hybrid correlator which make it superior for use with CDMA in the SLIM bus compared to the incoherent and coherent correlators.

The hybrid correlator requires a *hybrid coupler*: a device that couples light from

multiple input single-mode fibres to a single output multi-mode fibre. The theoretical performance of hybrid couplers has been analysed using both a simple ray-theory model and, for few-moded output fibres, using a full analysis of the field distributions. This work is described and the conclusions reported in **Chapter 6.**

A 4-1 hybrid correlator has been built and characterised for insertion loss and beating noise. The measurements are presented in **Chapter 7**, together with the results of measurements on the beating in an incoherent correlator.

A comprehensive model of the performance of a SLIM bus using optical CDMA has been developed and simulated. The model is described and results from the simulation, for each of the three correlators, are presented in **Chapter 8.**

The analysis of Chapter 8 shows that with dark signalling and hybrid couplers the SLIM bus can achieve the multiple-access interference (MAI) limited performance of optical CDMA.

Finally, the conclusions and recommendations for future work are in **Chapter 9**.

1.2 Background and context

This section explores the context of the work of the Ph.D., summarises some of the associated prior work reported in the literature and considers the motivation for the line of investigation identified by the red spine of Figure 1.2. Optical CDMA (the bottom of the spine) is explored more fully in Chapter 2.

In addition to the specific references below, for further details of optical networking the reader is referred to books by P. E. Green [14] and by R. Ramaswami and K. N. Sivarajan [15] as well as recent 'Special Issues' on optical networking [16, 17] in the relevant technical literature such as IEEE *Journal of Lightwave Technology* and *Journal on Selected Areas in Communications*.

1.2.1 Point-to-point and networks

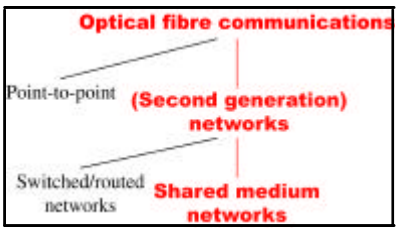

Optical fibre communication: point to point and networks. (Extract from Figure 1.2 on Page 3.)

Historically, optical fibre communication was first deployed for point-to-point communication in high-capacity links, such as inter-city trunk routes [14]. In the classification of Ramaswami and Sivarajan [15], the first generation of networks that

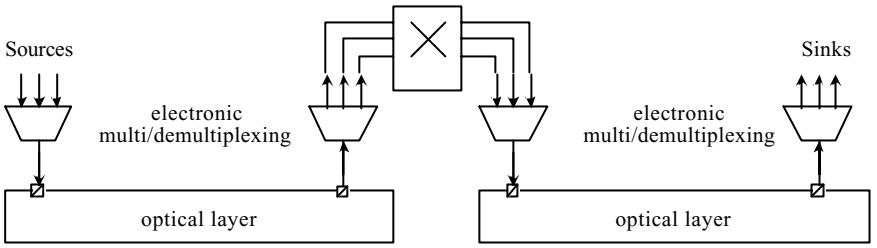

Figure 1.3: First generation optical networks

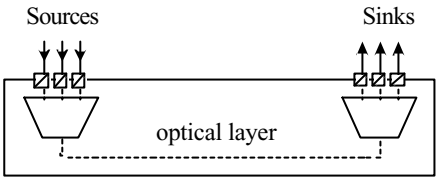

Figure 1.4: Optical multiplexing

exploited optical fibre (such as SONET, synchronous optical network, and FDDI, fiber-distributed-data-interface) use optics only for the transmission between nodes. Switching, routing and multiplexing was all done electronically as illustrated in Figure 1.3.

The terminal electronics in Figure 1.3 operates at the same speed as the optical channel, and the transmission capacity is limited by the state of the art of electronics. Year-on-year the limit increases following developments in electronics, and 'hero' experiments [18] regularly appear in the literature with the latest achievements. For example, systems operating at 40 Gbit/s [19] have been demonstrated recently.

The inherent capacity of optical fibre vastly exceeds the processing speed of electronics, however [15]. If some of the processing can be moved from the electronic to the optical domain the system can support a much greater data rate. For point-to-point transmission, for example, if multiplexing is done optically as shown Figure 1.4 then the electronics operates at the rate of the individual sources rather than the aggregate channel rate. Using optical multiplexing a total capacity of 3.2 Tbit/s has been demonstrated by wavelength division multiplexing 80 channels at 40 Gbit/s each [20].

It is convenient to distinguish between switched, or routed, networks and shared-medium networks. Generally, switched or routed networks are wide area networks (WANs) or telecommunication networks, and they are multi-hop with a mesh, ring or star topology. They currently use optical fibre transmission between the switching/routing nodes [21]. Most fibres currently carry only a single optical channel, but, increasingly, dense wavelength division multiplexing (DWDM) is being used to upgrade the capacity [22, 23, 24, 25]. Switching or routing is still electronic, but technological

developments are appearing that should eliminate the 'electronic bottleneck' in the network nodes to create 'all optical' networks [26]. Such developments include optical space switches [27], wavelength routing/switching [28, 29, 30, 31] and optical packet switching [32, 33, 34, 35].

Shared medium networks communicate on a 'broadcast and select' basis with address decoding done at the terminating nodes. This thesis primarily considers single-hop[1] networks with no intermediate routing or switching. These networks are generally characterised by having low-latency (because of the absence of intermediate switching or routing nodes) and flexibility in bandwidth allocation, and it has been the experience with similar electrical networks that they are more appropriate than switched or routed networks for LANs (local area networks). In the words of P. E. Green [36]:

> "It is no accident that PBX-based LANs never really made it compared to the more flexible Ethernets and token rings"

First generation fibre LANs and MANs such as FDDI and DQDB are 'broadcast and select' networks, but only use optical fibre as a point-to-point transmission medium with electrical access control [15]. This thesis is concerned with LANs and therefore will discuss only shared medium networks.

1.2.2 Topology

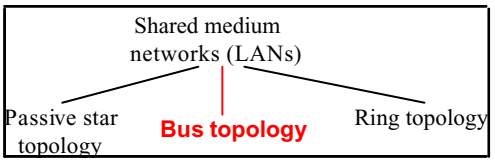

Optical fibre LAN topology. (From Figure 1.2 on Page 3.)

Shared-medium optical fibre LANs can be configured as stars (Figure 1.5), busses (Figure 1.6) or rings (Figure 1.10) [15], or combined topologies such as with a bus for gathering the light feeding into a star for distribution [37].

In the passive star topology shown in Figure 1.5, a transmit fibre from each node takes light from the transmitters to a passive star coupler [38]. The star coupler, constructed from a matrix of fused fibre couplers [39], splits light from each incoming fibre and broadcasts it on each of the output fibres. Star couplers have been demonstrated with low excess loss (0.13 dB for an 8×8 coupler in [40]) so that to a good approximation the loss from transmitter to receiver is given by $10 \log (1/N)$ dB, where N is the number of nodes in the network [38].

The star topology has been the basis of many proposals and demonstrations of fibre LANs, using WDMA (Section 1.2.4 below), CDMA (Chapter 2) and a few proposals

[1] Some proposals for optical fibre shared medium networks are multi-hop networks, however. See for example the discussion of the ring topology in Section 1.2.2 below.

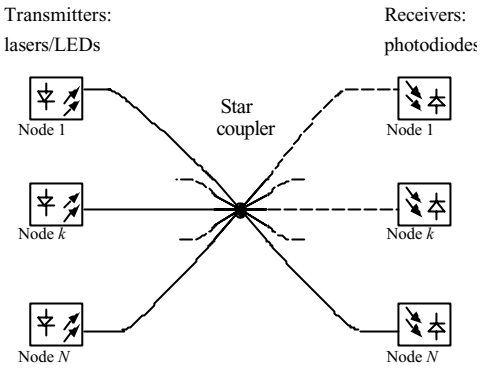

Figure 1.5: Passive star topology

for TDMA [41]. With TDMA, however, the timing synchronisation between nodes is easier to maintain with a bus topology.

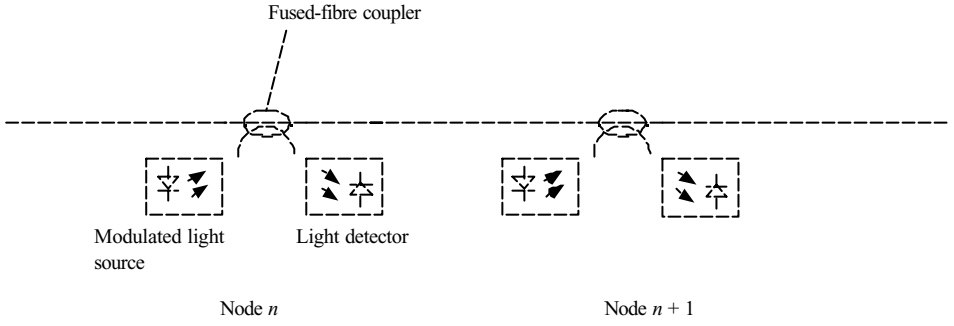

Figure 1.6: An optical fibre bus. (Shown with the same coupler used for tapping light on and off the bus.)

Figure 1.6 shows a passive optical fibre bus constructed by tapping light on and off a common fibre using fused fibre couplers. As Figure 1.6 illustrates, signalling is only possible in one direction (from left to right, as drawn). Bidirectional communication on a single fibre is possible, and was explored in [1] using multimode fibre, asymmetric couplers[2] and the configuration of Figure 1.7. A similar approach using single mode fibre, symmetric couplers and bidirectional optical amplifiers was proposed in [42]. There are practical problems with bidirectional signals on a single fibre, however, especially when amplifiers are used, and the benefits of bidirectional communication on a single fibre are small. Although bidirectional amplification is possible in principle [43, 42], very careful control of reflections is necessary to prevent excessive build-up of amplified spontaneous emissions, ASE, and the risk of lasing in the amplifiers. The more usual assumption is of signals propagating in one direction on the fibre with

[2] The asymmetric couplers allow a higher fraction of light to be coupled on to the bus than is coupled off. This is possible when the bus is multimode and the taps are single mode (or at least fewer-moded than the bus), but are impossible for single mode busses. Asymmetric taps are discussed again in Chapter 6.

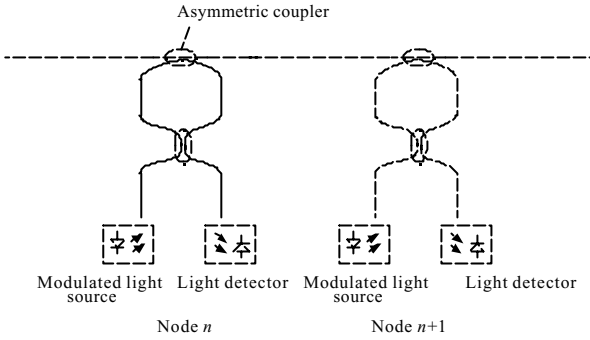

Figure 1.7: Bidirectional communication on a single fibre bus (from [1])

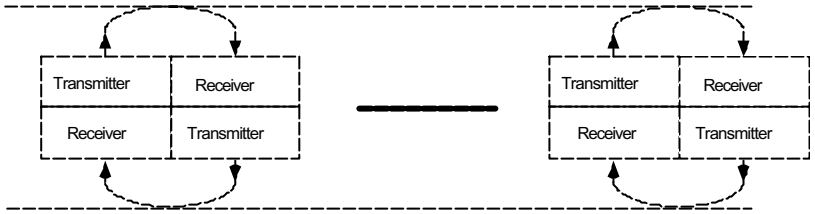

Figure 1.8: The dual bus topology

bidirectional communication achieved through the use of either the *dual bus* shown in Figure 1.8 or the *folded bus* shown in Figure 1.9 [14, 44] (called an *open loop* in [45]). The dual bus can support more terminals than the folded bus, but requires two transmitters and receivers at each node. The number of terminals supported by the folded bus is lower because some signals have to pass through more nodes on route to the destination, thereby suffering greater attenuation.

In [46], Cheung describes a range of possible implementations of a fibre dual bus using multiple channels through WDM. Cheung describes both regenerative (networks such as DTCAP[3] [47] which require optoelectronic conversion at each node, and are therefore not 'all-optical') and non-regenerative (all-optical networks such as WEMCOB[4] [48]). He identifies three benefits of the non-regenerative approach:

- node failures can be protected at no extra cost
- the transparency of the medium allows unused bandwidth to be exploited for other uses, such as subcarrier multiplexing to provide circuit connections or broadcasting on top of the dual bus protocol
- it has great potential to reduce the node complexity by channel tuning compared to regenerative schemes

[3] Distributed Tunable-Channel Access Protocol.
[4] Wavelength Encoded Multichannel Optical Bus.

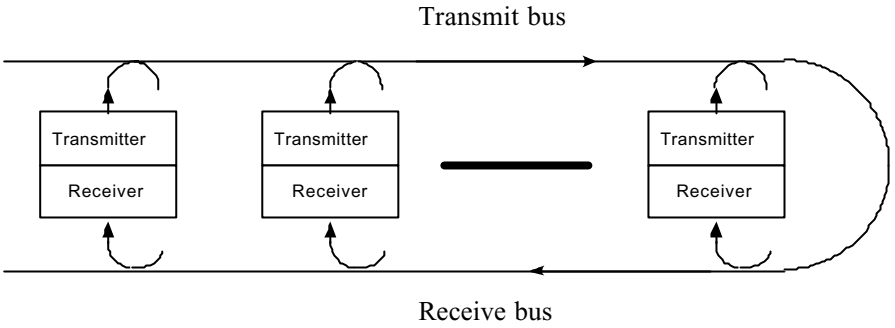

Figure 1.9: The 'folded bus' topology

A possible shared-medium fibre ring is shown in Figure 1.10. Reference [49] describes a ring like this which includes amplification that ensures that signals are maintained when propagating the whole way around the ring. The fibre in the ring has a low-level doping of erbium and is pumped so that there is gain in the ring that almost compensates for the total fibre and tap attenuation. The authors show that it is possible to have sufficient gain yet keep the ASE (amplified spontaneous emission) noise low. However, they do not address the issue of how signla are prevented from recirculating. It is difficult to see how the ring would function.

In [50] and [51] the authors propose a dual ring which relies on attenuation to prevent signals propagating continuously. It is a multi-wavelength network which they describe as a 'ring-bus', and is topologically equivalent to the dual bus of Figure 1.8 but with both fibres looped back on themselves. Each node transmits and receives on a fixed wavelength, and a multi-hop protocol allows communication between any pair of nodes. Attenuation (due to fibre and the taps) is assumed to be high enough to ensure that signals are significantly attenuated by the time they have been completely around the ring and, for large rings, frequency reuse is possible for distant segments of the ring.

In electrical LANs with a ring topology [52], and first generation optical fibre LANs such as FDDI [12], continuous propagation around the ring is prevented by the sending node removing the data when it arrives back. This is possible because the nodes interrupt the data path and in effect route the data – by either forwarding or removing it. This type of ring is therefore a routed rather than a broadcast and select shared medium network.

Ring topologies will not be considered further since the investigation in this thesis is confined to single-hop broadcast and select networks, which (as explained above), would not seem to be possible in an all-optical ring.

The passive star topology has been preferred over the bus because of power budget considerations (reference [38] and Chapter 4, Section 4.1 below), but the optical bus topology becomes viable with the availability of optical amplifiers [53].

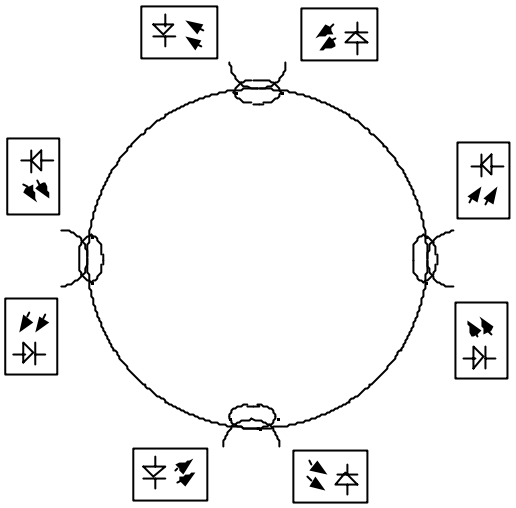

Figure 1.10: An optical fibre shared-medium ring

Even since the development of erbium-doped fibre amplifiers (EDFAs, [54]), however, there has been relatively little work on optical busses compared to stars, yet the bus topology has a number of advantages over the star. The bus topology reduces and simplifies the wiring[5] requirements in many office environments, and (assuming the signalling and the access protocol are suitable) is more flexible with regard to the insertion and removal of nodes to/from existing networks [48]. With a star topology, a new terminal always requires new wiring all the way to and from the star coupler. With a bus, it may be possible to insert a new terminal in-line with the bus, requiring little or no extra wiring. Furthermore, limits to the network dimensions have to be determined from the outset in a star, set by the 'hard limit' of the dimensions of the star coupler[6], whereas with the bus you can continue to add terminals until the performance is deemed unacceptable.

In [36] P. E. Green states that it is a fallacy that "[t]he advent of photonic amplifiers make busses preferable to stars". Green's justification for his opinion is:

> "This [the suggestion that amplifiers make busses preferable to stars] is true as long as only one transmitter is active, but if many are active simultaneously (at different wavelengths), the gain saturation effects are so harmful that the star (with a filter before each amplifier) remains a better solution".

The 'SLIM' (single light source with in-line modulation) concept which is explored in this thesis, however, operates with a single wavelength and so overcomes Green's

[5] The 'wiring' here, of course, is optical fibre cable.

[6] This means that the signal attenuation in the star coupler is determined by the maximum expected network dimensions, not by the current network dimensions.

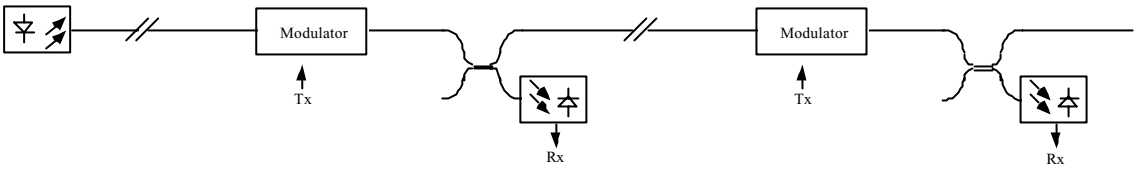

Figure 1.11: The SLIM bus. On-off keying by the modulators creates dark signalling.

objection. It is a conclusion of this work that the SLIM bus with optical amplifiers is indeed "preferable to stars".

1.2.3 Signalling in an optical fibre bus

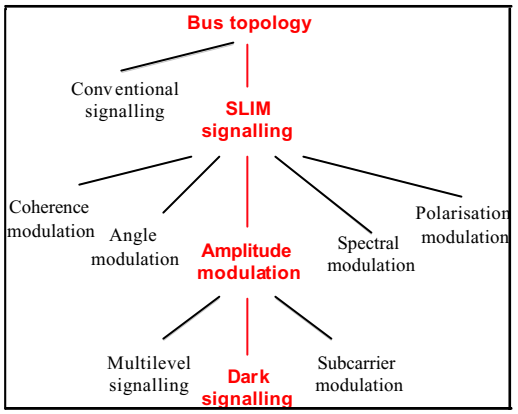

Signalling in optical fibre busses. (From Figure 1.2 on Page 3.)

Figure 1.6 (on page 7) shows what will be referred to in this thesis as *conventional signalling*: each node has its own light source (laser or LED) and signals by sending a pulse of light to represent a data 1. An alternative is SLIM[7] signalling (single light source with in-line modulation). SLIM is shown in Figure 1.11, and uses a single light source at the start of the bus and nodes signal using in-line modulators.

The conventional signalling fibre bus, its power budgets and its signal to noise ratio are analysed by Wagner in 1987 [53], the work of Ramaswami and Lui in 1990 [55] and 1993 [38].

Some work has been reported on systems with conventional signalling in which a synchronisation clock is launched from the head-end. The system analysed in [56], for example, is an amplified dual bus using two wavelengths. One wavelength is used for the synchronisation signal launched from the head end, and the other is used for

[7] The acronym 'SLIM' is used here in reference to all busses with a single light source and in-line modulation, even when referring to the work of others who did not, themselves, use the term.

the signalling from each node. A feature of this paper is that it points to the benefit of the suppression of the amplifier ASE (amplified spontaneous emission noise) by the synchronisation signal, which is also a virtue of the dark signalling bus as will be explained in Chapter 4.

Some large-scale projects have investigated high speed TDMA in conventional busses. The ARPA consortium on Wideband All-Optical Networks, for example, has proposed and demonstrated a slotted TDMA folded-bus: 'HLAN' (initially proposed with a helical ring topology – hence HLAN = 'helical-LAN' [57] – but revised to use a folded-bus topology [58]). As with all optical TDMA proposals, a fundamental limitation is the need for high-speed (aggregate channel rate) synchronisation. With present technology this means high-speed electronics, although all-optical or integrated electro-optic implementations are under investigation [2].

SLIM (Single Light-source with In-line Modulation) signalling potentially has a number of advantages over conventional signalling, because of the presence of a single optical carrier[8] on the fibre. These advantages include the simplified use of amplifiers in a bus (discussed in Chapter 4), the elimination of problems of optical beating (see Chapter 3) and that the network may be expanded with WDM [59].

Dark signalling, the scheme of Figure 1.1 (page 2), is one example of SLIM signalling. It is probably the simplest of modulation schemes that could be used in a SLIM bus and is possible with current technology. Other modulation schemes are possible with SLIM signalling, some of which have already been investigated by other workers (although they have not used the term SLIM).

The use of subcarrier modulation [60] in a SLIM bus was proposed by Domon et. al. [61]. Data electrically modulates a sinusoidal waveform (the subcarrier) using any of the usual modulation schemes (ASK, QPSK etc.) which in turn modulates the light in the bus using the in-line amplitude modulator. Addressing is determined by the frequency of the subcarrier. This scheme is simple, but each modulator severely attenuates the propagated signal, requiring substantial amplification to maintain the signal power in the bus leading to increased ASE and degraded signal to noise ratio. Also, a separate frequency is needed for each addressable node, so for large networks the subcarriers will have to extend to high frequencies.

Phase modulators can be used for phase and/or frequency modulation of the optical carrier in a SLIM bus. A scheme using phase modulators and described as *optical phase division multiplexing* was proposed by Cimini [62]. As with subcarrier modulation, this scheme involves electrically modulating a sinusoid, the frequency of which is used as the destination address. In this proposal, however, the modulated sinusoid phase-modulates rather than amplitude-modulates the light. The receiver uses an

[8] It is important to appreciate that this is a single carrier – all the light derives from a single optical source. This is different from multiple sources operating at the same, or nominaly the same, wavelength, as is the case for OTDMA with conventional signalling in a bus and with some proposals for CDMA in a star.

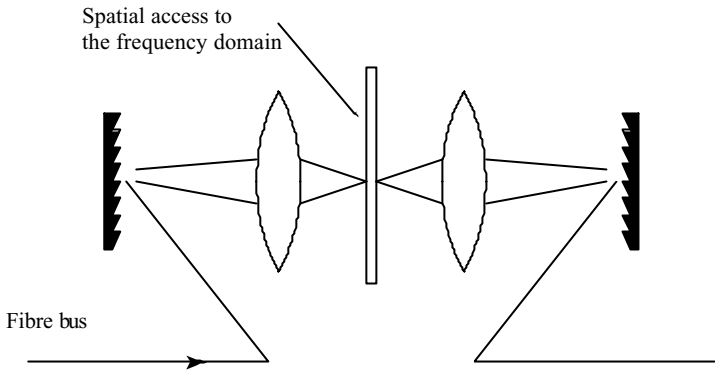

Figure 1.12: Access to the frequency domain

optical discriminator followed by integration[9] to extract the phase modulation, and electrical filtering selects the appropriate channel. Kiasaleh [63] has described a variation in which slow frequency hopping is used for the channel separation and addressing. There are no reports of demonstrations of these systems, and some authors [64] believe that the technical demands of the modulation scheme make it unrealistic with present technology. However, angle modulation has the characteristic of maintaining constant amplitude in the bus, which simplifies the use of optical amplifiers [62] and further work is recommended.

Spectral modulation refers to modulation directly applied in the frequency domain. Diffraction gratings could be used to access the frequency domain of the optical signal in a SLIM bus (Figure 1.12), allowing modulation and detection of individual portions of the optical spectrum. There may be scope for a form of spectral splicing WDM [65], for example. Alternatively, work on spectral encoding for optical CDMA in passive star networks has included a number of schemes which might be suitable for use in a SLIM bus, and these ideas will be discussed further in Section 2.3.

Coherence modulation, like spectral modulation, modulates the signal spectrum but the mechanism is rather different from that described above, so it is considered separately. It was originally proposed as a mechanism for multiplexing data from multiple fibre-optic sensors [66], but has since been proposed for LANs [67].

In point-to-point coherence modulation (Figure 1.13) a Mach-Zehnder interferometer at the transmitter has optical path length difference, τ_d, greater than the coherence length of the optical source. The signal is modulated with a phase modulator in one arm of the interferometer, but, because τ_d is larger than the coherence length of the source, the light in the output coupler of the interferometer combines incoherently and there is no observed interference effect – the output is just attenuated by 3 dB compared to the input. At the receiver there is another interferometer with the same path

[9] Alternatively the integration can be done at the transmitter – before phase modulation of the optical carrier. This is the approach proposed by Kiasaleh in his frequency-hopped systen [63].

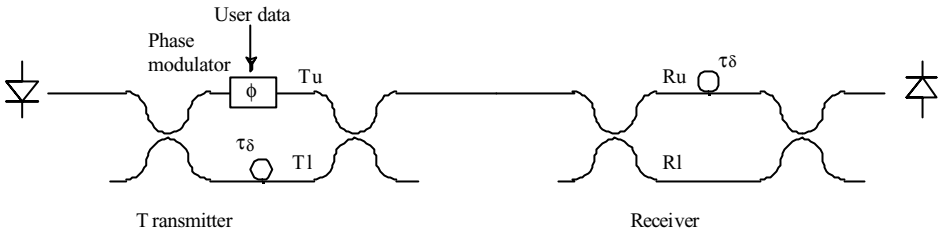

Figure 1.13: Coherence modulation

length difference before the photodiode. There are now four different paths between the light source and detector which are (with Tu and Tl identifying the upper and lower paths in the transmitter interferometer respectively, and Ru and Rl similarly for the receiver – see Figure 1.13): Tu-Ru, Tu-Rl, Tl-Ru and Tl-Rl. It can be seen from Figure 1.13 that the path lengths of Tu-Ru and Tl-Rl are equal so that (assuming the polarisation is aligned) there will be optical beating at the output coupler of the interferometer at the receiver, and the phase modulation imposed at the transmitter will appear as intensity modulation at the receiver output.

Coherence multiplexing [66] relies on path length differences for node addresses, and has been proposed both for passive star networks [68] and SLIM busses [69]. Coherence modulation was originally thought to be very secure since it was assumed that signal detection required knowledge of the precise value of τ_d, but it has now been demonstrated that data can be extracted by simple filtering [70].

Switching light between two polarisation states in the (single mode) fibre bus provides another form of modulation. Polarisation state modulation or polarisation shift keying (POLSK) [71] combined with CDMA has been proposed for channel sharing in passive star networks [72, 73], but there does not appear to be anything reported on its use in an optical bus. One possibility is discussed in Section 2.2.

1.2.4 Capacity sharing in a dark signalling bus

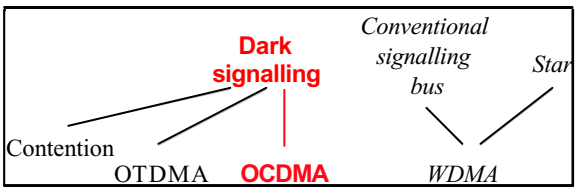

Restricting consideration to a dark signalling bus, the options for capacity sharing are code- and time-division, or contention with header address recognition. A brief discussion of WDMA in stars and conventional busses is also worthwhile, however, because of its importance as a competing technology.

It is convenient to distinguish between schemes in which destination addresses are

set up in hardware (wavelength channels in WDMA, time-slots in TDMA and signature sequences in CDMA) and schemes using addressed packets or frames. Schemes using the contents of the header to address the destination divide information in the time domain, but are distinguished from TDMA since the destination has to read the header to identify the intended destination, whereas in TDMA the address is determined by the position in time within a frame structure.

Ethernet use a contention scheme (CSMA/CD) for access to the medium and addressing via the frame header address, but in order to read the address it requires signal processing at the aggregate signalling rate on the medium. Work is under way to investigate packet switching in optical networks including all-optical processing for fast header recognition [74], but currently header recognition is electronic. Other approaches in the context of optical fibre busses have included encoding the address with a subcarrier [46] or with a parallel wavelength channel [48]. The work of this thesis, however, concentrates on optical hardware addressing to avoid the limitations of electronic processing.

Wavelength division multiple access has been proposed and demonstrated for capacity sharing/addressing in passive star networks. To allow addressing of nodes, wavelength tuning must be possible at the transmitters [75]), the receivers [76, 77, 78] or both [79]. (See [80] for an old but comprehensive review and categorisation of WDMA networks).

The available optical spectrum is divided into wavelength channels each of bandwidth B. To direct a signal to a given node (say node n), the transmitter sends data on a specific wavelength channel (say channel c) and the receiver has an optical filter selecting that channel. Channel c is the address of node n.

There are two possibilities:

1. Either node n has the channel c permanently associated with it, in which case the bandwidth B is reserved for use by node n

2. Or, if we want the bandwidth to be available to other nodes, then node n cannot have its own, unique, address and some sort of dynamic medium access protocol is needed, with tunable receivers and transmitters at each node.

Case 1 is wasteful of bandwidth, since the total available bandwidth has to be permanently divided between all addressable nodes – regardless of how active they are, or even whether they have yet been installed. Arguably case 1 is addressable wavelength division *multiplexing* (WDM)[10] not wavelength division *multiple access* (WDMA). Case 2 uses the bandwidth more efficiently, but at the cost of a complex medium access protocol which is likely to lead to access delays [81, 37].

It is possible for a conventional bus to use wavelength division multiple access (tunable lasers and/or receivers, as for a star) [82], but saturation effects when there

[10] Some authors refer to this as *fixed assignment* WDMA.

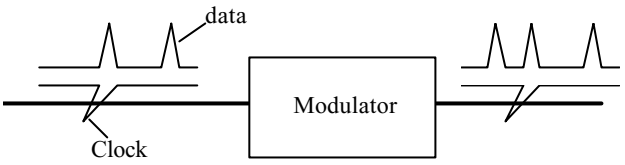

Figure 1.14: Generation of data pulses from clock pulses, with orthogonal polarisation states for clock and data (based on [2]).

are multiple wavelengths originating from different nodes in a single amplified bus limits the number of nodes compared to a WDM star topology [38], and, after [38], there has been little reported work on this approach. (Note that [48] uses WDM for parallelism in order to reduce the signalling rate on a fibre bus, but channel sharing is TDMA.)

An approach to TDMA in optical fibre LANs that has received much attention is a bus topology with a pulsed laser at the head end which provides a synchronisation clock. In the work reported in [83] and [2] and much similar work, addressing is by time slots, so that each node has a fixed time slot in a frame, and transmitting nodes direct data to the required destination by signalling in the appropriate slot. In other words they are 'addressable TDM' rather than true TDMA, with similar inflexibility in bandwidth allocation as for 'addressable WDM' discussed above. In [83] the pulses also form the data stream, and nodes signal by the removal of pulses (described as 'destructive signalling') creating a type of dark-signalling SLIM bus. In another variation of a 'SLIM bus', BT Labs have reported [2] on work in which data pulses are generated from clock pulses by electro-optic signal processing, and transmitted on the bus in an orthogonal polarisation state compared to the clock (Figure 1.14).

To exploit the optical bandwidth, signalling rates on an optical TDMA bus will need to be of the order of tens or hundreds of gigabits per second which makes the synchronisation for channel insertion and extraction a serious technical challenge.

A general characteristic of spread-spectrum modulation schemes is the need for a wideband channel because, in broad terms, spread-spectrum modulation trades signal power for bandwidth. Given the vast inherent bandwidth of optical fibre, therefore, it is not surprising that there has been a lot of interest in exploring the possibilities of optical spread-spectrum.

The virtues of CDMA are widely known [84], and in this context the principal benefits are:

1. A soft upper limit to the number of users
2. Compatibility with asymmetric and 'bursty' traffic
3. No access delay
4. Asynchronous transmission requiring no centralised control

5. Physical layer addressing with a large address space

CDMA is more flexible in bandwidth allocation than either WDMA or TDMA because with WDMA and TDMA the allocation of an address to channel in effect reserves channel capacity for that address.

With CDMA, in contrast, allocating a unique address code to a node does not reserve channel capacity for that node, so you can have permanent addresses as well as bandwidth flexibility.

Note that some authors have dismissed optical CDMA on entirely spurious grounds. Kazovsky et. al. in [85] say: "...the higher-speed synchronisation required for TDM and CDMA systems makes them unattractive for high-speed LAN applications". While this is true of TDM, much of the work on optical CDMA – see below, Section 2 – was undertaken precisely because implementations have been identified which avoid the need for high speed synchronisation. Green makes a similar error in [36].

As a consequence of the attractions of CDMA there have been many proposals for using CDMA in an optical network. Nearly all of these proposals assume the use of a passive star topology, but many of them are also suitable for use with a SLIM bus. Chapter 2 of this thesis reviews the proposals and considers their application for a dark signalling bus, and SLIM busses in general.

References to code division multiple access usually (as will be the case here) implicitly assume *asynchronous* CDMA. A number of authors, however, have explored the merits of synchronous optical CDMA [86, 87, 88] in which addressing uses the CDMA signature sequence as for asynchronous CDMA, but transmission of the signature sequences is constrained to be synchronised across all nodes.

Synchronous CDMA retains all the merits of asynchronous CDMA that were identified in the previous section, except that synchronous transmission requires centralised control. In exchange for relinquishing the flexibility of asynchronicity, synchronous CDMA benefits from dramatically improved efficiency in the trades-off between code length, multiple access interference and address space [87].

The work of this thesis has concentrated on asynchronous CDMA, but synchronous CDMA will be revisited in Section 2.8.

1.3 Conclusions: an all-optical LAN using OCDMA in a SLIM bus

On the wide-area network scale, the evolution to all-optical networking (the optical transport network) is becoming clear, with DWDM already being extensively installed in point-to-point links and switching with MEMS, wavelength conversion and reconfigurable wavelength routing in the medium term [26]. The position regarding LANs

is less clear[11], and the system investigated for the work of this thesis, CDMA in a dark-signalling SLIM bus, is one possibility among many contenders.

The key word characterising the present proposal is *flexibility*. As noted in Section 1.2.2 above (page 9), the bus topology is, physically, more flexible with regard to expansion with additional nodes, and this flexibility is supported by channel sharing with CDMA. CDMA is also flexible in the use of channel capacity because of the 'soft-limit' on the number of simultaneous users and because allocation of address space to nodes does not reserve bandwidth as is the case for fixed-assignment WDMA or TDMA.

In the past, these features of flexibility were found in Ethernet and go some way to explaining the success of Ethernet as the most widely installed electrical LAN technology. It can be seen as a goal of the work of this Ph.D. as being to create a LAN with the merits of the original Ethernet that exploits the capacity of fibre. Simply replacing the coaxial bus of Ethernet with fibre and using the CSMA/CD contention protocol is not an optical solution because:

- CSMA/CD becomes very inefficient at high signalling rates when the ratio between the propagation time and the frame transmission time becomes large [89]. In the evolution of the Ethernet standards this has led to the LAN switches with a star topology which can operate in full-duplex mode with no collisions [90], but at the cost of losing the benefits of the bus topology and substantially increased complexity in the switches.

- Amplification is needed to maintain power levels on the fibre bus. As will be seen in Chapter 4, Section 4.2, there are difficulties with controlling the signal to noise ratio in an amplified bus with conventional signalling.

In the present proposal CDMA provides similar characteristics to CSMA/CD – no access delay, soft limit to the number simultaneous users, compatibility with bursty traffic – and SLIM modulation in an amplified bus overcomes the problem of power levels in a fibre bus.

[11] Given the large-scale projects on WDMA in star networks in the industry – such as Rainbow II at IBM[76] and Lambdanet of Bellcore[77], going back as far as 1987 in the case of Lambdanet – it is perhaps surprising that this technology has not yet produced a commercial product. Green [26] has questioned whether LANs will ever go all-optical

Chapter 2

Review of optical CDMA

Given the potential merits of CDMA highlighted in the previous chapter, this chapter reviews the different schemes that have been proposed for implementing CDMA in optical fibre networks.

The main purpose of the review is to explore schemes for use in a SLIM bus, so prime consideration is given to how the proposals would work in a bus with in-line modulation, and how effective they would be used in that way. More generally, however, the inherent merits of the schemes are assessed and compared with the following in mind.

- The utilisation of the fibre, given by the maximum total aggregate data rate. This is calculated from the number of simultaneous users multiplied by the data rate per user, assuming all users operate at the same rate. In practical terms the data rate per user is generally limited either by the maximum electronic processing speed or by the system demand, so that often the more important criterion is the number of simultaneous users that the schemes can accommodate.

- The number of nodes that may be attached to the network. Destination addressing is built into the codes of CDMA, so the choice of CDMA scheme inherently limits the address-space and therefore the maximum number of nodes that may be connected to a network. In broad terms, the more addresses available the better.

- Power budgets. Network performance and dimensions may also be limited by power budget considerations as discussed in detail in Chapter 4, so the optical power loss through encoders and decoders will also need to be considered.

- Practical feasibility. One of the arguments for capacity sharing through CDMA was that it provided a practical way of accessing the fibre capacity, so the practicability of schemes needs to be taken into account. This is not to say that it should be possible to implement the schemes with currently available com-

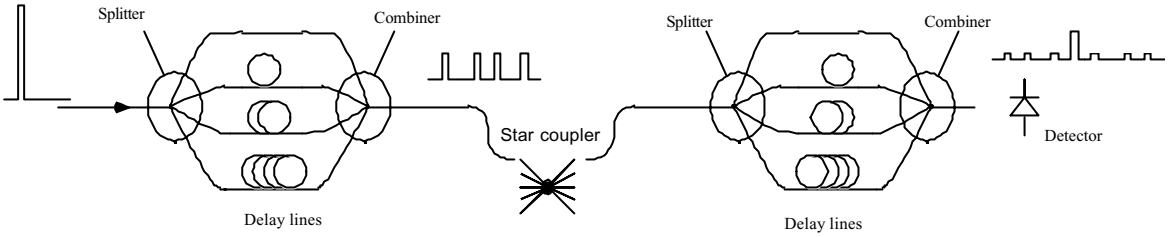

Figure 2.1: Optical CDMA scheme of Prucnal et. al. [3]

ponents, but it should be clear that the required technology is feasible in the medium term.

The review uses a classification based upon that of Karafolas and Uttamchandani [64]. In addition to the paper of Karafolas and Uttamchandani in 1996, there have been reviews of OCDMA by Iversen and Hampicke in 1995 [91], Parnham et. al. in 1992 [92] and Sampson et. al. [93]. The paper by Iversen and Hampicke in particular provides a useful qualitative comparison of the different schemes, although Karafolas and Uttamchandani is the most comprehensive.

Note that except where it is explicitly stated, throughout this Chapter it is assumed that all the optical fibre is single-mode.

2.1 Optical CDMA networks using matched filtering and incoherent detection: time addressing

Optical CDMA using matched filtering and incoherent detection was the concept that attracted the most research interest in the 1980s and 1990s because it was believed to offer the prospect of a simple way of the exploiting the high theoretical capacity of optical fibre using simple and readily-available optical devices without the need for high-speed electronics [94]. The approach is exemplified by the scheme proposed [3] and demonstrated [95] by Prucnal and shown in Figure 2.1. Short pulses are generated at the single channel data rate and electrically modulated by the channel data, then they are spread in time by a delay-line optical fibre filter to produce the signature sequence of the destination node. At the correct destination, the delay line matched filter superposes the pulses of the sequence to generate the autocorrelation peak which is detected by (electrical) threshold detection on the photodiode output. At the other receiving nodes the filter serves only to spread the incoming sequence further and there is no peak.

The attraction of the scheme comes from the fact that the electronics has only to modulate the data at the single channel rate and detect pulses (albeit very short pulses) at the single channel rate. The aggregate channel rate (chipping rate) processing is

handled by the optical delay-line filters and channel-rate time resolution is determined by optical path lengths in the delay lines. Millimetre accuracy in path lengths translates to time tolerances under 10 ps, allowing, potentially, the exploitation of hundreds of gigahertz of the channel bandwidth.

It should be noted that OCDMA in this form is rather different from CDMA as used in wireless communication (referred to here as 'traditional[1] CDMA'). Traditional CDMA relies on positive and negative contributions from orthogonal codes summing to zero. This is not possible with incoherent optical CDMA, and codes such as Gold codes [96] or Walsh functions [97] that were exploited in conventional CDMA are unsuitable for direct use in incoherent optical CDMA. This has led to the development of new code sets specifically for optical CDMA, referred to as 'optical orthogonal codes', OOCs[2]. These will be discussed further in Section 2.7, but, in general terms, OOCs are characterised by being low-weight (sparse) codes: they have few data 1s in long sequences of 0s to reduce the number of pulses that contribute to the interference. Notice that the coding is in the temporal relationship between the pulses in the code. This has led to the description *time address* coding [64] .

The correlator can be thought of as a 'mask' that lets light through in the (time) positions at which it expects pulses, according to its signature. This can be seen more clearly if the delay-line filter is drawn as a tapped-delay line, Figure 2.2, rather than in the form in which it is usually constructed, as it was shown in Figure 2.1 (the two forms are functional equivalent, but that of Figure 2.1 is easier to build). When the received sequence matches the 'mask', there are pulses at all the taps and the output (which, in the case of incoherent correlation, is an attenuated sum of the optical power coming from all the taps) is a maximum. If the received sequence does not match the mask, then there cannot be pulses on all the taps at the same time and the output will always be lower than when the matched sequence was received. Notice that with this, incoherent, system, the 'worst' that can ever come through a tap is zero: you cannot have negative power.

It is proposed in this thesis to translate the delay-line matched-filter optical CDMA to a SLIM bus implementation using the configuration of Figure 2.3. Correlation works in exactly the same way as with conventional (bright) signalling, except that with the matched code the delayed pulses of darkness emerge simultaneously, and the output will be zero.

[1] A better word would be 'conventional', but this might cause confusion with the use of 'conventional signalling' to distinguish bright signalling from dark signalling.

[2] There is some confusion in the use of the term 'OOC'. It is defined in [98] as a code set with constraints on cross-correlation ($\leq \lambda_c$) and offset autocorrelation ($\leq \lambda_a$), assuming unipolar correlation. Generally, though, the term is reserved for codes with λ_c and λ_a both 1 (ideal OOC) or 2, so, for example, prime sequences ($\lambda_c = 2$, $\lambda_a = P$) are sometimes called OOCs, sometimes not.

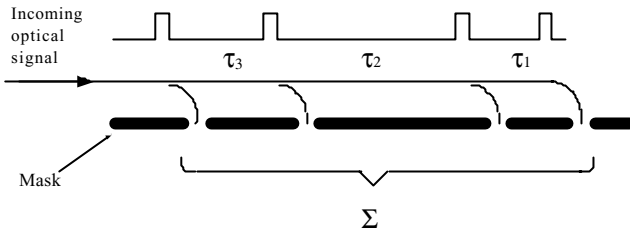

Figure 2.2: The fibre tapped delay-line as equivalent to a pattern mask

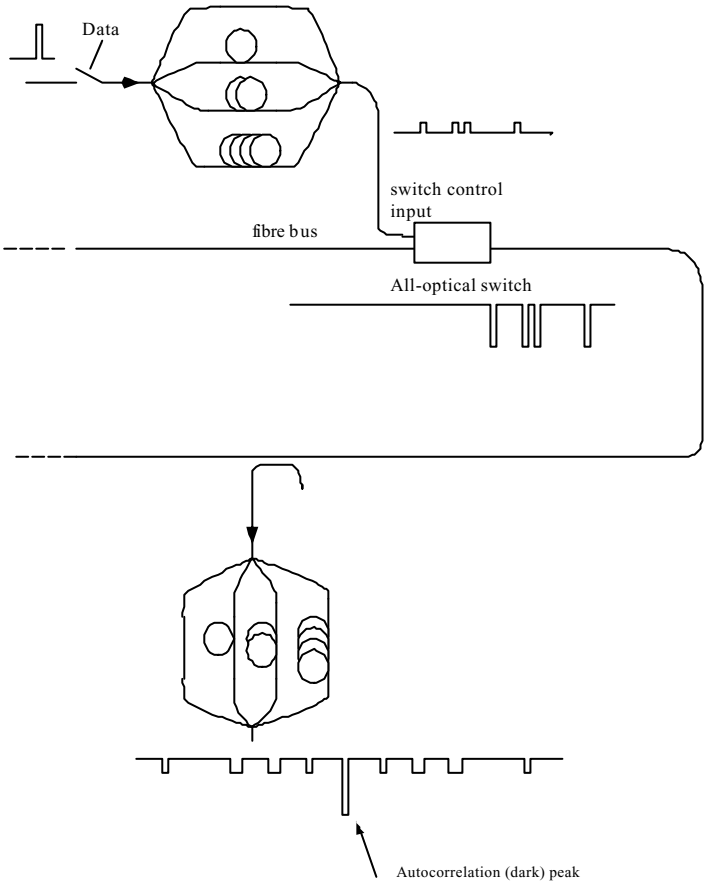

Figure 2.3: Using delay-line matched filters with CDMA in a SLIM bus

2.1.1 Improving the power budget: ladder networks

Even neglecting excess losses – considering only inherent losses – the incoherent delay-line matched-filter scheme has unfavourable power budgets.

The implementation of the delay-line filter of Figure 2.1 using single mode optical fibre is straightforward since the splitters and combiners are readily constructed from fused-fibre couplers. For an equal passive split into P ways, conservation of energy requires that there is an attenuation of $1/P$ to each output. Combining from P single-mode fibres to one single-mode fibre, however, also incurs an attenuation[3] of $1/P$. Following through the path in Figure 2.1, therefore, it can be seen that the autocorrelation peak will be attenuated by a factor $1/\left(P^3N\right)$, where N is the number of nodes (the splitting at the central passive star coupler in a star network configuration), compared to the initial pulse driving the filter at the transmitter. P, the number of paths – taps – in the encoder and correlator, is determined by the number of pulses in the spread sequence, and, as discussed in Section 2.7, useful network dimensions will require P to be greater than about 7. At the very minimum, with $P = 7$, there is therefore a loss due to the filters alone of at least $7^3 = 343$, $10\log_{10}(343) = 25.4$ dB.

Proposals motivated by a desire to reduce this loss suggest the use of ladder networks [99, 100] for the delay line filters (Figure 2.4), which have a total loss of 1/4 (6 dB) independent of the number of pulses. If the fixed couplers are replaced by switches (switchable between the 'straight through' and 'mix-and-split' states, where the mix-and-split state is a 3 dB coupler) the ladder network can be adjusted to select the destination address. The disadvantage of the use of a ladder network, however, is that it restricts the selection of codes – ladder networks can only generate codes that have symmetrical distribution of 2^n pulses, where n is the number of steps in the ladder [101]. Codes compatible with ladder networks ("2^n codes") have been developed [102, 103], but compared to codes for optical CDMA without this restriction the 2^n codes have to be much longer to support a given number of simultaneous users.

A variation of the use of a ladder network, however, is the proposal of Tančevski and Andonovic [104] in which ladder networks are used as programmable delay lines to generate 'block multiplexing codes' such as the prime codes [105]. For a single pulse in there is a single pulse out, but the delay from input to output is programmable. The technique proposed by Tančevski and Andonovic, shown in Figure 2.5 involves reconfiguring the delay-line during the generation of a sequence. For example, the prime codes are sequences of length P^2 and weight P, where P is a prime number, made up of P blocks of P chips, each containing a single pulse (i.e. each block is $P-1$ 'spaces' and 1 'mark'). To generate the code a source produces regular, short, pulses at the rate of one per block. The delay-lines then reposition the pulse in time within

[3] This is not strictly true, because so-called 'single' mode fibre actually conveys two (degenerate) polarisation modes. It is possible therefore in principle to couple without loss from two input fibres to one output fibre - in effect running a polarisation fibre beam-splitter in reverse. This is discussed further in Chapter 5

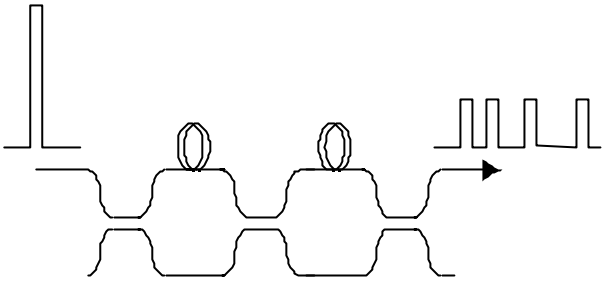

Figure 2.4: Delay-line filter with the 'ladder' topology

each block, using a different time delay for each block. Reconfiguration is done once per block, so the reconfiguration rate is P times the data rate, but $1/P$ times the chipping rate.

The method is not suitable for the matched filter at the receiver because the need to reconfigure during the sequence would require synchronisation between transmitter and receiver, so Tan□evski and Andonovic propose using a programmable encoder at the transmitter and a 'conventional' (parallel) fixed delay line correlator at the receiver.

For the proposed SLIM implementation (Figure 2.3), the loss in the transmitter is not necessarily a limiting factor since the optically generated chip sequence is used to operate the in-line modulator/switch: it is not transmitted directly. The attenuation of the encoder does not appear in the transmitter-to-receiver power budget and it will be seen in Chapter 5, furthermore, that the proposed hybrid correlator (the attenuation of which does appear in the power budget) has no inherent loss. The encoder must, however, be programmable in order to be able to address the destination node.

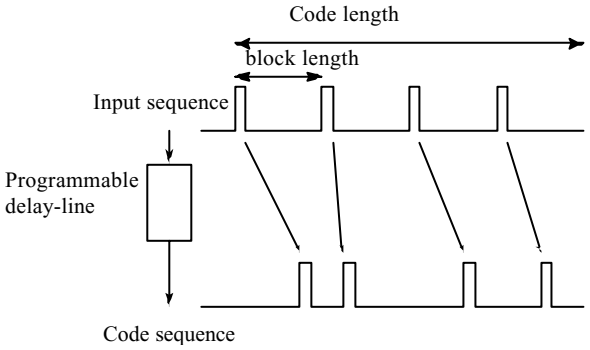

Figure 2.5: The block multiplexing coding scheme of Tan□evski and Andonovic

2.1.2 Unipolar/bipolar coding

Compared to bipolar codes such as Gold codes, the OOCs needed for incoherent OCDMA are very inefficient (in order to allow a given number of simultaneous users and a given number of discrete addresses, OOCs have to be much longer than Gold

codes) and this has led to investigations into methods that might allow the use of bipolar codes with optical CDMA.

There have been a number of proposals that have allowed bipolar codes to be used in conjunction with incoherent correlation through the use of balanced receivers in one form or another [106, 107, 108, 109]. In the case of [106] the correlator output is compared with a reference which is proportional to the number of simultaneous users – measured from the mean signal power on the input. The cross-correlation of the codes is known, so knowledge of the number of interfering users allows the appropriate offset to be subtracted by the reference. In [108] and [109] differential detection is used and the coding ensures that interfering users contribute equal signal levels to both components in the differential subtraction. [107] is sequence inversion keying and the receiver correlates against both the sequence (transmitted to represent a data 1) and its complement (transmitted to represent a data 0). The balanced receiver subtracts the output of the latter from the output of the former, and the coding ensures that interfering users contribute equally to both. Common to all of these schemes is the use of intensity information on the fibre on the (implicit) assumption that the fibre is an adder channel [110], in contrast to the OOCs which use the fibre as an OR-channel [111]. The proposed dark-signalling SLIM bus inherently uses the fibre as an OR channel. Indeed, as will be seen in the performance analysis (Chapter 8), the fact that dark signalling is inherently a logical OR channel is beneficial to the correlator performance with OOCs. The bipolar schemes [106, 107, 108, 109] are not, therefore, applicable to the dark-signalling SLIM bus. (It is perhaps also worth noting that in none of the proposals for these bipolar schemes examined was the effects of optical interference considered. In practice it would be a significant source of signal degradation and would probably be the limiting factor on the number if simultaneous users.)

2.1.3 Combining pulse-position modulation with time addressing OCDMA

Pulse position modulation (PPM) encodes M-ary input data by the location of a short pulse in one of M time slots within the symbol period (Figure 2.6(a)). In combined PPM-CDMA [112], the short pulse is replaced by the signature sequence of the destination node (Figure 2.6(b)). The signature sequence may either be entirely contained within the time slot (as drawn in Figure 2.6b), or may extend over several time slots for 'overlapping PPM-CDMA' (Shalaby [113]). In the limit of overlapping PPM the chip duration may equal the period of the slot – an approach proposed by Elmirghani and Cryan [114] and called here 'fully-overlapping PPM-CDMA'.

The pulse position is generated electrically by the data source, while the CDMA signature sequence may be generated (and detected) by optical delay lines. With the non-overlapping scheme, the chipping rate is much greater than the PPM slot-rate and the electrical components only operate at the slot rate. With the fully-overlapping

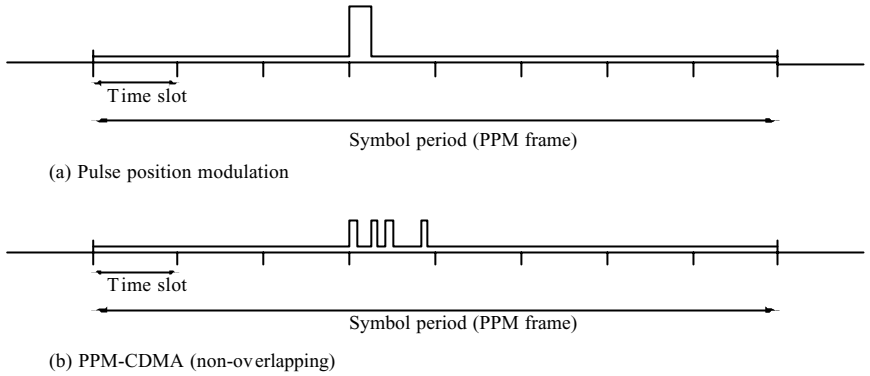

Figure 2.6: Using OCDMA with pulse position modulation (drawn with $M = 8$).

scheme, on the other hand, the chipping rate equals the slot rate and the electrical components operate at the chipping rate. Chan et. al. [115] have shown that if the constraint is the chipping rate, then fully-overlapping CDMA provides a higher per-channel data rate than OOK (on-off keying). With delay-line CDMA sequence generation and correlation, however, the constraint will be the PPM slot-rate, not the chipping rate, and the per-channel data rate is higher for OOK than for either overlapping or non-overlapping PPM.

The main benefit claimed for using PPM rather than OOK with optical CDMA is that PPM reduces the signal power level required for a given data rate (Shalaby in 1995 [116] and Elmirghani et. al. in 1996 [117]). In the application of interest to Elmirghani et. al. (infrared wireless LANs [118]) this is significant because power levels are low, but is probably not a major concern of optical fibre LANs in general.

These schemes – PPM-CDMA – may be readily employed in a dark-signalling form in a SLIM bus, replacing bright pulses by dark pulses. There may be benefits in using PPM rather than OOK since PPM-OCDMA frames using OOCs are even more sparse than OOCs alone (since all but one of the PPM slots is empty) which reduces the probability of 'hits' between users, but further work is required to determine whether this results in an overall improvement in performance.

2.2 Optical CDMA networks using matched filtering and coherent detection

The incoherent schemes discussed in the previous section have the advantage of simplicity, but using delay-line filters with highly coherent optical sources, such that the coherence length of the source is much longer than any path-length differences in the filter, results in significant performance benefits. In particular, with ladder networks [7], ideal performance is obtained if both outputs from the ladder of the encoding filter are connected to the inputs of the correlator at the receiver (links through both (c) and

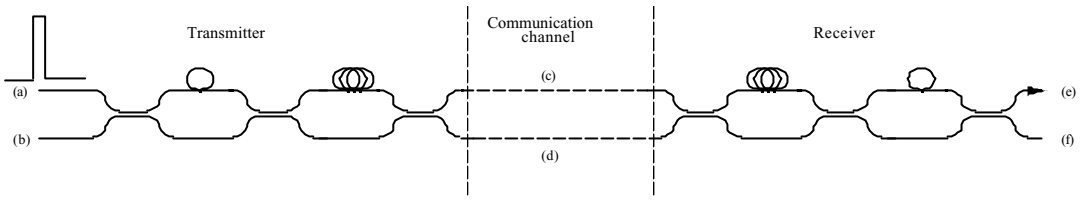

Figure 2.7: Configurations for coherent optical CDMA using ladder networks

(d) in Figure 2.7, which is based on Reference [7]). Assuming perfect and optically identical paths for (c) and (d) (no excess loss, no relative phase differences, matched polarisation states) the input pulse on (a) is perfectly and completely reproduced on (e). Furthermore, a second pulse may be transmitted simultaneously from (b) to (f).

While perfectly matching two fibres for paths (c) and (d) is impractical, Marhic proposes in [7] a scheme which he claims has practical possibilities. This is to use two orthogonal polarisation states on the same fibre for the paths (c) and (d). Furthermore, the correlators can be constructed from single segments of highly-birefringent (hi-bi) fibre, connected with 45^o rotations between the segments so that the optical path-length differences between the fast and slow polarisation states generate the differential correlator delays. Thus the whole system of Figure 2.7 becomes a single fibre with segments of hi-bi fibre spliced to form the filters. Star couplers can in principle be constructed with polarisation independence, so that single fibre may be linked as part of a passive star network.

The *2-channel coherent decoding* (also called *inverse decoding)* system just described has severe implementation difficulties even using the single fibre method, but a 1-channel version, in which only one of (c) or (d) are connected (it does not matter which) is more feasible and has been demonstrated by more than one research group (Chang and Marhic at Northwestern University, Illinois [119] and Griffin et. al. at the University of Kent at Canterbury [120])[4]. A necessary feature of the coherent correlation is the control of the relative phase in each of the arms of the correlator at the receiver and a method of doing this using thermal phase controllers has been developed and demonstrated by the group at Canterbury [121] – this is discussed further in Chapter 5. The 1-channel system has slightly inferior performance compared to the 2-channel system, but still exceeds that of incoherent correlation (Table 2.1).

Using a highly coherent source and polarisation and phase control in the correlator, the SLIM bus implementation of Figure 2.3 can be operated as a 1-channel coherent system – with some practical advantages as a consequence of the single, common, light source, compared to the passive star implementation – and this is considered further

[4] 2 channel decoding has also been demonstrated by Change and Marchic, both with a single ladder network used for encoding and decoding (reflecting the output back to the input [101]) and with separate encoders and decoders [7], but they do not appear to have been very robust since only: "...with appropriate care and patience ... was [it] possible to observe the desired results".

Scheme	Peak energy	Side lobes
Incoherent	P	$P-1$
Coherent 1-channel	P^2	< 1
Coherent 2-channel	$4P^2$	0

Table 2.1: Comparison of Ladder CDMA networks using Coherent or Incoherent decoding. P is the code weight. (From [7])

in Chapters 5 and 8.

There are also very interesting possibilities for two channel operation of a SLIM bus. If the bus is made of polarisation maintaining fibre the two polarisation modes of the fibre may be used as two channels, as in the proposal of Chang and Marhic previously mentioned [7]. The light is launched into one mode at the start of the bus and then at each node an in-line modulator acts to rotate the polarisation for the duration of each chip in the signature sequence of the destination node (see Figure 2.3, with the 'all-optical switch' acting as a polarisation rotator). This provides a mechanism for launching a 2-channel signal on to the bus which, in principle, can be detected by a 2-channel coherent correlator at the receiver.

An interesting feature of this scheme is that the bus behaves as an Ex-OR channel, because rotation of the state of polarisation twice returns it to the original state. Multiple access codes for an Ex-OR channel requires further study, but are discussed briefly in Section 2.7 below.

As with the passive star, however, there are severe practical problems with the implementation of a 2-channel bus, and it has not been pursued any further in this project, but is recommended for further study.

2.3 Spectral encoding CDMA

A technique that has been used to encode in the frequency domain is to distribute frequency components spatially with a diffraction grating, modulate the components with a mask, then recombine the components, again with a diffraction grating (Figure 2.8). The coded output signal is given by the Fourier transform of the pattern transferred by the mask on to the spectrum. At the destination a similar process recovers the original input signal by matching the encoding and decoding masks. Since the spreading is done in the frequency domain – implemented spatially by the mask – the processing all takes place at the single channel data rate.

Salehi et. al. [122] have proposed and demonstrated spectral encoded CDMA with coherent ultrashort input pulses using a phase mask. The mask contains a pseudorandom spatial pattern of 0 and π phase shifts which transforms the incident ultrashort pulse into a low intensity pseudonoise signal. At the addressed destination a conjugate mask recovers the original coherent pulse, but any other mask – the wrong address – changes the phase but does not recover the pulse: the output is still a

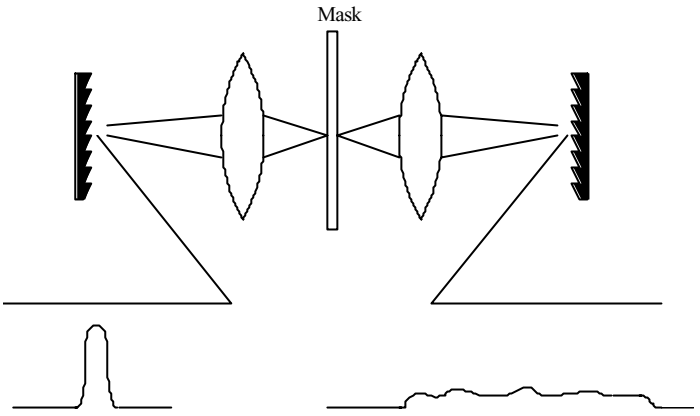

Figure 2.8: Spectral coding

low-intensity pseudonoise signal.

Although there has been a proof-of-concept experiment reported [123], there remain severe practical difficulties for the coherent ultrashort spectral coding system for a number of reasons, including: the need for coherent (near transform-limited) ultrashort pulses, the need for perfect alignment and matching of the masks, and problems of dispersion in the transmission.

Kavehrad and Zaccarin [124] have proposed a related but more robust system which uses a broadband, incoherent, optical source (LED) and amplitude (on-off) masks. Coding does not, in this system, spread the data pulses (because they are far from transform-limited), and signal discrimination is based upon a different principle from that of the coherent system, involving differential detection. Suppose that node destination d is addressed by a mask $A_d(\omega)$. The receiver of node d has both the mask $A_d(\omega)$ and the complementary mask, $\overline{A_d(\omega)}$, where $\overline{A_d(\omega)}$ lets through all frequency components blocked by mask $A_d(\omega)$ and blocks all components let through by mask $A_d(\omega)$. Clearly, if the received data is addressed for this node, then all the light will pass through $A_d(\omega)$ and be blocked by $\overline{A_d(\omega)}$. The codes are chosen such that for a signal encoded by any other mask used by the code set, the attenuation of $A_d(\omega)$ will be the same as that of $\overline{A_d(\omega)}$. The receiver therefore subtracts the signal passing through $\overline{A_d(\omega)}$ from that passing through $A_d(\omega)$, with the result that a net output only emerges when the received signal was addressed to this node. As explained in [124], suitable code sets (such as the phases of pseudo-noise signals – 'M-sequences') allow the number of orthogonal codes in the set to equal the number of steps in the mask – determined by the resolution of the grating.

The proposals for all of these spectral schemes are for use in a passive star, and a fundamental limitation, which was not considered by the original authors but has been shown [125] to provide a severe limit to the number of simultaneous users, is the effect of optical beating between different users. This limitation has been taken by some authors ultimately to disqualify the schemes as serious contenders for capacity

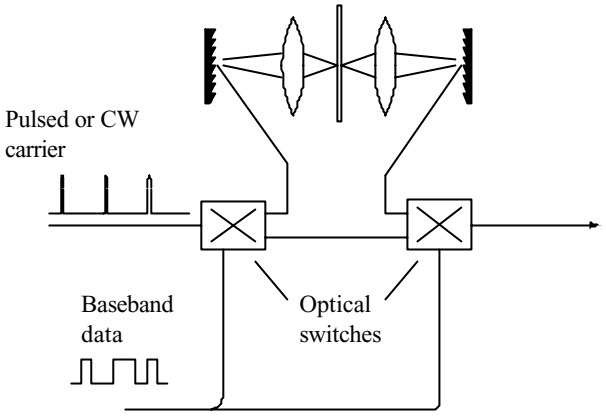

Figure 2.9: Spectral modulation in a SLIM bus.

sharing in an optical network [64]. It is a feature of the SLIM bus, however, that optical beating may be eliminated because there is only a single optical carrier shared by all users, so it is worth considering spectral modulation further in the context of SLIM signalling.

In-line spectral modulation might be possible with a scheme such that illustrated in Figure 2.9, whereby the baseband data diverts the light in the bus via a spectral encoder to represent a data 1. The light on the bus might be pulses, for a scheme based on that of Salehi et. al. [122], or continuous-wave, for a scheme based on that of Kavehrad and Saccarin [124]. The schemes would not transfer directly to the SLIM implementation, however, because the SLIM bus is not an adder channel, as assumed for the star implementation. Thus, for example, if one coherent pulse is spread by more than one transmitting node, the pulse can only be recovered by the use of *both* conjugate masks, not by *either alone* – as would be required for correct operation. Further work would be needed to investigate appropriate spectral encoding schemes.

2.3.1 Combined spectral coding and coherence multiplexing

A variation of coherence modulation (Section 1.2.3 above) has been proposed in which spectral coding by a phase mask is included in one of the arms of the interferometers at both the transmitter and receiver [126]. Signals are then only recovered both if the phase masks match at the transmitter and receiver and the optical path length differences are the same.

2.4 Frequency/wavelength hopping

Tančevski et. al. [127] have reported schemes combining wavelength-hopping with time addressing. In these schemes each of the pulses in a time-spread signature sequence is at a different wavelength, the sequence of wavelengths following a defined hopping

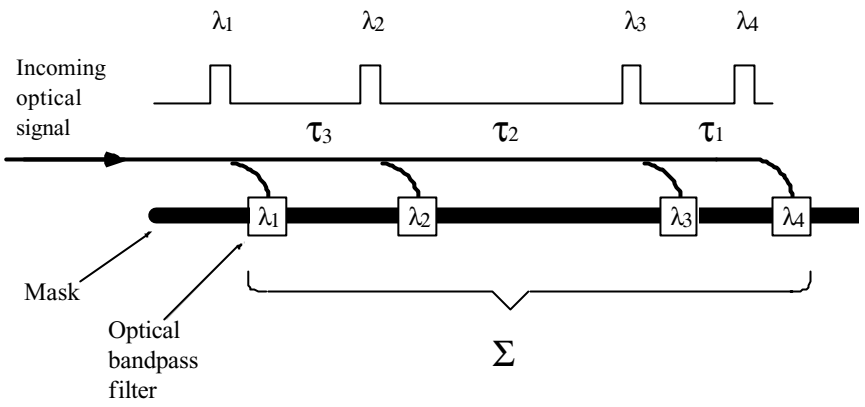

Figure 2.10: Correlator for wavelength-hopping, time spreading optical CDMA

pattern (Figure 2.10), and the matched filter at the receiver incorporates filters in each of the delay lines. In this way codes are defined both by the time sequence and the hopping pattern, resulting in a very large address space (which, it is claimed [128], gives the scheme inherent security) and the potential for many simultaneous users. An additional advantage is that since each of the pulses being brought together in the correlator output is at a different wavelength, the noise from optical beating is heterodyne rather than homodyne and provided the wavelengths are sufficiently widely spaced, can be removed by lowpass filtering[5].

The codes can be generated by:

- a tunable laser to change the wavelength for each pulse in a programmable delay line,
- a multiwavelength source and optical filters in the delay-line encoder

The tunable laser has no role in a SLIM bus, but there may be scope for a system based upon a multiwavelength source at the start of the bus and optical filters at the nodes. This requires further investigation.

An alternative method of generating a wavelength hopping sequence which uses fibre Bragg gratings was proposed by Fathallah et. al. [129] and is shown in Figure 2.11. A short, broadband, pulse is directed along a fibre in which is written a sequence of discrete fibre Bragg gratings. Each of the gratings has a different pitch and corresponds to a different frequency component of the pulse. The reflected signal is therefore a frequency hopping signal in which the frequencies are determined by the pitch of the grating and the pulse positions are determined by the positions of the gratings along the fibre. Piezoelectric devices can be used to stretch the gratings to provide frequency tuning. An optical circulator (or directional coupler, if the additional loss may be tolerated) directs the hopping sequence onto the output fibre.

[5] The beating due to different users on the network remains.

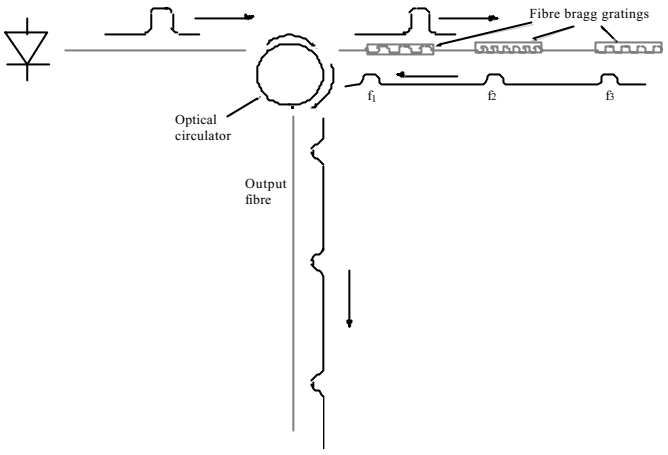

Figure 2.11: Frequency-hop coding using a fibre Bragg grating

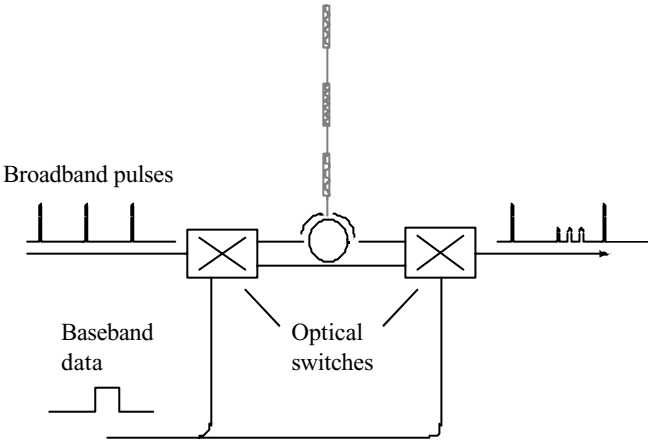

Figure 2.12: Use of Bragg gratings for frequency hop encoding in a SLIM bus

While the Bragg encoding method might be adapted for encoding signals in-line in a SLIM bus (Figure 2.12), further work is needed to investigate how usefully this could be exploited in a multiple access bus. In particular, the effects of multiple encoding of the same pulse need to be explored. (The first encoding generates a frequency hopping pattern and subsequent encodings would rearrange the pulses. Whether it is possible to devise a system in which the rearrangements convey the fact of the repeated encoding – and whether this information may be readily extracted at the destinations – is not immediately clear, but is an intriguing problem and recommended for further work.)

2.5 Optical frequency hopping

Kiasaleh has proposed [130, 63] a scheme in which electrically generated (slow) frequency-hopping signals modulate the phase of an optical carrier in a phase-modulation SLIM bus (see the optical phase division multiplexing scheme of Cimini [62] discussed ear-

lier).

The receiver extracts the frequency-hopped signal from the optical phase with a phase discriminator then decodes the signal with an electrical correlator in the usual way.

As proposed, this scheme seems to have little to commend it since it makes severe demands upon the optical components – the phase discriminator – yet the processing for the multiple access channel sharing is handled in electronics.

2.6 Systems using serial electro-optic correlation

There have been a number of proposals based upon serial correlation at the receiver – multiplying the received waveform with a replica of the signature sequence, as used in radio CDMA [131, 84]. The modulation and the correlation are done with amplitude or phase electro-optic modulators (for ASK/OOK or PSK/FSK respectively), and signal detection (following correlation) can be done:

- coherently, using a local oscillator (laser) [132, 133];
- coherently, using a self-homodyne receiver with either a differential modulation scheme[134] or distribution of a common carrier from a central source [135, 136];
- or non-coherently, using a narrowband optical filter [137, 138].

All these schemes – which were proposed for a passive-star network – are potentially compatible with a SLIM bus implementation, but they have not been investigated in this thesis because they require high-speed (chipping-rate) electronics.

2.7 Codes for incoherent optical CDMA

As was discussed in Section 2.1, optical CDMA (OCDMA) using incoherent detection differs fundamentally from 'conventional' CDMA because the optical channel is used as an 'OR' channel rather than an adder channel. Codes suitable for use with conventional CDMA [139] do not work well with OCDMA [140] unless special receiver designs are implemented as described in Section 2.1.2, so work has been undertaken to develop new codes (optical orthogonal codes, OOCs) specifically for OCDMA [98]. This section introduces some of the terminology and classes of OOCs and presents some results on the limitations and capabilities inherent in CDMA in an OR channel. The focus of the work of this thesis (in common with most other work on OCDMA) has been on asynchronous CDMA, but some authors have claimed advantages to synchronous CDMA in optical networks. This is examined briefly in Section 2.8.

In one of the earliest papers on optical CDMA [105, 141], Shaar and Davies in 1983 proposed the prime sequences [142] as suitable codes for use with optical CDMA. The key feature of the prime sequences exploited for OCDMA is that:

> [A set of prime sequences] possesses the property that the peak value of the periodic cross correlation function equals either one or two for all possible pair combinations of the sequence set, independent of the sequence length. [105]

In general, multiple access interference (MAI) is minimised by ensuring that the peak value of cross-correlation between any pair of code words in a code set never exceeds some (low) value, called the cross-correlation constraint, λ_c.

Another desirable characteristic of code sets for CDMA is a bound on autocorrelation. Ideally, each member of code set should have a 'drawing-pin'[6] autocorrelation characteristic: peak at zero time offset and close to zero for all time offsets beyond one chip. The autocorrelation characteristics of a code set are then specified by the autocorrelation constraint, λ_a, which is the upper limit to the value of the autocorrelation function for any time offset beyond one chip, for any code in the set.

In general, a code set, C, is described by the quadruple $(n, w, \lambda_a, \lambda_c)$ where n is the length of the code words (number of chips per bit), w is the weight (the number of 1s in each code word – assumed to be the same for all codes in the set), and λ_a and λ_c are the (cyclical) auto- and cross-correlations constraints described above. The number of codes in the set, the code *cardinality*, $|C|$, determines the address space of the CDMA scheme using the code. The prime sequences, however, do not have an autocorrelation constraint. (This absence of a constraint on autocorrelation does not necessarily disqualify them for use as in optical CDMA, but a system using prime sequences would have additional problems in attaining and maintaining synchronisation.) From a prime number, p, prime sequences of weight p and length p^2 form a $\left(p^2, p, p, 2\right)$ code with cardinality p.

2.7.1 Bounds on code cardinality

The maximum cardinality of an $(n, w, \lambda_a, \lambda_c)$ code is denoted by $\Phi\left(n, w, \lambda_a, \lambda_c\right)$ and an *optimal* code is one for which $|C| = \Phi\left(n, w, \lambda_a, \lambda_c\right)$. In general, both the calculation of $\Phi\left(n, w, \lambda_a, \lambda_c\right)$ and the construction of codes which approach optimality are difficult problems that have led to many publications in the literature. Exact formulae for $\Phi\left(n, w, \lambda_a, \lambda_c\right)$ are not available, but upper and lower bounds have been derived:

Upper bound, for $\lambda_a > \lambda_c$ (From [143])

$$\Phi\left(n, w, \lambda_a, \lambda_c\right) \leq \frac{\left(n - \lambda_a\right)}{w} \frac{\left(n-1\right)\left(n-2\right)...\left(n - \lambda_c\right)}{w\left(w-1\right)...\left(w - \lambda_c\right)} \tag{2.1}$$

Upper bound, for $\lambda_a = \lambda_c$ (This is a tighter bound than 2.1 when $\lambda_a = \lambda_c$. Derived in [98] using the Johnson Bound [144] from the theory of error correcting codes.

[6] Perhaps more usually called by the US word for a drawing-pin: a 'thumbtack' characteristic.

See also a direct derivation in [143])

$$\Phi(n,w,\lambda,\lambda) \leq \frac{(n-1)(n-2)...(n-\lambda)}{w(w-1)...(w-\lambda)} \tag{2.2}$$

Lower bound (Derived in [98] using the greedy algorithm, and strictly only valid when n is an odd prime [145])

$$\Phi(n,w,\lambda_a,\lambda_c) \geq \frac{\left(\begin{array}{c} n \\ w \end{array}\right) - \frac{n-1}{2}\left(\begin{array}{c} w \\ \lambda_a+1 \end{array}\right)\left(\begin{array}{c} n \\ w-\lambda_a-1 \end{array}\right)}{n\sum\limits_{i=\lambda_c+1}^{\min(n-w,w)}\left(\begin{array}{c} n-w \\ w-i \end{array}\right)\left(\begin{array}{c} w \\ i \end{array}\right)} \tag{2.3}$$

2.7.2 Code constructions

In addition to the prime sequence codes discussed above, notable code constructions include:

Extended Quadratic Congruence codes (EQC) These codes were proposed by Marić in [146], and are $(p(p-1), p, 1, 2)$ codes with cardinality $p-1$

$(n, w, 2, 1)$ **codes of Yang and Fuja** In [143], Yang and Fuja presented techniques for constructing $(n, w, 2, 1)$ codes with n prime and with cardinality $|C|$:

- for w odd, $n = \left(w^2-1\right)|C|/2+1$ (so cardinality $|C| = 2(n-1)/\left(w^2-1\right)$)
- for w even, $n = w^2|C|/2+1$, (so cardinality $|C| = 2(n-1)/w^2$)

2.7.3 A specific example

Some insight into these results can be derived by examining a particular case. For a network with 500 nodes, for example, a $(9001, 6, 2, 1)$ code can be constructed following the methods of Yang and Fuja with $w = 6$ and $|C| = 500$, so that $n = 36 \times 500/2+1 = 9001$ (which is indeed prime).

The formulae for the bounds on the cardinality of a $(9001, 6, 2, 1)$ code give an upper bound (using 2.1) of 600 and a lower bound (using 2.3) of 20. Clearly, with a known cardinality of 500, the code of Yang and Fuja cannot be far from optimal.

Looking at prime sequence and EQC codes of similar length leads to a prime sequence $(9409, 97, 96, 2)$ code with cardinality 97 and an EQC $(8911, 67, 2, 1)$ code with cardinality 66. The cardinality of these codes is too small for a network with 500 nodes, but to get a cardinality of at least 500 requires a $(253\,009, 503, 502, 2)$ prime code or $(505\,515, 503, 2, 1)$ EQC code.

The quarter- or half-million chip codes that would be required to uniquely address 500 nodes with prime or EQC codes are clearly unrealistic, but even a 9001-chip code of Yang and Fuja would have practical difficulties. The tapped delay lines (programmable

at the transmitter) would need to be accurate and stable to within 1 chip in 9000, or about 0.01%. Further work is needed to determine how feasible such tolerance would be. For comparison, TDMA with time-slot addressing to 500 nodes requires a frame length of something over 500 (for the frame alignment overheads), so that the relative synchronisation tolerances (again, programmable at either the transmitter or receiver) are of the order of 0.2%, but this tolerance has to be referenced to a global frame synchronisation.

(Petrovic and Holmes [147] have also pointed out that the cross-correlation constraint of most codes proposed for asynchronous OCDMA strictly require the *bit* timing of all the users to be matched to within one chip in a period – otherwise the designed chip alignments will not be maintained across chip boundaries. They have proposed in [147] alternative codes that remove this constraint, but further work is needed to examine the actual significance of a chip timing.)

2.7.4 Trade-offs and the use of error control coding

In general terms, for a given code length (n), increasing the code weight (w) for fixed cross-correlation constraint (λ_c), decreases the effects of MAI (because more interfering code 'hits' are necessary to imitate the auto-correlation peak) but decreases the code cardinality. Relaxing the cross-correlation constraint (increasing λ_c) has the converse effect: it increases the code cardinality but also increases the effects of MAI. The only way to increase code cardinality without degrading MAI is to increase the code length.

Code cardinality is a 'hard-limit', in the sense that there has to be sufficient codes for the required number of addresses, whereas the effects of MAI are soft – the error probability rises gradually as MAI increases.

For example, consider an application with the following constraints:

1. address space
2. maximum tolerable error probability
3. target minimum number of simultaneous users
4. signalling rate

Meeting the first three of these simultaneously determines the minimum code length, which, given the fourth (signalling rate), determines the data rate per channel. If a shorter code is used, it will need to have higher cross-correlation constraint in order to serve the address space, which in turn increases MAI. It is possible, however, to combat MAI through error control coding. Error control coding requires redundancy in the data and therefore decreases the user data rate. If, however, the reduced data rate due to redundancy for error control coding is less than the increased data rate due to the use of a shorter (CDMA) code, then there will be an overall gain.

The exploitation of error control coding in this way for optical CDMA has been investigated by a number of authors [148, 149, 150, 151] and it has been shown that a coding gain is indeed possible.

2.8 Synchronous optical CDMA (SCDMA)

As noted in Chapter 1, Section 1.2.4 (page 17), synchronous CDMA dramatically improves efficiency in the trade-offs between code length, multiple access interference and address space.

Since, in synchronous CDMA, the receiver examines the correlator output only at one instant in the chip-interval, code sets for SCDMA are described by the triple, (n, w, λ), where n is the code length, w the code weight and λ the maximum cross-correlation between any pair of codes in the set.

In general, a $(n, w, \lambda_a, \lambda_c)$ code, C_a, with cardinality $|C_a|$ designed for asynchronous CDMA can be used as a $(n, w, \max(\lambda_a, \lambda_c))$ code, C_s of cardinality $|C_s| = n\,|C_a|$ for SCDMA, since each of the n time shifts of each unique code word of C_a can be used as a unique code word in C_s. So, for example, the $(9001, 6, 2, 1)$ code with cardinality 500 discussed above can be used as a $(9001, 6, 2)$ code with cardinality 54 500 500: more than 54 million unique addresses. (There are also code sets designed specifically for SCDMA [152], but for comparisons with asynchronous CDMA it is convenient here to consider those derived from codes already discussed.)

Because of the absence of an autocorrelation constraint, this procedure cannot be usefully applied to the prime sequence codes. In [87], however, Kwong et. al. describe the construction of a *modified prime sequence code* which selects a subset of the prime sequences to generate a $(p^2, p, 1)$ code of cardinality p^2. The cardinality of the modified prime sequence codes is the same as their length, which is, in effect, the same as for fixed-assignment TDMA (neglecting frame alignment overheads). In [88] and [152] Kostic et. al. develop further codes for SCDMA, and again the sequence lengths equal the code cardinality. Comparing SCDMA using these sequences with fixed assignment TDMA, they both require synchronisation and offer the same data rate for a given signalling rate, but whereas TDMA is error-free (neglecting noise) for any number of simultaneous users, SCDMA suffers from multiple access interference. There is no apparent benefit to SCDMA in this case.

SCDMA could provide benefits over TDMA if the cardinality exceeded the code length [153], as in the example of the $(9001, 6, 2)$ code described above – the 9001-chip code is capable of uniquely addressing more than 54 million nodes. Looking at a more realistic possibility, Chung at. el. [98] describe a $(63, 3, 1, 1)$ code with cardinality 10. This could be used as a $(63, 3, 1)$ code with cardinality 630 to provide the addressing of the 500-node network (it could, of course, address up to 630 unique nodes). For a given signalling rate, S, SCDMA in this case allows individual nodes a significantly

higher data rate than fixed-assignment TDMA ($S/63$ compared to $S/500$, an increase of a factor $500/63 \approx 8$). The trade-off is that the error rate increases (softly) as the number of simultaneous users increases in SCDMA, but TDMA is always error-free (neglecting noise). With a weight of only 3, the number of simultaneous users accommodated by the $(63, 3, 1)$ code before the error probability becomes excessive would be relatively small, but other codes are possible (such as a $(156, 6, 1)$ code with cardinality 780, taken from a $(156, 6, 1, 1)$ code in [98]) and for a given system a code which provides the most appropriate balance for the expected loading would be selected. In general terms, SCDMA with short, low weight, codes are most appropriate for networks supporting very 'bursty' traffic while TDMA is most appropriate if the traffic loading is even.

It should also be noted that the comments of Vadja in [154] on MAI in asynchronous optical CDMA apply even more explicitly for SCDMA. Communication to given destination address (node D) will fail if the simultaneous users happen to have chips that, combined, replicate the signature sequence of D. While these users are active, communication to node D will be useless – it is not a case of individual errors – so for any given destination address the channel is either 'OK' or 'not OK'. There is still, however, a soft limit as a function of the number of simultaneous users on the *probability* of communication to node D being 'not OK' (the more interfering users there are the greater the probability of the channel being 'not OK'). In asynchronous optical CDMA the interference changes as the relative phases of the sequences from each user drifts, but in synchronous optical CDMA the phases are fixed so the interference conditions only change when users start or stop transmission.

SCDMA in a SLIM bus requires further work, but it is worth noting that synchonisation is easier in a bus topology than a star, since in the star some method is needed to accommodate the different path lengths to each terminal [155].

2.9 Conclusions: choosing OCDMA for a dark-signalling SLIM bus

Signalling schemes developed for passive star networks (the network topology assumed for most of the work on optical CDMA to date) do not necessarily transfer directly to a SLIM bus because the shared communication channel is fundamentally different in a SLIM bus compared to a passive star.

A passive star network is an 'adder channel' because the power on the combined channel is given by a summation (attenuated) of the power from each of the active nodes. The type of channel created by in-line modulation in a SLIM bus depends upon the type of modulation used. Dark-signalling creates an OR-channel: the output is dark for one or more simultaneous dark pulses. (Equivalently it could be described as an AND channel: the output is bright only if all nodes are simultaneously bright.) With

polarisation modulation the channel can be an exclusive-OR channel as discussed in Section 2.2 above, and it is possible to conceive of adder channels with angle modulation because if the modulator is a frequency-shifter, successive nodes shift the frequency further.

The OCDMA scheme chosen for further investigation in this thesis is described as time addressing with incoherent delay-line matched filters (Section 2.1). This transfers well to dark signalling on a SLIM bus, since not only is it compatible with an OR-channel created by dark-signalling, but in fact it performs *better* without the intensity information that comes with an adder channel [156]. Also, there has been a lot of previous work on developing codes sets for time-addressed incoherent OCDMA (Section 2.7). The proposed scheme does not require high-speed electronic processing (which was one of the main motivations for the original proposals for OCDMA [3]) and the required optical processing is possible with currently-known optical devices.

This final point – that the proposed system is possible with currently known optical devices – contrasts with some proposals for OCDMA which assumed the availability of exotic devices such as optical hard-limiters (usefully considered – in order to investigate possibilities – in some of the early papers [156], but taken to extremes in some later work [157, 158, 159]). No such unproved exotic devices are required for the networks proposed in this thesis.

Chapter 3

Optical beating

The error rate in a communication link is determined by the signal to noise ratio at the receiver, where noise in this context is taken to include naturally occurring effects such as thermal noise as well as interference. In the case of communication in a network using CDMA, multiple access interference (MAI) is particularly important. MAI is determined by the code alone and for some contexts is dominant to the extent that network performance may be adequately assessed without consideration of other sources of noise. This was the assumption of the early proposals for optical CDMA (see for example reference [140]), but the reality can be very different and performance can only be determined when performance modelling takes into account other sources of noise a well as MAI.

Shot, thermal (Johnson) and amplifier noise are found in the receiver as with all optical systems [160], but optical beating is a particularly important source of noise in optical CDMA networks [93], so this is analysed in some depth in this chapter.

Beating occurs when two or more optical fields are simultaneously present at a receiver, because of the square-law response of photodiodes (see Section 3.1). In conventional (bright-signalling) multiple-access optical networks the multiple fields can originate from different nodes in the network. In a dark-signalling bus, where there is only one light source, beating can still be encountered for two reasons. First, if there are optical amplifiers in the bus there will be amplified spontaneous emissions (ASE) which can beat with the signal. Second, if there are multiple paths from the light source to the receiver, homodyne beating might be encountered when the light recombines. Since multiple paths are inherent to delay-line correlators, this is an important consideration for optical CDMA.

Two categories of optical source need to be considered [161]: narrowband and broadband. The model for a narrowband source is of a monochromatic, coherent, field and will be used for the light output from a single mode laser diode. The model for a broadband source is of a band-limited, thermal-like chaotic field, and will be used for the output of an LED and for ASE from optical amplifiers. Depending on the network configuration, there can be multiple narrowband, multiple broadband or

combinations of both present simultaneously. Although more than two fields can be present simultaneously, an understanding of the general features of all possible beating combinations can be seen by considering the beating between pairs of fields in the three possible combinations: narrowband-narrowband, broadband-broadband and narrowband-broadband. Models for these combinations are derived in Sections 3.2, 3.5 and 3.3 respectively.

There is also noise from a broadband source alone which may be interpreted as beating between different Fourier components of the field. A model for this is presented in Section 3.3.

Although the main purpose of this chapter is to develop models that are used in simulations in later chapters, some initial conclusions about design choices for minimising noise can be drawn from the nature of the models (Section 3.7).

3.1 Photodetection

Photodiodes measure optical power and are therefore square-law devices with respect to the optical field strength. Where two optical carriers are simultaneously incident upon a photodiode, therefore, beating between the optical frequencies generates interferometric noise on the output. This can be the limiting factor in multiple access optical networks – a fact that has been overlooked in much of the analysis of optical CDMA until a paper by Smith et. al. in 1995 [125] (and has been overlooked in more recent papers), although it had earlier (1988) been analysed in subcarrier multiplexed systems [162] and led to proposals aimed at eliminating beating through the use of a common source [163].

It is usual ([164, 165], and many others) for the square-law relationship between field strength and photocurrent to be presented as:

$$i(t) = \mathcal{R} E(t)^2 \tag{3.1}$$

Where $\mathcal{R}$ is the photodiode responsivity and $E(t)$ is the electrical field of the optical signal. This is appropriate for many modelling applications, but it hides a number of assumptions and for the work of this thesis[1] it is important to appreciate precisely under what conditions Eqn. 3.1 may be used.

Consider a single-mode fibre, the end-face of which is in contact with the surface of a photodiode. The photocurrent is given by (using the convention of underlining to represent vectors):

$$\begin{aligned} i(t) &= \mathcal{R} P(t) \\ &= \mathcal{R} \int_S \left(\underline{E}(\underline{a}, t) \times \underline{H}(\underline{a}, t) \right) . \underline{da} \end{aligned}$$

[1] Specifically, it is significant that beating only occurs when two signals are in the same fibre mode. Equation 3.1 takes no account of the spatial distribution of the field.

$\mathcal{R}$ is the photodiode responsivity, $\underline{E}(\underline{a},t)\times\underline{H}(\underline{a},t)$ is the Poynting vector at position $\underline{a}$ on the photodiode surface and S is the detector area so that $P=\int_S\left(\underline{E}(\underline{a},t)\times\underline{H}(\underline{a},t)\right).d\underline{a}$ is the (instantaneous) power incident on the photodiode [166]. It is convenient now to make a number of simplifying assumptions:

- Using the weakly guiding approximation, the fields are well modelled by transverse modes [5], then $|\underline{E}(\underline{a},t)\times\underline{H}(\underline{a},t)|=\sqrt{\epsilon/\mu}E(\underline{a},t)^2$ ([166], ϵ is the permittivity and μ the permeability of the glass).
- the photodiode surface is normal to the (weakly guiding) fibre axis, so that $\left(\underline{E}(\underline{a},t)\times\underline{H}(\underline{a},t)\right).d\underline{a}=|\underline{E}(\underline{a},t)\times\underline{H}(\underline{a},t)|\,da=\sqrt{\epsilon/\mu}E(\underline{a},t)^2\,da$
- considering a single polarisation mode of the fibre, the field distribution is uniquely determined by the (single) mode distribution. Then

$$P(t)=\int_S\left(\underline{E}(\underline{a},t)\times\underline{H}(\underline{a},t)\right).d\underline{a}=E_t(t)^2\int_S\sqrt{\epsilon/\mu}E_s(\underline{a})^2.da \tag{3.2}$$

In the last step the time dependence of the field has been separated from the spatial dependence ($\underline{E}(\underline{a},t)=E_t(t)E_s(\underline{a})$). In choosing the scaling factors of E_t and E_s it is possible for E_s to be normalised so that $\int_S\sqrt{\epsilon/\mu}E_s(\underline{a})^2.da=1$, and $P(t)=E_t(t)^2$ (but E_t does not now have the dimensions of voltage), leading to Eqn. 3.1 for the photocurrent (dropping the suffix t):

$$i(t)=\mathcal{R}E(t)^2 \tag{3.3}$$

For the rest of this section, reference to 'electric fields', E, should be taken in this sense. (An alternative – as in [167] – is to use a revised responsivity: $\mathcal{R}_E=P_0\mathcal{R}$. However the responsivity $\mathcal{R}$, in amps/watt, is a specified parameter of photodiodes and so it is useful to keep it in the algebra.)

Squaring the optical field in equation 3.3 results in double optical frequency terms in the photocurrent (since $\sin^2(\omega t)=0.5-0.5\cos(2\omega t)$). Clearly fluctuation in the photocurrent at twice optical frequencies (i.e. of the order 10^{14} Hz) will not be detectable, and they can be dismissed by arguing that there are inherent low-pass filtering effects in the photodiode. A full analysis of the interaction of light with matter, however, requires a quantum mechanical model, and when this is done it can shown that the twice optical frequency terms never appear [168]. (Similarly, when examining beating between two optical fields the sum-frequency terms that emerge from the square-law detector are shown not to exist in a quantum mechanical model [169].) This point will be revisited below, but for the moment the analysis is continued using a purely classical model, and the inconvenient double-frequency terms removed by assumed low-pass filtering.

With the filtering, the measurable photocurrent will be given by:

$$i(t)=\mathcal{R}\overline{E(t)^2} \tag{3.4}$$

Where the bar represents time averaging over a time interval that is long compared to optical periods but short compared to any modulation or the effects or difference frequencies in optical beating. That is:

$$\overline{E^2(t)} = \frac{1}{T}\int_0^T E^2(t)\,dt \tag{3.5}$$

With $1/\omega \ll T \ll 1/(\Delta\omega)$ for ω the central optical frequency and $\Delta\omega$ the spectral width of the signal $E(t)$. Thus the photocurrent will not follow the optical frequency oscillations, but will reflect any noise due to optical beating.

It will be particularly convenient to use the analytic representation of optical signals [170, 171] and to describe the field by [164] (using bold face to represent complex variables):

$$\mathbf{E}(t) = \sqrt{2P_0}\mathbf{u}(t)\,e^{-i\omega t}$$
$$E(t) = \mathrm{Re}[\mathbf{E}(t)]$$

Where $\mathbf{E}(t)$ is the analytic signal and $E(t)$ is the real signal. P_0 is the optical power, and $\mathbf{u}[t]$ is a complex envelope function, normalised so that

$$\overline{|\mathbf{u}(t)|^2} = 1$$

A monochromatic signal $E(t) = \sqrt{2P}\sin(\omega t + \phi)$, for example, has the analytic representation $\mathbf{E}(t) = \sqrt{2P}e^{-i\phi}e^{-i\omega t}$.

It can be shown [171] that using the analytic representation the averaging of Eqn. 3.5 is given by $\frac{1}{2}\mathbf{E}[t]\,\mathbf{E}^*[t]$ (where $\mathbf{E}^*$ is the complex conjugate of $\mathbf{E}$.). Thus:

$$i(t) = \frac{1}{2}\mathcal{R}\mathbf{E}[t]\,\mathbf{E}^*[t] = \mathcal{R}P$$

As required.

Notice that by using the analytic representation and modelling the detector as responding to $\frac{1}{2}\mathbf{E}[t]\,\mathbf{E}^*[t]$ rather than $E(t)^2$, the classical model is effectively adjusted to accommodate the result from quantum mechanics that there are no double-frequency terms in the photocurrent. This approach of a classical model modified by 'rules' which take account of quantum mechanics is a recognised modelling technique referred to as the 'semi-classical' approach [168], and is the approach of this thesis.

The remaining sections in this chapter consider several different fields resulting from network and receiver configurations of interest.

3.2 Two narrowband fields

In conventional (bright-signalling networks) using lasers, two narrowband fields can be present simultaneously at a receiver. The fields might, for example, be combined with a directional coupler as in Figure 3.1.

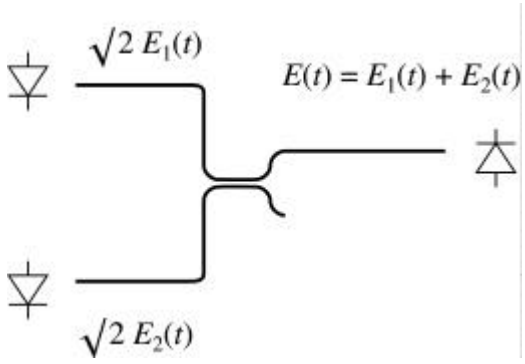

Figure 3.1: Combining two fields in single mode fibre using an ideal directional coupler. The lauched fields are scaled by $\sqrt{2}$ for the convenience of compensating for the splitting loss in the coupler.

The fields are modelled by analytic signals as above, neglecting, for the present, polarisation state by assuming that all signals are in the same state. Intensity noise (which, from a laser, is generally small [172]) is also neglected, but the effects of phase noise are included through the time dependence of ϕ. The two fields are described by: $\mathbf{E}_1(t) = \sqrt{2P_1}e^{-\phi_1[t]}e^{-i2\pi f_1 t}$ and $\mathbf{E}_2(t) = \sqrt{2P_2}e^{-\phi_2[t]}e^{-i2\pi f_2 t}$ and the photocurrent is given by:

$$\begin{aligned} i(t) &= \frac{1}{2}\mathcal{R}\left(\mathbf{E}_1(t) + \mathbf{E}_2(t)\right)\left(\mathbf{E}_1(t) + \mathbf{E}_2(t)\right)^* \\ &= \mathcal{R}\left(P_1^2 + P_2^2 + 2\sqrt{P_1P_2}\cos\left(2\pi\left(f_1 - f_2\right)t + \phi_1[t] - \phi_2[t]\right)\right) \end{aligned} \tag{3.6}$$

If one of the fields (say $\mathbf{E}_1$) is the incoming signal and the other derives from a local laser, then Eqn. 3.6 represents coherent optical detection [173]: homodyne if $f_1 = f_2$ or heterodyne if $f_1 \neq f_2$.

From [174, 175], if the two optical sources are modelled by a Lorentzian spectrum [171] of full-width at half maximum, (FWHM) linewidths ν_1 and ν_2 then the power spectrum of the photocurrent is given by:

$$i^2(f) = \frac{2}{\pi\nu_m}\mathcal{R}^2P_1P_2\left(\frac{1}{1 + \left(\left(f - \Delta f\right)/\nu_m\right)^2} + \frac{1}{1 + \left(\left(f + \Delta f\right)/\nu_m\right)^2}\right)$$

Where $\Delta f = f_1 - f_2$ is the difference between the centre frequencies and $\nu_m = (\nu_1 + \nu_2)/2$ is the average of the two FWHM linewidths. For identical sources with $\Delta f = 0$ and $\nu_1 = \nu_2$,

$$i^2(f) = \frac{4}{\pi\nu_1}\mathcal{R}^2P_1P_2\left(\frac{1}{1 + \left(f/\nu_1\right)^2}\right) \tag{3.7}$$

3.2.1 Noise power

In general there will be low-pass filtering in the receiver which is modelled by a 'brick-wall' filter with cut-off B_e (for the electrical bandwidth). For identical sources, the

power passed by the filtering is given by:

$$N = \frac{4}{\pi}\mathcal{R}^2 P_1 P_2 \tan^{-1}\left(B_e/\nu_1\right) \tag{3.8}$$

For $B_e \gg \nu_1$ this tends to $2\mathcal{R}^2 P_1 P_2$.

3.3 A single broadband field

In addition to narrowband, monochromatic, light, the other category of optical field that needs to be considered is that from a broadband source such as a non-lasing LED or the ASE from an optical amplifier. Light in this category is variously referred to as 'chaotic' [161], 'thermal-like' [170] or 'incoherent' [176], and many different physical mechanisms can result in light with a similar statistical description [161]. The statistics of chaotic light are such that even with light from a single source incident upon a photodetector there will be a significant noise component (*excess photon noise*, *wave interaction noise* [176] or *intermodulation noise* [177]) which can be interpreted as due to beating between different Fourier components in the source spectrum [177].

The analysis used here is based upon that of Goodman [170] and, as for the monochromatic source, uses an analytic field $\mathbf{E}_s(t) = \sqrt{2P_s}\mathbf{u}_S(t)\,e^{-i\omega_0 t}$ and considers a single polarisation state, but now ω_0 is the centre frequency of a broadband source of spectral width B_S Hz. Both $\mathbf{E}_s(t)$ and $\mathbf{u}_S(t)$ may be modelled by circular complex Gaussian random processes. (See Goodman [170], Section 4.2. In very general terms the Gaussian output is expected as a consequence of the central limit theorem, since the field is derived from a sum of a large number of independent contributions from exited atoms or molecules.)

The analysis proceeds by first deriving the autocorrelation function of $i(t)$ and then using the Wiener-Khinchin theorem [178] to derive the power spectrum (cf. [179]). As before, the photocurrent is given by:

$$i(t) = \frac{1}{2}\mathcal{R}\mathbf{E}_S(t)\,\mathbf{E}_S^*(t)$$

For the autocorrelation function of $i(t)$:

$$R_i(\tau) = \overline{i(t)\,i(t+\tau)} = \frac{1}{4}\mathcal{R}^2\overline{|\mathbf{E}_S(t)|^2\,|\mathbf{E}_S(t+\tau)|^2} \tag{3.9}$$

$\overline{|\mathbf{E}_S(t)|^2\,|\mathbf{E}_S(t+\tau)|^2}$ is evaluated in Appendix B, leading to:

$$\frac{R_i(\tau)}{\mathcal{R}^2} = P^2 + P^2\left(\frac{\sin(\pi\tau B_s)}{\pi\tau B_s}\right)^2 \tag{3.10}$$

From the Wiener-Khinchin theorem the power spectrum of $i(t)$ is derived by the Fourier transform of $R_i(\tau)$, which can be seen from Eqn. 3.10 to consist of :

1. a dc term (impulse at the origin) of strength $\mathcal{R}^2P^2$, corresponding to the signal power (current-squared)

2. (from the $(\sin(x)/x)^2$ term – see Section B.2) a triangular baseband spectrum, shown in Figure 3.2, of (single-sided) width B_S Hz, and zero-frequency power (current-squared) spectral density of $2\mathcal{R}^2P^2/B_S$. This represents the interferometric noise, for beating between the independent components of the source. Notice that for a given signal power, the power spectral density is inversely proportional to the source spectral width.

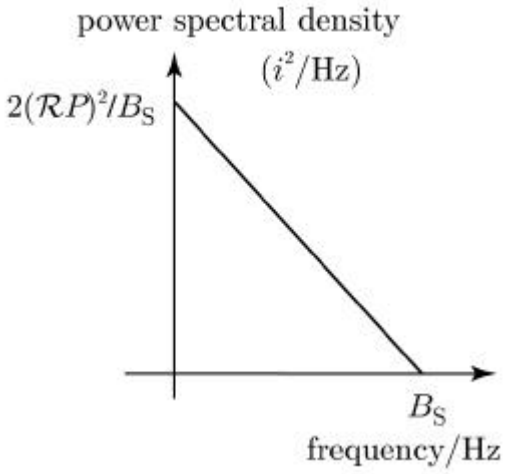

Figure 3.2: Power spectral density of the beating noise of a single thermal source

3.3.1 Noise power

For 'brick-wall' filtering with cut-off B_e, the noise power getting through is given by (for $B_e < B_S$):

$$N = \mathcal{R}^2P^2\frac{B_e}{B_S}\left(1-\frac{B_e}{4B_S}\right) \tag{3.11}$$

3.4 A narrowband and a broadband field

If a laser transmits in a fibre containing optical amplifiers there will be both a coherent field (from the laser) and a chaotic field (from the ASE – amplified spontaneous emission [54] – of the amplifier(s)) present simultaneously at the photodetector. This combination has been analysed by Olsson in [177], but is reformulated here to be consistent with the terminology of the thesis.

Assuming that the broadband field (of spectral width B_1) is centred on the frequency of the monochromatic signal and representing the combined analytic signal by

$$\mathbf{E}_s(t) = \mathbf{E}_1(t) + \mathbf{E}_2(t)$$

With $\mathbf{E}_1(t) = \sqrt{2P_1}\,\mathbf{u}_1(t)\,e^{-i\omega_0 t}$ and $\mathbf{E}_2(t) = \sqrt{2P_2}e^{-i\omega_0 t}$.

Then

$$i(t) = \frac{1}{2}\mathcal{R}\mathbf{E}_S(t)\,\mathbf{E}_S^*(t)$$

For the autocorrelation function of $i(t)$:

$$\begin{aligned} R_i(\tau) &= \overline{i(t)\,i(t+\tau)} \\ \frac{4R_i(\tau)}{\mathcal{R}^2} &= \overline{\mathbf{E}_S(t)\,\mathbf{E}_S(t)^*\,\mathbf{E}_S(t+\tau)\,\mathbf{E}_S(t+\tau)^*} \end{aligned} \tag{3.12}$$

Expanding the expression in terms of the individual fields gives 16 terms, which may be evaluated as follows:

1. The fields are statistically independent, so that averages of products may be replaced by products of averages
2. Both fields have zero mean, so $\overline{\mathbf{E}_1(t)}$, $\overline{\mathbf{E}_1(t+\tau)}$, $\overline{\mathbf{E}_2(t)}$ and $\overline{\mathbf{E}_2(t+\tau)}$ are all zero. This means that all 'unbalanced' terms – terms with three contributions from field 1 and one contribution from field 2 (such as $\overline{|\mathbf{E}_1(t)|^2\,\mathbf{E}_1(t+\tau)\,\mathbf{E}_2^*(t+\tau)}$) or vice versa – are zero.
3. The terms in $\mathbf{E}_2(t) = \sqrt{2P_2}e^{-i\omega_0 t}$ may be calculated directly:

$$\begin{aligned} \overline{|\mathbf{E}_2(t)|^2\,|\mathbf{E}_2(t+\tau)|^2} &= 4P_2^2 \\ \overline{\mathbf{E}_2^*(t)\,\mathbf{E}_2(t+\tau)} &= 2P_2\overline{e^{i\omega_0 t}e^{-i\omega_0(t+\tau)}} = 2P_2e^{-i\omega_0\tau} \\ \overline{\mathbf{E}_2(t)\,\mathbf{E}_2^*(t+\tau)} &= 2P_2e^{i\omega_0\tau} \end{aligned}$$

4. The terms in $\mathbf{E}_1(t)$ are calculated in Appendix B.

Finally:

$$\frac{R_i(\tau)}{\mathcal{R}^2} = (P_1+P_2)^2 + P_1^2\left(\frac{\sin(\pi\tau B_1)}{B_1\pi\tau}\right)^2 + 2P_1P_2\frac{\sin(\pi\tau B_1)}{B_1\pi\tau}$$

This transforms (Appendix B.2) to a spectrum with :

1. a dc term (impulse at the origin) of strength $\mathcal{R}^2(P_1+P_2)^2$
2. (from the $(\sin(x)/x)^2$ term) a triangular baseband spectrum of single-sided width B_1 Hz, and zero-frequency power (current-squared) spectral density of $2\mathcal{R}^2P_1^2/B_1$.
3. (from the $\sin(x)/x$ term) a rectangular baseband spectrum of (single sided) width $B_1/2$ Hz and power-spectral density $4P_1P_2/B_1$

These terms are displayed in Figure 3.3.

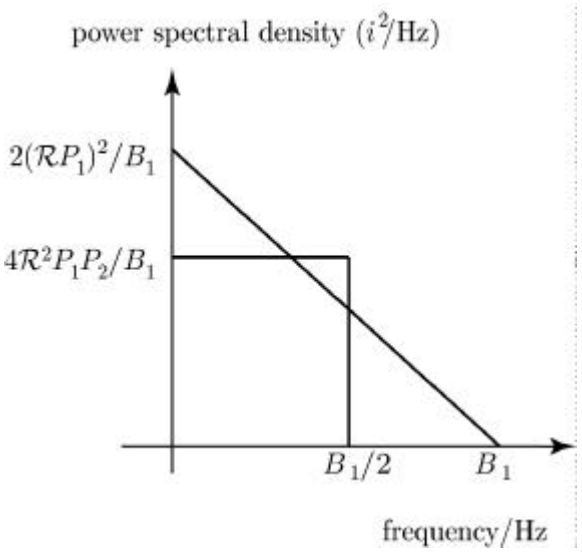

Figure 3.3: Power spectral density due to beating in the presence of one narrowband and one monochromatic field

3.4.1 Noise power

If the electrical filtering is modelled by a 'brick wall' low-pass filter of bandwidth B_e, then the contribution to the variance of the current from the two terms shown in Figure 3.3 can be derived from the area under each curve between 0 and B_e Hz. This gives:

1. $E_1 \times E_1$ beating (intermodulation noise): $\sigma^2_{1-1} = B_e\,(2B_1 - B_e)\,\mathcal{R}^2\,(P_1/B_1)^2$
2. $E_1 \times E_2$ beating (cross-modulation noise): $\sigma^2_{1-2} = 4B_e\mathcal{R}^2P_1P_2/B_1$

3.5 Two broadband fields

A system using an LED as a source with optical amplifiers will have two broadband fields present simultaneously.

Again:

$$\mathbf{E}_s\,(t) = \mathbf{E}_1\,(t) + \mathbf{E}_2\,(t)$$

But now $\mathbf{E}_1\,(t) = \sqrt{P_1}\,\mathbf{u}_1\,(t)\,e^{-i\omega_0 t}$ and $\mathbf{E}_2\,(t) = \sqrt{P_1}\,\mathbf{u}_2\,(t)\,e^{-i\omega_0 t}$ and both fields are modelled by flat power spectral densities of width B_1 and B_2, both centred on the same frequency f_0. The signal powers are P_1 and P_2 respectively, so their (double sided) power spectral densities are $P_{1,2}/2B_{1,2}$.

The autocorrelation of the photocurrent $\overline{(i\,(t)\,i\,(t+\tau))}$ again expands to 16 terms which are simplified as before ($\mathbf{E}_1\,(t)$ and $\mathbf{E}_2\,(t)$ statistically independent and zero mean). The remaining terms in $\mathbf{E}_1\,(t)$ and $\mathbf{E}_2\,(t)$ are both calculated using the results

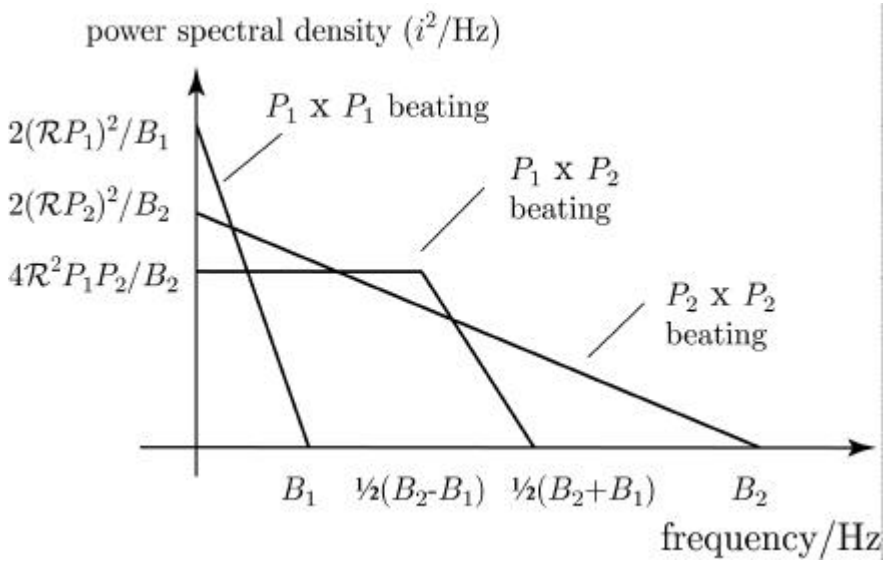

Figure 3.4: The power spectral-density of optical interference for two broadband signals

of Appendix B, leading to:

$$\begin{aligned}\frac{R_i(\tau)}{\mathcal{R}^2} &= (P_1+P_2)^2 + P_1^2\left(\frac{\sin(\pi\tau B_1)}{B_1\pi\tau}\right)^2 + P_2^2\left(\frac{\sin(\pi\tau B_2)}{B_2\pi\tau}\right)^2 \\ &\quad + \frac{P_2P_1}{\pi^2\tau^2B_1B_2}\left(\cos(\pi\tau(B_1-B_2)) - \cos(\pi\tau(B_1+B_2))\right) \qquad (3.13)\end{aligned}$$

This transforms to a spectrum with components (Appendix B.2):

1. $\mathcal{R}^2(P_1+P_2)^2$ is the D.C. current. In the frequency domain, it is an impulse at 0 Hz.
2. $\mathcal{R}^2P_1^2\left(\frac{\sin(\pi\tau B_1)}{\pi\tau B_1}\right)^2$ transforms to a triangular baseband spectrum of single-sided width B_1 Hz, and zero-frequency spectral density of $2\mathcal{R}^2P_1^2/B_1$
3. $\mathcal{R}^2P_2^2\left(\frac{\sin(\pi\tau B_2)}{\pi\tau B_2}\right)^2$ transforms to a triangular baseband spectrum of single-sided width B_2 Hz, and zero-frequency spectral density of $2\mathcal{R}^2P_2^2/B_2$
4. $\frac{P_2P_1}{\pi^2\tau^2B_1B_2}\left(\cos(\pi\tau(B_1-B_2)) - \cos(\pi\tau(B_1+B_2))\right)$ transforms to a trapezoidal baseband spectrum, flat at $n_0 = 4\mathcal{R}^2P_1P_2/B_2$ from 0 to $(B_2-B_1)/2$ Hz and falling linearly to 0 at $(B_1+B_2)/2$ Hz.

These terms are displayed in Figure 3.4.

3.5.1 Noise power

The electrical filtering is modelled by a 'brick wall' low-pass filter of bandwidth B_e. The contribution to the variance of the current from the three terms shown in Figure 3.4 can be derived from the area under each curve between 0 and B_e Hz. This gives:

1. $E_1 \times E_1$ beating (E_1 intermodulation noise): $\sigma_{1-1}^2 = B_e\left(2B_1 - B_e\right)\mathcal{R}^2\left(P_1/B_1\right)^2$
2. $E_2 \times E_2$ beating (E_2 intermodulation noise): $\sigma_{2-2}^2 = B_e\left(2B_2 - B_e\right)\mathcal{R}^2\left(P_2/B_2\right)^2$
3. $E_1 \times E_2$ beating (cross-modulation noise): $\sigma_{1-2}^2 = 4cB_e\mathcal{R}^2P_1P_2B_1/B_2$

Where the factor c depends upon the magnitude of B_e:

$$c = \begin{cases} 1 & \text{for } B_e \leq \left(B_2 - B_1\right)/2 \\ \left(3B + 12B_1B_e + 4B_2B_e^2 - 2B_1B_2 - B_2^2 - 4B_e^2\right)/8B_1B_e & \text{for } \left(B_2 - B_1\right)/2 < B_e < B_2 + B_1 \end{cases} \tag{3.14}$$

3.6 Beating in an interferometer

For the SLIM bus there is only a single light source (generally together with ASE, amplified spontaneous emissions, from optical amplifiers) but, with time-addressed CDMA using delay-line correlators, light from the source reaches the photodiode by more than one path. The resultant beating is explored by considering a system with two paths (Figure 3.5, a Mach-Zehnder interferometer) with fixed relative time delay of T. This configuration, the Mach-Zehnder interferometer, is similar to the Michelson interferometer and has similarities to that of the Young's slits experiment, both of which are extensively discussed in standard physics texts [180, 181]. The analysis in physics texts, however, focusses on different aspects of the interference from those of relevance to this thesis, so this section develops the models of the interferometer specifically to understand the way in which beating affects the noise in delay-line correlators and which can be used in the system analysis in later chapters (5 and 8).

In general, with reference to Figure 3.5, if the analytic function of the transmitter field is $\mathbf{E}_s\left(t\right)$ then the signal reaching the detector is described (neglecting excess losses and common time delays) by $\mathbf{E}_r\left(t\right) = \frac{1}{2}\mathbf{E}_s\left(t\right) + \frac{1}{2}\mathbf{E}_s\left(t+T\right)$.

3.6.1 Coherent source

The transmitted field of a coherent source is modelled by $\mathbf{E}_s\left(t\right) = \sqrt{2P}e^{-\phi_1[t]}e^{-i\omega_1 t}$ so that the field at the detector is described by $\sqrt{P/2}\left(e^{-\phi_1[t]}e^{-i\omega_1 t} + e^{-\phi_1[t+T]}e^{-i\omega_1(t+T)}\right)$, and the photocurrent is

$$\begin{aligned} i\left(t\right) &= \frac{P}{4}\mathcal{R}\left(e^{-i\phi_1[t]}e^{-i\omega_1 t} + e^{-\phi_1[t+T]}e^{-i\omega_1(t+T)}\right)\left(e^{-i\phi_1[t]}e^{-i\omega_1 t} + e^{-\phi_1[t+T]}e^{-i\omega_1(t+T)}\right)^* \\ &= \frac{P}{2}\mathcal{R}\left(1 + \cos\left(\omega T + \phi\left[t\right] - \phi\left[t+T\right]\right)\right) \end{aligned}$$

If $T \ll \tau_s$ where τ_s is the coherence time of the source, then $\phi\left[t\right] - \phi\left[t+T\right] \approx 0$ and $i\left(t\right) = \frac{1}{2}\mathcal{R}\left(P + P\cos\left(\omega T\right)\right)$ so that the power out is fixed by T. Of particular interest will be configurations in which T is chosen to maximise the power output, which requires $T = 2n\pi/\omega$, where n is an integer, and $i\left(t\right) = \mathcal{R}P$. In practice T is

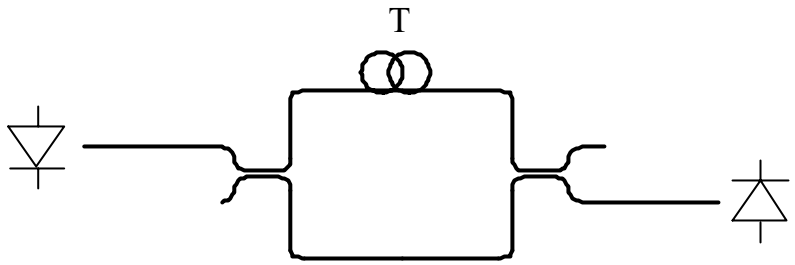

Figure 3.5: Fibre Mach-Zehnder interferometer.

several orders of magnitude greater than $1/\omega$ and thermal and mechanical perturbations prevent the open-loop stabilisation of T to the required tolerance, but feedback to a phase modulator in one of the paths can provide active stabilisation. This will be discussed further in Chapter 5, Section 5.2.1. Even with $T \ll \tau_s$ there will be residual noise due to $\phi[t] - \phi[t+T]$, but this is not explored in the work of this thesis: further analysis will be found in the work carried out at Strathclyde [172, 175].

If $T \gg \tau_s$ then the fields at the combiner may be modelled as independent [174] and the spectrum due to optical beating is given by 3.7 with $P_1 = P_2 = P/4$:

$$i^2(f) = \frac{1}{4\pi\nu_1}\mathcal{R}^2P^2\left(\frac{1}{1+(f/\nu_1)^2}\right)$$

and the noise power for low-pass filtering to $B_e$is:

$$N = \frac{1}{4\pi}\mathcal{R}^2P^2\tan^{-1}(B_e/\nu_1) \tag{3.15}$$

3.6.2 Chaotic source

The only regime of interest for the work of this thesis is when the path length difference exceeds the coherence length of the source and the fields at the combiner may be modelled as independent [174].

This is equivalent to the situation modelled in Section 3.5, but with $B_1 = B_2 = B$ and $P_1 = P_2 = P/4$. From Equation 3.13 the autocorrelation is given by:

$$\frac{R_i(\tau)}{\mathcal{R}^2} = \left(\frac{P}{2}\right)^2 + \left(\frac{P}{2}\right)^2\left(\frac{\sin(\pi\tau B)}{B\pi\tau}\right)^2 \tag{3.16}$$

This is the same as Equation 3.10 but with P replaced by $P/2$, indicating that the interferometer has no effect on the interferometric noise except, of course, its attenuation. Intuitively, a chaotic source is already fully incoherent so that the inclusion of an interferometer in the light path has no effect on the coherence properties.

The noise power for low-pass filtering to $B_e$is given by 3.11 with P replaced by $P/2$ (for $B_e < B_S$):

$$N = \frac{1}{4}\mathcal{R}^2P^2\frac{B_e}{B_S}\left(1 - \frac{B_e}{4B_S}\right) \tag{3.17}$$

3.7 Conclusion: beating in optical CDMA networks.

This chapter has developed a consistent analysis of beating effects that arise when optical fields are detected by photo-electric devices. The analysis has provided the models that will be used in later chapters to predict the performance of optical networks, but the final section of this chapter, Section 3.6, already indicates the origin of a fundamental problem with incoherent correlators: that the only way to keep the beating noise low is by having a source with a large spectral width. This is true in theory both for a coherent source (Equation 3.15, which requires $B_e \ll \nu_1$ for small N) and for a chaotic source (Equation 3.17, which requires $B_e \ll B_S$ for small N), but in practice only chaotic sources are available with sufficiently broad linewidths.

The other solutions to avoiding large beating noise in correlators (which will be considered further in Chapter 5) are to use a coherent source and a coherent correlator – one in which the path length differences are substantially less than the coherent length of the source – or to bypass interferometric beating by using the correlator proposed in section 5.2.3, the 'hybrid correlator'.

Before looking at correlators, however, the next chapter models the signal to noise ratio in optical busses and uses the results derived above to model the effects of noise from optical amplifiers in amplified busses.

Chapter 4

Signal to noise ratio

As was discussed in Chapter 1 (Section 1.2.2), there has been some debate in the literature on the comparative merits of the bus and star topology for optical fibre networks. This chapter contributes to that debate, first by examining the number of nodes that could be supported by each type of network based upon a simple power-budget analysis and assuming that amplifiers are not used. It is shown that without amplifiers the passive star can support many more nodes than a passive bus, and that the optical passive bus can in practice only support a few tens of nodes at most, severely restricting its viability.

The bus topology is nevertheless worth investigating further if it is assumed that optical amplifiers are used to overcome the power budget limitations. Amplifiers introduce new problems due to ASE (amplified spontaneous emissions) and saturation effects however, and to investigate these effects Sections 4.2 and 4.3 describe the results of simulating signals and noise in amplified fibre busses for both conventional and SLIM (single light-source with in-line modulation) busses. It is shown that there are problems with conventional busses due to the amplification of ASE that are overcome by the SLIM configuration.

Section 4.4 then uses the simulation models to investigate the maximum dimensions (number of nodes and signalling rate) of an amplified SLIM bus, and to investigate trade-offs in the bus design, such as that between the number of amplifiers used and the gain of each one.

Finally Section 4.5 draws together the conclusions, with the suggestion that an amplified optical fibre bus is a viable technology providing modulation is based on the SLIM principle, and that networks operating at over 100 bit/s can, in principle, support hundreds of nodes.

4.1 Bus and star without amplifiers

Three topologies will be examined:

- the passive star (Figure 4.1),
- 'conventional' busses configured as folded busses (Figure 4.2) and as dual busses (using either a single coupler to add and remove power from the bus, Figure 4.3, or a separate coupler for each function, Figure 4.4),
- and a SLIM (dark-signalling) bus (Figure 4.5). The SLIM bus is here described in terms of a folded bus, but, as discussed in Section 4.1.2, the worst-case power budget for a SLIM dual bus is the same as that for a SLIM folded bus so the conclusions apply to either. (In contrast, the conventional dual bus offers slightly better power budget than the conventional folded bus, as will be seen below.)

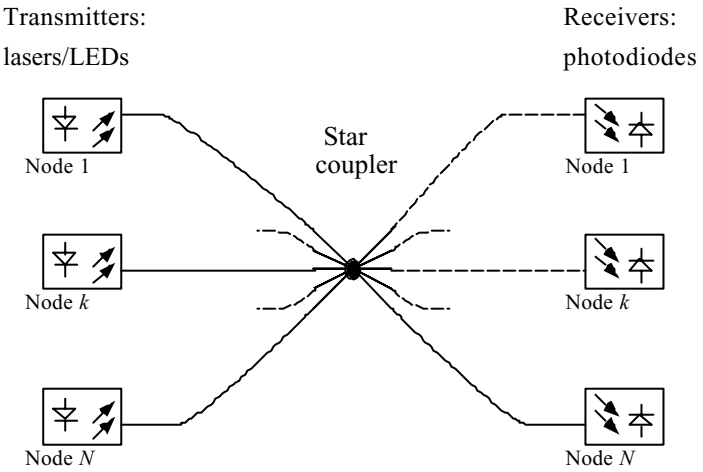

Figure 4.1: Passive star

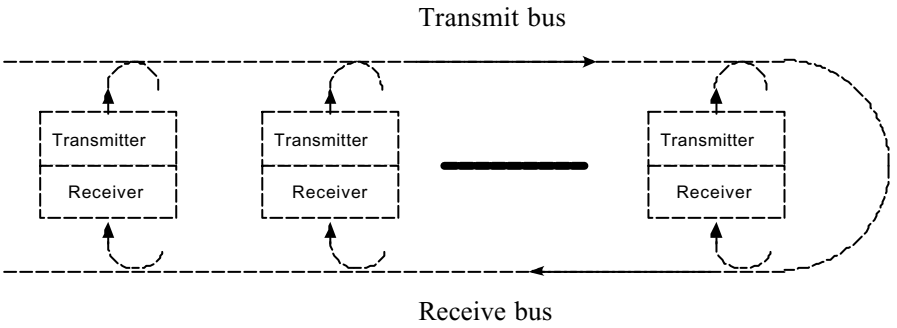

Figure 4.2: Folded bus

In the absence of amplifiers the only significant noise for any of the configurations is that generated at the receiver (shot and thermal noise), and it is adequate to analyse

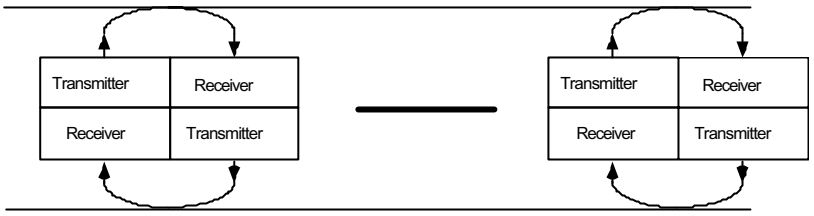

Figure 4.3: Dual bus

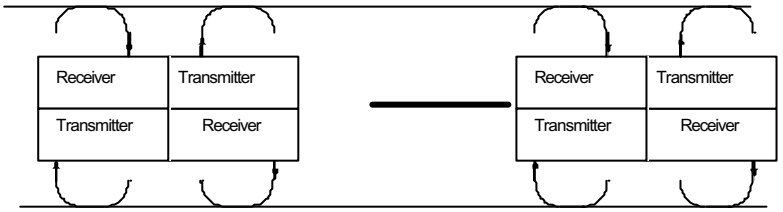

Figure 4.4: Dual bus, with separate couplers for adding and extracting power from the bus.

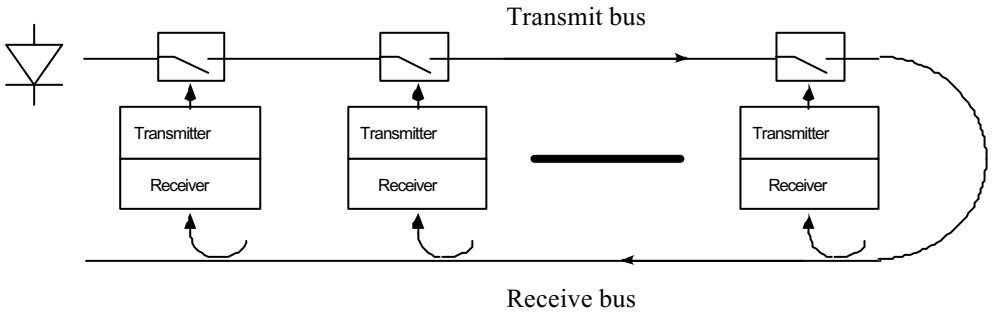

Figure 4.5: Dark signalling folded bus

network performance based on the power budget alone – if there is sufficient power at the receiver, the error performance will be acceptable. For the purposes of comparison, it is assumed that the system margin – available budget between the laser and photodiode – is 30 dB, corresponding to, for example, a 0 dBm source and -30 dBm receiver sensitivity. This is a fairly modest budget which would allow low error rates (below 10^{-9}) at high signalling rates [167]. The rest of this section looks at the maximum number of nodes that could be supported while meeting this budget for each of three topologies. Broadly speaking, the more nodes that can be supported the better.

4.1.1 Theoretical upper bound

To get an initial upper bound, it is assumed that the laws of physics are not violated but that 'perfect' engineering is possible. Thus the taps used to add power to the bus also remove power from the bus at the same ratio, but they can have zero *excess* loss and can be customised on a node-by-node basis down to any desired ratio. For the dark signalling bus the modulators are similarly assumed to have zero excess loss.

For the passive star the loss is the same for all nodes and is just the splitting loss, so that the ratio between the power at the receiver and the transmitter is given by $R = \frac{1}{N}$. With a 30 dB power budget 1000 nodes can be supported.

For the conventional folded bus the transmit bus gathers light from all nodes and the receive bus distributes it to all nodes. By customising the couplers the optimum splitting ratios will give equal powers to and from all nodes, and the bus is equivalent to two star couplers interconnected by a single fibre. The transmitter to receiver power ratio is therefore given by $R = \frac{1}{N^2}$ and a 30 dB power budget allows $\sqrt{1000} = 31$ nodes.

For the conventional dual bus Limb [182] has shown that more nodes can be supported if separate taps are used for adding and extracting power so the analysis is done assuming the configuration of Figure 4.4 rather than Figure 4.3. The calculation is more complicated than for the folded bus because the add and extract taps are interleaved, but an iterative method proposed by Limb [182] may be used to calculate maximum network dimensions numerically. With:

α_i The coupling ratio of the tap used to add power at node i

β_i The coupling ratio of the tap used to extract power at node i

p_i The normalised power (power/laser transmitted power) after node i

k The system margin (minimum power at the receiver/laser transmitted power)

The optimum values of α_i and β_i are given by:

$$\alpha_i = k/p_{i-1} \tag{4.1}$$

$$\beta_i = (p_{i-1} - k) \,/\, (p_{i-1} - k + 1) \tag{4.2}$$

And

$$p_i = (1 - \beta_i)(1 - \alpha_i)\, p_{i-1} \tag{4.3}$$

The maximum network dimension are found by iterative application of equations 4.1, 4.2 and 4.3 until $\alpha_i \leq 1$. This is readily done with a spreadsheet, and Figure 4.6 shows the results for a bus with a 30 dB margin, indicating that a maximum of about 50 nodes is possible.

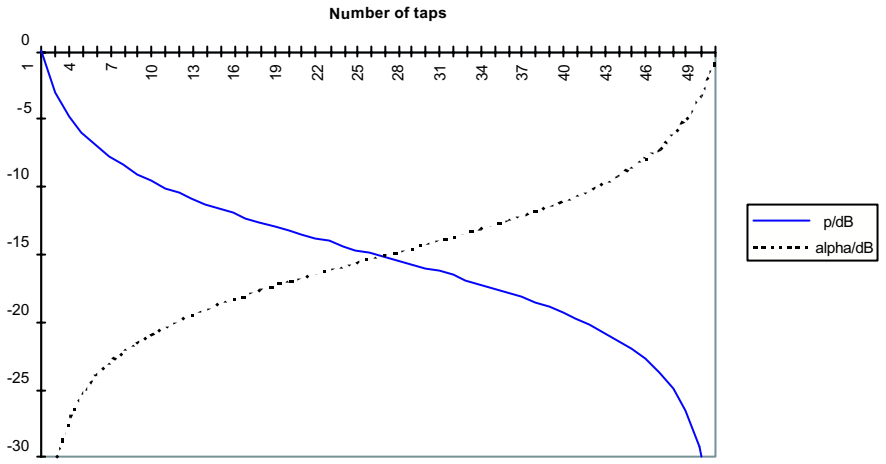

Figure 4.6: Optimised dual bus

For the SLIM bus there is no power loss in the transmit side (with the assumption of lossless modulators), so the power budget is determined only by the distribution of the receive side, giving the same loss as for a star ($R = \frac{1}{N}$), and the 30 dB budget allows 1000 nodes.

Analysis at this simplified level shows the SLIM bus to offer the same performance as the passive star in having a linear relationship between loss and number of nodes, whereas 'conventional' buses are significantly worse. This is because coupling light into a conventional bus also extracts light as a result of the reciprocity of couplers. In-line modulation, by contrast, in principle incurs no loss to the signal on the bus.

4.1.2 Practically achievable dimensions

To account for some of the practical limitations it is now assumed that the couplers have a fractional insertion loss of $\delta, 10\log_{10}\delta$ dB, ($-10\log_{10}\delta$ dB per 2×2 coupler within the star coupler in the case of the passive star), and the modulator has insertion loss of γ dB. For the busses it would be difficult to optimise the coupling ratio for each node, so it is also now assumed that all couplers in a bus have the same (optimised) coupling ratio

Based on [14] the loss for the passive star is given by

$$R = \frac{1}{N}\delta^{\log_2 N} \tag{4.4}$$

(For each factor of two in N, an extra stage of couplers is required, introducing an additional loss of δ.)

With a budget of 30 dB, and an insertion loss of 0.1 dB, this allows 800 nodes.

Following [14][1] and [183] the conventional folded bus is optimised by setting $\alpha = 1/N$, where α is the coupling ratio of the taps, and the worst-case loss is then given by:

$$R = \frac{1}{N^2}\left(1 - \frac{1}{N}\right)^{2N-2\delta 2N-1} \approx \frac{1}{e^2 N^2}\delta^{2N-1} \tag{4.5}$$

where the approximation is valid for large N. With a budget of 30 dB, and an insertion loss of 0.1 dB, this allows 9 nodes. (Even with a lossless coupler, only 12 nodes can be supported.)

Again following [14] and [183] the conventional dual bus is optimised by setting $\alpha = 1/N$, where α is the coupling ratio of the taps, and the worst-case loss (end-to-end) is then given by

$$R = \frac{1}{N^2}\left(1 - \frac{1}{N}\right)^{N-2}\delta^N \approx \frac{1}{eN^2}\delta^N \tag{4.6}$$

with the approximation again valid for large N. The 30 dB budget and 0.1 dB insertion loss in this case allows 16 nodes (20 for lossless couplers).

For both the dual and folded topologies of the SLIM bus, the worst case is for a signal received by the node farthest away from the light source – independent of the transmitting node, since the power all derives from the light source at the front of the bus. The light has passed through the same number of equivalent devices in the two cases – N modulators and N couplers, $N-1$ of which it goes through and at one of which it is tapped-off. Since the modulators always modulate all the light within the bus, the location of the modulators has no effect upon the budget.

In each case the light is attenuated by:

- the insertion loss of N modulators (loss of γ^N)
- the insertion loss of N couplers (loss δ^N)
- the straight-through attenuation of $N-1$ couplers (loss $(1-\alpha)^{N-1}$)
- the tapping loss of the final coupler (loss α)

[1] The formulae for the folded bus in [14] appears to be incorrect, since the loss should contain a factor of α squared (adding and extracting power from the bus). This seems to agree with the results used by [183].

giving a total loss of

$$l = \alpha (1-\alpha)^{N-1} \gamma^N \delta^N \tag{4.7}$$

This is optimised with respect to α by differentiating and setting to zero, from which it emerges that the optimum splitting ratio is again $\alpha = 1/N$ and gives:

$$l = \frac{1}{N} \left(1 - \frac{1}{N}\right)^{N-1} \gamma^N \delta^N \tag{4.8}$$

which approximates to

$$l = \frac{1}{eN} \gamma^N \delta^N \tag{4.9}$$

for large N

The 30 dB budget and 0.1 dB insertion loss for both couplers and modulators ($\delta = \gamma = 0.977$) allows 45 nodes. However, 0.1 dB is optimistic for the modulator insertion loss with current technology. With 1 dB modulator insertion loss, the number of nodes drops to 13.

4.1.3 Comparison

The results are summarised in Table 4.1. The merits of the SLIM bus depend critically upon the insertion loss of the modulator. Comparing the formulae for the worst-case path loss for the conventional folded bus and the SLIM bus it is possible to determine a threshold at which the SLIM bus performs better. The limit on γ for which the SLIM bus offers lower attenuation is given by:

$$\gamma > \frac{\left(1 - \frac{1}{N}\right) \delta}{\left(N \left(1 - \frac{1}{N}\right) \delta\right)^{1/N}} \tag{4.10}$$

Compared with the passive star, however, it is clear that all of the busses have worse power budgets since the losses in the power distribution to the receivers are greater for the busses even before taking into account the losses in the power collection from the transmitters.

One major advantage of the SLIM bus, nevertheless, is the absence of the 'near-far' effect. Conventional busses suffer from a very substantial near-far effect. In the folded bus, for example, the ratio between the signal from node 1 and the signal from node N is given by:

$$\left(1 - \frac{1}{N}\right)^{N-1} \delta^N$$

which is 5.2 dB (a ratio of over 3:1) for a 10 node network.

Even a passive star will suffer from significant near-far effects due to asymmetries in the star coupler (and differences in the power levels of the multiple optical sources) [184].

Topology	Upper-bound	Practically attainable
Star	1000	800
Dual bus	50	16
Folded bus	31	9
SLIM bus (dual or folded)	1000	45 (13)*

Table 4.1: The number of nodes that may be supported by various network topologies, with a 30dB power budget. (*45 for 0.1 dB modulator insertion loss: 13 for 1 dB insertion loss.)

4.2 Busses with amplifiers

It is clear from the previous section that bus networks supporting useful numbers of nodes are not viable unless the power level is maintained with optical amplifiers. This section looks at what is possible when optical amplifiers are used. Once again, in general terms the goal is to be able to support as many nodes as possible at as high a signalling rate as possible, up to extremes beyond which further increases would not be useful. Signalling at rates greater than a few terabaud is unlikely to be useful, for example, because even using all-optical processing it would not possible to operate at this speed in the foreseeable future. Also, a single shared-medium network with more than a few thousand nodes would be of limited value because the average capacity available to each node would be relatively low and reliability would be a problem (a single failure - a broken fibre - could affect too many nodes). It is important to keep in mind the constraint of the ultimate cost of the network, although it should also be remembered that costs can come down very significantly as technologies mature and production quantities increase. Of particular relevance in this respect is the cost of optical amplifiers which is very high at present, but which is likely to come down in the future.

There is no consideration in this chapter of the mechanisms used for addressing or channel sharing – it is implicitly assumed that a higher-level MAC (medium access control) protocol is used (see, for example, [185]).

4.2.1 Modelling busses with amplifiers

In the analysis of unamplified networks (Section 4.1) it was sufficient to investigate the power levels at the receiver in order to get an estimate of achievable dimensions. For a given signalling rate and receiver design, it was a reasonable approximation to assume that the error rate is determined only by the received signal power. In an amplified network, on the other hand, the spontaneous emissions (ASE) generated by the amplifier must also be considered [53].

The modelling used here is based upon that of Lui and Ramaswami [183], and involves tracking the evolution of the signal power and the noise power along the bus from the transmitting node to the receiving node. The sources of attenuation are the

fibre loss, the coupler splitting ratio and the insertion loss of the coupler. Optical amplifiers are assumed to be used after every m nodes, and as well as amplifying light in the bus they add optical noise (spontaneous emissions, SpE) from amplified spontaneous emissions (ASE[2]) [54]. The signal power is calculated separately for a data 1 and a data 0. It is assumed that the signalling rate is much greater than the gain relaxation time of the EDFAs, so that the amplifier performance (gain and spontaneous noise generation) is determined by the long-term mean optical power and the spontaneous emission power is the same during the transmission of data 1s and data 0s. The 'high' signalling rate also means that even when the amplifiers are saturated there is no significant distortion to the signal [54].

Signal loss at the nodes is characterised by an excess loss β dB and a tap coefficient α dB. β is taken to include splice losses and device excess losses, as well as fibre attenuation. Thus if the power on the bus at the output of a terminal is P, the power at the output of the following terminal is $P \times 10^{-(\alpha+\beta)/10}$ on the bus and $P \times 10^{-\beta/10} \times (1 - 10^{-\alpha/10})$ on the tap. Amplifiers are characterised by small signal gain G_0 and saturation power P_{sat}. In addition it is assumed that there is loss η_{in} on coupling light into the amplifier and η_{out} on coupling light out of the amplifier. Saturation is modelled by relating gain (G) to input power (P_{tot}) according to [55]:

$$P_{tot} = \frac{P_{sat} \ln(G_0/G)}{G-1} \tag{4.11}$$

P_{tot} is the total input power, averaged over data 0s and data 1s because of the high-signalling rate assumption (the signalling rate is greater than the inverse of the carrier lifetime). Then assuming equal numbers of 1s and 0s, $P_{tot} = 0.5(P_{as}(0) + N_{spe}(0)W + P_{as}(1) + N_{spe}(1)W)$ where $P_{as}(0)$ and $N_{spe}(0)W$ are the signal and spontaneous emission powers (SpE) during data 0s, and $P_{as}(1)$ and $N_{spe}(1)W$ are the signal and SpE powers during data 1s. In the simulation, Equation 4.11 has to be solved for G given G_0, P_{sat} and P_{tot} at each amplifier. The equation cannot be re-arranged to get an explicit solution for G, but may be solved numerically with the *Mathematica* 'FindRoot' function:

```
gain@power_D := G ê. FindRoot@power == pSat Log@gain0 ê GD ê G - 1, 8G, 82, gain0<<, MaxIterations → 20D
```

The power spectral density from amplified spontaneous emissions is modelled by

$$N_{ASE} = N_{sp}(G-1)h\nu$$

where $h\nu$ is the photon energy and N_{sp} is the spontaneous emission factor. N_{sp} is dependent upon the input power and modelled by [55]

$$N_{sp} = \left(\frac{1.65}{(G-1)^{.53}} + 1.15\right)\left(1 + \frac{P_{tot}}{P_{sat}}\right)$$

[2] SpE is used for the combined optical noise power in the bus; ASE for the amplified spontaneous emissions from individual amplifiers

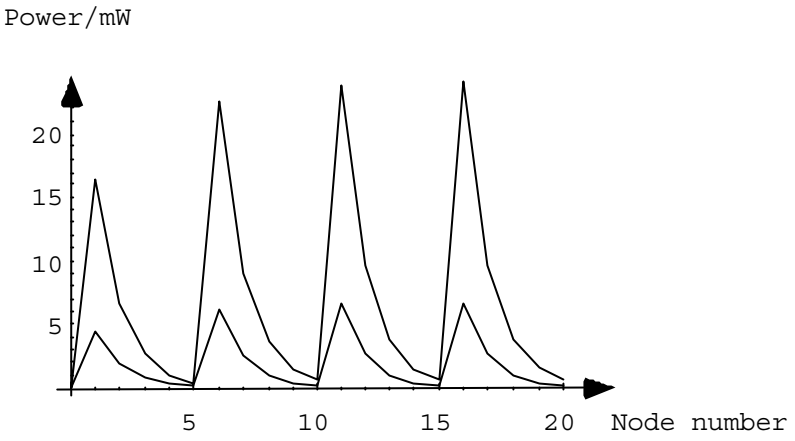

Figure 4.7: Signal power (upper curve) and noise power (lower curve) evolution along a 'conventional' optical fibre bus.

4.2.2 Signal and noise power evolution in a conventional bus

To illustrate the signal and noise evolution in a conventional bus, Figure 4.7 shows the signal power (during data 1s) and SpE power at each node in a 20-node bus with an amplifier after every five nodes, in which the signal is launched at the first node. Note that strictly speaking Figure 4.7 shows only the values of the powers at the nodes - joining the points between nodes is technically incorrect. However, the use of lines helps to emphasise the power evolution.

The fall in power levels between amplifiers is due to the fibre attenuation, splice loss, and losses from the couplers. Signal and noise power are attenuated equally, so the optical signal to noise ratio is constant between amplifiers and for some purposes it will be more informative to plot the values only at one of the nodes between amplifiers. Thermal noise contributed by the receivers is independent of optical power level, so the 'worst case' node between a pair of amplifiers is the one immediately before an amplifier - the node at which the optical power levels are lowest. Joining the points on a plot in which only the 'worst case' nodes are plotted generates a curve which is effectively a lower bound to the signal and noise powers, or a lower bound to the signal to noise ratio. This approach is used in the subsequent figures of this thesis, except where stated otherwise.

4.2.3 The problem of unsuppressed noise in a conventional bus

Launching a signal from the first node (the situation described in the previous section) and receiving this signal at the last node, was taken to be the 'worst case' in the analysis in [183]. In fact, assuming that the amplifiers are operated in saturation (as was done by the authors of [183][3]) the worst-case occurs when there is no signal in the

[3] The alternative to operation in saturation is to match the amplifier gain to the section loss. It is, however, one of the advantages of EDFAs that their saturation characteristics provide an inherent

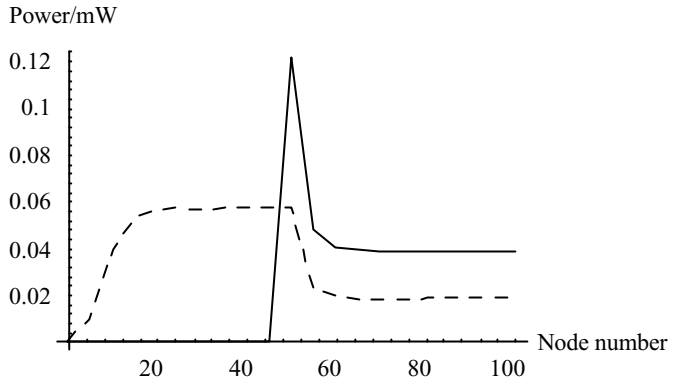

Figure 4.8: Signal (continuous curve) and SpE (dashed curve) power during a data 1 along a 'conventional' optical fibre bus. The signal is added at node number 50.

fibre at the front end of the bus.

This is illustrated by Figure 4.8, in which the signal is launched at node 50 in a 100 node bus.

Because there is no signal in the bus prior to node number 50, the amplifiers in the first part of the bus do not saturate and have high gain. This amplifies the SpE, so that eventually (after about only 3 amplifiers in the example here) the amplified SpE power alone is sufficient to saturate the amplifiers. At the point at which the signal is added the rise in the power within the bus causes the amplifier gain to drop, suppressing, to some extent, the SpE power.

To suppress noise in the bus when the signal does not originate at the first node, Koai and Olshansky [56] proposed a design in which a synchronising clock signal is transmitted from the head-end, using a different wavelength from the wavelength used for none-to-node communication. Dark-signalling is an alternative solution, which is discussed further in the next section.

4.2.4 Modelling the signal power evolution in a dark signalling bus

Modelling the signal and SpE power in the dark-signalling bus is essentially the same as for the conventional bus. There is extra attenuation due to the insertion loss of the modulator (this is discussed further in Section 4.3.3) and the model must take account of the fact that the modulator imposes a signal on the SpE power as well as the signal power.

For comparison with the conventional bus illustrated in the previous section, Figure 4.9 shows the mean amplified source, AS, power ('signal'[4]) and SpE ('noise') for a 100-node bus with the signal added at node number 50. The in-line modulator is assumed

automatic gain control. For this, and other reasons explained in [55], the EDFAs should be assumed to be in saturation

[4] Prior to the sending terminal, of course, the AS power conveys no signal

to have a modulation depth of 15 dB. Prior to the active terminal in this case it is the source power which dominates, being amplified by the first amplifiers until saturation.

At the active terminal the in-line modulator impresses a signal on all the power in the bus, so both the AS and SpE power are approximately halved (assuming equally probable data 1s and 0s). However the subsequent amplifiers increase the AS and SpE powers until saturation is again achieved. This effect can be seen more clearly in Figure 4.10, which shows the AS and SpE for data 1s and data 0s separately, with an artificially low extinction ratio (3 dB) for clarity. Because the in-line modulator impresses a signal upon the SpE power as well as the AS power, it might appear that the SpE at the input to the active terminal contributes to the effective signal power. The SpE power is likely to be broadband however (without in-line optical filters it will extend over the bandwidth of the EDFAs), so that at useful signalling rates the fibre dispersion is likely to prevent the SpE component from contributing significantly to the useful signal (Section 4.3.1).

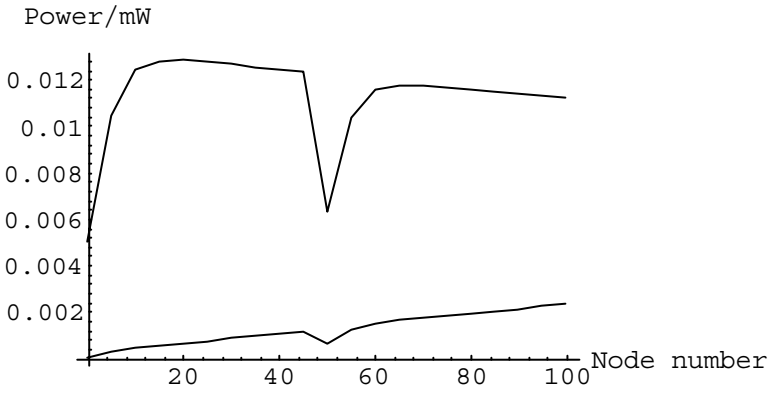

Figure 4.9: Amplified source (upper curve) and SpE (lower curve) power in a dark-signalling bus.

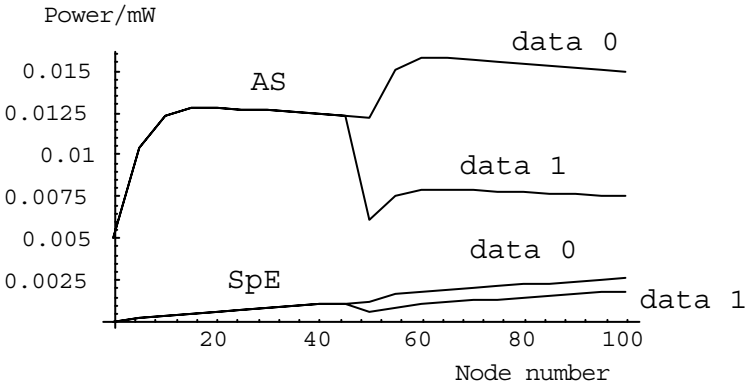

Figure 4.10: AS and SpE for data 1s and data 0s, with a 3dB extinction ratio.

Description	Default value
G_0, Amplifier small signal gain	40 dB
P_{sat}, Amplifier saturation power	0 dBm
η_{in}, Power loss coupling light into the amplifier	1.5 dB
η_{out}, Power loss coupling light out from the amplifier	1.5 dB
Optical bandwidth of the bus	30 nm
Optical bandwidth of the receiver input	30 nm
α, Splitting ratio of the couplers (optical taps)	1 dB
Insertion loss of the in-line modulators (dark bus only)	3 dB
β, Fibre and splice losses between nodes	3 dB
Extinction ratio of the modulated signal	15 dB
Node at which the signal is added	50
Power of the optical source	50 mW
m, the number of nodes between amplifiers	4
Total number of nodes in the bus	100
Signalling rate in the bus	10 Gbaud

Table 4.2: Parameters of the simulations

4.3 Signal to noise ratio comparisons between conventional and dark-signalling busses

The parameter used to examine the performance of the busses is the electrical signal to noise ratio at the receiving terminals. This is calculated assuming the use of direct detection, taking into account shot noise, thermal noise, and the effects of the received SpE, as described in Section 4.3.1. It is assumed that only one terminal transmits at a time (controlled by a multiple access protocol).

Unless otherwise shown, the parameters not used as variables in these comparisons are as given in Table 4.2.

4.3.1 Derivation of the signal to noise ratio

The optical power incident upon the receiver photodiode consists of the amplified source power, P_s (taken for the moment as a constant optical power) and spontaneous emission power, with spectral density N_{spe}. It is assumed that the spontaneous emission power is white over a bandwidth W Hz, centred on the source frequency. The source is itself assumed to have a much narrower bandwidth than the spontaneous emissions. The receiver is modelled by a PIN photodiode with quantum efficiency η connected to a load resistor of resistance R_l. Subsequent processing is taken to be noise-free with frequency response modelled by a brick-wall low-pass filter of bandwidth B followed by threshold detection at the optimum threshold. This situation was modelled in Section 3.4 with $P_1 = N_{spe}W$ (the power of the broadband signal), $B_1 = W$ (the spectral width of the broadband signal) and $P_2 = P_s$, (the power of the monochromatic signal).

The results of Section 3.4 give the noise terms on the photocurrent from source-spontaneous cross-modulation noise (σ^2_{s-sp}), and spontaneous-spontaneous inter-modulation noise (σ^2_{sp-sp}),

$$\sigma^2_{s-sp} = 4\mathcal{R}^2 P_s N_{spe} B \tag{4.12}$$
$$\sigma^2_{sp-sp} = 2\mathcal{R}^2 N^2_{spe}(2W - B)B \tag{4.13}$$

where $\mathcal{R}$ is the responsivity, $= \frac{\eta e}{hf}$ (hf = photon energy at the source frequency $= 1.3 \times 10^{-19}$ joules, $e =$ charge on an electron $= 1.6 \times 10^{-19}$ coulombs).

In addition, there is shot noise (σ^2_{shot}) and thermal noise ($\sigma^2_{thermal}$), given by [165]:

$$\sigma^2_{shot} = 2e\mathcal{R}(P_s + N_{spe}W)B$$
$$\sigma^2_{thermal} = 4kTB/R_l$$

The total noise power (current-squared) is the sum of these four terms:

$$N = 2e\mathcal{R}(P_s + N_{spe}W)B + 4kTB/R_l + 4\mathcal{R}^2 P_s N_{spe} B + 2\mathcal{R}^2 N^2_{spe}(2W - B)B$$

The component which contributes to the signal is the mean power (current-squared) given by

$$S = (\mathcal{R}(P_s + N_{spe}W))^2$$

The incoming modulated signal is modelled as intensity modulation, with amplified source and spontaneous optical powers during data 0s and 1s equal to $P_s(0)$ and $N_{sp}(0)$, and $P_s(1)$ and $N_{spe}(1)$ respectively. The resulting noise and signal components during data 0s and data 1s are

$$\begin{aligned}
N(0) &= 2e\mathcal{R}(P_s(0) + N_{spe}(0)W)B + 4kTB/R_l + 4\mathcal{R}^2 P_s(0)N_{spe}(0)B + 2\mathcal{R}^2 N_{spe}(0)^2(2W - B)B \\
S(0) &= (\mathcal{R}(P_s(0) + N_{spe}(0)W))^2 \\
N(1) &= 2e\mathcal{R}(P_s(1) + N_{spe}(1)W)B + 4kTB/R_l + 4\mathcal{R}^2 P_s(1)N_{spe}(1)B + 2\mathcal{R}^2 N_{spe}(1)^2(2W - B)B \\
S(1) &= (\mathcal{R}(P_s(1) + N_{spe}(1)W))^2
\end{aligned} \tag{4.14}$$

This implicitly assumes, however, that there is no dispersion. At the signalling rates of interest and with practicable optical bandwidth, a better assumption is that the dispersion effectively merges the spontaneous emission power during data 1s and data 0s, so that $N_{spe}(0)$ and $N_{spe}(1)$ in equations 4.14 are both replaced by

$$N_{spe} = \frac{N_{spe}(0) + N_{spe}(1)}{2}$$

This gives:

$$\begin{aligned}
N(0) &= 2e\mathcal{R}(P_s(0) + N_{spe}W)B + 4kTB/R_l + 4\mathcal{R}^2 P_s(0)N_{spe}B + 2\mathcal{R}^2 N^2_{spe}(2W - B)B \\
S(0) &= (\mathcal{R}(P_s(0) + N_{spe}W))^2 \\
N(1) &= 2e\mathcal{R}(P_s(1) + N_{spe}W)B + 4kTB/R_l + 4\mathcal{R}^2 P_s(1)N_{spe}B + 2\mathcal{R}^2 N^2_{spe}(2W - B)B \\
S(1) &= (\mathcal{R}(P_s(1) + N_{spe}W))^2
\end{aligned} \tag{4.15}$$

(Notice that although the spontaneous emission power is independent of the data state, the noise power is not. Both the shot noise and the source-spontaneous cross-modulation term are signal-dependent.)

It is a reasonable approximation at the power levels in this analysis to treat the total noise as Gaussian so that if the probability of data 0s and data 1s are $Pr(0)$ and $Pr(1)$ respectively, then the total error probability is

$$Pe = Pr(0)Q\left(\frac{i_t - \sqrt{S(0)}}{\sqrt{N(0)}}\right) + Pr(1).Q\left(\frac{\sqrt{S(1)} - i_t}{\sqrt{N(1)}}\right)$$

where i_t is the decision threshold, referred to the photodiode output as a current, and the 'Q function', Q(z), returns the area under the tail of a normalised Gaussian curve beyond z [160]. Assuming equally probable 0s and 1s:

$$Pe = 0.5Q\left(\frac{i_t - \sqrt{S(0)}}{\sqrt{N(0)}}\right) + 0.5Q\left(\frac{\sqrt{S(1)} - i_t}{\sqrt{N(1)}}\right)$$

which is approximately minimised by choosing i_t such that

$$\frac{i_t - \sqrt{S(0)}}{\sqrt{N(0)}} = \frac{\sqrt{S(1)} - i_t}{\sqrt{N(1)}}$$

so that for small error rates a good approximation to the total error probability is given by

$$Pe \approx Q\left(\frac{\sqrt{S(1)} - \sqrt{S(0)}}{\sqrt{N(1)} + \sqrt{N(0)}}\right) \tag{4.16}$$

(This is the Q parameter of Olsson [177].) Thus the signal to noise ratio is defined as $\frac{\sqrt{S(1)}-\sqrt{S(0)}}{\sqrt{N(1)}+\sqrt{N(0)}}$ and, noting that with $Q(6) = 10^{-9}$, networks are assumed to operate satisfactorily provided the signal to noise ratio exceeds 6 (7.8 dB).

4.3.2 Node at which the signal is added

Figure 4.11 shows the signal to noise ratio at the node at the end of a 100-node conventional bus as a function of the node at which the signal originates, assuming that the launch power is independent of node. The large 'oscillatory' effect mirrors the rising and falling of the noise (SpE) power seen in Figure 4.7: if the signal is launched at a node just before an amplifier then, since the noise in the fibre at that point is low, the signal to noise ratio is high; if the signal is launched just after an amplifier then, since the noise power is high, the signal to noise ratio is low.

In addition to the oscillatory effect there is a long-term trend which can be seen by plotting the 'worst-case bound': plotting and joining only the values due to the nodes between amplifiers which generate the worst signal to noise ratio (in this case, the nodes immediately after an amplifier). This is shown in Figure 4.12.

The main feature of this plot is that the first nodes in the bus generate a much larger signal to noise ratio than subsequent nodes. This effect is due to the problem

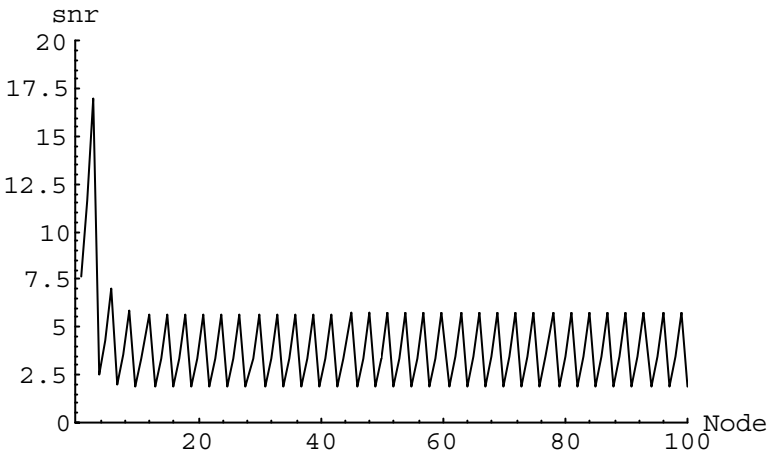

Figure 4.11: Signal to noise ratio at the end of a conventional optical fibre bus as a function of the location of the transmitting node, plotted for each node.

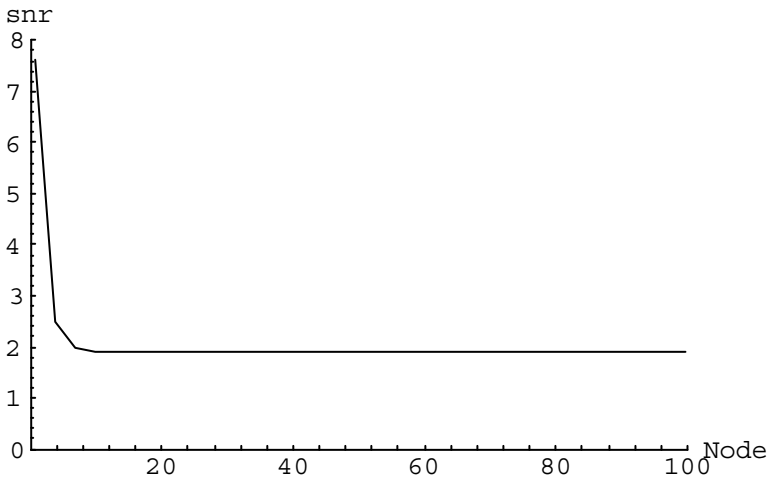

Figure 4.12: Signal to noise ratio at the end of a conventional optical fibre bus as a function of the location of the transmitting node, worst-case envelope.

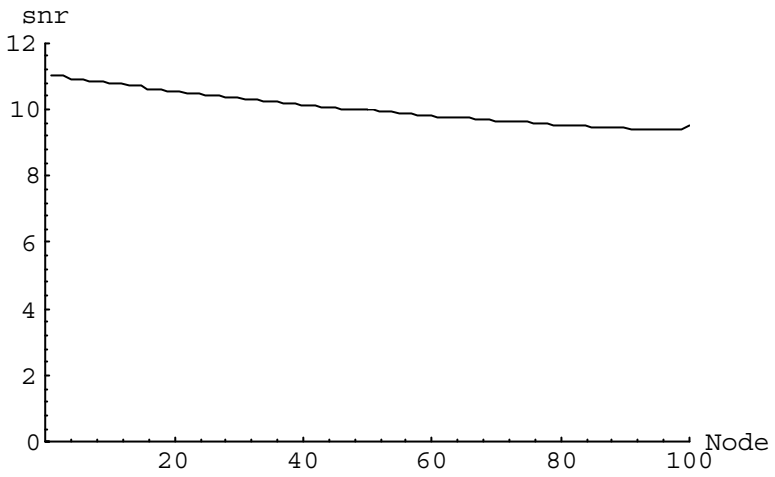

Figure 4.13: Signal to noise ratio at the end of a conventional optical fibre bus as a function of the location of the transmitting node.

of unsuppressed noise, discussed above. If the signal is not launched until after about the tenth node, the bus is already saturated with SpE power at the point at which the signal is injected, and the consequent signal to noise ratio is small.

Figure 4.13 shows the signal to noise ratio at the end of a dark-signalling bus as a function of the node at which the signal is launched. This is not a worst case bound: the value from *each* node is plotted. There is no oscillatory effect however because the modulator imposes the signal on whatever signal power is in the bus. There is no problem with unsuppressed noise because, regardless of where the signal is added, light is launched at the head-end. The only effect is a gradual falling as the sending node is further along the bus.

4.3.3 Number of terminals per amplifier

The analysis of conventional busses in [38] looked at the optimum amplifier spacing assuming that the amplifier gain can be freely chosen such that the ratio of loss between amplifiers to the amplifier gain is kept constant. The conclusion is that the optimum loss between amplifiers is about 8 dB, which, with the parameters assumed in [38], equates to two terminals per amplifier. In practice, however, amplifiers are expensive and it would seem desirable to minimise the number of amplifiers required in a network by using high gain and as many terminals per amplifier as possible. (Alternatively it may be more appropriate to assume that there is an amplifier at every node. A single device might be constructed to combine the modulator with optical amplification – and possibly also the extraction tap and photodetector. This is approach is considered later.)

For the comparisons in this section the (small signal) amplifier gain is taken as

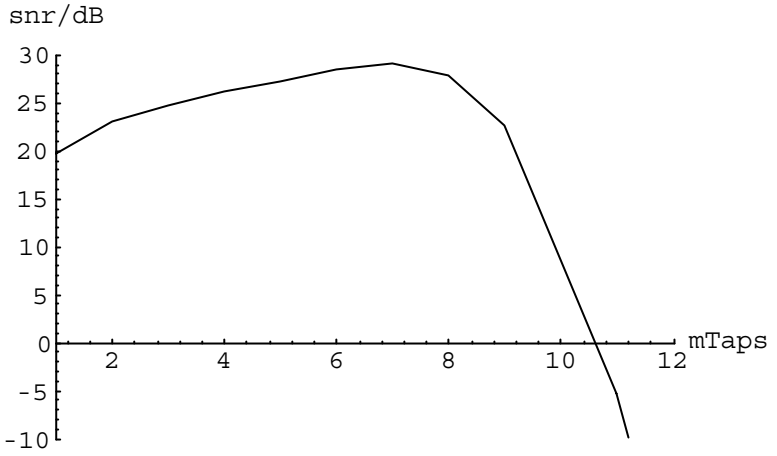

Figure 4.14: Signal to noise ratio at the end of a conventional optical fibre bus as a function of the spacing between amplifiers

fixed at 40 dB[5] and the maximum acceptable number of terminals between amplifiers is investigated by looking at the signal to noise ratio at the end of the bus. This is done for a conventional bus in Figure 4.14 and a dark-signalling bus in 4.15. (For both these plots, the signal is assumed to be launched from a 'worst-case' node close to node number 50: i.e. the node immediately after an amplifier close to node 50. Similarly the exact length of the bus – around 100 nodes – is chosen so that the last node is immediately before a location for an amplifier.)

The main feature of both Figure 4.14 and 4.15 is the threshold effect as the attenuation between amplifiers becomes greater than the gain available, so that the amplifier is unable to maintain the signal power. The threshold occurs for fewer nodes per amplifier for the dark signalling bus than for the conventional bus because of the extra attenuation per node due to the insertion loss of the in-line modulator (taken to be 3 dB in the model which generated Figure 4.15). Clearly, the threshold will be dependent upon the insertion loss of the modulators: if the insertion loss per modulator can be reduced, the number of modulators between each amplifier can be increased.

In the conventional bus, for node numbers below the threshold the signal to noise ratio *increases* as the number of nodes per amplifier increases. As a result there is an optimum number of nodes per amplifier (7 for the parameters of Figure 4.14). This effect is only seen if the sending node is some way along the bus (Figure 4.14), rather than at the head-end (Figure 4.16), and is another result of the effect of unsuppressed noise prior to the launch node. The more closely spaced the amplifiers, the greater power of the SpE noise which builds-up before the signal is injected.

[5] This is towards the upper end of the gains of commercially-available EDFAs [186].

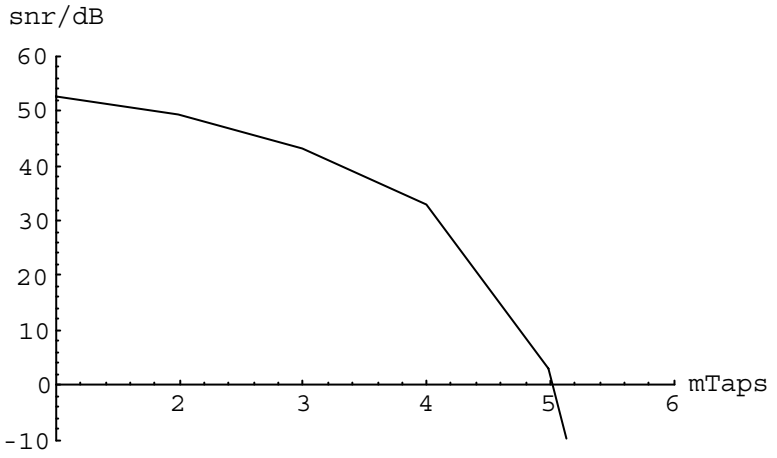

Figure 4.15: Signal to noise ratio at the end of a dark-signalling bus as a function of spacing between amplifiers.

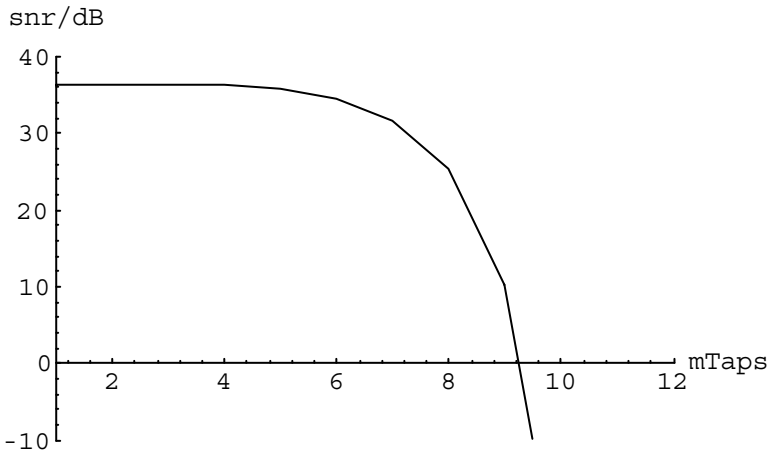

Figure 4.16: Signal to noise ratio at the end of a conventional optical fibre bus as a function of the spacing between the amplifiers. The signal is launched at the start of the bus.

4.3.4 Optical bandwidth

There are two different possible locations for filtering the optical bandwidth: at the receiver input and in-line with the bus (such as at the amplifier input or output).

For both conventional and dark-signalling busses filtering at the receiver input has the effect of reducing the amount of SpE noise reaching the receiver and therefore increasing the signal to noise ratio[6]. Filtering in-line affects conventional and dark-signalling very differently however – again as a consequence of the problem of unsuppressed noise in a conventional bus. In a conventional bus, (Figure 4.17(a)), narrowing the in-line optical bandwidth has the effect of forcing more of the SpE power into the optical spectrum close to the signal wavelength. The SpE noise power at the front-end of the bus still rises to saturate the amplifiers, but if the bandwidth is narrower, the spectral density is higher. This has the effect of reducing the signal to noise ratio[7].

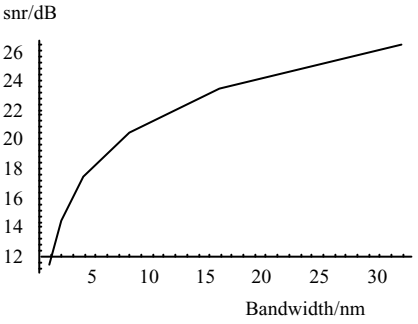

(a) Conventional bus

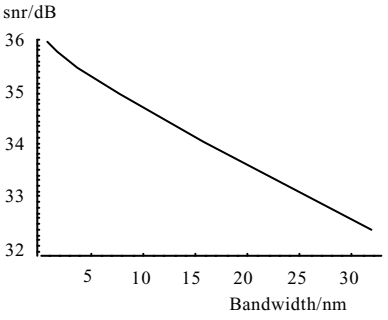

(b) Dark signalling bus

Figure 4.17: Signal to noise ratio at the end of an optical fibre bus as a function of the bandwidth of in-line filtering.

By contrast, in-line filtering in a dark-signalling bus (Figure 4.17(b)) reduces the fraction of the power in the saturated bus which is taken-up by the SpE, thereby

[6] Filtering at the receiver input reduces the SpE bandwidth, W, but does not change the SpE power-spectral density, N_{spe} increases. This reduces the spontaneous-spontaneous beating power (Eqn. 4.13 on page 66) but does not change the signal-spontaneous beating power (Eqn. 4.12).

[7] Roughly speaking, the SpE power, $P_{spe} = N_{spe}W$, remains constant, but W decreases and N_{spe}. This increases both spontaneous-spontaneous beating power (Eqn. 4.13) and signal-spontaneous beating power (Eqn. 4.12).

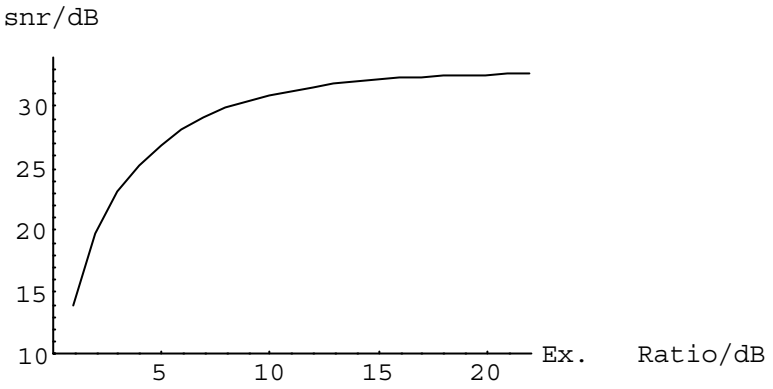

Figure 4.18: Signal to noise ratio at the end of a dark-signalling optical fibre bus as a function of the extinction ratio of in-line modulators.

increasing the signal to noise ratio.

The dark signalling bus also has a practical advantage with regard to optical filtering because there is only a single light source. It would be a relatively simple matter to match optical filters at each amplifier to the wavelength of the source. A conventional bus on the other hand would need to ensure that all the sources (one per terminal) are matched to the filters.

4.3.5 Extinction ratio

Potentially, a practical difficulty with dark-signalling might be the demands upon the extinction ratio of the in-line modulator. High extinction ratio is achievable in Lithium Niobate modulators, but to some extent there is a trade-off between low insertion loss and high extinction ratio, and low insertion loss is a necessary parameter for a viable network.

It can be seen from Figure 4.18 however, that the signal to noise ratio is not significantly degraded provided the extinction ratio is above about 10 dB. This is not an excessive demand on the modulator.

4.4 Achievable dimensions of a dark-signalling bus

It will be clear from the discussions above that the number of terminals which could be supported by a dark-signalling optical fibre bus will depend strongly upon the parameters of the components available, especially the insertion loss of the modulator (section 4.3.3). However, it is useful to assess the viability of the technique by making reasonable assumptions about the parameters achievable.

Figure 4.19 shows the maximum signalling rate achievable on a dark-signalling bus for a worst-case signal to noise ratio of 6 (corresponding to an error rate of 10^{-9}, see Section 4.3.1). Results are shown both for 4 nodes per amplifier (dashed curve), and

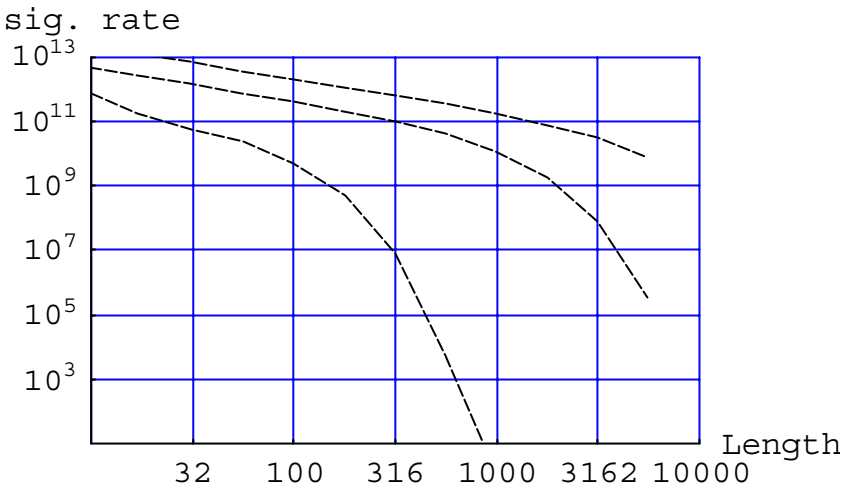

Figure 4.19: The trade-off between bus length (number of terminals) and signalling rate. Dashed curve assumes one 40 dB amplifier for every four nodes. The upper continuous curve is for a 40 dB amplifier at every node, and the lower continous curve is for a 15 dB amplifier at each node.

for an amplifier at each node (continuous curves). The parameters used for the model are given in Table 4.2 (on page 65), except where indicated differently on the figure. The lower of the two continuous curves is for lower gain (15 dB) amplifiers at each node.

4.5 Conclusion: the merits of dark signalling in an optical fibre bus

The optical bus topology is only viable if the signal power is maintained with optical amplifiers. When optical amplifiers are used, dark-signalling has a number of advantages over conventional signalling:

- noise due to amplified spontaneous emissions (ASE) from the amplifiers is suppressed by the presence of light from the source along the whole length of the bus
- there is almost no near-far effect, removing the need for the receivers to cope with a wide dynamic range in the incoming signal and simplifying the implementation of multiple access
- the presence of only a single optical wavelength in the bus allows the use of narrow-band optical filters to reduce noise

Busses operating at high signalling rates and supporting large numbers of nodes are possible with an amplifier after every four nodes, but the best performance is

achieved with a (lower-gain) amplifier at every node. It is theoretically possible for dark-signalling networks with hundreds of amplifying nodes to operate at over 100 Gbit/s.

It would be difficult to exploit this potential capacity using conventional access protocols with currently available electronics and electro-optic components, but optical CDMA might be used.

Chapter 5

Optical fibre delay-line correlators

It has been shown in Chapter 4, Section 4.4, that large networks can theoretically be operated at very high signalling rates using the amplified dark-signalling bus topology, and it has been suggested that the capacity can be exploited by using optical CDMA with optical fibre delay-line correlators (See Chapter 2). This chapter compares options in the design of delay line correlators for use in a dark signalling bus, and proposes a new correlator (the hybrid correlator), which is explored in more depth in Chapter 6.

Section 5.1 briefly introduces the general concept of fibre optic tapped delay-line filters, Section 5.2 describes the three types of delay-line correlator that were investigated in this work (coherent, incoherent and hybrid) and Section 5.3 contains an initial comparison of the three correlators in terms of the signal powers at the output.

It was noted in Chapter 3 that optical beating is a major source of noise in optical networks, and the extent of beating in a CDMA network depends both on the type of correlator and on the optical source (whether coherent or chaotic). Section 5.4 therefore compares the theoretical noise performance of the correlators for coherent and chaotic light through the use of a noise figure.

Section 5.5 draws together some conclusions about the use of fibre optic delay line correlators in the SLIM bus, noting the superiority of the hybrid correlator.

5.1 Background

The fibre optic delay line correlator is one application of the general technique of using optical fibres to construct transversal filters.

The idea that optical fibres could be used to construct high-frequency filters appeared in 1976 [187] – soon after the development of fibres themselves [188]. Papers

by Moslehi at. al. in 1984 [189] and Jackson et. al. in 1985 [190] provide overviews of the field.

The early proposals assumed that all optical path differences in the delay lines were much greater than the coherence length of the optical source. No use was made of the phase of the optical signals and measurements were entirely in terms of intensity. These are described here as incoherent filters, and Figure 5.1 shows a number of possible configurations, together with the corresponding impulse responses. (a) to (c) show feedforward configurations and (d) and (e) feedback configurations. (a) and (b) are equivalent, but (b) shows the tapped delay-line implementation which closely reflects one of the methods of construction used in some early experiments [190] in which a single length of fibre was tapped through the use of, for example, local macrobends. (a) implies an implementation using a splitter, multiple fibre lengths, and a combiner. With the ready availability of low-loss splitters and combiners this is now an easier approach to the construction for small numbers of taps. Both (a) and (b) will be referred to in the following as tapped delay-line filters (distinguishing them from ladder networks of (c), (d) and (e)), although the implementation of (a) will generally be assumed.

(c) shows a (two-stage) ladder or lattice structure which can be more power-efficient than the delay-line structure, but at the cost of the constraint that the impulse response must be symmetrical. Ladder structures are also used for feedback filters as shown in (d) (one stage) and (e) two stages.

5.2 Correlators for the dark-signalling SLIM bus.

Optical fibre delay line filters can be used to build matched filters for optical communication systems [191, 192]. Because of the limitations of code sets usable with ladder networks, correlators based upon tapped fibre delay lines were investigated for the SLIM bus. Three approaches were explored in detail: incoherent, coherent and a new proposal for a 'hybrid' correlator. They all use single-mode fused-fibre couplers to divide the light equally into W paths, but they differ in the details of the way in which the light is combined at the output, which can be: coherently in a fused fibre coupler (the 'coherent correlator'), incoherently in a fused fibre coupler (the 'incoherent correlator'), or incoherently in a hybrid coupler (the 'hybrid correlator'). With reference to Figure 5.2, the differences between the correlators is in the mechanism used for the summation.

5.2.1 Coherent correlation

To get coherent signal combination at the output it is necessary for the optical signal to have a narrow linewidth (nominally monochromatic) so that the coherence length of the signal is greater than any path-length differences in the correlator, and phase control is

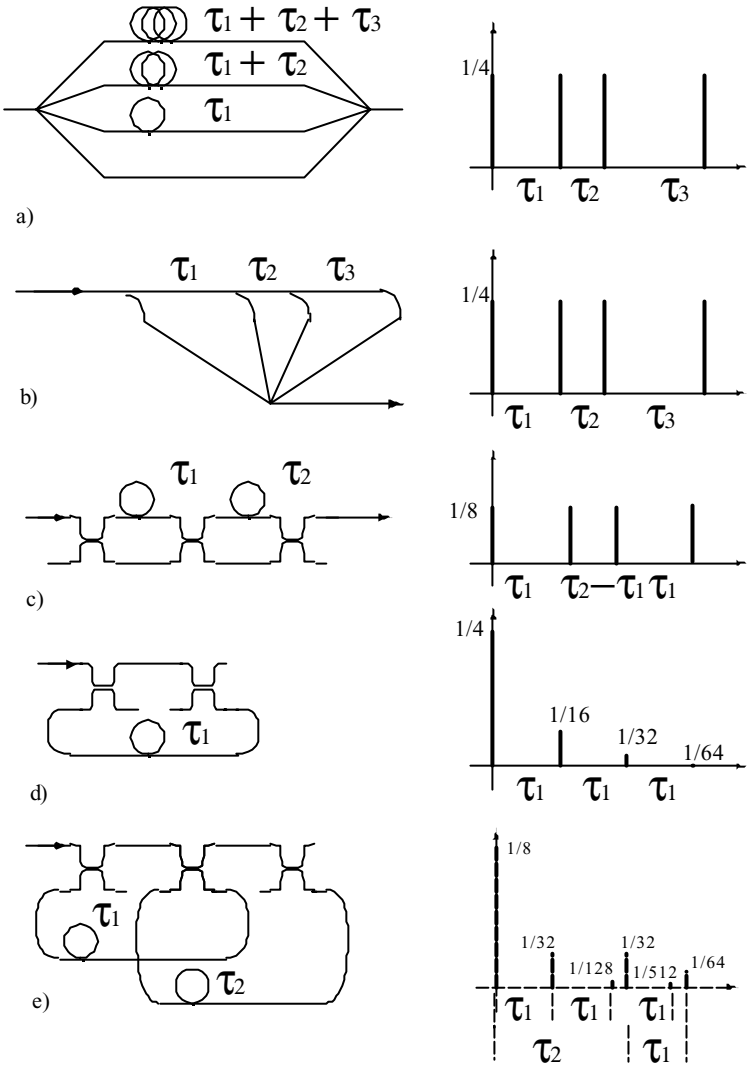

Figure 5.1: Optical fibre delay line filter configurations. For the impulse responses, assumptions have been made about the coupler and splitter coupling ratios: (c), (d) and (e) assume 3 dB (50%) couplers; (a) assumes equal 4-way splitting and lossless coupling and (b) assumes 25%, 33% and 50% splitting for the taps and lossless combining.

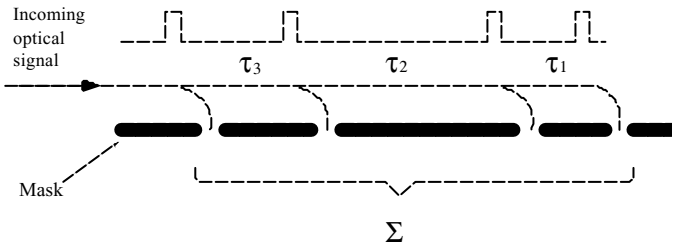

Figure 5.2: Tapped fibre delay line matched filter

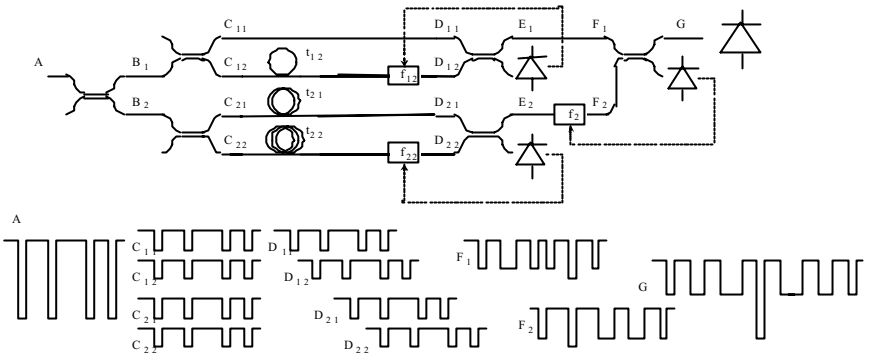

Figure 5.3: Coherent delay line correlator with phase control

required to ensure that in the 'no (dark) signal' state all the incoming power is directed to the photodiode (Figure 5.3). The phase modulators are in a feedback loop for active control of the phase relationships, but since phase drift will only occur on a relatively long time scale (of the order of milliseconds) the phase modulators can be based upon thermal devices, as in the work at the University of Kent (UKC) [121][193]. In the UKC systems, which used ladder networks, low frequency modulation was imposed on the phase using a different modulation frequency for each modulator so that separate control loops could be used for each modulator. The same scheme could be used here, but a simpler approach might be possible with the configuration of Figure 5.3, since separate photodiodes on each of the unused coupler outputs can provide the feedback to the 'local' phase controller. (These additional photodiodes would be low-cost, low frequency devices since they are only required to operate on the 'thermal drift' time-scale.)

5.2.2 Incoherent correlation

Figure 5.4 shows the mode of operation that was assumed for the early work on optical CDMA [140], in which it is assumed that the path-length differences in the correlator are all much greater than the coherence length of the source so that the power combines incoherently in the output coupler. In order to get a short coherence length and reduce the effects of optical beating (discussed below) it is necessary for the source to have a very broad linewidth.

5.2.3 Hybrid correlator

To overcome the limitations of incoherent correlation (need for very broad linewidth source and the loss of power on combining) without the need for phase control, it is possible to combine the light from parallel delay lines, not with couplers, but at the

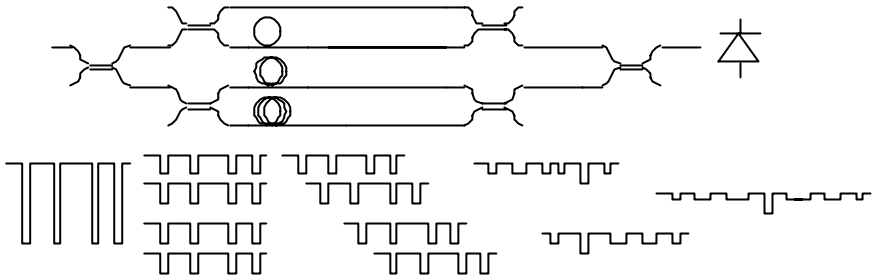

Figure 5.4: Incoherent fibre delay line

photodiode itself, Figure 5.5.

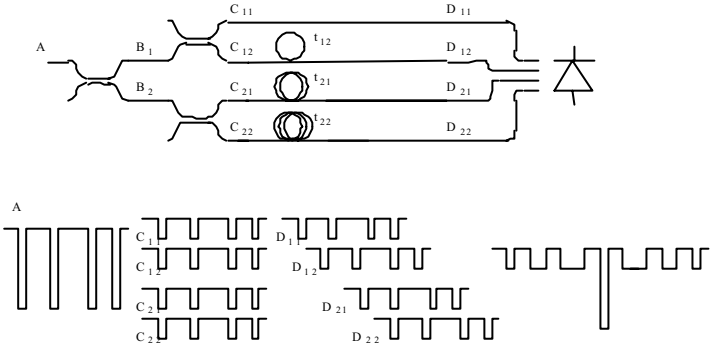

Figure 5.5: Power combination at the photodiode

Alternatively, since it is common practice for photodiodes to be supplied with a ($50/125\,\mu$m or $62.5/125\,\mu$m) multimode fibre pigtail, the proposal here is to couple light from single-mode fibre taps directly into a multimode fibre. Intuitively it can be appreciated that if the light from each (single mode) tap couples into a different mode of the multimode output fibre then, because of the orthogonality of the modes, there will be no beating. In fact it will be shown in Chapter 6 that, provided the number of modes in the output fibre is equal to or greater than the number of input fibres, in principle essentially all the light from the single mode fibres may be coupled into the multimode output fibre, independently of the phase and coherence of the light in the input fibres. Although the light conveyed by any one of the modes of the output fibre may be noisy (due to beating between light originating in different input fibres), the sum of the power over all modes is free from beating noise. Provided there is no subsequent

mode-selective loss there will be no noise due to optical beating at the photodiode output. (The hybrid correlator can be thought of as an extrapolation of the device proposed in Reference [194] that uses orthogonal polarisation modes in a birefringent fibre to eliminate optical beating in a two-path delay-line filter.) Since the output is from a multimode fibre the photodetector will need a larger area than for single mode correlators, which will limit the speed of operation of the receiver (which must respond within chip periods) due to the capacitance of the detector. However, Metal-Semiconductor-Metal (MSM) photodetectors have recently been shown to combine large detection areas with high speed performance [195, 196].

5.3 Power levels on the correlator outputs.

For all three correlators the output is (nominally) zero during the autocorrelation (dark) peak. At the other extreme, when there are no dark pulses in the signal arriving at the correlator, the output of the coherent and hybrid correlators is equal to the input power, while the incoherent correlator introduces a loss of $1/W$, where W is the number of paths (taps) in the correlator.

For the more general condition, when there are dark pulses on the incoming signal so that there are dark pulses on w of the paths feeding into the combiner ($0 \leq w \leq W$), the ratio of the output power, P_o, to the input power, P_i, is calculated as follows:

Incoherent correlator Each tap without a dark pulse contributes P_i/W^2 to the output power, so the total output power is $(W-w)P_i/W^2$ and the input-output power ratio is $(W-w)/W^2$.

Hybrid correlator Each tap without a dark pulse contributes P_i/W to the output power, so the total output power is $(W-w)P_i/W$ and the input-output power ratio is $(W-w)/W$.

Coherent correlator Because of the phase control, the field strengths from each tap add constructively. Each tap without a dark pulse contributes E_i/W, where $E_i = \sqrt{P_i}$ is the field strength[1] on the input[2], so the field strength on the output is $E_o = ((W-w)/W)\,E_i$. The ratio between in output and input power is therefore $(E_o/E_i)^2 = (W-w)^2/W^2$.

These formulae are plotted in Figure 5.6 for the specific example of $W = 8$.

The difference in power levels out from the three correlators has no significance on their performance in the absence of noise provided the decision threshold is set to be between zero and the power corresponding to the presence of $W-1$ interfering pulses in each case. An error will only occur when W (dark) pulses happen to coincide at

[1] The field strength is again defined as in Section 3.1, so that $P = E^2$.

[2] An ideal coupler, whether used as a splitter or combiner, attenuates the field by $1/\sqrt{W}$ [39], so the attenuation in going through the splitter and combiner is a total of $1/W$.

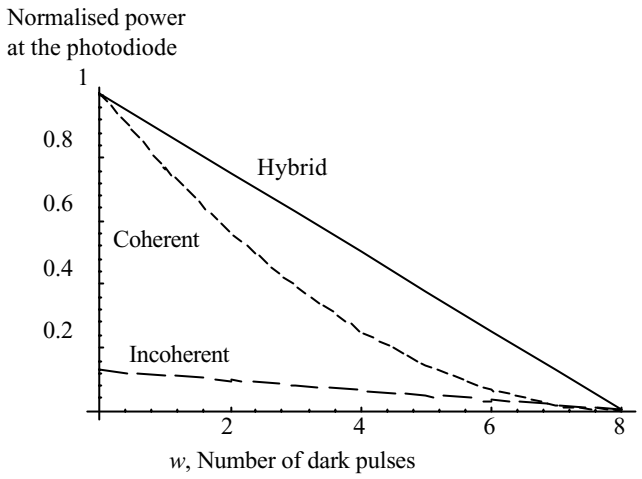

Figure 5.6: Power at the photodiode against the number of dark pulses for the three correlators and a code of weight eight. (Continuous curves are drawn to show the trends, although values are only physically meaningful at integer numbers of pulses.)

the correlator delay lines, so as to mimic the signature sequence of the code (multiple access interference: MAI).

For a real system, where noise (thermal, shot etc.) is present, power levels are important and the hybrid and coherent correlators are superior to the incoherent correlator because of the higher loss of the incoherent correlator. The steeper gradient of the hybrid correlator between $w = 7$ and $w = 8$ confers an advantage to the hybrid correlator when the threshold is set for maximum MAI tolerance, but there are further considerations which complicate the comparison between the three correlators (the coherent correlator provides a degree of noise rejection in the presence of broadband optical noise, amplified spontaneous emissions (ASE), from optical amplifiers, for example).

The best performance overall will be an optimised compromise taking into account MAI characteristics and sources of noise for a particular implementation. This is done by computer modelling in Chapter 8.

5.3.1 Interferometric noise in optical correlators

As discussed in Chapter 3, there is ideally no noise due to optical beating in a coherent correlator for which the path length differences are all very much shorter than the coherence length of the source. If, however, the path length differences are greater than coherence length of the source, as is the case for an incoherent correlator, then the effects of optical beating need to be considered. In a hybrid correlator there should be no beating because of the use of a multimode output fibre. This has not been proved rigorously, but is consistent with the measurements reported in Chapter 7 and the modelling of Chapter 6.

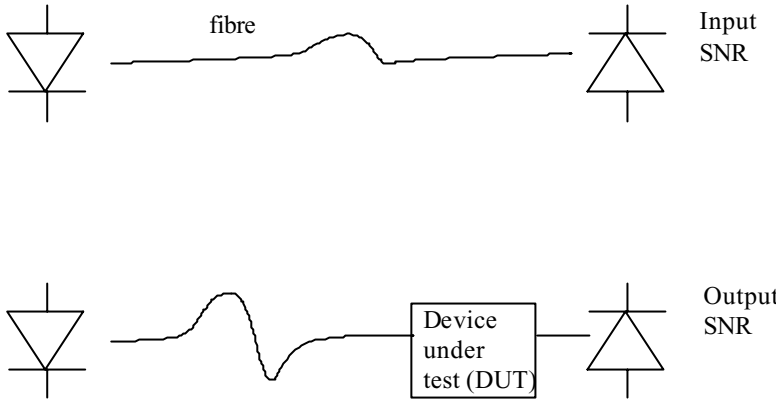

Figure 5.7: Measuring the noise figure of an optical device (SNR = signal to noise ratio).

The significance of interferometric noise and power levels on the performance of optical correlators will be seen in the results of the following section which looks at the noise figure of each of the three types of correlator.

5.4 Noise figure of optical correlators

For comparison purposes a noise figure is defined for the correlators, using a definition similar to that used in the characterisation of optical amplifiers: the ratio between the electrical signal to noise ratio in the absence of the device under test (the input signal to noise ratio) and the electrical signal to noise ratio in the presence of the device under test (the output signal to noise ratio), Figure 5.7. This Figure is determined under quiescent conditions (no dark pulses), with the signal to noise ratio calculated as the ratio between the mean photocurrent and the rms ac photocurrent.

Writing input signal to noise ratio, SNR_i for the electrical signal to noise ratio that would be measured in a receiver if the device under test (DUT) were not present, and output signal to noise ratio, SNR_o for the electrical signal to noise ratio that would be measured in a receiver after the DUT, then

$$\text{Noise Figure} = \frac{\mathrm{SNR}_i}{\mathrm{SNR}_o}. \tag{5.1}$$

The values for the noise figure depend upon the coherence properties of the optical source as well as the correlator type, so the analysis that follows considers systems using single- and multi-mode lasers as well as LEDs for both incoherent and hybrid correlators. The coherent correlator, however, can only be used with a narrowband coherent source and so is only analysed with a single-mode laser source. In general

terms there are two factors which contribute to the noise figure of a correlator: the attenuation of the optical signal (which reduces the signal power) and optical beating (which increases the noise power). The following therefore includes an analysis of the noise figure of an optical attenuator so that the effects of attenuation can be distinguished from the effects of optical beating in the correlators.

For the purposes of the analysis the optical receiver is taken to be a PIN photodiode followed by a high-impedance receiver [160], but the general conclusions are not dependent upon the details of the receiver design.

5.4.1 Single mode laser

This section assumes that the light in the correlator is from a narrowband coherent source – such as a laser diode. The signal to noise ratio without a correlator or attenuator (SNR_i in equation 5.1) is first calculated, then the output signal to noise ratio (SNR_o) and the noise figure, using equation 5.1, for an attenuator and each of the three types of correlator.

Input signal to noise ratio

The input signal to noise ratio is, of course, the same for each of the three correlators, and is calculated by deriving formulae for the signal power and the noise power referred to the photodiode output as follows. In general, for received optical signal power P_S, the electrical signal power (current-squared) at the photodiode is given by:

$$i^2 = \mathcal{R}^2 P_S^2$$

Following [160] for a high-impedance receiver design the noise is modelled by three components: shot, thermal and amplifier noise:

$$\begin{aligned} \sigma_{shot}^2 &= 2e\mathcal{R}B_e P_S \\ \sigma_{thermal}^2 &= \frac{4kTB_e}{R_L} \\ \sigma_{amp}^2 &= \left\{i_A^2\right\} B_e + \frac{\left\{v_A^2\right\} B_e}{R_L^2} + \frac{4\pi^2 B_e^3 C^2 \left\{v_A^2\right\}}{3} \end{aligned}$$

Where B_e is the electrical bandwidth (typically modelled as half the signalling rate, corresponding to signalling at the Nyquist rate [197]). Noise from the amplifier is modelled by the two sources, one current source $\left\{i_A^2\right\}$ and one voltage source $\left\{v_A^2\right\}$ [167, 160], R_L is the photodiode load resistance and C the capacitance on the photodiode. In this analysis the interest focusses on the dependency of the terms on signal power, so it is convenient to group together thermal and amplifier noise into a single term which is independent of the received signal power, designated σ_{fixed}^2.

The combined noise power is then given by

$$\sigma_{noise}^2 = 2e\mathcal{R}B_e P_S + \sigma_{fixed}^2 \tag{5.2}$$

And the signal to noise ratio is then:

$$SNR_i = \frac{\mathcal{R}^2 P_S^2}{2e\mathcal{R}B_e P_S + \sigma^2_{fixed}} \tag{5.3}$$

Noise figure of an attenuator with a single-mode laser

As noted earlier, it is useful to have the noise figure of an attenuator for comparison with the correlators so as to be able to distinguish between effects due to the attenuation of correlators and the effects due to optical beating. This section therefore assumes that the 'device under test' is a device which simply reduces the optical power by a factor of L. The output signal to noise ratio is then given by equation 5.3, but with P_S replaced by P_S/L, and the noise figure is:

$$NF = \left[\frac{\mathcal{R}^2 P_S^2}{2e\mathcal{R}B_e P_S + \sigma^2_{fixed}}\right] / \left[\frac{\mathcal{R}^2 P_S^2/L^2}{2e\mathcal{R}B_e P_S/L + \sigma^2_{fixed}}\right] = L\frac{P_S/P_0 + L}{P_S/P_0 + 1}$$

Where $P_0 = \sigma^2_{fixed}/2eB_e\mathcal{R}$. This is plotted in Figure 5.8. In the limit of high power (shot noise is greater than fixed noise, $P_S >> P_0$) this reduces to $NF = L$ and in the limit of low power (fixed noise is greater than shot noise, $P_S << P_0$) $NF = L^2$

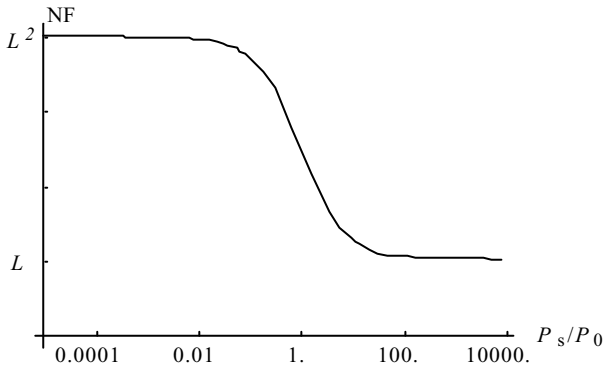

Figure 5.8: Noise Figure as a function of (normalised) signal power for an attenuator.

A lower-bound on P_0 is given by using $\sigma^2_{fixed} = \sigma^2_{thermal} = \frac{4kTB_e}{R_L}$ and $\mathcal{R} = e/hf$ (corresponding to unity quantum efficiency) for which

$$P_0 = \frac{2kThf}{R_L e^2} = \frac{2kTc}{R_L (e^2/h)\,\lambda}$$

For example, with the values of T, R_L, and λ typical of later experiments and listed in Table 5.1, P_0 is approximately -22 dBm ($6\,\mu$W). Note that typical optical fibre transmission systems operate with a receiver power in the range -30 dBm to -40 dBm [160], so -22 dBm is relatively high, supporting the familiar result [160] that receivers are generally limited by thermal or other noise internal to the receiver rather than by shot noise.

Parameter	Symbol	Value
Temperature	T	290 K
Photodiode load	R_L	8 k-
Wavelength	λ	1300 nm
Electrical bandwidth	B_e	100 MHz
Optical bandwidth, thermal source	B_S	1.8×10^{12} Hz (10 nm)

Table 5.1: Typical parameter values

Noise figure of a hybrid correlator with a single-mode laser

Given that there is no beating in a hybrid correlator (as claimed above and analysed in Chapter 6), the only contribution to the noise figure of a hybrid correlator is attenuation. Furthermore there is no inherent loss in a hybrid correlator, and so the only attenuation is the excess loss, α. Following the calculation for an attenuator, therefore, the noise figure of a hybrid correlator should be equal to α at low signal powers and α^2 at high signal powers. An 'ideal' hybrid correlator, with no excess loss ($\alpha = 1$), has unity noise figure (no increase in noise) at any power.

Noise figure of an incoherent correlator with a single-mode laser

An incoherent correlator introduces an additional noise due to beating between light taking different paths through the correlator, as was analysed in Chapter 3, Section 3.6. For an incoherent correlator the path differences are very much greater than the coherence time of the light, so Equation 3.15 provides the additional term, σ^2_{S-S}, which must be included in the total noise power. Modified to include the excess loss, α and to take account of the splitting losses this additional noise term is:

$$\sigma^2_{S-S} = \frac{1}{4\pi\alpha^2}\mathcal{R}^2 P_S^2 \tan^{-1}(B_e/\nu_1)$$

Where B_e is the electrical bandwidth of the receiver as before and ν_1 is the full width at half maximum linewidth of the optical source. With a total power reaching the photodiode of P_S/α the combined noise power is then given by

$$\sigma^2_{noise} = \sigma^2_{fixed} + \frac{e\mathcal{R}B_e}{\alpha}P_S + \frac{\tan^{-1}(B_e/\nu_1)}{4\pi\alpha^2}\mathcal{R}^2 P_S^2$$

the signal to noise ratio is:

$$\frac{\mathcal{R}^2 P_S^2/\alpha^2}{\sigma^2_{fixed} + \frac{e\mathcal{R}B_e}{\alpha}P_S + \frac{\tan^{-1}(B_e/\nu_1)}{4\pi\alpha^2}\mathcal{R}^2 P_S^2}$$

and the NF

$$NF = \frac{\left[\frac{\mathcal{R}^2 P_S^2}{2e\mathcal{R}B_e P_S + \sigma^2_{fixed}}\right]}{\left[\frac{\mathcal{R}^2 P_S^2/\alpha^2}{\sigma^2_{fixed} + e\mathcal{R}B_e P_S/\alpha + \tan^{-1}(B_e/\nu_1)\mathcal{R}^2 P_S^2/4\pi\alpha^2}\right]} = \frac{\beta\left(\frac{P_S}{P_0}\right)^2 + \alpha\frac{1}{2}\frac{P_S}{P_0} + \alpha^2}{\frac{P_S}{P_0} + 1}$$

Where $P_0 = \sigma^2_{fixed}/2eB_e\mathcal{R}$ (as before) and $\beta = \frac{\sigma^2_{fixed}}{4\pi(2eB_e)^2}\tan^{-1}(B_e/\nu_1)$
At high signal power:

$$NF = \beta\frac{P_S}{P_0} = \tan^{-1}(B_e/\nu_1)\frac{\mathcal{R}P_S}{8\pi eB_e} \tag{5.4}$$

There are some counter-intuitive aspects to this high-power noise figure:

- It *increases* with increasing signal power. This is because the noise due to beating increases with increasing signal power.
- It *decreases* with increasing electrical bandwidth. This is because beating noise is band-limited but the other sources of noise are modelled as white.

In the limit of low signal power the noise figure becomes α^2, the same as an equivalent attenuator (at low enough power the beating noise is less than the fixed noise). Care has to be taken about the interpretation of 'low power' in this case however, because (as will be seen with illustrative values below) it is not necessarily sufficient for $P_S \ll P_0$; it is also necessary for $\beta\left(\frac{P_S}{P_0}\right)^2 \ll 2\alpha^2$, so $P_S \ll \alpha P_0/\sqrt{\beta/2}$.

Using the illustrative values of Table 5.1 and assumptions from above again gives a lower limit of 6 μW for P_0. A value for β additionally requires knowledge of B_e/ν_1, but assuming $B_e \gg \nu_1$ (a reasonable assumption for $B_e = 100\,\text{MHz}$) gives:

$$\begin{aligned}\beta &= \frac{\sigma^2_{fixed}}{4\pi(2eB_e)^2}\tan^{-1}(B_e/\nu_1) = \frac{\left(\frac{4kTB_e}{R_L}\right)}{4\pi(2eB_e)^2}\frac{\pi}{2} \\ &= \frac{1}{8}\frac{kT}{e^2B_eR_L} = \frac{1}{8}\frac{\left(1.38\times10^{-23}\,\text{J K}^{-1}\right)(290\,\text{K})}{(1.6\times10^{-19}\,\text{C})^2(100\,\text{MHz})(8\,\text{k-}\ )} \\ &\approx 25\,000.\end{aligned}$$

The 'low power' regime therefore requires $P_S \ll P_0/\sqrt{25\,000/2} \approx 0.05\,\mu$W. This is about -43 dBm, indicating that for typical receiver sensitivities the beating noise would be significant. Figure 5.9 shows the noise figure as a function of P_S/P_0 with $\beta = 25000$ and $\alpha = 1$ (no excess loss).

Noise figure of a coherent correlator with a single-mode laser

The coherent correlator is assumed to have perfect phase control and to have attenuation (excess loss) of α. Given the optical path length differences are all much less than the coherence length of the light, the device appears as an attenuator with noise figure equal to α at low signal powers and α^2 at high signal powers.

5.4.2 Noise figures with a multimode source

This section looks at the noise figure of an attenuator and correlators when the light source is a multimode laser diode. Although it is unlikely that this type of optical

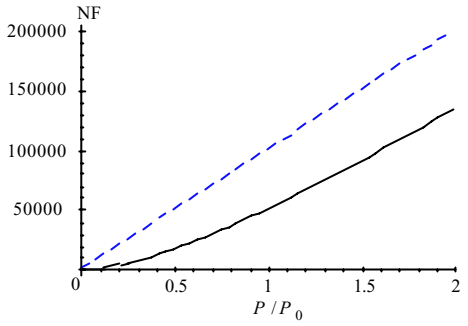

Figure 5.9: Noise Figure as a function of incoming optical power, normalised to P_0, for an incoherent correlator and a single mode laser.

source would be used in a developed system, the results are important for this project because a Fabry-Perot laser diode was used in the experimental work described in later chapters. It is assumed that the mode spacing is large enough that beating between modes is removed by electrical filtering (see ref. [175] Section 2.3.1). (For example, for mode spacing greater than 0.1 nm beating frequencies will be greater than 15 GHz. The noise measurements described in Chapter 7 used low pass filtering at 20 MHz.).

Because each of the modes is coherent (like a single mode laser) and the beating between modes is removed by filtering, there is no measurable beating in the input field and the formula for the input signal to noise ratio for the multimode laser is the same as for the single mode laser. Furthermore neither an attenuator nor a hybrid coupler introduce further beating, so the noise figures of both these devices are the same when used with a multimode laser as with a single mode laser. An incoherent correlator, however, does introduce beating and requires further analysis.

The multimode source spectrum is modelled so that the power is distributed between n modes: $P_S = \sum_{i=1}^{n} r_i P_S$ where r_i is the fraction of the source power in mode i ($\sum_{i=1}^{n} r_i = 1$). The analysis then follows that of Section 5.4.1 but beating noise is analysed separately for each mode. At the splitter each mode is divided two ways so that the power in the modes in the taps is $P_{o1i} = r_i P_{o1} = r_i P_S/2\alpha$. When the power is re-combined the light from the two paths is statistically independent and beating takes place in each mode resulting in a noise component due to beating of:

$$\begin{aligned}\sigma^2_{S-S} &= \sum_{i=1}^{n} \frac{1}{\pi}\mathcal{R}^2 \left(r_i P_S/2\alpha\right)^2 \tan^{-1}\left(B_e/\nu_{1i}\right) \\ &= \frac{1}{\pi}\mathcal{R}^2 \left(P_S/2\alpha\right)^2 \tan^{-1}\left(B_e/\nu_1\right) \sum_{i=1}^{n} r_i^2\end{aligned}$$

The last step assumes that all the modes have the same spectral (Lorentzian) linewidth: ν_1. This differs from the case of the single mode laser (Equation 5.4) only by the factor $\sum_{i=1}^{n} r_i^2$, which takes account of the power distribution among the modes. For more than one mode ($n > 1$) this is less than unity, and in general is lower the

more 'spread' the power is between modes.

The modelling proceeds as for the single mode laser, leading to

$$\sigma^2_{noise} = \sigma^2_{fixed} + 2e\mathcal{R}B_eP_o + \frac{1}{\pi}\mathcal{R}^2\left(P_S/2\alpha\right)^2\tan^{-1}\left(B_e/\nu_1\right)\sum_{i=1}^{n} r_i^2 \qquad (5.5)$$

for the noise and

$$NF = \frac{\beta\left(\frac{P_S}{P_0}\right)^2\sum_{i=1}^{n} r_i^2 + \frac{1}{2}\alpha\frac{P_S}{P_0} + \alpha^2}{\frac{P_S}{P_0} + 1}$$

Where $P_0 = \sigma^2_{fixed}/2eB_e\mathcal{R}$ and $\beta = \frac{\sigma^2_{fixed}}{4\pi(2eB_e)^2}\tan^{-1}\left(B_e/\nu_1\right)$ as for the single mode laser. The noise figure at higher powers is reduced by spreading the power between more modes, but it must be remembered that it was assumed that the modes are sufficiently spaced so that beating between different modes may be neglected. Thus the model does not cover the limiting case in which a many moded laser tends to show the characteristics of an LED.

For illustration, suppose the laser has modes spaced by $\Delta\nu$ Hz in a Gaussian envelope of width ν_0 Hz, such that $r_i = Re^{-(\Delta\nu\, i/\nu_0)^2}$ where the mode indices are taken positive and negative. Normalisation requires $R = 1/\sum_{i=-\infty}^{\infty} e^{-(\Delta\nu\, i/\nu_0)^2}$, and the weighting factor is therefore given by:

$$\sum_{i=1}^{n} r_i^2 = \frac{\sum_{i=-\infty}^{\infty} e^{-2(\Delta\nu\, i/\nu_0)^2}}{\left(\sum_{i=-\infty}^{\infty} e^{-(\Delta\nu\, i/\nu_0)^2}\right)^2}$$

This depends only on $\Delta\nu/\nu_0$ and, taking some numerical examples, $\Delta\nu/\nu_0$ of 0.5, 1, 1.5, 2 gives 0.20, 0.40, 0.70 and 0.93 respectively.

The spectrum of the laser used in the measurements reported in Chapter 7 has the spectrum of Figure 5.10. Neglecting for the moment the subsidiary (transverse) modes, it can be estimated that $\Delta\nu/\nu_0 \approx 0.6$ for which the weighting factor would be approximately 0.24. The splitting of the longitudinal modes into multiple transverse modes will further reduce the effective weighting factor, but this has not been modelled in the current work, since only general trends are important, not detailed quantitative models.

5.4.3 Broadband, thermal-like, source (LED)

This section examines the noise figures of attenuators and correlators when the light source is broadband and incoherent, such as from an LED. The source is modelled by a uniform power spectral density n_S over bandwidth B_S giving total power $P_S = n_SB_S$, and because the source is incoherent it displays significantly different noise characteristics compared to a single- or multi-mode laser.

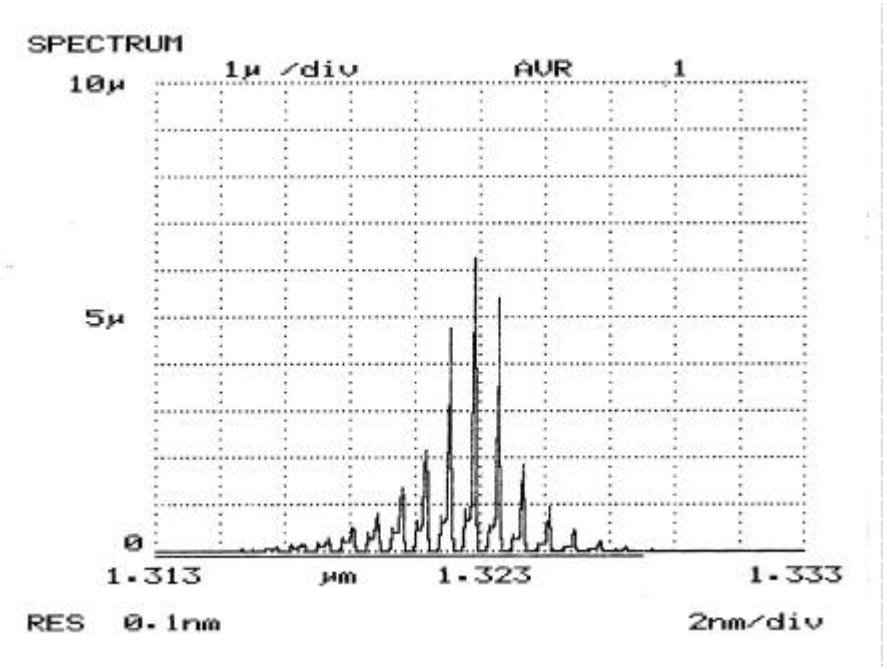

Figure 5.10: Spectrum of multimode Fabry-Perot laser diode.

Input signal to noise ratio for an LED

Because the source is incoherent there is a contribution to the noise due to optical beating effects even in the absence of multiple paths to the receiver. Using results from Section 3.3 there will therefore be a contribution to the noise on the input signal to noise ratio of:

$$\begin{aligned}\sigma^2_{S-S} &= B_e\mathcal{R}^2 n_S^2(2B_S - B_e)\\ &\approx 2\mathcal{R}^2 n_S^2 B_e B_S = 2\mathcal{R}^2 B_e P_S^2/B_S\end{aligned}$$

(Where the approximation is for $B_S \gg B_e$).

So:

$$SNR_i = \frac{\mathcal{R}^2 P_S^2}{2e\mathcal{R}B_e P_S + \sigma^2_{fixed} + \mathcal{R}^2 2B_e P_S^2/B_S}$$

For a high power limit ($2e\mathcal{R}B_e P_S + \mathcal{R}^2 2B_e P_S^2/B_S \gg \sigma^2_{fixed}$):

$$SNR_i = \frac{\mathcal{R}P_S/2B_e}{e + \mathcal{R}n_S}$$

The responsivity can be written as $\mathcal{R} = \eta e/h\upsilon$, where η is the quantum efficiency ≈ 1 (electrons/photon) and $h\upsilon$ is the photon energy. Then if $n_S \gg h\upsilon$ beating noise dominates and:

$$SNR_i = \frac{\mathcal{R}P_S/2B_e}{\mathcal{R}n_S} = \frac{P_S}{2B_e n_S} = \frac{n_S B_S}{2B_e n_S} = \frac{B_S}{2B_e}$$

If $n_S \ll h\upsilon$ (but still $2e\mathcal{R}B_eP_S \gg \sigma^2_{fixed}$) then the shot noise limit is the same as for a single mode laser:

$$SNR_i = \frac{\mathcal{R}P_S}{2eB_e}$$

At low power, as before:

$$SNR_i = \frac{\mathcal{R}^2P_S^2}{\sigma^2_{fixed}}$$

For example, with the parameters of Table 5.1 the beating noise dominates shot noise for $n_S \gg h\upsilon = 1.53 \times 10^{-19}$, so $P_S \gg 0.28\,\mu$W

The low power limit obtains as before when $P_S \gg 6\,\mu$W. Since this is greater than $0.28\,\mu$W, it would appear that shot noise is never dominant (for these parameters): thermal noise dominates for $P_S \ll 6\,\mu$W and beating dominates for $P_S \gg 6\,\mu$W.

Noise figure of an attenuator with an LED

As with other light sources, the signal to noise ratio after an attenuator is given by the same formula as the input signal to noise ratio but with received power reduced by the attenuation, L. The noise figure is then,

$$\mathrm{NF} = \frac{\left[\frac{\mathcal{R}^2P_S^2}{2e\mathcal{R}B_eP_S+\sigma^2_{fixed}+\mathcal{R}^2 2B_eP_S^2/B_S}\right]}{\left[\frac{\mathcal{R}^2P_S^2/L^2}{2e\mathcal{R}B_eP_S/L+\sigma^2_{fixed}+\mathcal{R}^2 2B_eP_S^2/L^2B_S}\right]}$$

Considering then the limiting cases:

1. (High power limit – optical beating) if $n_S \gg h\upsilon$ and $P_S \gg \sigma^2_{fixed}/2e\mathcal{R}B_e$ then

$$SNR_o = SNR_i = \frac{B_S}{2B_e}$$

and NF = 1. Attenuation does not affect the signal to noise ratio because the noise is attenuated equally with the signal.

2. (Shot noise) If $n_S \ll h\upsilon$ and $P_S \gg \sigma^2_{fixed}/2e\mathcal{R}B_e$ then NF $= L^2$

3. (Low power limit – thermal/receiver noise) if $n_S \ll h\upsilon$ and $P_S \ll \sigma^2_{fixed}/2e\mathcal{R}B_e$ then NF $= L$

Noise figure of the correlators with an LED

As discussed in Section 3.6.2, provided the path length differences are much greater than the coherence length of the source, interferometers do not generate any further interference in an incoherent optical signal. The effect of incoherent and hybrid correlators on the noise figure is therefore the same as an attenuator with the same loss. The loss of the hybrid correlator is defined to be α, while the loss of a (2-path) incoherent correlator is 2α, so the correlator noise figures are given by the formulae above, with $L = \alpha$ for the hybrid correlator and $L = 2\alpha$ for the incoherent correlator.

5.4.4 Comparisons

Insight into the differences between the different correlators for the different optical sources can be gained by comparing noise figures in the limits of high or low optical power, and this is summarised in Table 5.2. In this table α is the excess loss of the correlators, L is the loss of the attenuator and the other symbols are discussed below. In the limit of low power, when the noise is dominated by the fixed noise in the receiver, all devices tend to a noise figure of $(\text{loss})^2$ but the incoherent correlator is inferior because of the splitting loss. (This appears as a factor 2^2 in the table because the modelling was based upon a two-path correlator. More generally, the incoherent correlator would have an addition factor W^2 for an W-path correlator.)

At higher powers the performance is limited either by shot-noise or optical beating.

With an incoherent source (LED) at high power, the noise figure results entirely from the attenuation because the interferometer does not cause any additional beating (see Chapter 3). Two regimes are identified: if $n_S \ll h\upsilon$ (the power spectral density is much less than the photon energy) then the performance is limited by shot noise, which results in a noise figure equal to the attenuation. If, on the other hand, $n_S \gg h\upsilon$, the performance is dominated by optical beating intrinsic to the source. Since this is independent of power level it results in unity noise figure: the devices do not degrade the signal to noise ratio.

With a coherent source (single or multimode laser) at high power, the hybrid and coherent correlators (and the attenuator) are dominated by shot noise which results in a noise figure equal to the attenuation. The incoherent correlator however is dominated by beating noise resulting in a substantially greater noise figure. For a single mode laser the noise figure for an incoherent correlator at high power is given by $\beta P_S/P_0$ where typical values of β and P_0 are 10^5 and $6\,\mu$W respectively (assuming the parameters of Table 5.1, on page 86: see Section 5.4.1). For a multimode laser, on the assumption that beating between modes will be at frequencies removed by the low-pass filtering in the receiver, the beating is less than for a single mode laser.

For typical parameters (Table 5.1), the transition between the 'low power' and 'high power' regimes is around $P_0 = 6\,\mu$W (-22 dBm), except for the incoherent correlator with a coherent source. For the incoherent correlator with a coherent source the transition is around $P_0/\sqrt{\beta/2} \approx 0.03\,\mu$W (-45 dBm) for a single mode laser and of the order of $P_0/\sqrt{(\beta/2)\sum_{i=1}^{n} r_i^2} \approx 0.06\,\mu$W (-42 dBm) for multimode source. Bearing in mind that typical receiver sensitivities in point-to-point optical links are of the order of -30 dBm to -40 dBm (depending upon signalling rate, see, for example, reference [160]) these values indicate that system performance will always be seriously degraded by optical beating if an incoherent correlator is used with a coherent source.

Device	Single mode		Multimode		LED		
	High	Low	High	Low	High		Low
					$n_S \gg h\upsilon$	$n_S \ll h\upsilon$	
Attenuator	L	L^2	L	L^2	1	L	L^2
Hybrid	α	α^2	α	α^2	1	α	α^2
Incoherent	$\beta\frac{P_S}{P_0}$	$(2\alpha)^2$	$\beta\frac{P_S}{P_0}\sum_{i=1}^{n} r_i^2$	$(2\alpha)^2$	1	2α	$(2\alpha)^2$
Coherent	α	α^2	-	-	-	-	-

Table 5.2: Noise Figure bounds for delay-line filters, with single- and multi-mode lasers and LEDS, in the high- and low-power limits. Attenuation included for comparison. See text for explanation of symbols.

5.5 Conclusions: the merits of the hybrid correlator

An incoherent optical fibre delay line filter has been used as the correlator in many previous proposals for optical CDMA (see Chapter 2), but it suffers from a higher insertion loss than both the coherent correlator and the hybrid correlator. The incoherent correlator also introduces substantial additional noise due to optical beating when used with a coherent source such as laser diode. The hybrid and coherent correlators have similar performance in terms of loss and noise figure, but the coherent correlator requires optical phase control and is only suitable for use with narrowband light sources (single mode lasers), whereas the hybrid correlator may be used with any optical source and requires no phase control.

The effects of optical beating can have a substantial impact upon the performance of optical CDMA (see discussion on page 29 in Chapter 2). In conventional optical networks where more than one optical carrier are simultaneously present on the fibre, the performance is limited by beating between carriers, and beating is a problem whatever type of correlator is used. The SLIM network only has a single, shared, optical carrier so there is no beating between carriers and any beating introduced by multiple paths in the correlator has a significant impact upon the network performance. The hybrid correlator therefore offers a substantial performance advantage in a SLIM network as will be seen more clearly in the network simulations presented in Chapter 8.

Chapter 6

Modelling and design of hybrid couplers

The previous chapters have established the merits of the hybrid correlator, which, it has been claimed, has a lower inherent loss than an incoherent correlator and is free from optical beating. The benefits of the hybrid correlator derive from the detection of all the light from the correlator taps at the photodiode, independent of the relative optical phase in the taps. It was postulated in Chapter 5 that this could be done by coupling light from single-mode taps into a multimode output fibre, using a device called here a hybrid coupler, and detecting the multimode fibre output at a photodiode in the usual way.

This chapter now explores the feasibility of a hybrid coupler by proposing a coupler structure based upon bulk optics and modelling the coupler properties. The coupling model is presented in Section 6.4, but first Sections 6.2 and 6.3 investigate the coupler geometry using geometrical optics. Although the principal concern is with coupling from multiple single mode fibres to a single multimode fibre (the hybrid coupler, Section 6.2), additional insight is achieved by initially investigating multimode-to-multimode coupling (the multimode coupler, Section 6.3).

6.1 Past work

Coupling at joints between pairs of similar fibres has been extensively investigated (see the standard texts such as Snyder and Love [5] and Neumann [198], as well as early papers such as Di Vita and Rossi [199]) as has been the coupling from lasers to multimode fibre [4].

Also, there has been work done on evanescent field coupling between single- and multi-mode fibres [200, 201, 202] (shown in Figure 6.1(a)), with the aim of creating asymmetric taps that couple light efficiently on to a (multimode) bus without extracting much of the light from the bus. With a small number of single mode fibres and a highly-moded multimode fibre it would be possible to use this approach to build

a hybrid coupler. The more direct approach of Figure 6.1(b) should be much more efficient, however, and is the method explored in this chapter.

The only previous work that appears to have been published on direct coupling from multiple single mode to single multimode fibre is that described in a paper presented at NOC 98 [203]. This was a silica-based planar lightwave circuit which couples 16 single mode fibres to one multimode fibre. The paper contains no theory but says that it was analysed by the beam propagation method (BPM [204]).

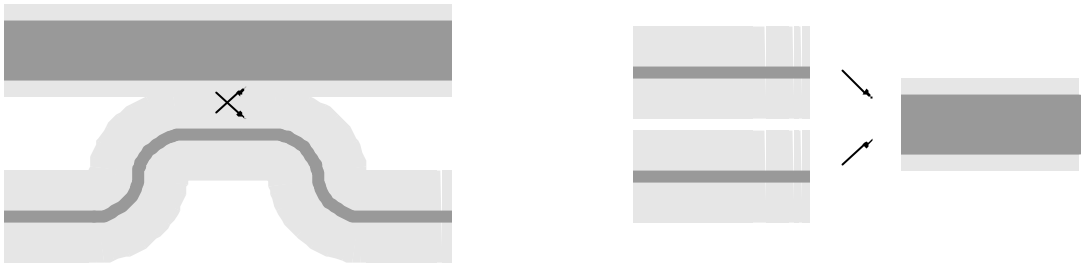

a) Evanescent field coupling b) Direct coupling

Figure 6.1: Coupling between single mode and multimode fibres.

6.2 Multimode coupler geometry

This section examines the geometry for the limiting case of high V-number input and output fibres, but with the restriction that the V-number of the input fibres is less than that of the output fibre. Because of the high V-numbers, the angular distribution of the light out from a fibre and the light gathering capacity of a fibre is adequately described by the fibre numerical aperture [5]. Specifically, it is assumed that the light out from a fibre end is all contained within a cone with a half-angle equal to the fibre numerical aperture[1], and that light impinging on the fibre core within the same cone will all be gathered.

The imaging optics is then configured so that:

1. all light from each input fibre is imaged within the core of the output fibre
2. the angle the light path makes with the axis of the output fibre does not exceed the numerical aperture of the output fibre for any of the input fibres

With the modelling assumptions given, these two conditions ensure that all light from each of the input fibres is gathered by the output fibre (neglecting reflections, scattering and absorption).

[1] The paraxial asssumption is made throughout this document: that the divergence angles are small enough that we can equate $\sin(\theta) = \tan(\theta) = \theta$

6.2.1 Focusing with a single lens.

The geometry of focussing with a single lens is shown in Figure 6.2. The lens focusses all the axial rays (black on Figure 6.2) to a point at the centre of the output fibre. Divergent rays (red and blue) from the input fibres are focussed to points offset from the centre of the output fibre so that the image size on the output fibre is spread to a width of $d = 2\mathrm{NA}_i f$, where NA_i is the numerical aperture of the input fibres which, for multimode fibres, corresponds to the divergence half-angle of the light emerging from the fibre [5], and f is the lens focal length [205].

Given the diameter of the output fibre core, d_o, this places an upper limit upon f if there is to be no loss. That is, $d_o \geq d$ so $d_o \geq 2\mathrm{NA}_i f$, which rearranges to:

$$f \leq d_o / 2\mathrm{NA}_i \tag{6.1}$$

For typical communications-grade 50/125 μm multimode fibre $d_o = 50\,\mu$m and the numerical aperture of typical fibres which is around 0.1 - 0.3 [206], so that $f \leq 2.5 \times 10^{-4}$ m. Although it would be difficult to work with a lens with a focal length around a quarter of a millimetre, it is instructive to ignore the practicalities for the moment and pursue the analysis further, taking into account the second of the requirements identified earlier – the need to ensure that the angle the light path makes with the axis of the output fibre does not exceed the numerical aperture of the output fibre for any of the input fibres.

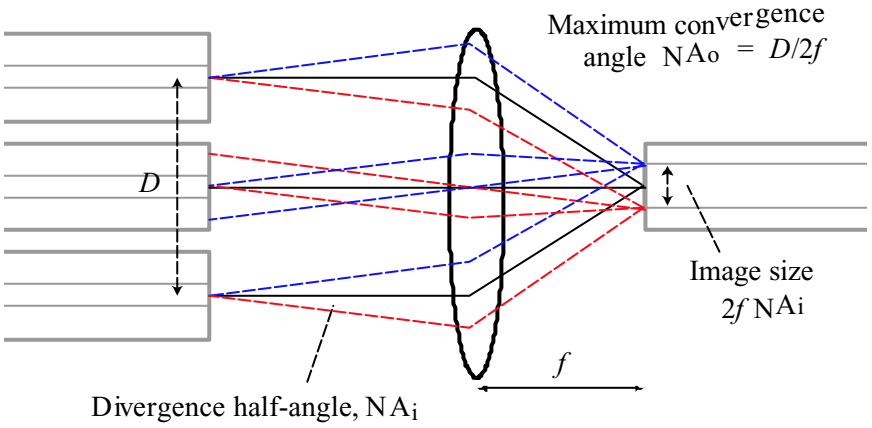

Figure 6.2: Geometry of focussing with a single lens. (The dashed-lines are used to determine the image size, they do not represent rays.)

This places a constraint upon how far off-axis the input fibres may be placed, and therefore how many input fibres may be used. For a multimode fibre the maximum input angle is given by the numerical aperture, $\mathrm{NA_o}$ [5], so from the geometry of Figure 6.2:

$$D/2 \leq f\mathrm{NA_o} \tag{6.2}$$

The input fibres must fit within a circle of diameter $2f\mathrm{NA_o}$. In principle the cladding of the input fibre could be etched to reduce their outside diameter in order to pack them more closely. The core diameter, d_i, therefore provides a lower limit to the possible input fibre diameter, and the limit to the number of input fibre that may be used is given by the maximum number of circles of diameter d_i that will fit within a circle of diameter $D = 2f\mathrm{NA_o}$. (Etching too close to the core would result in high losses from the evanescent field, but this is neglected in the current analysis and the result treated as an upper bound on the packing density. Section 6.2.2 describes a configuration which allows the bound to be approached more closely.)

For $d_i \ll D$ 'edge effects' are small and from Figure 6.3 the maximum packing density is [207]:

$$\frac{\pi r^2}{6r^2 \cot(\pi/6)} = \frac{\pi}{2\sqrt{3}} = .91$$

and an upper limit to the number of input fibres, n, is given by

$$n = \frac{0.91D^2}{d_i^2} \tag{6.3}$$

Combining equations 6.3, 6.2 and 6.1 and rearranging, gives:

$$n = 0.91\left(\frac{d_o\mathrm{NA_o}}{d_i\mathrm{NA_i}}\right)^2 \tag{6.4}$$

The 'V number' of a fibre at (free-space) wavelength λ is defined by $V = 2\pi\mathrm{NA}d/\lambda$ (where NA and d are the fibre numerical aperture and the fibre core diameter respectively) [5] and so Equation 6.4 can be rewritten as:

$$n = 0.91\left(\frac{V_o}{V_i}\right)^2 \tag{6.5}$$

The number of modes for highly-multimoded fibres is proportional to V^2[5], so 6.5 can be written as:

$$N = 0.91\frac{M_{bmo}}{M_{bmi}} \tag{6.6}$$

where M_{bmo} and M_{bmi} are the number of bound modes in the output and input fibres respectively.

Equation 6.6 can be thought of as 'mode conservation' and is consistent with results for coupling from sources to fibre[2] [208].

6.2.2 Two-stage focussing

The small focal length required of the lens was a consequence of the divergence of the light from the output beam (Equation 6.1). This section examines the consequence of collimating the light prior to focussing as shown in Figure 6.4.

[2] This is to be expected, since the input fibre can be considered to be a 'source' to be coupled into the output fibre.

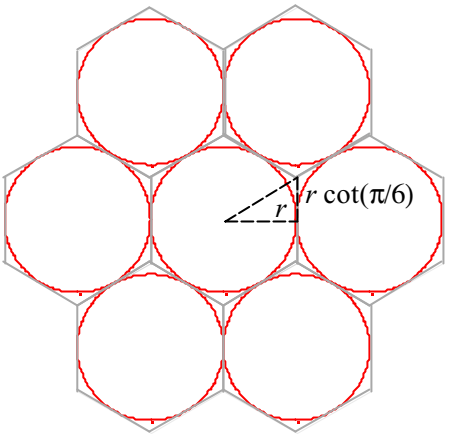

Figure 6.3: Circle packing density. The hexagons tessellate, so that the packing density is given by the ratio of the area of a circle to the area of the hexagon.

Light emerges from the input fibres at angles of up to NA_i from the fibre axis, and from anywhere across the fibre core, which has diameter d_i. Taking the focal length of the collimation lens as f_1, the collimated beam width, A, will be:

$$A = 2f_1\mathrm{NA}_i + d_i \simeq 2f_1\mathrm{NA}_i \tag{6.7}$$

the approximation being valid provided $2f_1\mathrm{NA}_i \gg d_i$.

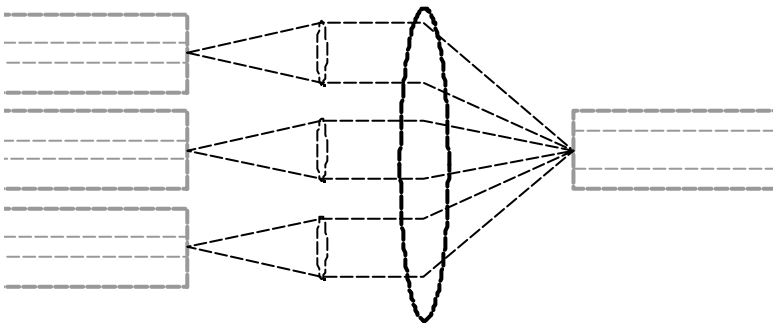

Figure 6.4: Focusing light from multiple input fibres onto one output fibre

The finite diameter of the core results in a non-zero divergence in the collimated beam equal to $d_i/2f_1$ (Figure 6.5), and this residual divergence results in an image size on the output fibre of $2\left(d_i/2f_1\right)f_2 = d_i f_2/f_1$(where f_2 is the focal length of the focussing lens).

As before, the image must be no bigger than the output fibre core, d_o, so $d_o \geqslant d_i f_2/f_1$ which re-arranges to:

$$\frac{d_o}{d_i} \geqslant \frac{f_2}{f_1} \tag{6.8}$$

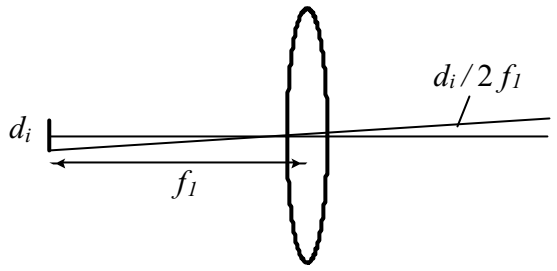

Figure 6.5: Divergence as a consequence of finite core diameter

Assume now:

1. the collimating lens diameter is equal to the collimated beam width, A
2. the collimated beams must lie within a circle of diameter D, restricted by the requirement that the angle the light path makes with the axis of the output fibre must not exceed the numerical aperture of the output fibre for any of the input fibres

As before this becomes a problem of fitting circles of diameter A within a circle of diameter D, and is approximated by Equation 6.3 (replacing the fibre core diameter, d_i, by the collimated beam width, A):

$$N = \frac{0.91 D^2}{A^2}$$

Substituting for A from Equation 6.7, for D from Equation 6.2, using Equation 6.8 and rearranging gives:

$$N \leq \frac{0.91 \left(d_o \mathrm{NA_o}\right)^2}{\left(d_i \mathrm{NA_i}\right)^2}$$

This is identical to Equation 6.4, and it is concluded that the collimation does not alter the number of input fibres that can be coupled into the output fibre. However, there were two practical difficulties in the scheme without collimation that are overcome:

1. The impractically small focal length required for the focusing lens. This is replaced by a constraint on the ratio between the focal lengths of the two lenses (Equation 6.8)
2. The need to remove all of the cladding of the input fibres in order to maximise the number of fibres that are placed alongside each other. This is replaced by the need to make the diameter of the collimating lenses equal to the collimated beam width.

6.3 Hybrid coupler geometry

This section examines the geometry of a coupler with single mode input fibres and a multimode output fibre: a 'hybrid coupler'. The geometry using collimating and focusing lenses (Figure 6.4) is assumed for coupling from single mode fibre, but for single mode fibre the output beam is not well modelled by a cone. Instead the emerging beam is modelled as Gaussian (see Appendix C) with the beam waist located at the fibre end-face, and a spot size equal to the field radius.

6.3.1 '*ABCD* law' model

If the input fibre is on the same axis as the output fibre, the '*ABCD* law' model (references [209, 171] and Appendix C.2) can be used to track the Gaussian beam through the system. The fibre and lens spacings are shown in Figure 6.6, where f_1 and f_2 are equal to the focal lengths of the collimating and focusing lenses respectively, and g is the spacing between the lenses.

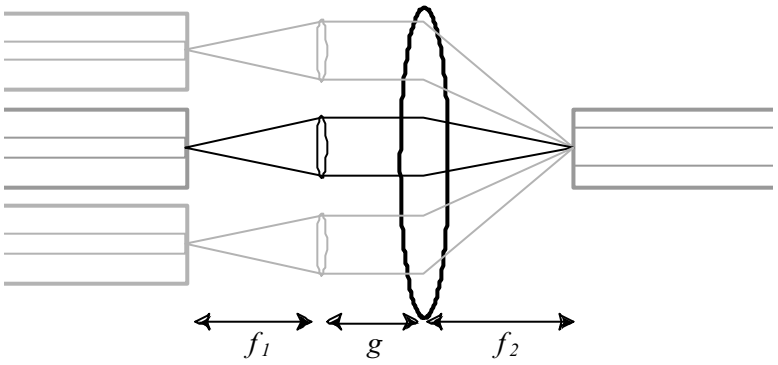

Figure 6.6: Configuration for the ABCD model

The two lenses and three gaps are represented by matrices as in Table 2.1 of Yariv [171], leading to a system matrix:

$$\begin{pmatrix} A_s & B_s \\ C_s & D_s \end{pmatrix} = \begin{pmatrix} \left(-\frac{f_2}{f_1}\right) & 0 \\ \left(-\frac{1}{f_2}\left(1-\frac{g}{f_1}\right)-\frac{1}{f_1}\right) & \left(-\frac{f_1}{f_2}\right) \end{pmatrix}$$

In the *ABCD* law model a Gaussian beam is described by the q parameter (Appendix C) which is given by:

$$\frac{1}{q} = \frac{1}{R} - i\frac{\lambda}{\pi\omega^2} \tag{6.9}$$

where R is the radius of curvature of the wavefront and ω is the spot size.

The input signal is here modelled by a Gaussian beam with waist in the plane of the input fibre endface and the spot size equal to the single mode spot size, ω_0, so that at the input $R = \infty$ (so $\frac{1}{R} = 0$) and $\omega = \omega_0$ giving the input q parameter:

$$q_i = i\frac{\pi\omega_0^2}{\lambda}$$

At the system output – the plane of the end of the output fibre – the output q parameter, q_o, is given by:

$$q_o = \frac{A_s q_i + B_s}{C_s q_i + D_s} = \frac{-\frac{f_2}{f_1} i\frac{\pi\omega_0^2}{\lambda}}{\left(-\frac{1}{f_2}\left(1-\frac{g}{f_1}\right)-\frac{1}{f_1}\right) i\frac{\pi\omega_0^2}{\lambda} - \frac{f_1}{f_2}}$$

Inverting and rearranging gives:

$$\frac{1}{q_o} = \frac{f_1 - g + f_2}{f_2^2} - i\frac{\lambda f_1^2}{\pi f_2^2 \omega_0^2} \tag{6.10}$$

Equating the real and imaginary components of 6.10 and 6.9 gives:

$$R(z) = \frac{f_2^2}{f_1 + f_2 - g} \tag{6.11}$$

$$\omega(z) = \omega_0 \frac{f_2}{f_1} \tag{6.12}$$

In other words the spot size is simply imaged on the output fibre endface, and its size is independent of the spacing between the lenses. The radius of curvature of the wavefront, however, does depend upon the spacing between the lenses. If $g < f_1 + f_2$ then R is positive indicating a diverging beam. If $g > f_1 + f_2$ then R is negative indicating a converging beam. If $g = f_1 + f_2$ then R is infinite, which represents a plane wave and corresponds to the waist of the Gaussian beam coinciding with the output fibre endface.

Intuitively, the optimum coupling is expected with $g = f_1 + f_2$ since all rays in the image will be normal to the fibre endface. The beam propagation with the ideal spacing of $g = f_1 + f_2$ is illustrated (with the curvature much exaggerated) in Figure 6.7.

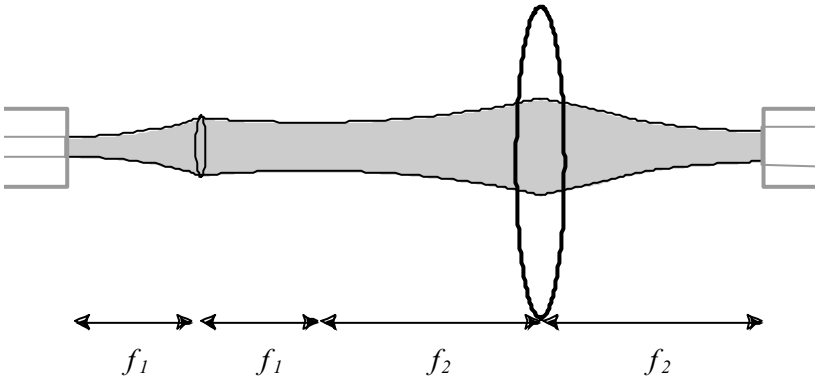

Figure 6.7: Gaussian beam propagation through the collimating and focusing lenses with $g = f_1 + f_2$.

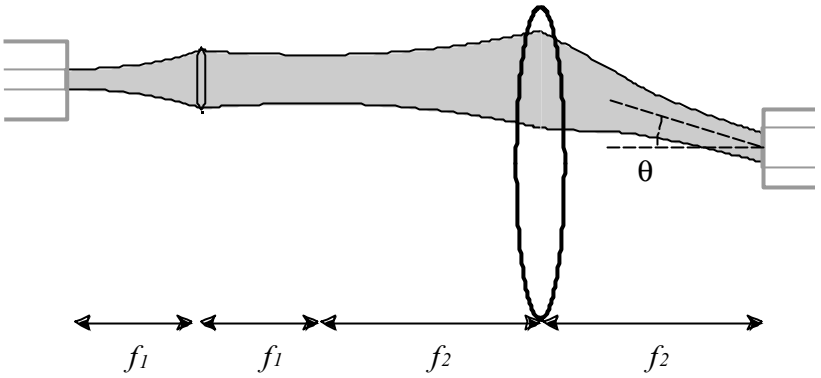

Figure 6.8: Focussing of the Gaussian beam when the input fibre is not on the same axis as the output fibre

6.3.2 Off-axis input fibres

If the input fibre is not on the same axis as the output fibre (Figure 6.8) then the beam is narrowed in the direction of the displacement from the axis, so that the beam will be oval in a plane perpendicular to the direction of propagation. The projection on the fibre end-face, however, will be circular, as for the on-axis beam. The difference in the case of the off-axis beam, however, is that the wavefront is at an angle to the plane of the fibre end-face. This illustrated by a projection drawing in Figure 6.9.

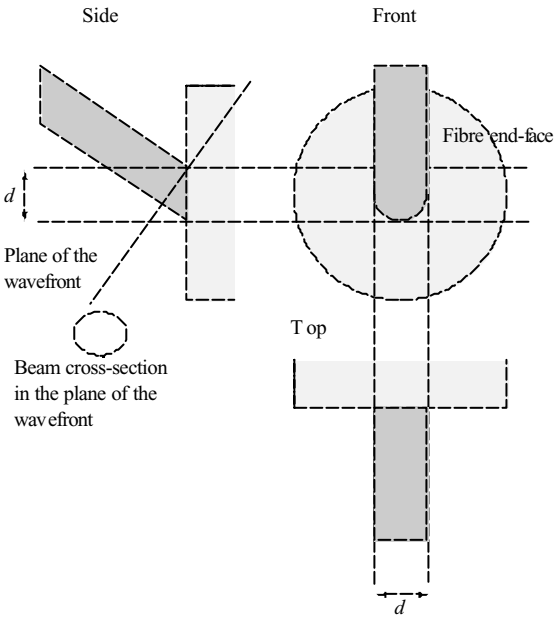

Figure 6.9: Off-axis beam at the fibre end-face.

If the beam waist is at the output fibre end-face, all light rays are incident at the same angle, because the beam is perfectly collimated at the waist. On a ray-

propagation model, then, the light power coupled to the output fibre will be independent of the offset of the input fibre from the axis, provided that the angle between the beam and the axis is less than the numerical aperture. In other words, when moving the input fibre off the axis the coupling efficiency will be constant until the angle ϕ_δ reaches the numerical aperture, at which value there will be a sharp cut-off.

One refinement which might be thought to explain angular dependence is the angular dependence of Fresnel reflection, but Appendix G shows that this an insignificant factor, affecting the efficiency by the order of 0.04%.

Kawano et. al. [4] argued that the angular dependence may be explained by the higher losses of higher-order modes, and proposed a weight function of the form

$$w(\theta_0) = \begin{cases} 1 - \left(\frac{\theta_0}{\theta_{0c}}\right)^\alpha & \text{for } \theta_0 \leq \theta_{0c} \\ 0 & \text{for } \theta_0 > \theta_{0c} \end{cases}$$

where θ_0 is the angle of incidence of the ray on the fibre end, θ_{0c} is the critical angle for the fibre input on the fibre axis and α is an attenuation parameter. In [4], α was chosen heuristically for a good match to experiment and was found, for the graded-index multimode fibre used, to be about 4. Clearly, for the configuration of interest here, the use of the weight function would introduce a 'soft cut-off' in the dependence of the coupling efficiency on offset of the input fibre from the output fibre axis.

If the offset from the output fibre axis is d, and the focal length of the focusing lens is f_2, then the weighting factor will be given by

$$w(d) = \begin{cases} 1 - \left(\frac{d}{f_2\theta_{0c}}\right)^\alpha & \text{for } \frac{d}{f_2} \leq \theta_{0c} \\ 0 & \text{for } \frac{d}{f_2} > \theta_{0c} \end{cases} \tag{6.13}$$

As will be seen in section 6.4, however, a cut-off that resembles the measured performance much more closely emerges from a model that takes account of the input and mode field distributions.

6.3.3 Number of input fibres

By an argument analogous to that of Section 6.2.1 the number of input fibres is explored by consideration of the packing of collimating lenses in the area of the focusing lens. Since, however, the input beam is modelled as Gaussian, there is not a hard limit to the size required of the focusing lenses: instead a choice has to be made as to the fraction of power that is to be collected in the lens. For example, if the lens radius is equal to the spot-size of the Gaussian beam in the plane of the lens, then 86% of power from the input fibre is gathered (Appendix C.3.1). If the lens is twice the spot-size, 98% is gathered.

For the purposes of this analysis the lens radius is set to equal the spot size. Using Eqn. C.3 the spot size at the lens will be (with $n_r \approx 1$ for air):

$$\omega_{lens} = f_1\lambda/\pi\omega_0$$

The maximum focusing lens size is given by Eqn. 6.2 again:

$$D/2 \leq f_2 \mathrm{NA_o}$$

And the packing-density argument gives a limit to the number of input fibres:

$$n = \frac{0.91 D^2}{d_i^2} = \frac{0.91 \left(2 f_2 \mathrm{NA_o}\right)^2}{\left(2 f_1 \lambda / \pi \omega_0\right)^2}$$

Using Eqn. 6.12 the spot size of the image is: $\omega_2 = \omega_0 f_2 / f_1$, so replacing f_2/f_1 by ω_2/ω_0 and rearranging gives:

$$n = \frac{0.91 \left(\omega_2 \mathrm{NA_o}\right)^2}{\left(\lambda/\pi\right)^2}$$

Setting the spot size of the image equal to the radius of the output fibre core and using $V = 2\pi \mathrm{NA} d/\lambda$ gives:

$$N = \frac{0.91 \left(d_o \mathrm{NA_o}/2\right)^2}{\left(\lambda/\pi\right)^2} = \frac{0.91 V^2}{16} \tag{6.14}$$

Which gives the useful result that the number of single mode input fibres that may be coupled to a single output fibre depends only upon the V-number of the output fibre. For example, typical 50/125μm fibre has $V \approx 50$, so that the number of input fibres that could be coupled into it is of the order of 142.

Further, for step-index fibres with large V, the number of bound modes (M_{bm}) is approximately $V^2/2$ (see Snyder and Love [5], Eqn. 36.41) so that:

$$N = \frac{0.91 M_{bm}}{8}$$

This predicts a linear relationship between number of input fibres and number of bound modes of the output fibre, but allowing fewer input fibres than would be limited simply by mode conservation – unlike the coupling from high V-number input fibres which was predicted to approach the mode conservation limit closely (Eqn. 6.5). It may be that the difference is that when the input fibres are single-mode, all the input fields are Gaussian and these do not couple efficiently to all of the higher-order modes of the output fibre, whereas when the input fibres are also multimode, there is a range of modes in the input field which can couple to the output fibre modes.

It may also be that different configurations of the collimating and focussing optics (such as making the image smaller than the core and focussing on different regions of the core) might be able to couple more modes. This requires further work.

6.4 Hybrid coupler, coupling efficiency

The geometric calculations of the previous sections take no account of interference between light from more than one input fibre. They model the coupling of light between individual input fibres and the output fibre in isolation, but are not necessarily valid for light simultaneously on more than one input. To model the coupling into the output fibre under more general conditions, the analysis of this section derives the field distribution at the end-face of the output fibre from the combined fields from the input fibre and uses an overlap integral to calculate the coupling from this field to each of the modes of the output fibre.

In general, the coupling efficiency between an input field E_i and the LP_{lm} mode of a fibre is given by the overlap integral which, in the simplified form of Neumann [198] (Eqn. 7.14), is given by:

$$\eta = \left| \frac{n_2}{Z_0} \int_{A_\infty} (\mathbf{E}_{i\mathrm{t}} \times \mathbf{E}^*_{lm\mathrm{t}})\, dA \right|^2 \tag{6.15}$$

$\mathbf{E}_{it}$ is the transverse component of the input field distribution (as a function of position) in the plane of the fibre end-face and $\mathbf{E}^*_{lmt}$ is transverse component of the LP_{lm} mode field distribution. The integral is taken over A_∞ which represents the infinite plane of the fibre end-face, and the asterisk represents complex conjugation. The total coupling efficiency is given by the sum of the coupling efficiency to each mode (this is valid because of the orthogonality of the fibre modes, see [198]).

The calculation of η using Equation 6.15 was done in *Mathematica* (the use of Mathematica in the work of this thesis is discussed in Appendix D) using formulae for the input field, E_i derived in Section 6.4.1 and the modes of the output fibre derived in Section 6.4.2. The details of the hybrid coupling calculation and the results are presented in Section 6.4.4 but before that Section 6.4.3 uses the model to look at the coupling from one single mode fibre to a multimode fibre as a function of axial offset. This initial, simpler, calculation serves to give confidence in the validity of the modelling as well as to provide insight into the nature of coupling between dissimilar fibres.

6.4.1 Input field

The focusing optics is assumed to locate the waist of the input Gaussian beams on the output fibre end-face (Figure 6.7 on page 101). For off-axis input beams (Figure 6.8 on page 102), the angle between the beam axis and the output fibre axis is modelled by a linear phase shift in a direction of the angle. The beam is modelled as perfectly collimated, with the convergence before and divergence after the waist being neglected (Figure 6.10). The angle subtended, θ, is assumed to be small so that the paraxial approximations apply: $\sin(\theta) \approx \theta$ and $\cos(\theta) \approx 1$.

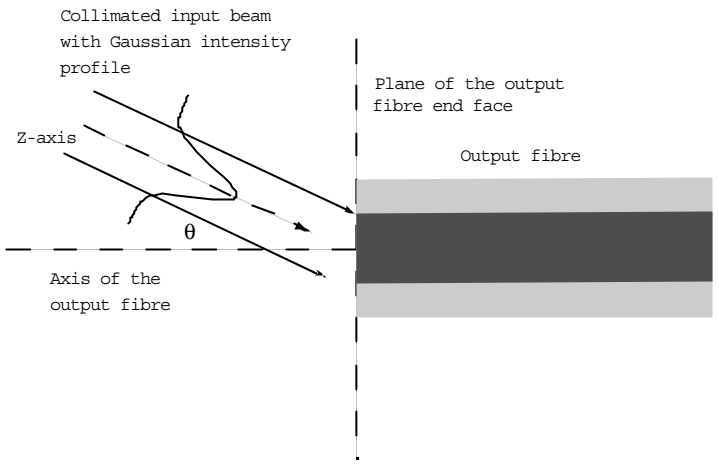

Figure 6.10: Geometry for the overlap integral calculations

In cylindrical coordinates (r, ϕ) of the end face, with $r = 0$ located at the centre of the output fibre and the input fibre offset in the direction ϕ_i, the input field from one single mode fibre is described by (see Appendix C, Eqn. C.1, with $z = 0$ for the waist):

$$E_i(r, \phi) = \frac{1}{\omega_0}\sqrt{\frac{2}{\pi}} e^{-\frac{r^2}{\omega_0^2}} e^{j\beta\theta r\cos(\phi-\phi_i)} e^{j\psi} \tag{6.16}$$

ω_0 is the Gaussian radius of the field at the fibre end-face, $\beta = 2\pi/\lambda$ is the free-space propagation constant (λ is the wavelength) and ψ represents a constant phase offset.

For multiple input fibres the input field becomes a summation of several copies of Eqn. 6.16 with different θ, ψ, and ϕ_i for each input. For example, with two inputs on opposite sides of the axis, in the directions $\phi_i = \pm\pi/2$:

$$E_i(r, \phi) = \frac{1}{\omega_0}\sqrt{\frac{2}{\pi}} e^{-\frac{r^2}{\omega_0^2}} \left(e^{j(\psi_1+\beta\theta r\sin(\phi))} + e^{j(\psi_2-\beta\theta r\sin(\phi))} \right) \tag{6.17}$$

For four inputs equally spaced around the axis, in the directions $\phi_i = 0, \pi/2, \pi, -\pi/2$:

$$E_i(r, \phi) = \frac{1}{\omega_0}\sqrt{\frac{2}{\pi}} e^{-\frac{r^2}{\omega_0^2}} \left(e^{j(\psi_1+\beta\theta r\sin(\phi))} + e^{j(\psi_2-\beta\theta r\sin(\phi))} + e^{j(\psi_3+\beta\theta r\cos(\phi))} + e^{j(\psi_4-\beta\theta r\cos(\phi))} \right) \tag{6.18}$$

Figure 6.11 shows the combined field for various values of the relative phase for four input fields, with the angle subtended to the axes, θ, equal to 0.10 radians. (This value of θ is that used in the later simulations, and the reason for the choice is explained in Section 6.4.4.) The errors from the paraxial assumption are of the order $0.12 - \sin(0.12) \approx 3 \times 10^{-4}$ and $1 - \cos(0.12) \approx 7 \times 10^{-3}$. The field amplitude and phase are shown separately (left- and right-hand columns respectively), with the scaling on the amplitude plots representing 0 to maximum by black to white, and the scaling on the phase plots representing $-\pi/2$ to $\pi/2$ by black to white.

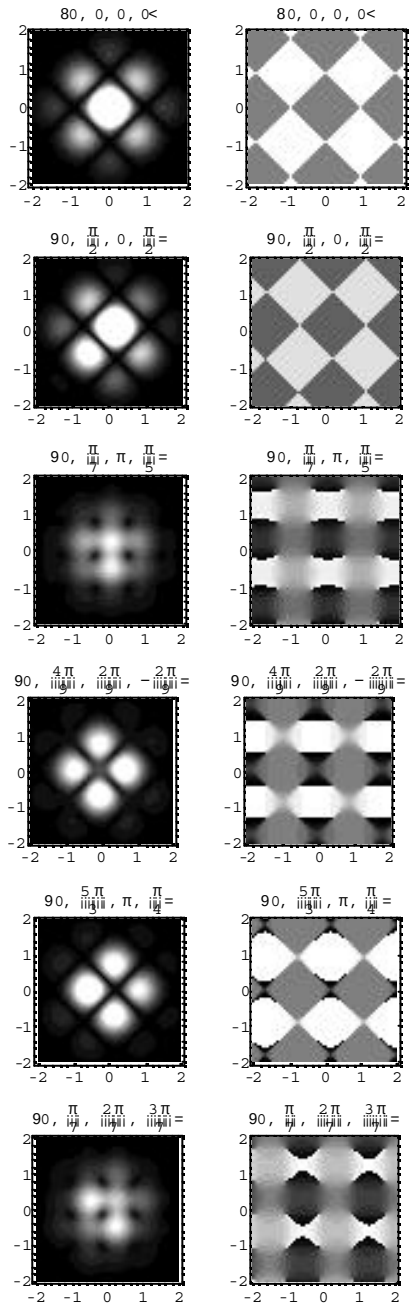

Figure 6.11: Amplitude (left-hand column) and phase (right-hand column) distribution of the combined input field in the plane of the output fibre end-face for four single mode input fibres. The labels show the relative phase of each input in the plane. (So {0,0,0,0} is for all with the same phase. $\{0, \pi/2, 0, \pi/2\}$ is for two inputs out of phase by 90° from the other two.) Axes labels are normalised to the input fields spot size (ω_0).

6.4.2 Modes of the output fibre

To derive some numerical results the output fibre model was chosen so that it had several guided modes, but few enough for the calculations to be manageable. It is assumed to be a step-index weakly-guiding circular fibre [210], and the modes modelled by linear polarisation, LP, modes [211]. Further, the 'Gaussian Approximation' which allows a single formula to represent the mode field distribution in both the core and the cladding (the Gaussian approximation is summarised in Appendix C.5) was used.

Further insight into the nature of the coupling was obtained by modelling two different multimode output fibres, referred to as 'mm4' and 'mm6':

mm4 Characterised by: core radius: 7.5 μm, numerical aperture: 0.12, V-number (normalised frequency) at 1300 nm: 4.36. The guided LP modes of this fibre are: LP_{01}, LP_{11} (two orientations), LP_{02} and LP_{21}(two orientations), making a total of six modes

mm6 Characterised by: core radius: 7.5 μm, numerical aperture: 0.16, V-number (normalised frequency) at 1300 nm: 5.84. The guided LP modes of this fibre are: LP_{01}, LP_{11} (two orientations), LP_{02}, LP_{21} (two orientations), LP_{31} (two orientations) and LP_{12} (two orientations), making a total of ten modes

For all modes there are two (linear) polarisation states, but the input is assumed linearly polarised and the overlap between orthogonal polarisation states is zero, so the analysis considers only a single polarisation state. The Gaussian approximations of the mode field distributions of the mm6 fibre are listed in Figure 6.12, and plotted in Figure 6.13. Note that on the weakly guiding approximation the fibre modes are modelled as plane waves, so that phase is constant across the fibre and field amplitude (with positive and negative values) provides a complete description of the mode. The scaling in Figure 6.13 runs from black to white for largest negative amplitude to the largest positive: 0 amplitude is grey.

6.4.3 Hybrid coupling with an axial offset.

Before investigating a full hybrid coupler, the coupling from one single-mode fibre to a multimode fibre was modelled with an axial offset between the input and output fibres (Figure 6.14). This developed confidence in the modelling methodology as well as providing insight into the nature of coupling between dissimilar fibres. The coupling to each of the modes of the output fibre was evaluated in *Mathematica* using Equation 6.16 for the input field and the fibre modes as described in Section 6.4.2, and the total coupling efficiency calculated from the sum of the coupling to all of the guided modes. For the input field the fixed phase ψ and orientation angle ϕ are arbitrary for this single input calculation, so were set to zero for simplicity. The fibre parameters and focusing were chosen so that the spot size of the focused input field, ω_0, matched

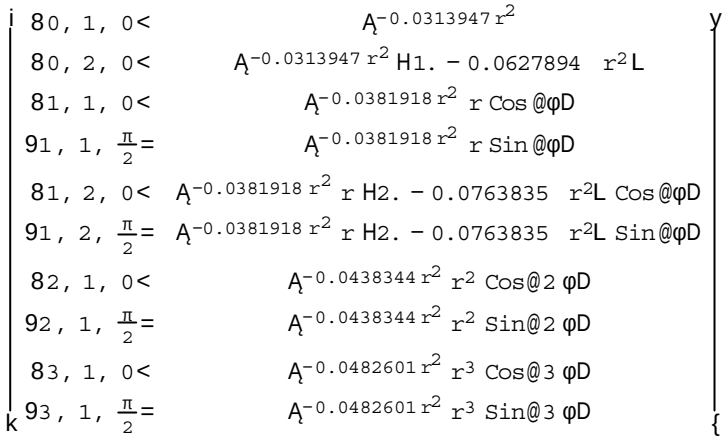

Figure 6.12: The formulae for the Gaussian approximation of the ten modes of the 'mm6' fibre, derived from a model implemented in *Mathematica*. The modes are identified by: $\{l, m, \text{orientation}\}$ for the LP_{lm} mode, where the 'orientation' is either 0 or $\pi/2$.

the field radius of the output fibre fundamental mode. The angle θ (see Figure 6.14) was kept as a variable. Further details of the *Mathematica* programming of this calculation are summarised in Appendix D.3, and the results are plotted as a function of θ in Figures 6.15 and 6.16..

The results are broadly in line with expectations. Because the spot size of the focused input field is the same as the field radius of the output fibre fundamental mode all the light is coupled to the fundamental mode at zero angle. As the angle is increased, the coupling efficiency to the fundamental mode decreases, but the light coupled to higher modes increases from zero such that at first the total coupling efficiency is almost constant. As the incident angle approaches the output fibre numerical aperture, however, the total coupling efficiency starts to drop. Coupling remains higher for larger angles with the higher-moded fibre (mm6) than the lower moded fibre (mm4).

For comparison, the heuristic weight function of Kawano (see Appendix 6.3.2 for a discussion of Kawano's weight function) is shown in Figure 6.17, with the parameters of Kawano's function chosen so that θ_c is the numerical aperture and the α is chosen to get a good fit at low angles ($\alpha = 5.4$ for the mm4 fibre, $\alpha = 6$ for the mm6 fibre). Clearly Kawano's function does not contain the point of inflexion that is found in the overlap integral calculations and is unable to model the 'tail' at angles above the numerical aperture.

6.4.4 Hybrid coupling efficiency from four input fibres

The overlap integral model was now used to calculate the coupling efficiency when light is input simultaneously from all four input fibres. The fields from the four fibres are assumed to be at the same optical frequency and to have the same amplitude,

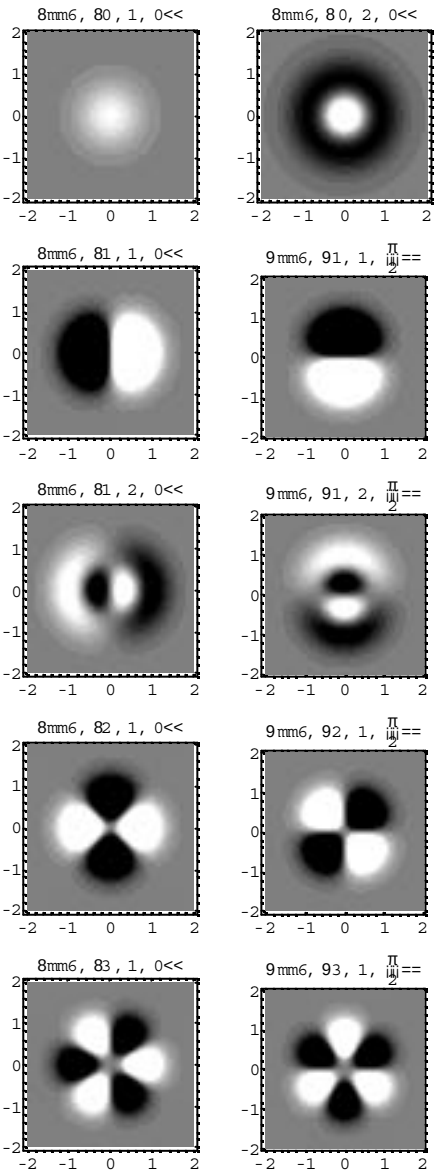

Figure 6.13: Amplitude plots of the ten modes of the 'mm6' fibre, derived from a model implemented in *Mathematica*. Plot labelling is {fibre type, {l, m, orientation}} for the LP_{lm} mode.

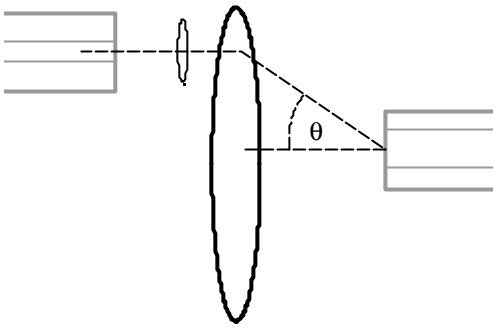

Figure 6.14: Single to multimode coupling with axial offset.

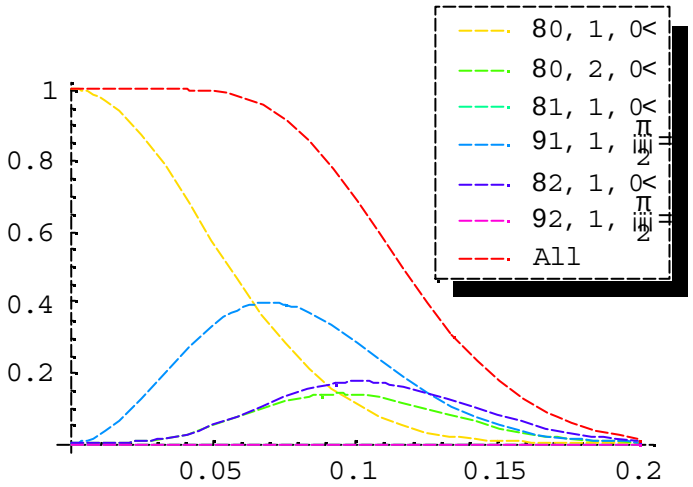

Figure 6.15: Coupling efficiency from one single-mode fibre to the six-moded 'mm4' multimode fibre (NA= 0.12), as a function of incident angle in radians. (The mode labelling is {l,m,orientation} as in Figure 6.13.)

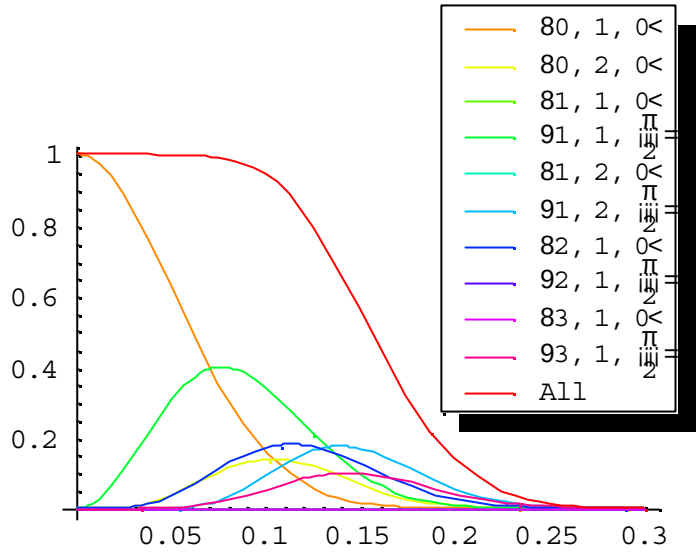

Figure 6.16: Coupling efficiency from one single-mode fibre to the ten-moded 'mm6' multimode fibre (NA= 0.16), as a function of incident angle in radians. (Mode labelling as in Figure 6.15.)

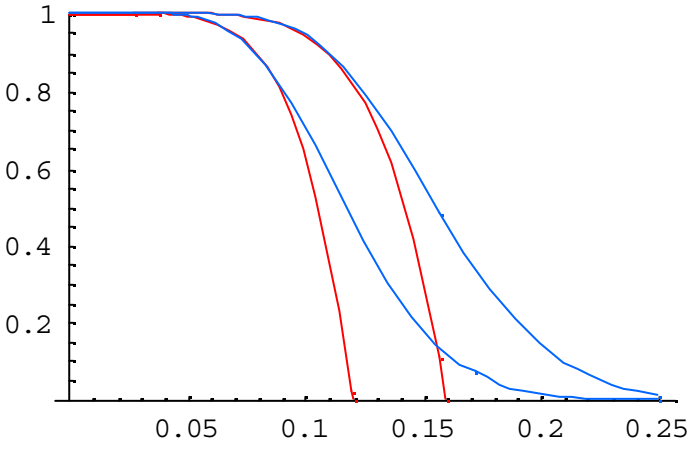

Figure 6.17: Comparison between Kawano's weight function and the overlap integral calculations of coupling efficiency as a function of incident angle. Red curves are Kawano's weight function and blue curves the overlap integral calculations. Left hand curves for the mm4 fibre and right hand curves for the mm6 fibre.

but the relative phases can take on any values corresponding to the light originating from a common source and being split four ways by a fused fibre coupler. The field on the output fibre end face is then given by Equation 6.18 as explained above. For this calculation the angle θ is fixed, determined by the assumed geometry, but the relative optical phases, ψ_1, ψ_2, ψ_3 and ψ_4, are kept as parameters.

To determine θ it was necessary to make assumptions about the geometry:

- The four collimating lenses are packed in a square, so the distance between opposite centres is given by $\sqrt{2}d_c$, where d_c is the collimating lens diameter.
- The angle subtended by the centres to the output fibre axis, θ, is therefore $d_c/f_1\sqrt{2}$.
- The waists of the incoming beams are located at the output fibre end-face.
- The spot size of the incoming beams at the fibre end-face ω_0 is equal to the radius of the output fibre fundamental mode, ω_f

With these assumptions, the convergence angle of the beam is $2\lambda/\pi\omega_f$ and $d_c = 2\lambda f_1/\pi\omega_f$, and the angle subtended by the centres of the collimating lenses is given by:

$$\theta = \frac{2\lambda f_1/\pi\omega_f}{f_1\sqrt{2}} = \frac{\sqrt{2}\lambda}{\pi\omega_f}$$

For the mm6 fibre ω_f was calculated to be 5.64 μm, giving $\theta = 1.3\sqrt{2}/(5.64\pi) = 0.10$. From Figure 6.16 the coupling efficiency from a single fibre at this angle is predicted to be about 93%.

Calculations were again done in *Mathematica* as outlined Appendix D, leading to formulae for the coupling to each of the output modes as a function of the four phases, ψ_1, ψ_2, ψ_3 and ψ_4 shown in Figure 6.19 and total coupling efficiency shown in Figure 6.20.

These results are presented graphically in Figures 6.21, 6.22 and 6.23, which show the coupling efficiency as a function of the phase of one of the inputs, for various combinations of the phase in the other three. As the relative phase relationship between the inputs is varied the distribution of power among the modes varies substantially, but the total coupled power varies much less. Looking for the minimum and maximum coupling efficiency using the *Mathematica* programme established that the total coupling efficiency varies between 84% and 98%.

6.4.5 Discussion

In an ideal hybrid correlator the coupling efficiency from the input fibres to the output fibre would be independent of the relative optical phase of the light in the single mode

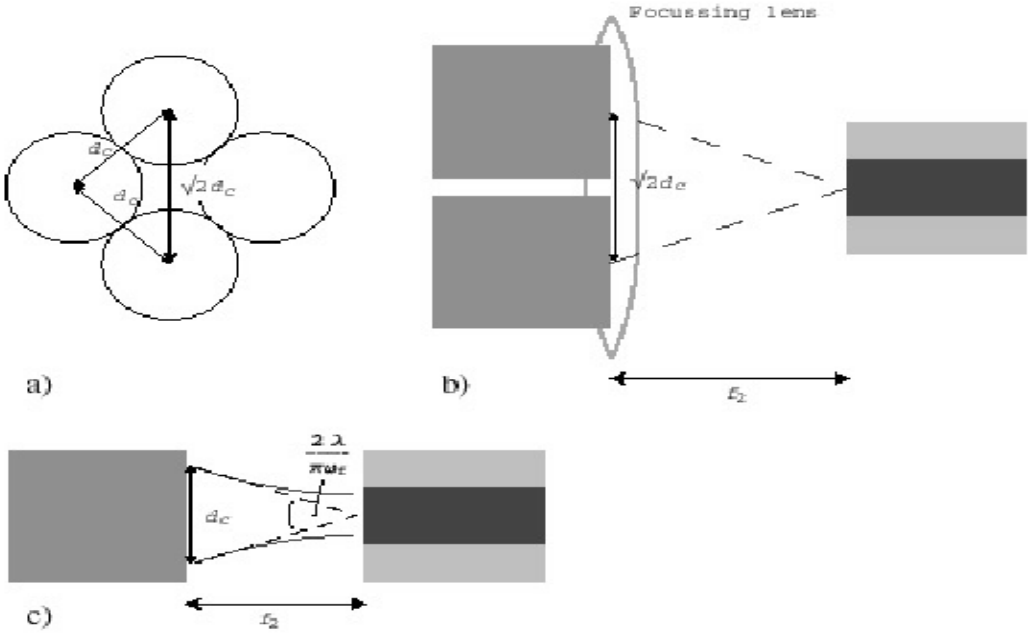

Figure 6.18: The geometry of coupling from four Gaussian beams to the mm6 fibre

Out[75]//MatrixForm=

$$\begin{pmatrix} \{0,1,0\} & 0.54+0.27\cos(\psi1-\psi2)+0.27\cos(\psi1-\psi3)+0.27\cos(\psi2-\psi3)+0.27\cos(\psi1-\psi4)+0.27\cos(\psi2-\psi4)+0.27\cos(\psi3-\psi4) \\ \{0,2,0\} & 0.54+0.27\cos(\psi1-\psi2)+0.27\cos(\psi1-\psi3)+0.27\cos(\psi2-\psi3)+0.27\cos(\psi1-\psi4)+0.27\cos(\psi2-\psi4)+0.27\cos(\psi3-\psi4) \\ \{1,1,0\} & 0.65-0.65\cos(\psi3-\psi4) \\ \{1,1,\frac{\pi}{2}\} & 0.65-0.65\cos(\psi1-\psi2) \\ \{1,2,0\} & 0.2-0.2\cos(\psi3-\psi4) \\ \{1,2,\frac{\pi}{2}\} & 0.2-0.2\cos(\psi1-\psi2) \\ \{2,1,0\} & 0.69+0.35\cos(\psi1-\psi2)-0.35\cos(\psi1-\psi3)-0.35\cos(\psi2-\psi3)-0.35\cos(\psi1-\psi4)-0.35\cos(\psi2-\psi4)+0.35\cos(\psi3-\psi4) \\ \{2,1,\frac{\pi}{2}\} & 0 \\ \{3,1,0\} & 0.057\cos(\psi3)^2-0.11\cos(\psi3)\cos(\psi4)+0.057\cos(\psi4)^2+0.057\sin(\psi3)^2-0.11\sin(\psi3)\sin(\psi4)+0.057\sin(\psi4)^2 \\ \{3,1,\frac{\pi}{2}\} & 0.057\cos(\psi1)^2-0.11\cos(\psi1)\cos(\psi2)+0.057\cos(\psi2)^2+0.057\sin(\psi1)^2-0.11\sin(\psi1)\sin(\psi2)+0.057\sin(\psi2)^2 \end{pmatrix}$$

Figure 6.19: The coupling efficiency for the hybrid coupler to each of the modes of the mm6 fibre.

Out[76]//NumberForm=

$$3.7-0.076\cos(\psi3)\cos(\psi4)+0.19\cos(\psi2)(\cos(\psi3)+\cos(\psi4))+\cos(\psi1)(-0.076\cos(\psi2)+0.19(\cos(\psi3)+\cos(\psi4)))-0.076\sin(\psi1)\sin(\psi2)+0.19\sin(\psi1)\sin(\psi3)+0.19\sin(\psi2)\sin(\psi3)+0.19\sin(\psi1)\sin(\psi4)+0.19\sin(\psi2)\sin(\psi4)-0.076\sin(\psi3)\sin(\psi4)$$

Figure 6.20: Total coupling efficiency of the hybrid coupler. (The sum of the coupling to all of the modes.)

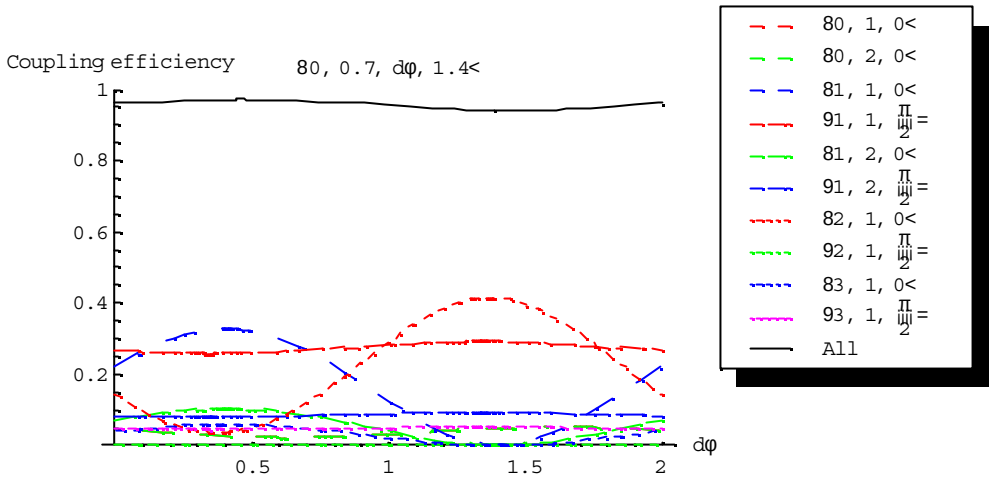

Figure 6.21: Coupling efficiency from four Gaussian beams (four single mode fibres) to the modes of the mm6 fibre. The plot title of {0, 0.7, dϕ, 1.4}describes the relative phase relationships between the four inputs. The first input is taken as the reference (0), the second has a phase offset of 0.7π, the third is the plot parameter and the last has a phase offset of 1.4π.

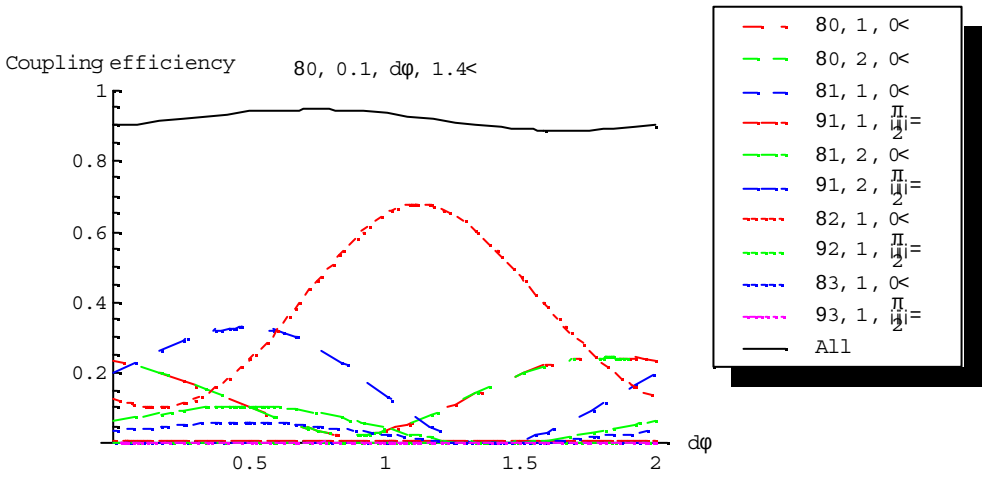

Figure 6.22: Coupling efficiency from four Gaussian beams to the mm6 multimode fibre. See caption of Figure 6.21 for explanation of the plot.

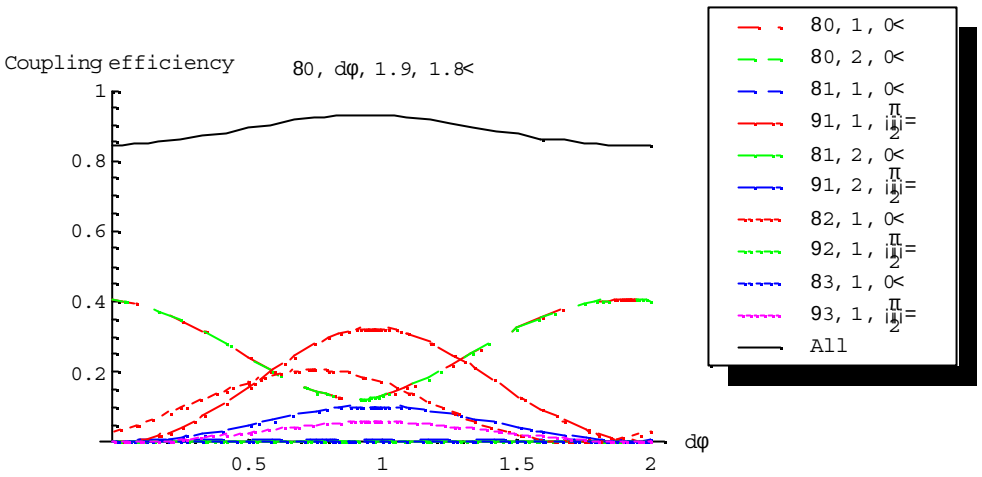

Figure 6.23: Coupling efficiency from four Gaussian beams to the mm6 multimode fibre. See caption of Figure 6.21 for explanation of the plot.

fibres. The overlap integral calculations for the four single-mode input fibres and few-moded output fibre have shown the coupling efficiency to be largely independent of the phase, but displays a residual dependence of around 15%.

It is expected that for a more highly moded output fibre the phase dependence would reduce further, but further work is needed to investigate this.

6.5 Conclusion: characteristics of the hybrid coupler

The merits claimed and desired of the hybrid coupler are low insertion loss and the absence of optical beating. This chapter has investigated those claims by proposing a hybrid coupler design and analysing it in detail, and the extent to which each of them has been established can now be assessed.

Consider first the insertion loss of the couplers. For the case of a coupler with highly-moded input and output fibres a ray-optics model has predicted low insertion loss provided 'mode conservation' applies. Mode conservation means in this context that the combined number of modes on the input fibres needs to be less than the number of modes on the output fibre.

A different approach to the modelling was needed to investigate a coupler with single-mode input fibres and a highly-moded output fibre, because a single mode fibre is not well represented by a ray-model. Using Gaussian beams for the input and ray-optics for the output, it has been predicted in this case that low insertion loss requires that the number of input fibres is fewer than $0.91V^2/16$, where V is the normalised frequency of the output fibre ('V-number').

For the specific example of coupling from four single mode fibres to a ten-moded output fibre, a detailed calculation based upon the overlap integral between the input

field and the fields of the output fibre modes has been done, and again predicted low overall coupling loss (coupling greater than 85%).

Optical beating is the conversion of time-dependent phase variations to intensity variations. The overlap integral calculations for the 4-to-1 coupler were done with phase as a parameter for each of the four inputs, and it was shown that the power distribution between the modes of the output fibre depended strongly upon the relative phases of the inputs, but that the total coupling efficiency was relatively independent of phase. This suggests that optical beating will result in time variations in the distribution of power between the modes, but, provided all the power in the output fibre is detected by the photodiode, there should be little or no noise due to beating on the photodiode output.

It is believed, but has not been demonstrated, that if the output fibre had more modes the residual (15%) phase-dependent coupling would be reduced still further.

The angular dependence of the total coupling efficiency predicted by the overlap-integral calculations is, in general terms, in line with the experimental measurements. In particular it is constant and close to one for small angles, falls rapidly as the angle approaches the numerical aperture of the output fibre and has a 'tail' at larger angles. The first two of these features can be described by the heuristic weight function of Kawano et. al. [4], but the last (the tail at large angles) cannot.

On the strength of the analysis in this chapter it is believed that the hybrid coupler does indeed allow the construction of a correlator that overcomes the limitations of the incoherent correlator (high inherent loss and optical beating) without the constraints of the coherent correlator.

Chapter 7

Construction of a hybrid coupler

The concept of the hybrid coupler has been described (Chapter 5) and its predicted merits of low insertion loss and absence of optical beating were supported by theoretical modelling in Chapter 6.

To prove the principle and demonstrate that the calculated performance can be achieved in practice, a four to one hybrid coupler was constructed and measurements taken on the coupler in isolation as well as part of a correlator and compared with previous models.

Measurements were first done on the angle-dependence of the input coupling from one single-mode fibre to the multimode output fibre (Section 7.1) for comparison with overlap integral calculations of Section 6.4.3 in Chapter 6. The efficiency of coupling from four input fibres was then measured (Section 7.2) to confirm the expected low inherent insertion loss. Simple geometry was used to show that a seven to one coupler could be constructed from the commercial devices used in his work, although many more inputs would be possible using custom-made collimators (Section 7.3).

To investigate optical beating the coupler was used in a two-path correlator and the noise power measured on the electrical output. For comparison, measurements were also taken on an incoherent correlator. These are reported in Section 7.4.

7.1 Single to multimode coupling demonstration: 1 input

Initial measurements looked at the angular dependence of the efficiency of coupling from a single single-mode fibre to a multimode fibre, using a collimating and focusing lens as in the configuration of Figure 6.4 (page 98).

Collimator The collimators were OzOptics GRIN lens fibre-pigtailed collimators, device code: LPC-05-1310-9/125-S-0.57-2.6GR-25-X-0.25-2.

This device has a focal length of 2.6 mm and outside diameter (including casing) of 2.4 mm. The diameter of the lens itself is 2.0 mm.

Using the formula for the divergence angle on the device data sheet, $DA(\text{ mrad}) = a(\,\mu\text{m})/f(\,\text{mm})$ with f (focal length), 2.6 mm, and a (core diameter of the fibre), 9.3 μm, gives 3. 6 mrad. The angle was measured to be less than 4.3 mrad.

Focusing lens The lens used for focusing was a commercial device from Thor Labs, part no. F220FC-C. It is sold for either collimating light from a fibre or coupling light into single or multimode fibres from source such as lasers or LEDs, and has an integral FC connector located so that when a fibre with an FC connector is attached, the fibre end-face is accurately located at the focal point of the lens. The lens has a focal length of 11 mm, a diameter of 6.5 mm and is treated with an anti-reflection coating to give a reflectivity of less than 1% between the wavelengths of 1050 nm and 1550 nm.

Assembly See Figure 7.1. Both the focusing lens and the collimator are held in mounts allowing angular adjustment about vertical and lateral (wrt the fibre axis) horizontal axes.

The focusing lens mount is on translating stages to allow calibrated movement in the horizontal lateral and axial directions, and the GRIN collimator is mounted on a calibrated vertical translating stage.

This combination allows calibrated x-y-z movements, and angular adjustments to align the input and output fibre axes.

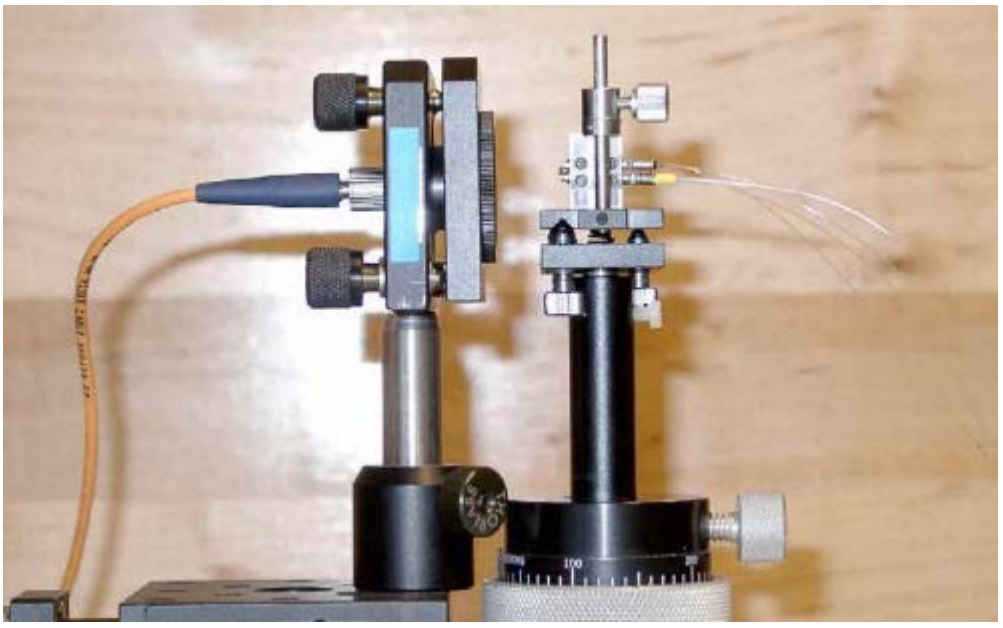

Figure 7.1: The assembly for experimental investigations of single to multimode coupling. The focusing lens and multimode fibre are on the left hand side, the collimators and single mode fibre on the right. The rig holding four collimators is discussed in Section 7.2 below. For the work reported in Section 7.1 only one of the collimators carried light.

7.1.1 Expected coupling efficiency

The image size (Gaussian beam spot size) on the output fibre endface is given by Equation 6.12 (page 101), $\omega = \omega_0 f_2 / f_1$. ω_0 is the single mode spot size (9.3 μm diameter), and f_1 and f_2 are the collimating and focusing lens focal lengths respectively: $f_1 = 2.6\,\text{mm}$ and $f_2 = 11\,\text{mm}$ leading to $\omega = 39\,\mu\text{m}$

The coupling efficiency is given by Eqn. C.5 (page 189):

$$\eta = \zeta \left(1 - \exp\left(-2\frac{r_o^2}{\omega^2}\right)\right)$$

ζ is the loss due to Fresnel reflections. Since both focusing and collimating lenses have anti-reflection coatings for 1300 nm, it is acceptable to neglect this loss (at the level of accuracy applicable here) and set $\zeta = 1$. r_o is the output fibre core diameter, which is $62.5/2\,\mu$m for the fibre used in the measurements, and from above, $\omega = 39\,\mu$m, leading to $\eta = 0.994$. The expected coupling efficiency is therefore 99.4%.

7.1.2 Expected off-axis coupling efficiency

On the simplest model (which was discussed in Section C.3.1) the coupling efficiency off-axis is the same as on-axis, up to the point at which the angle at the fibre endface exceeds the critical angle of the output fibre.

For typical $62.5/125\,\mu$m fibre the numerical aperture is 0.275 [206]. This corresponds to the input fibre being displaced from the axis by $0.279 \times 11\,\text{mm} = 3.1\,\text{mm}$.

Using the heuristic model of Kawano et. al. [4] leads to Eqn. 6.13 (page 103) with $f_2 = 11\,\text{mm}$ and $\theta_{0c} = 0.279$:

$$w(d) = \begin{cases} 1 - \left(\frac{d}{3.1}\right)^{\alpha} & \text{if } d \leq 3.1 \\ 0 & \text{if } d > 3.1 \end{cases} \tag{7.1}$$

For example, Figure 7.2, shows the weighting function with $\alpha = 4$.

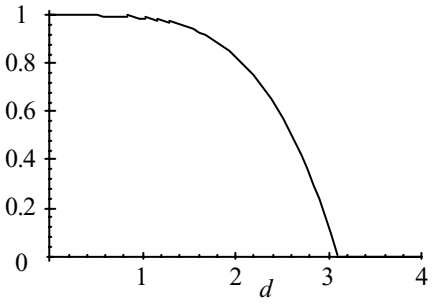

Figure 7.2: The Kawano weight function [4]

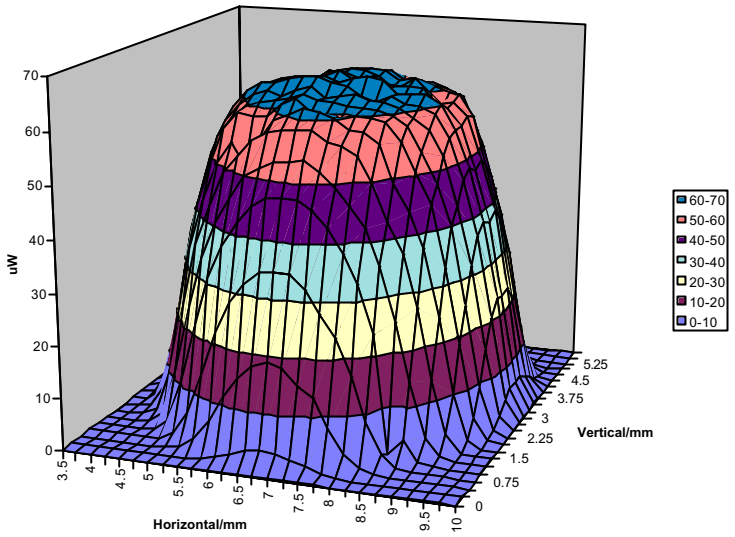

Figure 7.3: Output power as a function of lateral displacement

7.1.3 Measurements

Figure 7.3 shows the output power from a 62.5/125 μm graded-index multimode fibre attached to the focusing lens as a function of transverse displacement of the input collimator (input collimator serial no. 16984-01). The input power (power from the end of the input single mode fibre) that was connected to the collimator was 77 μW, and Figure 7.4 shows the contours of the total insertion loss as a function of lateral displacement. From this figure it can be seen that the diameter of the 3 dB contour is approximately 4.8mm.

Measurements on the three other collimators (serial nos. 17842-01R, 17842-02R and 17842-03R) were done in a single plane only (horizontal translation, vertical position adjusted for maximum coupling efficiency) and the results are shown (together with those using the previous collimator) in Figure 7.5. Note that no significance should be read into the relative horizontal position of the curves, since separate alignment adjustments were necessary for each of the collimators.

7.1.4 Comparison with Kawano's weight function

The measurements of Section 7.1.3 are compared with the model of Section 7.1.2 in Figure 7.6. The model (continuous curve) is based upon the equation of Kawano (Eqn. 6.13), with parameters determined by non-linear regression for a best fit with the data, using a Mathematica programme (file MM62fitting2.nb). They were determined to be: $\alpha = 4.68$, $f_2\theta_{0c} = 2.97\,\mu$m and a zero offset power of $P_0 = 63\,\mu$W. Note that this gives a slightly different value for $f_2\theta_{0c}$ than expected (2.97 μm rather than 3.1 μm),

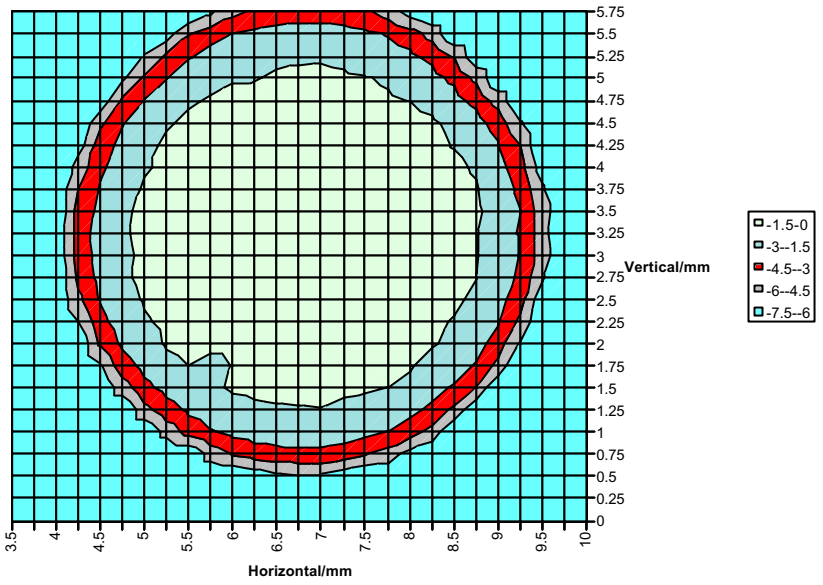

Figure 7.4: Total insertion loss (in dB) as a function of lateral displacement

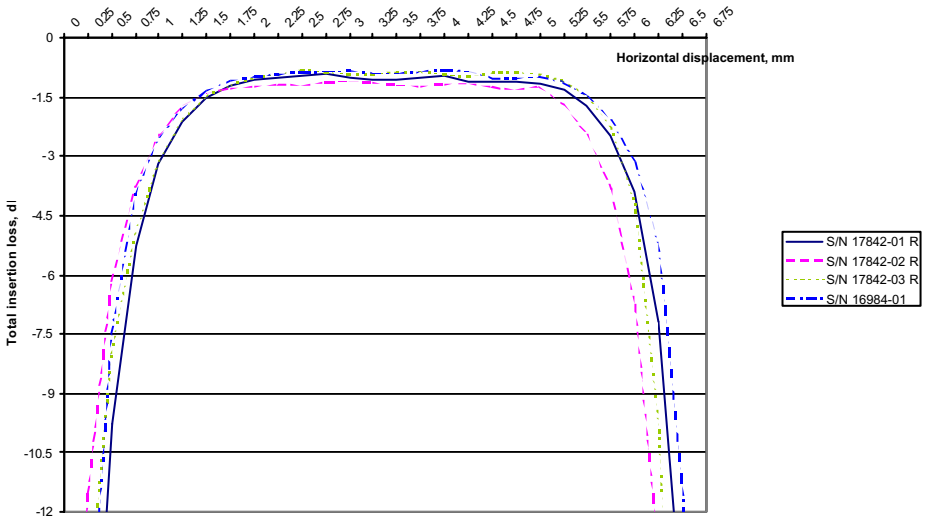

Figure 7.5: Total insertion loss for each of four single mode collimators

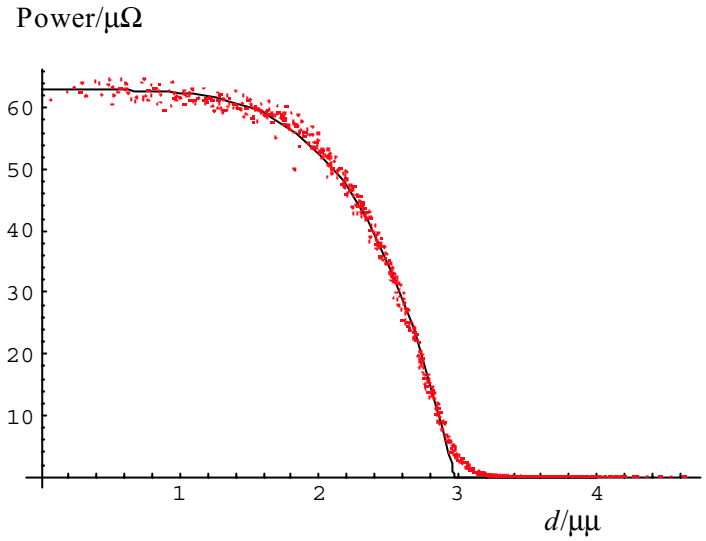

Figure 7.6: Best fit by nonlinear regression.

but since the precise value of neither f_2 nor θ_{0c} is known slight variations from the nominal values are to be expected.

The data points in Figure 7.6 are the measurements of Figure 7.3 transformed to a function of radial distance from an assumed origin – the location of which was itself determined by a best fit on the Mathematica regression analysis.

The measurements have a 'tail' at high angles similar to that which was observed in the overlap integral calculations but not modelled by Kawano's formula.

7.2 Single to multimode coupling demonstration: 4 inputs

In order to align four collimators with their centres close enough to ensure a low insertion loss, a miniature rig was constructed from perspex as shown in Figures 7.7 and 7.8. Sixteen adjustment screws, four for each collimator, allow the collimators to be aligned.

The configuration for the measurements is shown schematically in Figure 7.9 and photographed in Figure 7.10. The beams from the collimators were initially made parallel by observation of the spots on an infrared viewing card approximately 1 m from the rig, then the combined beams were directed to a focussing lens attached to a 62.5/125 μm output fibre. To get a value for the input power to the hybrid coupler the power from each of the four outputs from the 1-4 splitter was measured at the optical power meter. The output power was then measured as a function of lateral displacement (angular alignment having been adjusted for minimum insertion loss), and the results are displayed in Figure 7.11.

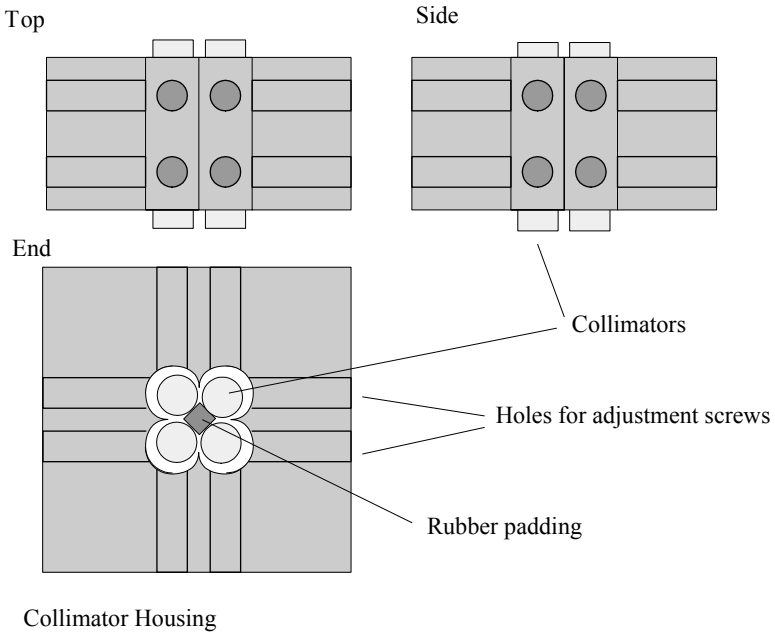

Figure 7.7: Housing for four collimators

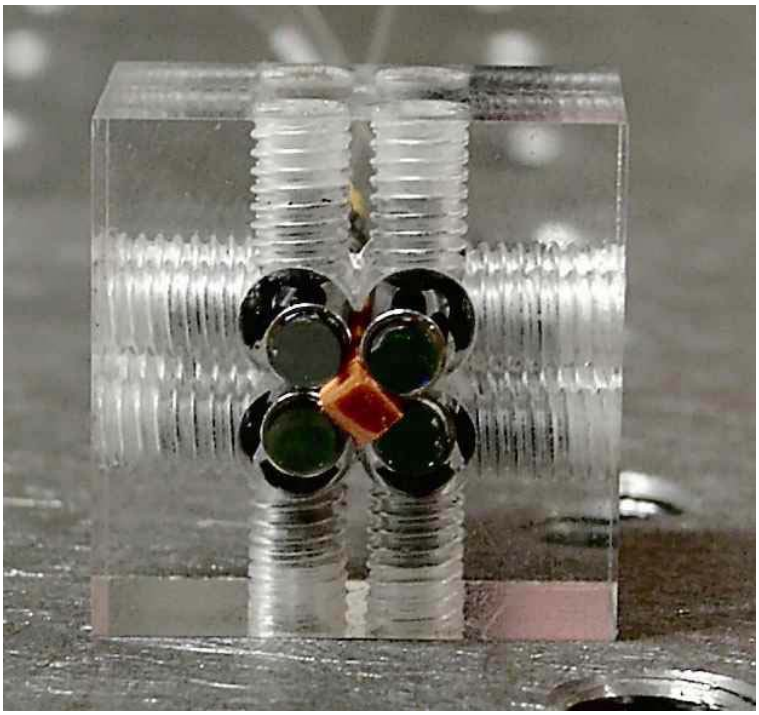

Figure 7.8: Photograph of the housing for four collimators.

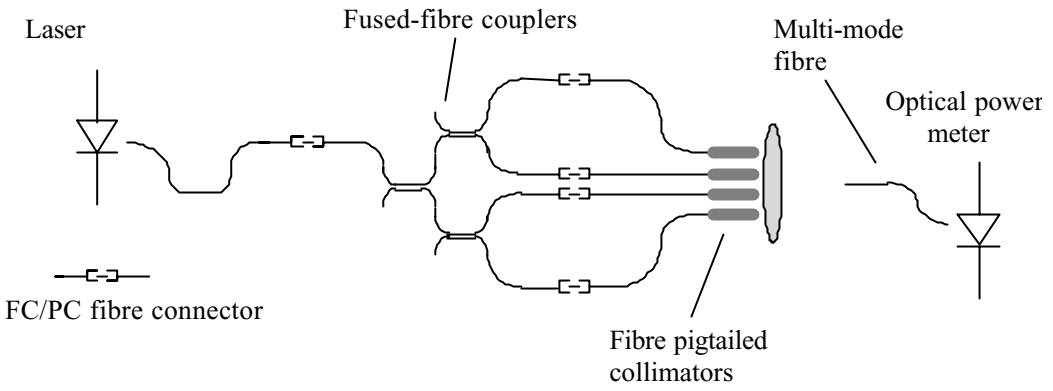

Figure 7.9: Schematic of the experimental configuration for measurements on the 4-1 hybrid coupler.

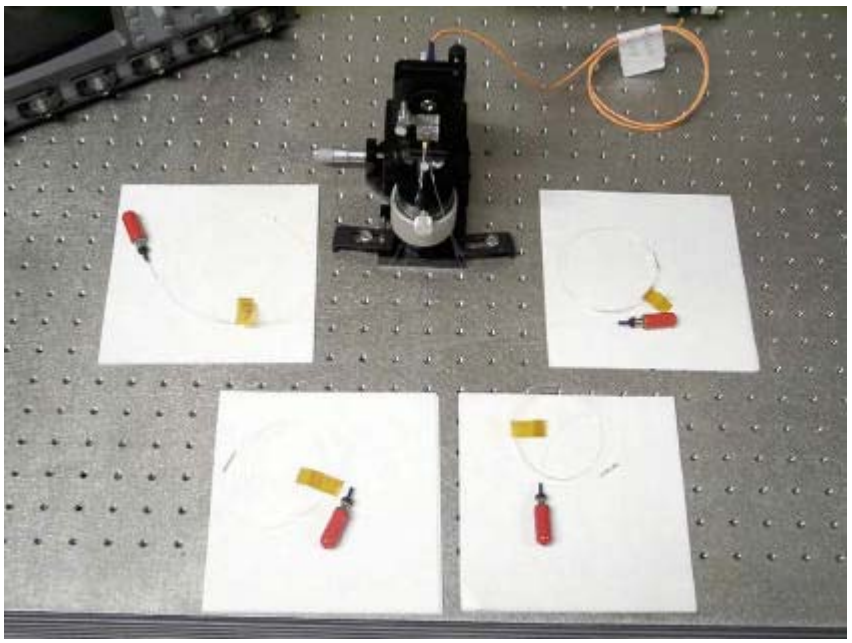

Figure 7.10: Photograph of the four-to-one hybrid coupler. (See also Figure 7.1 on page 119.)

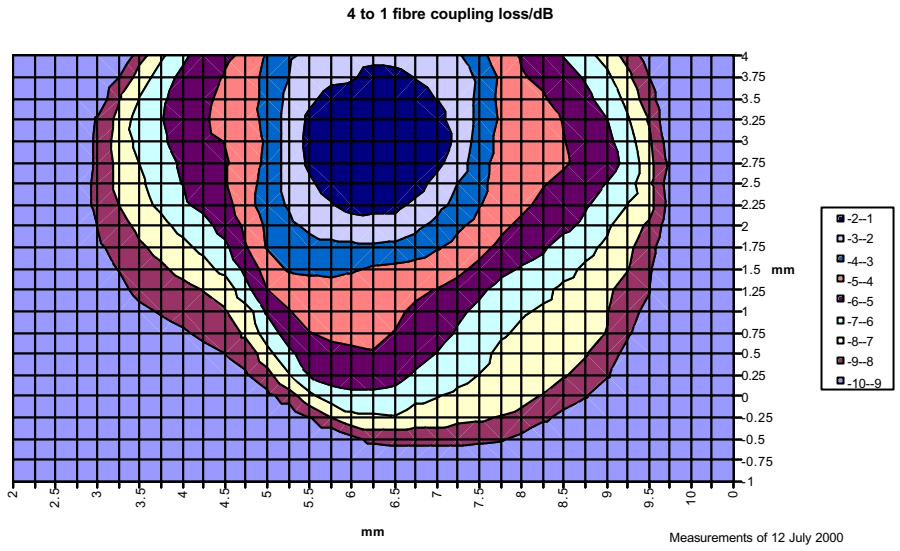

Figure 7.11: The coupling loss from four input fibres to one multi-mode output fibre, as a function of lateral displacement

The minimum total insertion loss through the 4 to 1 combiner (ratio between the measured output power and the sum of four input powers) was determined to be 1.25 dB. Note that this includes the loss coupling into connectors of the pigtailed collimator and the loss from the pigtails to the collimators themselves.

7.3 Maximum number of inputs

From the measurements in Section 7.1.3 the diameter of the circle of displacement within which the input fibre has less than 3 dB loss is 4.8 mm. The outside diameter of the collimators (including steel sheath) is 2.4 mm. It is entirely coincidental that this is a ratio of precisely 2:1, but it means that the maximum number of these input correlators that in principle could couple to the output with a loss of no more than 3 dB from any one is seven, with the simple packing geometry shown in Figure 7.12.

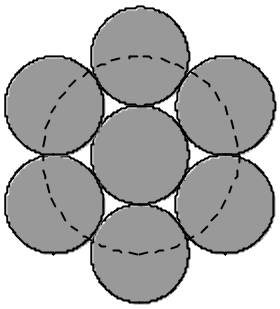

Figure 7.12: The maximum number of correlators that can couple into the output fibre with no more than 3 dB loss. The circle of displacement for a 3 dB loss is shown dashed, and has twice the diameter of the collimators (filled circles).

This is a much smaller number than the theoretical values calculated in Chapter 6 because the outside diameter of the collimator is substantially greater than the collimated beam width. (Using Eqn. C.3 the Gaussian beam diameter at the collimator output should be $2f\lambda/\pi\omega_0 = 2 \times 2.6 \times 1.3/(9.3\pi) = 0.23\,\text{mm}$.) If a device were to be manufactured specifically as a hybrid coupler it is reasonable to assume that better packing could be achieved - the collimators would not, for example, need the metal sheaths. In fact, though, even as few as seven inputs is potentially of practical value. The systems calculations in Chapter 8 assume a weight-6 code and show that it allows very large networks with hundreds of simultaneous users.

7.4 Measurements of correlator noise

Measurements were made on the noise at the output of:

- an attenuator
- a two-path hybrid correlator
- a two-path incoherent correlator, with polarisation adjusted to minimise noise (orthogonal polarisation states in the combiner)
- a two-path incoherent correlator, with polarisation adjusted to maximise noise (aligned polarisation states in the combiner)

The experimental configuration is shown in Figure 7.13. The optical source was a multimode laser diode, and noise was measured using a LeCroy digital oscilloscope, sampling at 50 MSamples/s for 1000 samples ($20\,\mu$s). A low pass filter on the oscilloscope input with cut-off of 20 MHz prevented aliasing. A built-in facility of the oscilloscope calculated the standard deviation of the 1000 samples, which represents the rms noise voltage in the frequency band from 50 kHz ($1/20\,\mu$s) to 20 MHz (input filter of the oscilloscope). The oscilloscope was also capable of averaging parameters

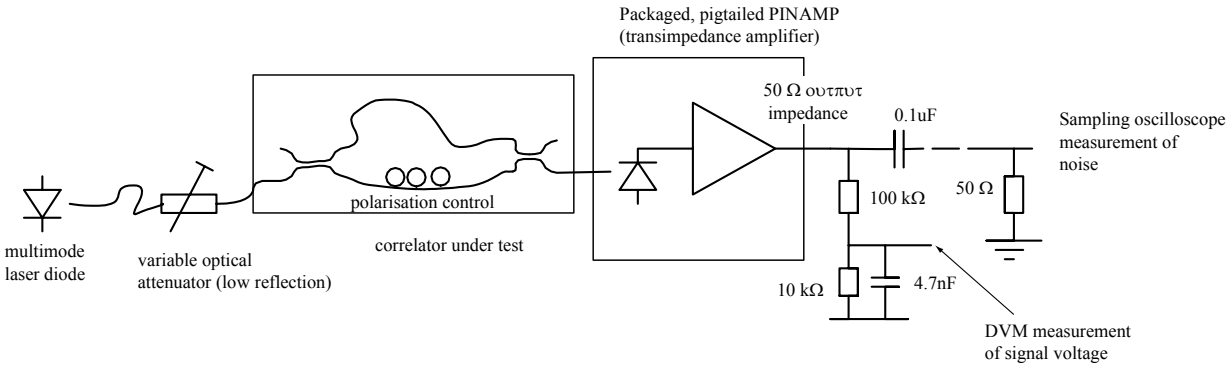

Figure 7.13: Experimental configuration for noise measurements

from multiple sweeps, and in the measurements that follow each point was taken as the average of approximately 200 sweeps. (See Appendix E.2 for further details.)

The PINAMP output was calibrated for dc signals, measured with a DVM before the ac coupling, and ac signals into the oscilloscope (see Section E.1), from which it was determined that the DVM measurements represented 9 mV/μW and the oscilloscope measurements represented 4 mV/μW, in line with the data supplied with the device.

7.4.1 Model

Even with the pure attenuator, reflections at connectors result in the signal at the receiver containing 'multi-path' interference. It is shown in Appendix F that under these conditions the measured noise power (voltage-squared) is expected to be a quadratic function of the mean received signal (voltage):

$$\left\langle v_{noise}^2 \right\rangle = v_{fixed}^2 + c_{lin} v_{dc} + c_{quad} \alpha_1 \alpha_2 v_{dc}^2$$

The fixed term is thermal noise and other noise originating in the receiver, the linear term is shot noise and the quadratic noise is beating. The constant of the quadratic term is written as $c_{quad}\alpha_1\alpha_2$ on the assumption that the beating involves two components of relative (optical) power α_1 and α_2 (where $\alpha_1 + \alpha_2 = 1$), but in general the quadratic form applies even if there are more than 2 components to the beating (see Section F.2).

Estimates of the values of the constants for the equipment used in the measurements are derived in Appendix F.1.1, leading to the conclusions:

- v_{fixed}^2 has a lower bound given by thermal noise, which is estimated to be $1.6 \times 10^{-9}\,\mathrm{V}^2$
- c_{lin} results from the shot noise and is estimated to be $1.5 \times 10^{-7}\,\mathrm{V}$
- c_{quad} needs further knowledge of the spectrum of the laser, but has an upper bound (based on a single mode laser with spectral linewidth much less than the low-pass electrical filtering in the receiver, so that all beating noise is 'in-band') of 12.

7.4.2 Attenuator

As a reference, initial measurements were made with no correlator, measuring the noise as a function of attenuation alone (Figure 7.14). The measurements were found to change when connectors were separated and reconnected, and Figure 7.14 shows two sets of measurements.

The receiver was known to saturate at about $30\,\mu$W, which corresponds to a dc voltage of about 0.13 volts. This can be seen in the limiting and then falling of the noise power.

The dashed curves are calculated from a least-squares best fit on the lower-power data points, choosing those points below a dc voltage of 0.12 V, judged by eye to be the level above which the saturation of the receiver could be taking effect.

The parameters of the least-squares fit gives values for the constants of the quadratic (Eqn. F.1) shown in Table 7.1. The values for v_{fixed}^2 are the right order of magnitude for thermal noise, and c_{lin} is within a factor of 2 of the expected value. As explained above, there are several additional possible sources of noise contributing to v_{fixed}^2 so that the measured values are not unreasonable. The significance of the error on c_{lin} is investigated by the short-dashing curves in Figure 7.14, which show the fit that is obtained if c_{lin} is fixed to the theoretical value of 1.5×10^{-7} and a least-squares fit done with v_{fixed}^2 and $c_{quad}\alpha_1\alpha_2$ as the only parameters. The fact that a good fit is still possible suggests that small errors in the data values could easily explain the discrepancy between the best fit c_{lin} and the theoretical value.

With the value (0.39) for c_{quad} that is derived in Section 7.4.4 below, the least-squares fit of $c_{quad}\alpha_1\alpha_2$ can be used to get an estimate of the reflections that must be present in the system.

For the upper curve: $\alpha_1\alpha_2 = \frac{3.17\times10^{-5}}{0.39} = 8.1 \times 10^{-5}$. Since this is small, and remembering that $\alpha_1 + \alpha_2 = 1$, to a good approximation it is reasonable to use $\alpha_1 = 1$, $\alpha_2 = 8.1 \times 10^{-5}$. Taking this to be due to two reflections at connectors, and approximating the loss at each connector to be the same, the approximate reflection

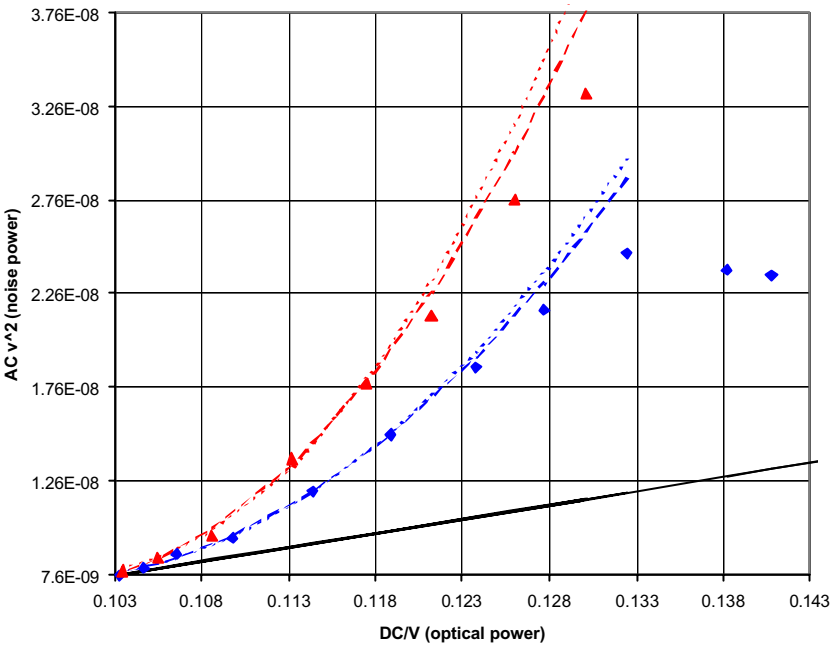

Figure 7.14: Noise power (voltage-squared) as a function of received optical power (measured by detector voltage) for an attenuator. Two sets of measurements are shown by the blue square and red triangular points respectively. The continuous black line is the theortical shot-noise bound, and the dashed lines are quadratics fitted by least-squares error to the points at low optical power levels (below 0.12 V). Long dashes for unconstrained fits, short dashing with the linear term fixed by the shot noise.

Parameter	Fit, upper curve	Fit, lower curve	Predicted value
v^2_{fixed}	$7.74 \times 10^{-9}\,\mathrm{V}$	$7.68 \times 10^{-9}\,\mathrm{V}$	$\geq 1.6 \times 10^{-9}\,\mathrm{V}^2$
c_{lin}	$2.64 \times 10^{-7}\,\mathrm{V}$	$1.93 \times 10^{-7}\,\mathrm{V}$	$1.5 \times 10^{-7}\,\mathrm{V}$
$c_{quad}\alpha_1\alpha_2$	3.17×10^{-5}	1.8×10^{-5}	$0.39\alpha_1\alpha_2$

Table 7.1: Parameters of the quadratic fit to attenuator noise measurements

Parameter	Fitted value	Predicted value
v^2_{fixed}	$8.23 \times 10^{-9}\,\mathrm{V}$	$\geq 1.6 \times 10^{-9}\,\mathrm{V}^2$
c_{lin}	$8.37 \times 10^{-8}\,\mathrm{V}$	$1.5 \times 10^{-7}\,\mathrm{V}$
$c_{quad}\alpha_1\alpha_2$	3.59×10^{-5}	$0.39\alpha_1\alpha_2$

Table 7.2: Parameters of the quadratic fit to the incoherent filter noise measurements, polarisation adjusted for minimum noise

at each connector is $\sqrt{8.1 \times 10^{-5}} = .009$. To consider whether this is reasonable, note that if there were no physical contact on the connectors, there would be two Fresnel reflections due to the difference between the refractive index of glass and air, each of which contributes about 4% (14.9 dB return loss) reflected power. A reflection of 0.9% (20.5 dB return loss) at each connector, for the physical-contact connectors, is therefore not unreasonable.

For the lower curve: $\alpha_1\alpha_2 = \frac{1.8\times10^{-5}}{0.39} = 4.6\times10^{-5}$ corresponding to a double reflection with $\sqrt{4.6 \times 10^{-5}} = 0.0068$, about 0.7% (21.7 dB return loss) at each connector.

7.4.3 Two-path incoherent correlator, with polarisation adjusted to minimise noise

With the polarisation in one of the paths adjusted so that the polarisation states of the light from the two paths are orthogonal on coupling to the multimode fibre, there should be no beating and the noise should be the same as for a pure attenuator. Figure 7.15 shows measurements taken with the polarisation adjusted to minimise the measured output noise, together with the theoretical bound due to shot noise taken from Figure 7.14.

As for the attenuator, a least-squares best fit was used to get the parameters of the quadratic which is shown in Figure 7.15, and the parameters given in 7.2. The very low value of $\alpha_1\alpha_2$ ($3.59 \times 10^{-5}/0.39 = 9.2 \times 10^{-5}$), comparable with the pure attenuator, supports the belief that there is no beating between the light coming from the two paths. Following the argument above, the values suggest reflections at couplers of the order of $\sqrt{9.2 \times 10^{-5}} = 9.\,6 \times 10^{-3}$, about 1% (20 dB return loss).

The minimisation of beating through the use of orthogonal polarisation has been proposed as an approach to overcoming the coherence limitations of delay line filters by Zhang et. al. [194], but it would require active polarisation control and, especially in correlators with more than two paths, the practicalities are likely to prevent this being a viable option for an optical CDMA network.

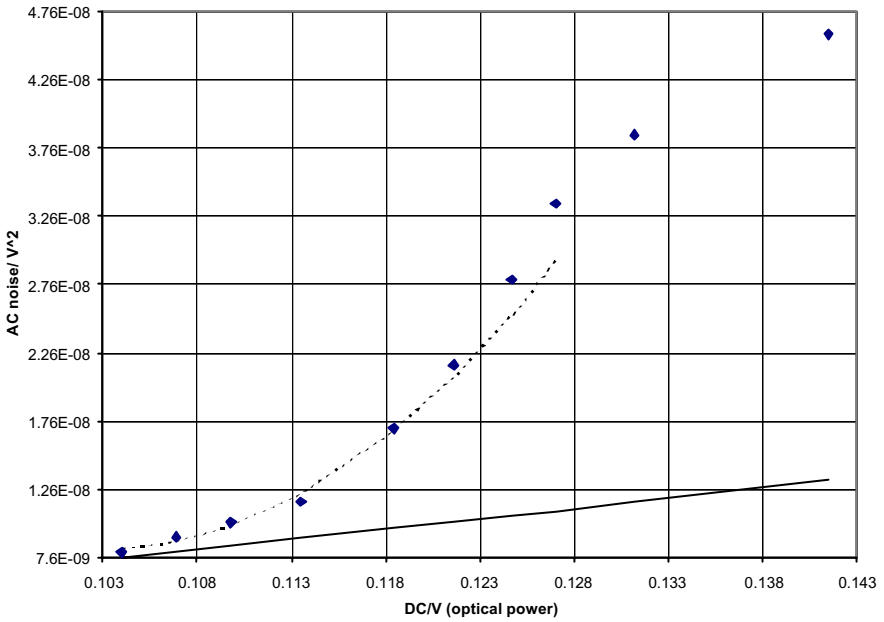

Figure 7.15: Noise power (voltage-squared) as a function of received optical power (measured by detector voltage) for the incoherent correlator, adjusted for minimum noise. The continuous line is the theoretical shot noise bound and the dashed line is the quadratic best fit to points at low optical power (PINAMP output voltage < 0.12 V).

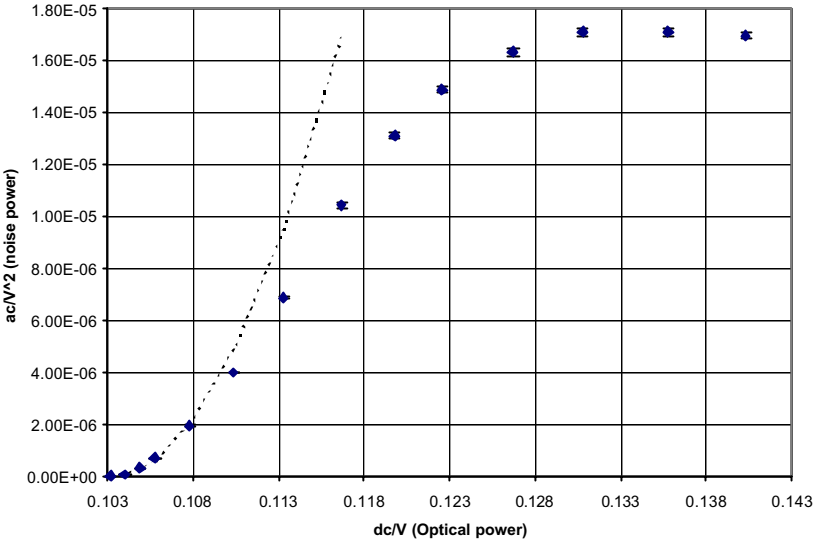

Figure 7.16: Noise power as a function of received optical power for the incoherent correlator, with polarisation adjusted for maximum interference. The dashed line is the quadratic best fit for low optical power (DC voltage < 0.11 V).

7.4.4 Two-path incoherent correlator, with polarisation adjusted to maximise noise

Figure 7.16 shows measurements taken with the polarisation adjusted to maximise the measured output noise. Note the vertical scale in this Figure is $2 \times 10^{-6}\,\mathrm{V}^2$/division compared to $5 \times 10^{-9}\,\mathrm{V}^2$/division in Figures 7.15 and 7.14. This is more than 2 orders of magnitude greater, and the theoretical 'shot noise bound' would not be visible off the axis on of Figure 7.16.

Fitting a quadratic to the data points gives the dashed curve in Figure 7.16, and comparing the parameters of the fitted curve with Eqn. F.1 gives a value for $c_{quad}\alpha_1\alpha_2 = 0.093$. From measurements, $\alpha_1 = 0.42$ and $\alpha_1 = 0.58$ so $\alpha_1\alpha_2 = 0.24$. This gives:

$$c_{quad} = 0.093/0.24 = 0.39 \tag{7.2}$$

This value is more than an order of magnitude below the upper bound of 12 derived earlier, but there was no reason to suppose that the bound was tight, so this result is not unreasonable. In particular, the upper bound was based upon the assumption that the electrical low-frequency cut-off was much greater than the spectral width of the laser modes. Since the low-frequency cut-off was only 20 MHz and the spectral width could be an order of magnitude or more *larger*, this assumption alone could account for the difference. (It was assumed that $\tan^{-1}(B_e/\nu_1) = \pi/2$. If, instead, $B_e/\nu_1 \approx 1/10$, then $\tan^{-1}(1/10) \approx 0.1$.)

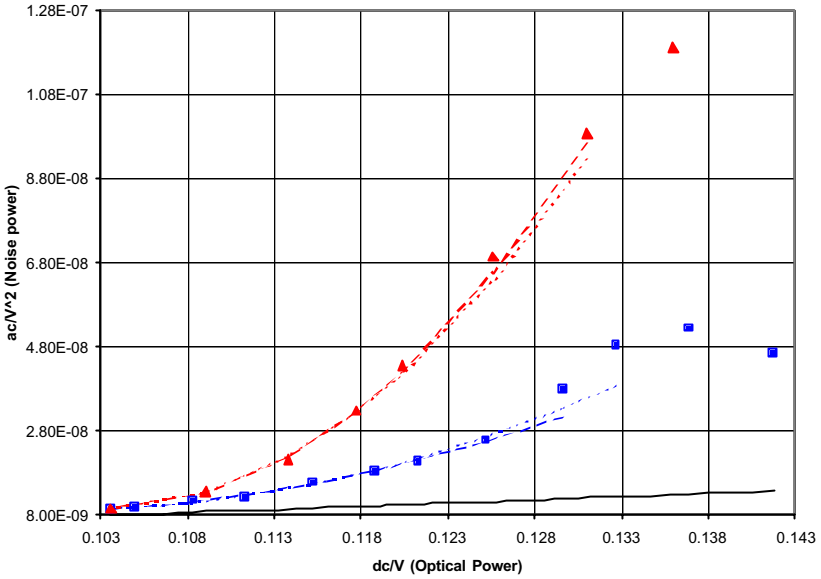

Figure 7.17: Noise measurements in a hybrid correlator, with the relative polarisation adjusted for maximum (red triangles) and minimum (blue squares) noise. See text for explanation of the fitted curves.

Parameter	Fit, upper curve	Fit, lower curve	Predicted value
v^2_{fixed}	$9.46 \times 10^{-9}\,\mathrm{V}^2$	$9.02 \times 10^{-9}\,\mathrm{V}^2$	$\geq 1.6 \times 10^{-9}\,\mathrm{V}^2$
c_{lin}	$-1.08 \times 10^{-8}\,\mathrm{V}$	$2.61 \times 10^{-7}\,\mathrm{V}$	$1.5 \times 10^{-7}\,\mathrm{V}$
$c_{quad}\alpha_1\alpha_2$	11.6×10^{-5}	2.26×10^{-5}	$0.39\alpha_1\alpha_2$

Table 7.3: Parameters of the quadratic fit to hybrid filter noise measurements

7.4.5 Hybrid correlator

Figure 7.17 shows the noise power for a hybrid correlator. Although there should not be any beating and therefore the noise power should be independent of the relative polarisation state in the two paths, it was found in practice that the noise level did show some dependence upon polarisation state. Measurements were taken with the polarisation adjusted for maximum and minimum noise, and both sets of measurements are shown in Figure 7.17.

Parameters from a best fit are in Table 7.3. The negative value for c_{lin} is clearly erroneous, but, as with the attenuator, the effect of the precise value of c_{lin} on the fit is small and the value derived is easily changed by small errors in the data points. Constraining c_{lin} to 1.5×10^{-7} and determining the revised best fit gives the short-dashed curves in Figure 7.17 and the parameters of Table 7.4.

The higher value quadratic term (10.5×10^{-5}) is larger than that of the attenuator or the coherent correlator with orthogonal polarisation states, but can still be explained by reflections at connectors and the lenses in the hybrid coupler. If it were caused

Parameter	Fit, upper curve	Fit, lower curve	Predicted value
v^2_{fixed}	$9.14 \times 10^{-9}\,\mathrm{V}^2$	$9.25 \times 10^{-9}\,\mathrm{V}^2$	$\geq 1.6 \times 10^{-9}\,\mathrm{V}^2$
c_{lin}	$1.5 \times 10^{-7}\,\mathrm{V}$ (fixed)	$1.5 \times 10^{-8}\,\mathrm{V}$ (fixed)	$1.5 \times 10^{-7}\,\mathrm{V}$
$c_{quad}\alpha_1\alpha_2$	10.5×10^{-5}	2.94×10^{-5}	$0.39\alpha_1\alpha_2$

Table 7.4: Parameters of the quadratic fit to hybrid filter noise measurements, fixed linear term

by one double reflection it would require $\sqrt{\frac{10.5\times10^{-5}}{0.39}} = 0.016$, 1.6% reflection (18.0 dB return loss) at each reflection, which is still lower than the Fresnel reflection. In the experiment for the hybrid correlator, furthermore, there are more locations likely to contribute to reflections and, as shown in Section F.2, having more source beams increases the beating power. The dependence on the polarisation controller is understandable because the reflections arising in the separate paths of the correlator will in general have different polarisation states.

7.5 Conclusion: observed performance of the hybrid coupler

This chapter has reported experimental work on a hybrid coupler that has:

- demonstrated the feasibility of constructing a hybrid coupler from off-the-shelf optical components
- proved that the insertion loss of a hybrid coupler can be lower than the inherent loss of an equivalent incoherent coupler
- demonstrated a 4-to-1 coupler, shown that it would be relatively straightforward to construct a 7-to-1 coupler with under 3 dB loss, and predicted that much higher coupling ratios should be possible with custom-built components
- measured the angle-dependency of coupling from single mode fibre to a multi-mode fibre, and shown that in general terms it has the characteristics predicted by overlap integral calculations of Chapter 6 (it does *not* have the sharp cut-off predicted by simple ray-optics analysis)
- shown that there is little or no optical beating as a result of combing optical waves in a hybrid coupler

In addition, strong optical beating has been observed in an incoherent correlator as predicted in Chapter 5. Quantitative measurements of beating noise power have been shown to be consistent with the modelling predictions to within experimental error.

In general terms, this chapter has confirmed experimentally the merits of the hybrid coupler and its suitability for use in an fibre optic delay line correlator.

Chapter 8

Performance of a dark-signalling bus

It has been proposed that optical CDMA used with a SLIM bus offers an attractive way of exploiting the potential capacity of optical fibre in a high-speed LAN (Chapter 2, see Figure 2.3 on page 22). Designs for the correlator have been analysed theoretically (Chapters 5 – 6) and experimentally (Chapter 7), and this chapter now reports on a simulation of a complete network using CDMA in a SLIM bus, in order to explore the possibilities and limitations of the proposal, and to derive further insight into how the network would perform.

The chapter starts with a description of the network that is to be modelled (Section 8.1) then describes the development of the model itself in Section 8.2. Results from an implementation of the model in *Mathematica* are presented in Section 8.3 and conclusions discussed in Section 8.4.

8.1 Network description

The network is assumed to have a folded bus topology (Figure 8.1) and has a single light source at the start of the bus which is operated continuously. Signals are applied to the bus by in-line modulators [13] which generate 'dark pulses'. A possible optical implementation of the modulator is shown in Figure 8.2. A pulsed laser generates short pulses at a repetition rate equal the single channel data rate. The pulses are gated by the data stream and enter a delay-line filter which spreads a single pulse into the signature sequence of the destination node. The output of the filter operates an all-optical switch in-line with the fibre bus. The details of the modulator will not be discussed further, but it should be noted that all-optical switches are the current focus of intense research activity, with progress being reported regularly in the literature [212, 213].

Optical amplifiers are used to maintain the power level in the bus, and for the purposes of the modelling in this chapter, it is assumed that there is an amplifier

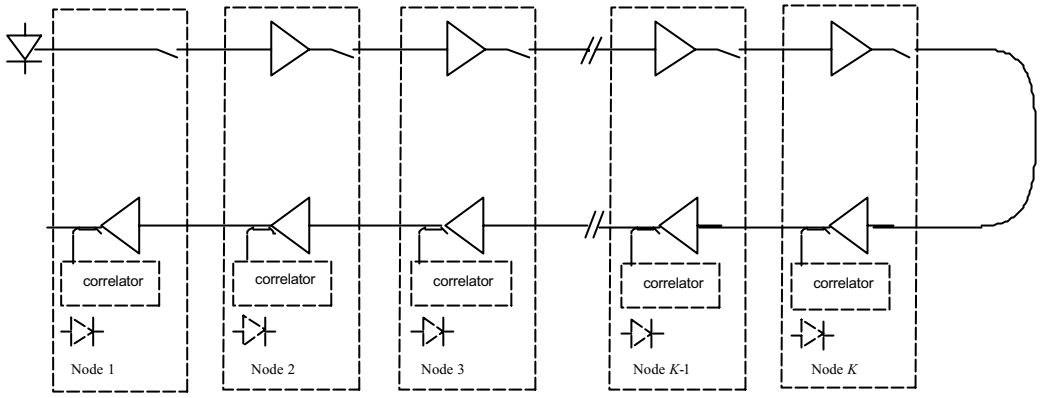

Figure 8.1: The SLIM bus

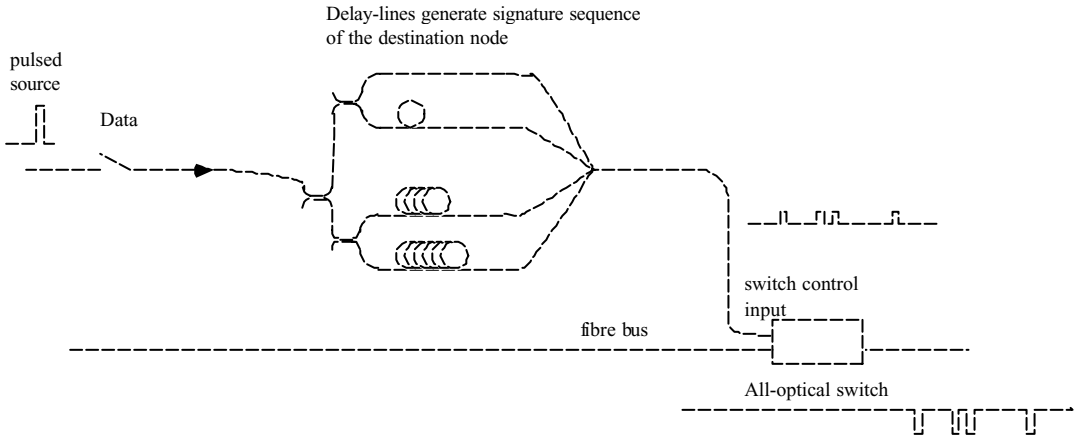

Figure 8.2: Possible configuration of a modulator for a SLIM bus.

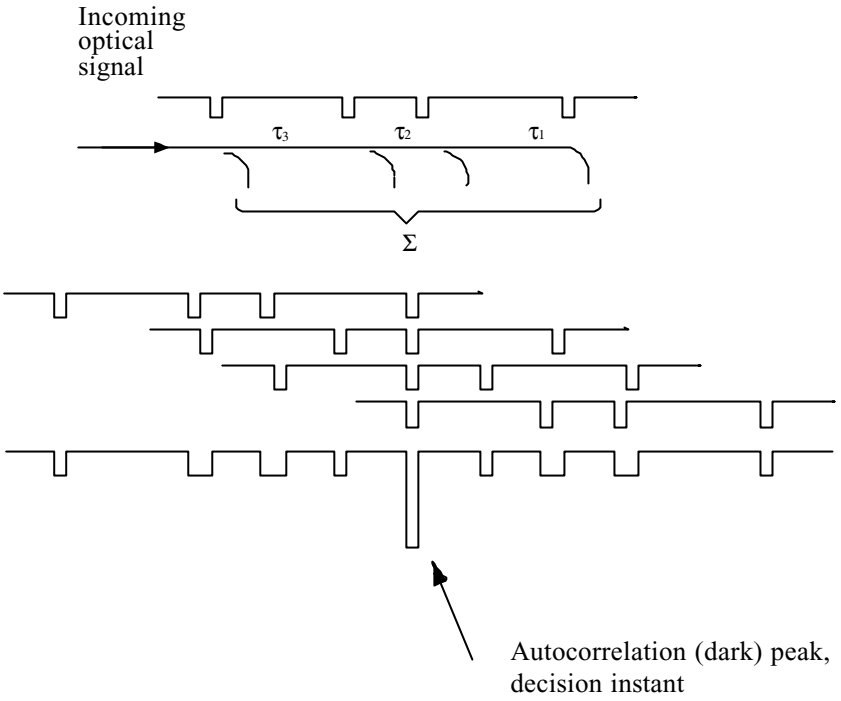

Figure 8.3: Correlation in the tapped-fibre delay line

in the transmit and receive path at each node (Figure 8.1). From node to node the bus is therefore effectively lossless, but knowledge of the intermediate attenuation and amplifier gains is needed in order to model the effects of ASE (amplified spontaneous emission) noise.

At the receive terminals, a fraction of the power is extracted from the bus and fed into a fibre tapped-delay line optical correlator, which may be a coherent, incoherent or hybrid correlator. As the chip-sequence passes the correlator of the target node during data 1s, the optical output of the correlator traces a quantized auto-correlation function of the signature sequence (Figure 8.3). Because of the dark signalling, the autocorrelation 'peak' is ideally represented by zero optical power at the correlator output because there is a dark chip on each tap of the correlator.

The optical output of the correlator is incident upon a photodiode and produces a photocurrent, and this is filtered to give the signal current.

The receiver synchronizes to the originator's data rate by locking a local clock to the (dark) peak of the autocorrelation functions. Once synchronized, the receiver examines the chip period corresponding to the autocorrelation peak (the decision instant) in each bit interval, and uses threshold detection on the signal current to decide on the data value.

8.2 System model

This Section develops a model of the system in order to determine the potential network dimensions, in terms of data rates, number of nodes attached to the network and number of simultaneous users. Section 8.2.1 first considers the limiting performance due to multiple access interference, then Section 8.2.2 looks at how the effects of noise degrade the network performance. Networks using incoherent and coherent correlators are simulated as well as networks using hybrid correlators in order to compare performance, and investigated further the expected merits of the hybrid correlator that were discussed in previous chapters.

It is assumed throughout that the receiver has already synchronized to the data of the source node, and that the decision instant is in the chip corresponding to the autocorrelation (dark) peak. When describing signals on the network a time frame is used that moves around the bus with the light. Suppose, for example, node 1 puts a dark chip on the bus and that when this chip passes node 2, node 2 also activates its modulator to generate a dark chip. In this situation chips are said to have been sent *simultaneously* from nodes 1 and 2.

The network is modelled as chip synchronous (chips from all nodes start and end at the same instant – in the time frame travelling with the light). The real network would not be synchronized in this way, but the assumption simplifies the modelling and it was shown in [214] that chip-synchronicity provides a worst-case bound on the probability of error. It is also assumed in this analysis that the codes have maximum cross-correlation of one, like the optical orthogonal codes.

8.2.1 Ideal channel: Multiple Access Interference (MAI) alone

Consider initially an 'ideal' dark bus, in which:

- the receivers are assumed to be capable of ideal threshold detection on the summation of the optical power on the correlator taps
- the optical amplifiers provide gain with no signal degradation (no ASE)
- all noise in the receivers is neglected
- modulators have 100% extinction ratio – the light is completely blocked by a dark pulse.

Consider communication between two specific nodes: from the source node to the destination node. When the source node sends a data 1 the destination correlator output will be zero at the auto correlation peak and there is no mechanism in the idealized model that can change this, so there are no errors during data 1s.

When the source node sends a data 0 it generates no dark pulses and the destination correlator output should be high. There may, however, be dark pulses on the bus from

communication taking place between other pairs of nodes, and some of these interfering pulses may hit the destination node at the decision instant. If there are interfering pulses on all the taps of the correlator at the decision instant then the correlator output will be zero, and there will be an error. If there are interfering pulses on some but not all taps, the output power will be reduced, but not to zero. Provided the decision threshold has been set close to (but above) zero, this will not cause an error. More precisely, the error probability is minimised by setting the decision threshold between 0 and the power corresponding to dark pulses on all but one tap so that errors *only* occur if there are dark pulses on all taps during a data 0 (cf. [140]).

Calculation of the error probability is then possible by calculating the probability that the interfering users happen, between them, to supply at least one pulse on each tap. This is a problem of combinatorics and can be solved using the same calculation that has been done for optical CDMA in a star network using light pulses where optical hard-limiters are included in the correlators. The hard limiters in the correlators of a conventional star network ensure that the signal from any one tap can never exceed the power corresponding to one chip – so each tap can contribute at most one 'chip's-worth' of interference, which reduces the error probability [214]. An optical hard limiter converts the channel from an adder-channel to a binary OR-channel by removing intensity information from the fibre beyond the two levels of 'off' and 'on'. The ideal dark bus is inherently a binary OR-channel because once the light is blocked by one active node the states of nodes further downstream have no further influence on the light power. Consequently the hard-limited performance is achieved without the need for an additional device in the dark-bus.

Azizoğlu et al. [215] have derived an exact formula for the probability of error given the use of OOCs:

$$P_{\text{error}} = \begin{cases} \frac{1}{2}\sum_{m=0}^{W}(-1)^m \binom{W}{m}\left(1-\frac{mW}{2L_c}\right)^{N-1} & N-1 \geq W \\ 0 & N-1 < W \end{cases} \tag{8.1}$$

Where W is the code weight (number of dark chips in the signature sequence, equal to the number of taps in the delay line), L_c is the code length (total number of chips in the signature sequence) and N is the number of simultaneous users.

It will be informative later to consider the case when the threshold is higher using an approximate formula of Salehi's [140]:

$$P_{\text{error}}(Th) = \begin{cases} \frac{1}{2}\binom{W}{Th}\prod_{m=0}^{Th-1}\left(1-\left(1-\frac{W}{2L_C}\right)^{N-1-m}\right) & N-1 \geq W \\ 0 & N-1 < W \end{cases} \tag{8.2}$$

Where the integer Th is the threshold, such that there will be an error during a data 0 if there are chips from interfering users on at least Th of the taps. (Equation 8.2 closely approximates Equation 8.1 when $Th = W$.)

These two formulae will be used to calculate upper bounds on the network performance in the simulations of Section 8.3.

8.2.2 Performance degradation due to noise

In the idealized model of the previous section the distribution of chips in the correlator determines completely the presence or absence of an error. There is an error if and only if the source node sends a 0 and the interfering users combine to contribute at least one chip to each of the arms of the correlator.

When noise is included in the model, there may or may not be an error for any distribution of interfering chips among the arms of the correlator, and the modelling process proceeds by considering all possible distributions of interfering chips and calculating the associated probability of error for each. Then:

$$\mathrm{P}_{\mathrm{error}} = \sum_{\mathbf{k}\in\mathcal{K}} \mathrm{P}(\mathrm{error}|\mathbf{k})\mathrm{P}(\mathbf{k}) \tag{8.3}$$

Where $\mathbf{k}$ represents the distribution of interfering chips among the correlator taps at the decision instant, $\mathcal{K}$ is the set of all possible $\mathbf{k}$ and $\mathrm{P}(\mathrm{error}|\mathbf{k})$ is the conditional probability of error given the distribution $\mathbf{k}$.

The probabilities $\mathrm{P}(\mathrm{error}|\mathbf{k})$ depend upon the optical power levels at the correlator output, which are derived in Section 8.2.3, and the magnitude of the noise on the signal at the receiver (Section 8.2.4). The distribution of $\mathbf{k}$ and associated probabilities $\mathrm{P}(\mathbf{k})$ are derived in Section 8.2.5.

8.2.3 Power levels on the bus

Consider:

- The power launched by the laser into the bus, P_L. Broadband sources are modelled by a linewidth of B_S and constant power spectral density $n_S = P_L/B_S$.
- If nodes $x_1, x_2 ... x_k$ are all signalling simultaneously, the power from the laser reaching the taps of a correlator is $P_S(\mathcal{A})$, and the ASE power spectral density from the amplifiers reaching the taps of a correlator is[1] $n_N(\mathcal{A})$, where $\mathcal{A} = \{x_1, x_2 ... x_k\}$ is the set of active nodes.
- The loss from the bus to the correlator taps is given by γ/W, where γ accounts for the fraction of light extracted from the bus as well as all excess losses in the tap and the correlator (γ is taken to be the same for all nodes). W is the number of taps in the correlator (which is equal to the code weight).
- The ASE power spectral density added by each amplifier is n_t for the amplifiers in the transmit path and n_r for those in the receive path. It is modelled as a function of the amplifier gain G according to $n_{t,r} = n_{sp}(G_{t,r} - 1)h\nu$, where

[1] Subscripts S and N indicate parameters of the signal and noise (ASE) respectively. Lower-case n is used for power spectral densities and upper case (italic) P for powers. Upper case P is also used in roman font to indicate probabilities, as in P(error) to mean the probability of error.

n_{sp} is the spontaneous emission factor, h is Planck's constant and ν the optical frequency [165].

- To model extinction ratio below 100%, when a node is sending a dark chip it attenuates the light in the bus by M, where M is finite.

A consideration of the power evolution in the bus leads to:

For the signal:

Since the bus is effectively lossless (the amplifier gains precisely compensate for the segment losses), the attenuation suffered by the signal is just M for each active node and γ/W on tapping off the bus and into the delay-line tap, giving $P_S(\mathcal{A}) = P_L\gamma/M^kW$.

Notice that $P_S(\mathcal{A})$ does not depend upon which nodes are the active ones, only how many there are (k). It will simplify the algebra later therefore if P_S is redefined as a function of the integer k rather than the set $\mathcal{A}$:

$$P_S(k) = P_L\gamma/M^kW \tag{8.4}$$

If the light source is broadband, the power spectral density is similarly given by

$$n_S(k) = n_L\gamma/M^kW \tag{8.5}$$

For the ASE

Because the bus is effectively lossless, it sums the ASE power from the amplifiers when there are no active nodes. The total noise power spectral density in the correlator taps of node y when there are no active nodes is given by:

$$n_N(\phi) = (n_tK + (K-y)\,n_r)\,\gamma/W \tag{8.6}$$

(ϕ is the empty set, signifying no active nodes. K is the total number of nodes on the bus.) This is a maximum when at node number 1 ($y = 1$), where it is $(n_tK + (K-1)\,n_r)\,\gamma/W$.

When there are active nodes described by the set $\mathcal{A} = \{x_1, x_2...x_k\}$, then each of the active nodes attenuates ASE from all the nodes that come earlier in the bus, so assuming that $x_1, x_2...x_k$ are ordered such that $x_1 < x_2... < x_k$ then

$$n_N(\mathcal{A}) = \left[\left(\frac{x_1-1}{M^k} + \sum_{i=1}^{k-1}\left(\frac{x_{i+1}-x_i}{M^{(k-i)}}\right) + (K-x_k+1)\right)n_t + (K-y)\,n_r\right]\gamma/W$$

Again the worst-case is for $y = 1$.

Whereas the signal power depended only upon the total number of active nodes, k, not which nodes they are, the ASE depends upon the location of the active nodes.

The modelling is substantially simplified, however, if n_N as well as P_S can be written as a function of k alone, which can be done assuming the worst-case situation. This is when the active (transmitting) nodes are the first k nodes on the bus, giving a function $n_N(k)$:

$$n_N(k) = \left[\left(\frac{M^{(k-1)} - 1}{M^{(k-1)}\,(M-1)} + (K - k + 1) \right) n_t + (K - y)\, n_r \right] \gamma / W \tag{8.7}$$

8.2.4 Probability P(error|**k**)

Separating the conditions corresponding to the source node sending a 1 or a 0:

$$\mathrm{P}(\mathrm{error}|\mathbf{k}) = p_0 \mathrm{P}_0(\mathrm{error}|\mathbf{k}) + p_1 \mathrm{P}_1(\mathrm{error}|\mathbf{k})$$

where p_0 and p_1 are the probability of the source node sending a data 0 or 1 respectively (taken to be 0.5 in the simulations of Section 8.3).

To calculate the probability of error the signal current at the threshold detector is modelled by a Gaussian distribution with mean μ and standard deviation σ. μ and σ are determined by the optical power in the correlator taps, which in turn is a function of **k**.

For **k** to provide a full description of chips in the correlator during the decision instant it would need to be a W-dimensional vector, each coordinate of which identifies the origin of the chips hitting one of the taps. That is: $\mathbf{k} = (\mathcal{A}_1, \mathcal{A}_2, ...\mathcal{A}_W)$, where $\mathcal{A}_u = \{x_1, x_{2,...}x_k\}_u$ is the set of nodes that result in chips on tap u of the correlator at the decision instant. From the previous section, however, it is assumed that the power at the correlator taps depends only upon the number of chips 'hitting' the tap, not on which node they originate from. Using integers for the coordinates of **k**, therefore, gives $\mathbf{k} = (k_1, k_2, ...k_W)$ where k_u is the number of interfering chips on tap u of the correlator. During a data 0 the chips on the taps are only those from the interfering users, which is given directly by the vector **k**. During a data 1, however, there is also a chip from the source node on each tap, so the pattern of chips is described by $(k_1 + 1, k_2 + 1, ...k_W + 1)$ written as $\mathbf{k} + \mathbf{1}$.

The probability of error is then given by the Q-function [160]:

$$\begin{aligned} \mathrm{P}_0(\mathrm{error}|\mathbf{k}) &= Q\left(\frac{\mu(\mathbf{k}) - i_{\mathrm{threshold}}}{\sigma(\mathbf{k})} \right) \\ \mathrm{P}_1(\mathrm{error}|\mathbf{k}) &= Q\left(\frac{i_{\mathrm{threshold}} - \mu(\mathbf{k}+\mathbf{1})}{\sigma(\mathbf{k}+\mathbf{1})} \right) \end{aligned} \tag{8.8}$$

The receiver is modelled by a PIN photodiode with responsivity $\mathcal{R}$ and thermal noise from a resistance of R_L[2]. Subsequent processing is taken to be noise-free with

[2] If the receiver users an integrating design, R_L would be the photodiode load impedance. Alternatively if a transimpedance receiver is used, R_L would be used in calculating the thermal noise, but the effective load impedance would be reduced by the amplifier gain (see the discussion of receiver design in Bissell and Chapman [160])

frequency response modelled by a brick-wall low-pass filter of bandwidth B_e followed by threshold detection. Thermal noise is modelled by [160] $\sigma^2_{thermal} = 4kTB_e/R_L$ (where k is the Boltzmann constant.) Other terms contributing to $\mu(\mathbf{k})$ and $\sigma(\mathbf{k})$ are different for the three different correlator types, and are discussed separately below.

Incoherent correlator

An incoherent correlator (Chapter 5 Section 5.2.2) requires a broadband signal so that the output of the combiner is a sum of the optical power on the taps. The optical source is therefore modelled by a signal with constant power spectral density n_S over a bandwidth of B_S Hz, and is assumed to have the characteristics of a thermal source – the same as the spontaneous emission. The spontaneous emission noise power (N) is modelled as white over a bandwidth B_N Hz.

The incoherent combiner has a loss of $1/W$ and adds the powers. The total signal and noise power spectral densities at the output of the correlator (incident upon the photodiode) are given by:

$$n_{S,N}(\mathbf{k}) = \frac{1}{W}\sum_{w=1}^{W} n_{S,N}(k_w)$$

Optical beating occurs between the signal and ASE, and, because they are both broadband, there is also optical beating within both of them. There are therefore five noise terms: thermal noise ($\sigma^2_{thermal}$, see above), shot noise (σ^2_{shot}), signal-spontaneous cross-modulation noise (σ^2_{S-N}), spontaneous-spontaneous inter-modulation noise (σ^2_{N-N}) and source-source inter-modulation noise (σ^2_{S-S}). The total optical power reaching the photodetector is $(n_N(\mathbf{k})B_N + n_S(\mathbf{k})B_S)$ so the shot noise is given by:

$$\sigma^2_{shot} = 2e\mathcal{R}B_e\left(n_N(\mathbf{k})B_N + n_S(\mathbf{k})B_S\right)$$

For the cross- and inter-modulation terms the results of Section 3.5 are used, with $B_1 = B_S$ and $B_2 = B_N$, so:

$$\begin{aligned}
\sigma^2_{S-N} &= 2c\mathcal{R}^2 B_e B_S n_S(\mathbf{k}) n_N(\mathbf{k}) \\
\sigma^2_{N-N} &= B_e\mathcal{R}^2 (n_N(\mathbf{k}))^2 (2B_N - B_e) \\
\sigma^2_{S-S} &= B_e\mathcal{R}^2 (n_S(\mathbf{k}))^2 (2B_S - B_e)
\end{aligned} \tag{8.9}$$

The factor c in σ^2_{S-N} is given by Equation 3.14. σ^2_{S-N} has been halved to account for the random polarisation state of the ASE compared to the signal.

The variance of the signal current is the sum of noise terms:

$$\sigma^2(\mathbf{k}) = \sigma^2_{thermal} + \sigma^2_{shot} + \sigma^2_{S-N} + \sigma^2_{N-N} + \sigma^2_{S-S}$$

The mean signal current is given by

$$\mu(\mathbf{k}) = \mathcal{R}\left(n_S(\mathbf{k})B_S + n_N(\mathbf{k})B_N\right) \tag{8.10}$$

Coherent correlator

For the coherent correlator (Section 5.2.1) the signal is narrowband and the spontaneous emission is broadband.

The coherent combiner affects the spontaneous emission in the same way as does the incoherent correlator: it has a loss of $1/W$ and adds the powers, so that:

$$n_N(\mathbf{k}) = \frac{1}{W}\sum_{w=1}^{W} n_N(k_w)$$

For the signal, however, the coherent correlator adds the field strengths with no loss (neglecting excess losses, which are accounted for separately). If the signal powers in the taps are given by $P_S(k_w)$ the field strength is proportional to the square root of the power and so $E(k_w) = \beta\sqrt{P_S(k_w)}$ where β is a constant, then:

$$P_S(\mathbf{k}) = \beta^{-2}E(\mathbf{k})^2 = \left(\sum_{w=1}^{W}\sqrt{P_S(k_w)}\right)^2$$

Using the results of Section 3.4 with $B_1 = B_N$ ($P_1 = n_N B_1$) and $P_2 = P_S$, and again halving σ^2_{S-N} to account for polarisation:

$$\begin{aligned}
\sigma^2_{shot} &= 2e\mathcal{R}B_e\left(n_N(\mathbf{k})B_N + P_S(\mathbf{k})\right)\\
\sigma^2_{S-N} &= 2\mathcal{R}^2B_e n_N(\mathbf{k})P_S(\mathbf{k})\\
\sigma^2_{N-N} &= 2B_e\mathcal{R}^2\left(n_N(\mathbf{k})\right)^2(2B_o - B_e)
\end{aligned} \tag{8.11}$$

The variance of the signal current is the sum of noise terms:

$$\sigma^2(\mathbf{k}) = \sigma^2_{thermal} + \sigma^2_{shot} + \sigma^2_{S-N} + \sigma^2_{N-N}$$

The mean signal current is given by:

$$\mu(\mathbf{k}) = \mathcal{R}\left(P_S(\mathbf{k}) + n_N(\mathbf{k})B_N\right) \tag{8.12}$$

Hybrid correlator

Within each tap of the hybrid correlator (Section 5.2.3) there is a signal component and a spontaneous emission component. At the photodiode beating takes place between the signals within each tap, but not between signals in different taps. The photodiode output is then a sum of the contributions from each tap:

$$\begin{aligned}
\sigma^2_{shot} &= 2e\mathcal{R}B_e\sum_{w=1}^{W}\left(P_S(k_w) + n_N(k_w)B_N\right)\\
\sigma^2_{S-N} &= 2\mathcal{R}^2B_e\sum_{w=1}^{W}P_S(k_w)n_N(k_w)\\
\sigma^2_{N-N} &= 2B_e^2\mathcal{R}^2\sum_{w=1}^{W}\left(n_N(k_w)\right)^2(2B_o - B_e)
\end{aligned} \tag{8.13}$$

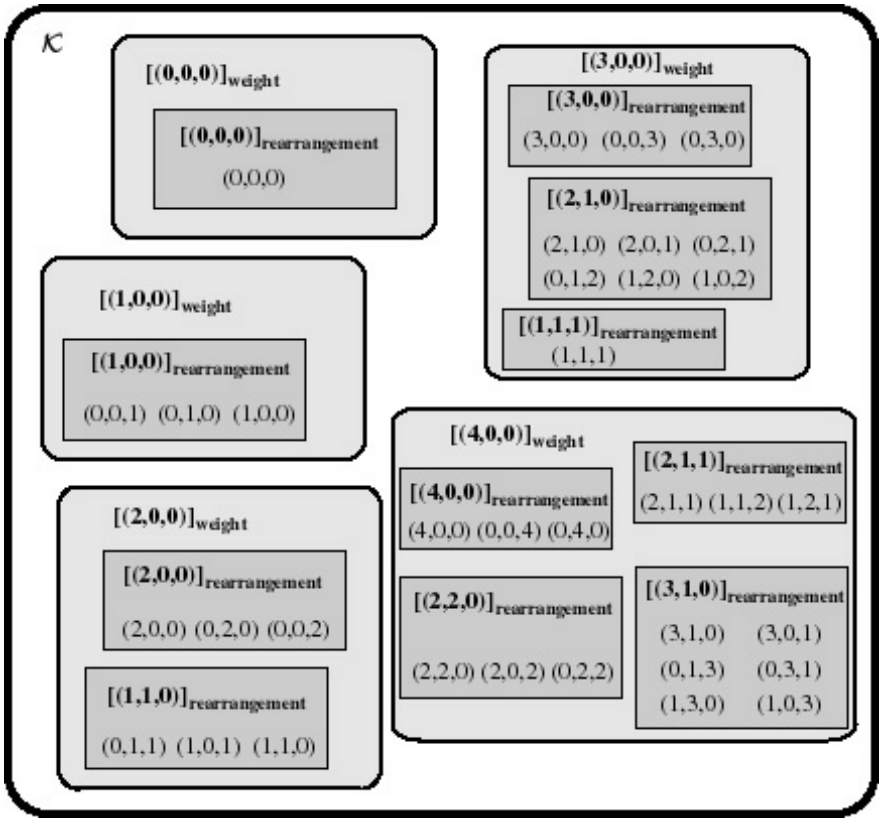

Figure 8.4: Partitioning $\mathcal{K}$ for $W = 3$ and $N = 5$

The variance of the signal current is the sum of noise terms:

$$\sigma^2(\mathbf{k}) = \sigma^2_{thermal} + \sigma^2_{shot} + \sigma^2_{S-N} + \sigma^2_{N-N}$$

The mean signal current is given by:

$$\mu(\mathbf{k}) = \mathcal{R} \sum_{w=1}^{W} (P_S(k_w) + n_N(k_w) B_N) \tag{8.14}$$

8.2.5 Distribution k and probabilities P(k)

The analysis in this section is based on Kwon [216] and Azizoğlu et al. [215], but whereas Kwon and Azizoğlu et. al. were only interested in the number of 'empty' taps, the present analysis needs the number of coincident chips on each tap of the correlator.

Calculation of the error probability could be done from Equation 8.3 by generating all possible $\mathbf{k}$ (the set $\mathcal{K}$), but unless the number of simultaneous users is very small, the size of $\mathcal{K}$ is very large. To simplify the calculation the sum is broken down by partitioning $\mathcal{K}$ into equivalence classes [217] at two levels, as illustrated in Figure 8.4 for $W = 3$ and $N = 5$.

'Weight' equivalence classes The first level of partitioning is according to the weight of the vectors (the total number of interfering pulses that hit the correlator), described by the variable j_u. The equivalence class of all vectors of weight j_u is designated $[(j_u, 0, ..0)]_{\text{weight}}$.

'Rearrangement' equivalence classes The second level partitions the weight equivalence classes according to the relationship that vectors are equivalent if you can get one from the other by a rearrangement of the coordinates. Each of these classes is defined by a representative vector, $\mathbf{k_r}$, where the representative vector is chosen as the one with non-increasing coordinate values, and the equivalence classes will be designated by $[\mathbf{k_r}]_{\text{rearrangement}}$.

The summation of Equation 8.3 is done in three stages: over the all possible weight classes (identified by values of j_u), over all possible rearrangement classes of weight j_u (identified by $\mathbf{k_r}$), then over all members of the rearrangement class $[\mathbf{k_r}]_{\text{rearrangement}}$. Thus:

$$P_{\text{error}} = \sum_{j_u=0}^{N-1} \sum_{\mathbf{k_r} \in [(j_u,0,..0)]_{\text{weight}}} \sum_{\mathbf{k} \in [\mathbf{k_r}]_{\text{rearrangement}}} P(\text{error}|\mathbf{k}) P(\mathbf{k}) \tag{8.15}$$

None of the correlators distinguish between the taps, so the probability of error is the same for all members of any one rearrangement class. That is: $P(\text{error}|\mathbf{k}) = P(\text{error}|\mathbf{k}_r)$ for all $\mathbf{k} \in [\mathbf{k_r}]_{\text{rearrangement}}$. Then, writing $P(\mathbf{k}) = P(\mathbf{k}|j_u)\, P(j_u)$, Equation 8.15 becomes:

$$\begin{aligned} P_{\text{error}} &= \sum_{j_u=0}^{N-1} \sum_{\mathbf{k_r} \in [(j_u,0,..0)]_{\text{weight}}} \sum_{\mathbf{k} \in [\mathbf{k_r}]_{\text{rearrangement}}} P(\text{error}|\mathbf{k_r}) P(\mathbf{k}|j_u)\, P(j_u) \\ &= \sum_{j_u=0}^{N-1} P(j_u) \sum_{\mathbf{k_r} \in [(j_u,0,..0)]_{\text{weight}}} P(\text{error}|\mathbf{k_r}) \sum_{\mathbf{k} \in [\mathbf{k_r}]_{\text{rearrangement}}} P(\mathbf{k}|j_u) \end{aligned} \tag{8.16}$$

References [215] and [216] provide formulae for $P(j_u)$ and for $\sum_{\mathbf{k} \in [\mathbf{k_r}]_{\text{rearrangement}}} P(\mathbf{k}|j_u)$:

$$P(j_u) = \binom{N-1}{j_u} p^{j_u} (1-p)^{N-1-j_u} \tag{8.17}$$

$$\sum_{\mathbf{k} \in [\mathbf{k_r}]_{\text{rearrangement}}} P(\mathbf{k}|j_u) = \frac{\text{Multinomial}(\mathbf{k_r})\, \text{Multinomial}(\text{reps}(\mathbf{k_r}))}{W^{j_u}} \tag{8.18}$$

Where $p = \frac{W^2}{2L_c}$ is the probability of one interfering user 'hitting' the correlator taps, W is the code weight, L_c is the code length and $\text{reps}(\mathbf{k})$ is the set of repetitions within $\mathbf{k}$: the number of times terms are repeated (so $\text{reps}(3,1,1) = (0,2,0,1)$, because '0' appears zero times, '1' appears twice, '2' appears zero times and '3' appears once.) Eqn. 8.18 is discussed further in the description of the *Mathematica* implementation in Appendix D.4.3.

Parameter	Value	Note
Laser launch power, P_L	1 dBm	
Fibre attenuation between nodes	3 dB	Includes any splice or connector losses
Modulator excess loss	3 dB	
Modulator extinction ratio, M	20	13 dB
Loss from bus to taps, γ	16 dB	Does not include splitting loss of $1/W$
Amplifier noise parameter, n_{sp}	2	
Photodiode responsivity, $\mathcal{R}$	1.25	
Thermal noise resistance, R_L	10000-	See footnote on page 143
Electrical bandwidth, B_e	10^{10} Hz	Corresponds to signalling rate of 20 GBaud
ASE optical bandwidth, λ_N	25 nm	
Laser linewidth, λ_S	1 nm	Used only for the incoherent correlator
Number of nodes, K	49	
No. simultaneous users, N	8	
Code length, L_C	883 chips	
Code weight, W	6 chips	

Table 8.1: Default Parameters for the simulation. See text for changes.

Using Equations 8.17 and 8.18 in 8.16, and the results of Section 8.2.4 for P(error$|\mathbf{k_r}$), allows the calculation of the probability of error for each of the correlators and any W and N.

8.3 Numerical Results

The potential network performance is explored by numerical simulation using *Mathematica* (see Appendix D.4.3 at the end of this chapter for more information), starting with the default parameters listed in Table 8.1.

The code dimensions (weight of 6 and length 883 chips) correspond to one of the codes described by Yang and Fuja in [143]. On the definition of Salehi [140] it is not strictly an optical orthogonal code (OOC), because although it has a cross-correlation bound of 1, it has an auto-correlation bound of 2. However, the modelling presented here is independent of auto-correlation, so remains valid for this code. The code has a cardinality of 49, allowing a network with up to 49 uniquely addressable nodes. Other parameters are chosen as typically achievable values with present day technology.

8.3.1 Decision threshold

Figure 8.5 shows the probability of error as a function of the current used for the decision threshold, for each of the three correlators.

The steps in the curve correspond to chips (dark pulses) 'hitting' different numbers of correlator taps, and the optimum threshold in each case lies between the current corresponding to chips on five of the six taps and the current corresponding to chips on all six taps. The width of this interval is smaller for the coherent correlator than

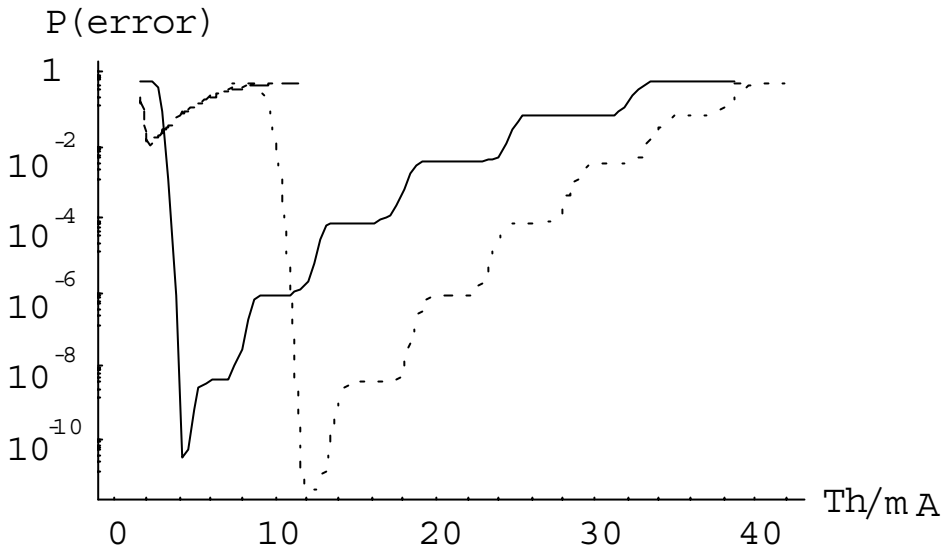

Figure 8.5: Probabilty of error as a function of threshold current, for the incoherent correlator (dashed line), coherent correlator (unbroken line) and hybrid correlator (dotted line).

for the hybrid correlator because the coherent correlator adds optical fields rather than powers. Photocurrent, which is proportional to optical power, is therefore proportional to the square of the number of bright taps in the coherent correlator, as can be seen by the increasing width of the steps in the curve. When all six taps are bright (no dark chips on the taps) all the light is directed to the photodiode for both the hybrid and coherent correlator, but when there is only one bright tap the hybrid correlator delivers 1/6 of the power whereas the coherent correlator delivers $(1/6)^2$ of the power. The offset of the hybrid thresholds compared to the coherent thresholds is explained by the $1/W$ attenuation of the ASE in the coherent correlator.

The 'smoothing' of the steps is due to noise (thermal, shot and beating). If all the sources of noise are artificially – and unrealistically – reduced by increasing the load resistance to reduce thermal noise, reducing the amplifier noise figure to reduce beating noise and reducing the electrical bandwidth to reduce shot noise, then the smoothing is reduced. This is shown in Figure 8.6 for the hybrid correlator, with load resistance, 100 k- , amplifier noise figure of 0.01, and 1 MHz electrical bandwidth.

Another departure from the MAI steps described above comes from the fact that the signal on the channel is not purely binary - it is not a pure 'OR' channel. In particular, the signal power is attenuated by $1/M^r$ where M is the modulator extinction, and r is the number of simultaneous pulses. The effect of this 'fine structure' is made more apparent in Figure 8.7 by making the extinction ratio artificially low (3) and again suppressing the 'smoothing' by reducing all the other sources of noise.

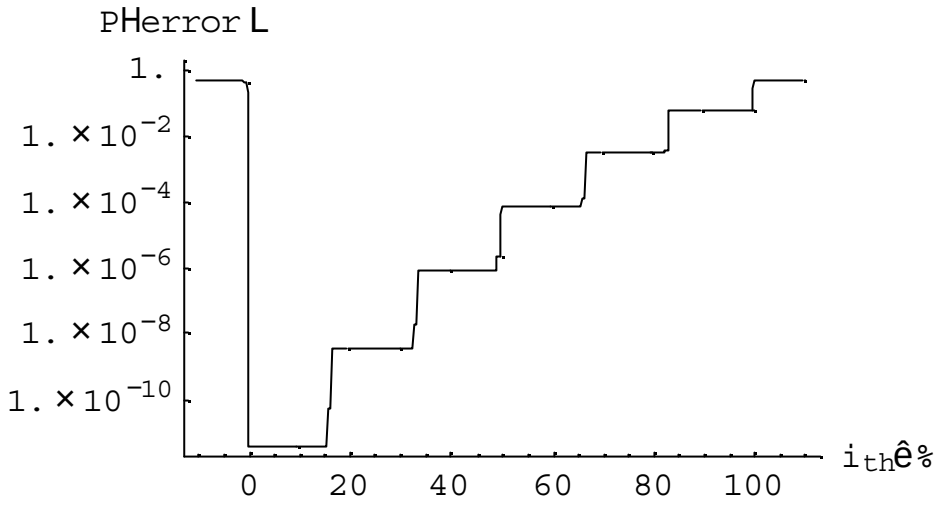

Figure 8.6: Probabilty of error as a function of threshold for the hybrid correlator, with the noise reduced. The threshold has been normalised so that 0% is the current when there is one dark pulse on each of the taps, 100% is the current when there are no dark pulses on any of the taps.

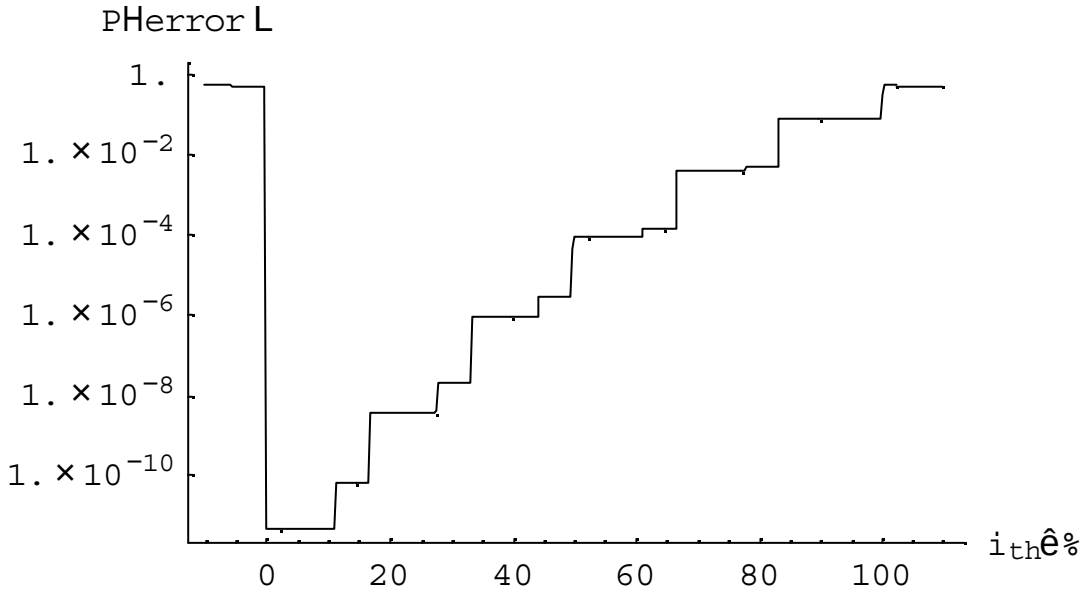

Figure 8.7: Probabilty of error as a function of threshold for the hybrid correlator, with the noise reduced and $m = 3$ to show the 'fine structure'. The threshold has been normalised as in Figure 8.6.

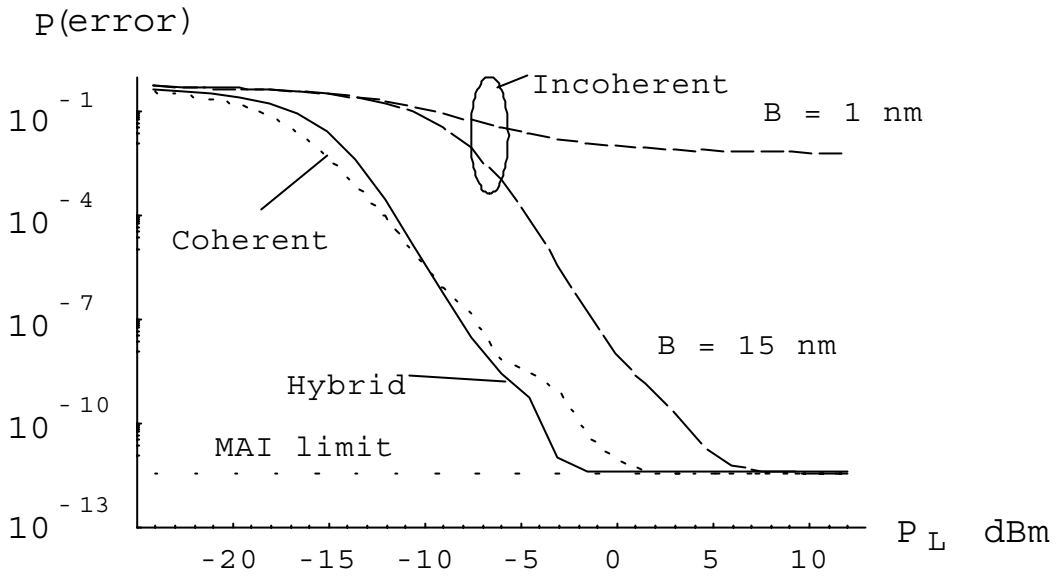

Figure 8.8: Probability of error as a function of the power of the light source, for each of the three correlators.

8.3.2 Laser source power

Figure 8.8 shows the probability of error (with the optimised decision threshold) as a function of laser source power. With the default parameters of Table 8.1, the high-power error floor for both the hybrid and coherent correlators is equal to the multiple access interference, MAI, (calculated from Equation 8.1) alone. The error floor for the incoherent correlator is much higher, however, due to the optical beating. As noted above, the effects of optical beating in the incoherent correlator can be decreased by increasing the optical bandwidth, and this effect is shown in Figure 8.8 with the laser bandwidth increased to 15 nm. In this case the incoherent correlator can deliver MAI-limited performance, but requires a higher signal power due to the $1/W$ loss in the correlator.

8.3.3 Network size

Adding more nodes to the network increases the noise from the amplifiers' ASE. The consequences of this are demonstrated in Figure 8.9, for 10 simultaneous users. The codes of Table 8.1 would only allow 49 uniquely addressable nodes, so for Figure 8.9 the code is changed to a 9001 chip code of weight 6 which, from [143] (using Construction 1), will allow an address space of 500.

Increasing the number of nodes increases the error rate because of the increased ASE from the amplifiers at each node. ASE can be reduced by optical filtering at the receiver, and the effect of this is shown by the lower curves in Figure 8.9, assuming a 1 nm filter. Some aspects of the shapes of the curves of Figure 8.9 can be explained

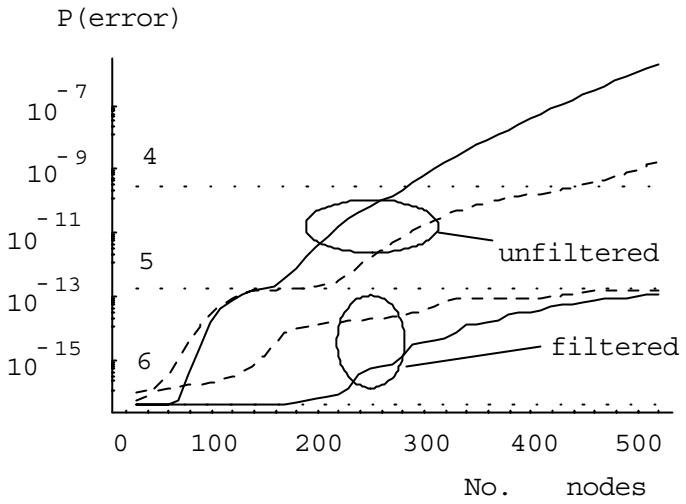

Figure 8.9: Probability of error for 10 simultaneous users as a function of the number of nodes. Dashed curves for coherent correlator, unbroken line for the hybrid correlator. Horizontal dotted lines show the MAI limit with the threshold set to 4, 5 and 6 chips, calculated using Equations 8.1 and 8.2.

qualitatively with reference to Figure 8.5. At small numbers of nodes the optimum MAI-limited performance is achieved with the decision threshold set at the lowest point of the curves in Figure 8.5, corresponding to chips hitting all six of the correlator taps. As the number of nodes increases the ASE 'smooths out' the curves of Figure 8.5 and the lowest dip is lost. The best performance then corresponds to the next lowest step of Figure 8.5 which is due to interfering chips hitting five of the six correlator taps. On Figure 8.9 the error probability can be seen to rise from the MAI limit with the decision threshold set to 6 hits to that corresponding to five hits, and the coherent correlator rises earlier than the hybrid correlator because of the smaller width of the bottom step of the coherent correlator in Figure 8.5. For further increases in ASE (seen for the unfiltered curves in Figure 8.9) the error probability rises to the next level – chips hitting four of the taps – but the coherent correlator now performs better than the hybrid correlator, because of its $1/W$ ASE rejection.

8.3.4 Number of simultaneous users

Figure 8.9 indicates that a 500 node network is possible, so Figure 8.10 investigates the maximum number of simultaneous users that could be accommodated. The simulation time rises steeply for large numbers of simultaneous users due to the exponential rise in the number of rearrangements in Equation 8.18, so for the results of Figure 8.10 a close upper bound was used, based the observation that with the given parameters the probability of a large numbers of hits at the correlator is small (for example, with

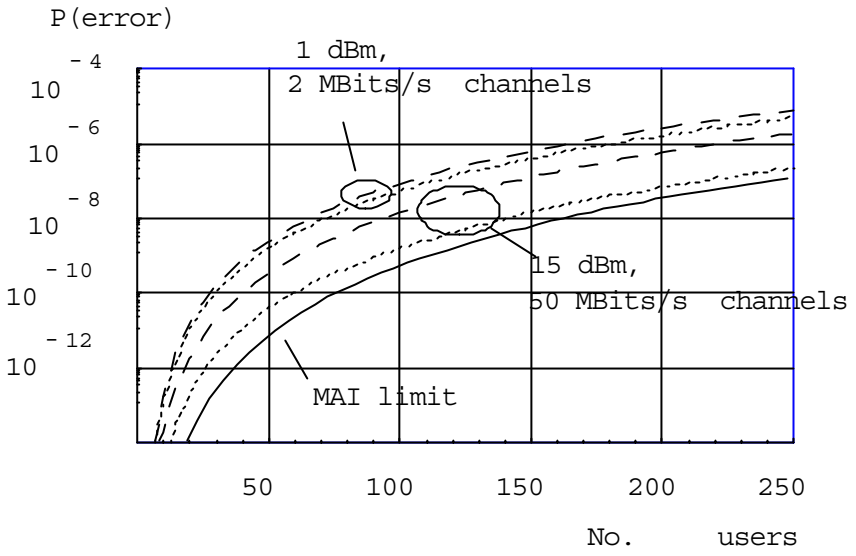

Figure 8.10: Error probability as a function of the number of simultaneous users for a 500-node network. Dashed line for the coherent correlator and dotted line for the hybrid correlator.

$N = 250$, $P(30) \approx 10^{-43}$) and that when the number of hits is large then the error probability approaches 0.5. A very good approximation was obtained by replacing the higher terms (for $j_u > 30$) in the sum of Eqn. 8.16 by $0.5P(j_u)$. There are more details on the implementation and validity of this approximation in Section D.4.3.

With the parameters of Table 8.1 and the 9001-chip, weight-6, code, approximately 50 simultaneous users are possible for an error rate under 10^{-9}. However, the parameters of Table 8.1 are conservative in terms of the technology and from Figure 8.8 it can be seen that increasing the signal power allows MAI-limited performance to be approached with hybrid and coherent correlators. Optical processing at more than 500 Gbit/s has been reported in TDM experiments [218, 219], so Figure 8.10 also shows results from a simulation that assumes signalling at 500 Gbaud (giving a data rate per channel of more than 50 Mbit/s), optical filtering (which has to be increased to accommodate the higher signalling rate) of 6 nm and an optical launch power of 15 dBm. With the optical power increased still further, above about 25 dBm , both the coherent and the hybrid correlators provide essentially MAI-limited performance. Notice the 'soft limit' characteristic of CDMA in Figure 8.10, appearing as a slow rise in error probability as the number of simultaneous users increases so that, with the hybrid correlator and 15 dBm for example, 100 simultaneous users each operating at over 50 Mbits/s result in an error probability of about 10^{-9}, but even with more than 250 users the error probability is below 10^{-6}. The gradual increase in error probability with increasing numbers of users can be converted to a slower data

rate at constant error probability through the use of channel coding for error control [148, 149, 150, 151]. Such large numbers of simultaneous users are impossible with previously reported optical CDMA [93], because of optical beating.

8.4 Conclusion: the performance of a dark-signalling bus with CDMA

The modelling and simulation in this chapter has shown that the use of either a coherent or a hybrid correlator in a dark-signalling SLIM bus allows the MAI-limited performance of optical CDMA to be achieved even at very high signalling rates.

For example, a 500 Gbaud network with 500 uniquely addressable nodes can have an error probability of about 10^{-9} with 100 simultaneous users and an error probability of less than 10^{-6} with 250 simultaneous users, each operating at more than 50 Mbit/s.

Chapter 9

Conclusions

The research reported in this thesis investigated a novel design of optical fibre local area network: the SLIM (Single Light-source with In-Line modulation) bus. The network has an amplified bus topology and signalling is by means of dark pulses in an otherwise continuously bright fibre (dark signalling). Sharing of channel capacity through code division multiple access has been investigated in detail, and for signal correlation at the receivers a new type of tapped delay-line optical fibre correlator, the 'hybrid correlator', has been proposed, analysed and demonstrated. The hybrid correlator would be suitable not only for use with the network described in this thesis, but also for optical CDMA using conventional signalling as well as other applications requiring incoherent optical correlation.

9.1 Conclusion

The overall conclusion from the work reported in this thesis is that an optical fibre bus using the SLIM principle, dark signalling and optical CDMA with hybrid correlators is technically feasible and capable of supporting many simultaneous users on a network with large numbers of attached nodes. For example, a 500 GBaud SLIM network with 500 uniquely addressable nodes can have an error probability of about 10^{-9} with 100 simultaneous users, and an error probability of less than 10^{-6} with 250 simultaneous users, each operating at more than 50 Mbit/s. The bus topology and CDMA provides network flexibility similar to that of the original Ethernet standard, but at vastly greater data rates than are possible in an Ethernet bus.

The performance is possible because the SLIM principle combined with a hybrid correlator overcomes the main difficulty in realising the benefits of optical CDMA in a fibre LAN. This is the problem of optical beating, caused either by light from multiple optical sources or from a single source combined with an interferometer. The SLIM principle ensures there is only a single light source used in the network, and the hybrid correlator is a delay-line correlator which does not act as an interferometer. In addition, the SLIM principle simplifies the use of amplifiers in a fibre bus, eliminating problems

of excess build-up of ASE (amplified spontaneous emissions, from the amplifiers) or saturation due to multiple carriers.

The SLIM bus is able to deliver MAI (multiple access interference) limited performance of time-addressed incoherent optical CDMA, but this type of CDMA is inherently inefficient in terms of the exploitation of the signalling rate. Using the figures quoted above, the aggregate data rate on the 500 GBaud network is 250×50 Mbits/s for an error rate of 10^{-6}, giving an efficiency of 2.5%. When optical CDMA was first proposed this low efficiency was acceptable because the technology did not exist to exploit high signalling rates in fibre. Optical CDMA offered a practicable way of accessing some of the massive potential capacity of fibre, and it was reasoned that even if optical CDMA was inefficient, the capacity released would be greater than could be accessed though any other technology. Since the work of this thesis started, however, electronic and optoelectronic technology has developed so fast that this line of reasoning needs to be questioned. At the time of writing, for example, standards for 10 Gbit/s Ethernet are emerging which will be able to deliver fibre utilization close to the 12.5 Gbit/s of the 500 Gbaud SLIM network. The SLIM bus nevertheless offers advantages over 10G Ethernet because of the bus topology and the merits of CDMA, including no access delay, soft-limit on the number of users and physical-layer addressing.

9.2 Results and discussion

The results emerging from this work are summarised below.

9.2.1 Dark signalling compared with conventional signalling in an amplified fibre bus

Previous work has established that the bus topology for a local area network using optical fibre is only viable if the optical power level is maintained through the use of optical amplifiers, which could be either EDFAs (erbium doped fibre amplifiers) or SOAs (semiconductor optical amplifiers). A particularly elegant implementation is possible by using EDFAs in saturation, since the gain of the amplifiers would then automatically adjust to maintain the power level in the bus.

In the work undertaken for this thesis a model of the optical power levels in an amplified fibre bus has been developed and used to compare dark signalling with conventional signalling. Based on an implementation of the model in *Mathematica* (described in Chapter 4) a number of conclusions have been possible:

□ Dark signalling suppresses the build-up of ASE

There is a problem with excessive ASE (amplified spontaneous emissions) with conventional signalling that is overcome by dark signalling. Amplifiers upstream of

any active nodes are unsaturated when using conventional signalling, and therefore have high gain. This amplifies the ASE and significantly reduces the signal to noise ratio (Figure 4.8). When using dark signalling, there is an optical carrier present over the whole length of the bus, regardless of which nodes are active, and this keeps all amplifiers in saturation and suppresses the build-up of ASE (Figure 3.8).

- Dark signalling virtually eliminates near-far problems

With conventional signalling, unless there is control over the power level injected into the bus on a node-by-node basis, there will be wide variation in the power level of signals originating from different nodes (Figures 3.10 and 3.11). Since there is only a single optical carrier when dark-signalling is employed, the signal level is essentially independent of the originating node (Figure 3.12), which simplifies the receiver design and improves the performance of CDMA.

- Optical filtering in-line with the fibre bus can improve the signal to noise ratio when dark signalling is used, but degrades performance when conventional signalling is used

Narrowband optical filters in front of the receivers can be used to reduce the level of ASE and increase signal to noise ratio with both conventional and dark signalling. With dark signalling, optical filters placed in the path of the bus have a similar beneficial effect (Figure 3.17). With conventional signalling, by contrast, optical filters in-line with the fibre bus are counter-productive (Figure 3.16) since they drive the ASE into a narrower bandwidth around the signal carrier, which increases the amplitude of the optical beat noise (signal-noise beating) contained within the signal bandwidth on the electrical output of the receiver. The practical significance of this is that the benefits of optical filtering are only delivered to the conventional bus if there is a filter at every receiver. With the dark-signalling bus, filters in-line with the bus reduce ASE for all nodes further downstream.

- The modulators required for dark signalling should have low insertion loss but do not need to generate high extinction ratios

The modelling reported in Chapter 3 was also used to explore the sensitivity of dark-signalling buses to the parameters of various components on the bus. The loss per node (fibre, splice and connector losses, and the insertion loss of the modulator) are very significant, since higher losses require higher gain per amplifier or more amplifiers. High extinction ratio in the modulators was not found to be necessary, however, with diminishing returns on increasing the extinction ratio above about 10 dB (Figure 3.18).

- Large networks at high signalling rates are possible using a SLIM bus

To illustrate the possible network dimensions when using dark signalling, realistic assumptions where made about component parameters (Table 3.1) and the trade-off between number of nodes and signalling rate was investigated (Figure 3.19). For example, for an error probability of 10^{-9} in bus using saturated EDFAs, a network of 1000 nodes could operate at more than 1 Gbit/s.

□ A SLIM bus would need a large number of amplifiers

The SLIM approach to constructing an optical fibre amplified bus eliminates one of the sources of loss present in a conventional fibre bus – the taps used to add light to the bus at each node. However, the modulator itself introduces additional loss, and that, combined with the fibre, connector and splice losses, as well as the loss due to the taps extracting light for the receivers, means that amplifiers are still needed after every few nodes (Figure 3.14).

9.2.2 Optical fibre delay-line correlators

It has been shown that when using dark signalling in a fibre bus, optical CDMA can be used with delay-line correlators in essentially the same way as widely proposed for use with conventional signalling in passive optical star networks, with the difference that when using dark signalling correlation is identified by a dark pulse (nominally zero optical power) at the correlator output.

Three different designs of delay-line correlators for use with CDMA in a SLIM bus have been investigated: coherent, incoherent and the new proposal for a 'hybrid' correlator. The details of the design of the 'hybrid correlator' are described in Chapter 5 together with details of the noise characteristics (due to optical beating) of the three correlators.

□ Coupling the output from the delay-line taps of a single-mode fibre correlator into a multimode fibre rather than a single mode fibre creates a low-loss correlator: the 'hybrid correlator'.

It has been shown theoretically that it is possible to couple light from multiple single-mode input fibres to a single multi-mode output fibre with virtually no inherent loss. An experiment demonstrated a 4 to 1 coupler with an excess loss of 1.25 dB.

□ There is no optical beating between light in different taps of a hybrid coupler

The absence of beating between light in different taps of a hybrid coupler has been demonstrated experimentally, and contrasted between the beating that is readily observed in a fused fibre coupler, as used for both incoherent and coherent correlators.

The increase of noise as quantified by a Noise Figure has been determined theoretically and measured experimentally for the hybrid coupler and a fused fibre coupler.

- The 'hybrid' correlator offers performance similar to that of a coherent correlator with the simplicity of an incoherent correlator.

An incoherent correlator is seriously degraded by optical beating between light in different taps. There is no such beating in a coherent correlator (when used by a SLIM bus), but the coherent correlator is more difficult to build because it requires control of optical phase and polarisation in the correlators taps. The hybrid correlator does not require the phase control yet does not suffer from optical beating.

Slightly more ASE gets through the hybrid correlator than the coherent correlator, because in the hybrid correlator all light on all of the taps reaches the photodiode (neglecting excess loss). In a coherent correlator, the ASE combines incoherently so that it suffers a loss of $10\log(1/k)$ dB, where k is the number of taps. In the simulations performed in Chapter 8, this did not result in a significant degradation of performance for the hybrid correlator compared to the coherent correlator.

- When coupling from multiple input fibres to a single output fibre of higher V-number, mode conservation provides a bound on the number of input fibres. Lenses can be used to make the coupling easier in practice, but cannot overcome mode conservation.

Algebraic models have been used to model the coupling of light between dissimilar fibres, with and without lenses. The coupling efficiency has been predicted, and the focal lengths and dimensions of collimating and focussing lenses needed for the coupling have been calculated.

The special case of coupling from multiple single mode fibres to a multi mode fibre has been analysed in detail, and the efficient coupling from four input fibres to a single output fibre has been demonstrated experimentally.

9.2.3 Optical CDMA in a SLIM bus

Chapter 8 describes a model that was developed and implemented in *Mathematica* to determine the probability of error in a SLIM bus using optical CDMA. From the work described in Chapter 8 the following conclusion may be drawn.

- The SLIM principle overcomes some of the practical limitation of using optical CDMA in a passive star

1. The presence of multiple optical carriers on a passive optical fibre star network leads to problems of optical beating when using CDMA. This is eliminated in the SLIM bus because of the presence of only a single optical carrier used by all nodes.

2. The virtual absence of a near-far effect removes one of the major sources of degradation usually encountered with CDMA.

- A SLIM bus using optical CDMA can deliver MAI (multiple-access interference) limited performance

The ideal performance of optical CDMA envisaged by its original proponents is not, in practice, achievable in simple passive star networks with incoherent correlation. The problem is that the signal to noise ratio is dominated by optical beating rather than MAI.

The modelling undertaken for this thesis has demonstrated that because of the absence of multiple carriers in the SLIM bus, a SLIM bus using optical CDMA can approach the limits of MAI with useful data rates when coherent or hybrid correlators are used.

For example it has been shown that with optical orthogonal codes, networks operating at a 500 Gbaud SLIM network with 500 uniquely addressable nodes can have an error probability of about 10^{-9} with 100 simultaneous users, and an error probability of less than 10^{-6} with 250 simultaneous users, each operating at more than 50 Mbit/s.

- CDMA with sparse optical orthogonal codes cannot utilise more than a few percent of the capacity of the fibre

Even when MAI-limited, optical CDMA using optical orthogonal codes can, typically, only access of the order of 2-10% of the channel capacity (in terms of aggregate data rate/channel signalling rate). This low efficiency was acceptable when optical CDMA was first proposed since the potential capacity of optical fibre was seen as so vast that a mechanism of accessing even a small percentage of the capacity was worthwhile, and trading efficiency for the advantages of CDMA was acceptable.

Since then, however, the methods of exploiting the potential of optical fibre – especially through wavelength division techniques – have improved, and at the same time the demand for bandwidth has increased dramatically, so that very low efficiency in the use fibre capacity is not as acceptable as it was previously.

Further work is needed to explore more efficient optical CDMA schemes appropriate for dark signalling.

9.2.4 Modelling with *Mathematica*

Most of the modelling and simulation was done in *Mathematica*. In some cases it was used largely for algebraic manipulation while in other cases for programmed simulations.

Mathematica was very effective for the algebraic manipulation. For example, the mode field distribution of multimode fibre and parameters of the fields for the corresponding Gaussian approximations (Chapter 6) were concisely and elegantly derived, and the generation of density plots of the fields was straightforward. *Mathematica* was also effective for derivation of the overlap integrals. In particular, it was possible

to evaluate the overlap integrals algebraically, keeping the phase of each optical input as a variable. This step, however, involved 'hands-on' intervention to simplify the integrand using 'craft knowledge' of specific features of *Mathematica*. Simplifying complex formulae, for example, sometimes requires *Mathematica* to be told explicitly both that a variable is real *and* that its imaginary component is zero.

The bus simulations of Chapter 4 involved relatively simple formulae which were then used in programmed simulations. *Mathematica* code does not run fast, so some of the simulations took a long time to run and arguably Mathematica was not the optimum tool in this case. In practice, though, since there was a fairly small number of simulations required, it was adequate and there was no necessity to transfer to a different package. Had it been necessary, however, one option would have been to continue to use *Mathematica*, but to implement the repeating loops in external *c* code which could be called from within *Mathematica*.

Possibly the simulations which most fully exploited the power of *Mathematica* were those of optical CDMA in a SLIM bus in Chapter 8. It was possible to implement the algebraic models derived in the text of Chapter 8 in *Mathematica* using a functional programming style, then to explore the models by varying one parameter at a time. A standard *Mathematica* package of combinatoric functions provided the starting point for the functions used to account for multiple access interference (MAI).

9.3 Recommendations for further work

Specific topics for further work have been identified throughout the text, but if the network proposed in this thesis were to be progressed, the focus of development should be the practical implementation of the modulator, correlator and amplifier. It is possible to envisage a single integrated electro-optical device that combines the three functions and would be inserted into the path of the fibre bus where a node is added.

Whether or not the SLIM bus with time-addressed incoherent optical CDMA finds application in the form described here, techniques developed in this work have opened up promising lines for further research. The low efficiency of the network is due to the use of the optical fibre as a logical OR channel with incoherent CDMA, but the SLIM principle can be used with different multiple access schemes and/or different modulators, potentially delivering the merits of the SLIM bus at higher channel utilisation. Also since the SLIM bus uses only one wavelength and there are possibilities (explored in reference [59]) of extending the bus through wavelength division techniques. The hybrid correlator has been investigated for use with optical CDMA, but fibre delay-line filters have been proposed for general signal processing applications and the role of the hybrid correlator could be explored in this wider context.

Bibliography

[1] P. Karioja, S. Tammela, A Tervonen, and S. Honkanen. Passive fiber optic bus using bidirectional integrated-optic bus access couplers. *Optical Engineering*, 34(9):2551–2559, 1995.

[2] D. Cotter, J. K. Lucek, and D. D. Marcenac. Ultra-high-bit-rate networking: from the transcontinental backbone to the desktop. *IEEE Communications Magazine*, 35(4):90–95, April 1997.

[3] P. R. Prucnal, M. A. Santoro, and T. R. Fan. Spread-spectrum fibre optic local area network using optical processing. In *FOC/LAN*, 1986.

[4] K. Kawano, H. Miyazawa, and O Mitomi. New calculations for coupling laser diodes to multimode fiber. *Journal of Lightwave Technology*, 4(3):368–374, March 1986.

[5] A. W. Snyder and J. D. Love. *Optical Waveguide Theory*. Chapman and Hall, 1983.

[6] J. D. Love and C. D. Hussey. Variational approximations for higher-order modes of weakly-guiding fibers. *Optical and Quantum Electronics*, 16:41–48, 1984.

[7] M.E. Marhic. Coherent optical CDMA networks. *Journal of Lightwave Technology*, 11(5-6):854–864, May-June 1993.

[8] C. E. Spurgeon. *Ethernet: The Definitive Guide*. O'Reilly and Associates, 2000.

[9] IEEE. Carrier sense multiple access with collision detection (CSMA/CD) access method and physical layer specifications, 2002.

[10] 10 Gigabit Ethernet Alliance. 10 Gigabit Ethernet. www.10gea.org, 2002.

[11] G. Einon, N. Moss, and D. Reed. *Local Area Networks*. T305 Digital Communications. The Open University, 1999. Block 6, Part 1 of T305.

[12] D. Reed and A. Rawlings. *Networks*. T821 Digital Telecommunication Systems. The Open University, 1996. Block 5 of T821.

[13] D. A. Chapman and D. A. Gorham. Passive signalling in optical fibre multiple access networks. In *Digest of the IEE colloquium on Optical Multiple Access Networks*, March 1991.

[14] P. E. Green, Jr. *Fiber-Optic Communication Networks*. Prentice Hall, 1993.

[15] R. Ramaswami and K. N. Sivarajan. *Optical Networks: A Practical Perspective*. The Morgan Kaufmann Series in Networking. Morgan Kaufmann Publishers Inc., San Fancisco, 2nd edition, 2002.

[16] R. L. Cruz, G. R. Hill, A. L. Kellner, R. Ramaswami, G. H. Sasaki, and Y. Yamabayashi (Guest editors). Special issue on optical networks. *IEEE Journal on Selected Areas in Communications:*, 14(5):761–1056, June 1996.

[17] G.-K. Chang, K.-I. Sata, and D. K. Hunter (Guest Editors). Special issue on optical networks. *Journal of Lightwave Technology*, 18(12):1603–2122, December 2000. Issued late, dated March 2001.

[18] H. Kogelnik. High-capacity optical communications: Personal recollections. *IEEE Journal on Selected Topics in Quantum Electronics*, 6(6):1279–1285, November/December 2000.

[19] S. B. Alleston, P. Harper, I. S. Penketh, I. Bennion, N. J. Doran, and A. D. Ellis. 1000 km transmission of 40 Gbit/s single channel RZ data over dispersion managed standard (non-dispesion shifted) fibre. *Electronics Letters*, 35(10):823–824, May 1999.

[20] M. Agapie. WorldCom places 3.2 Terabits of traffic per second on existing network fibre. 'Letter to the Editor', IEEE Communications Magazine, Vol. 39, No. 8, p12, August 2001.

[21] K. Kear and N. Moss. *Communication Networks*. T305 Digital Communications. The Open University, 1999. Block 1, Part 1 of T305.

[22] J. P. Ryan. WDM: North American deployment trends. *IEEE Communications Magazine*, 36(2):40–45, February 1998.

[23] E. Lowe. Current European WDM deployment trends. *IEEE Communications Magazine*, 36(2):46–51, February 1998.

[24] T. Tsuritani, A. Agata, I. Morita, and N. Edagawa. 21.4 Gbit/S x 56 WDM 9170 km transmission using symmetrically dispersion-managed fibre span. *Electronics Letters*, 37(25):1536–1538, December 2001.

[25] E. Yamada, H. Takara, T. Ohara, K. Sato, K. Jinguji, Y. Inoue, T. Shibata, and T. Morioka. 106 channel x 10 Gbit/S, 640 km DWDM transmission with

25 GHz spacing with supercontinuum multi-carrier source. *Electronics Letters*, 37(25):1534–1536, December 2001.

[26] P. Green. Progress in optical networking. *IEEE Communications Magazine*, 39(1):54–61, January 2001.

[27] A. Neukermans and R. Ramaswami. MEMS technology for optical networking applications. *IEEE Communications Magazine*, 39(1):62–69, January 2001.

[28] S. Dixit and Y. Ye. Streamlining the internet-fiber connection. *IEEE Communications Magazine*, 38(4):52–57, April 2001.

[29] J. Gruber and R. Ramaswami. Moving toward all-optical networks. *Lightwave*, 17(13):60–68, December 2000.

[30] A. Ghanwani, B. Jamoussi, D. Fedyk, P. Ashwood-Smith, and N. Feldman. Traffic engineering standards in IP networks using MPLS. *IEEE Communications Magazine*, 37(12):49–53, December 1999.

[31] D. Awduche and Y. Rekhter. Multiprotocol lambda switching: Combining MPLS traffic engineerng control with optical crossconnects. *IEEE Communications Magazine*, 39(3):111–116, March 2001.

[32] M. J. O'Mahony, D. Simeonidou, D. K. Hunter, and A. Tzanakaki. The application of optical packet switching in future communication networks. *IEEE Communications Magazine*, 39(3):128–135, March 2001.

[33] D.J. Blementhal, T. Ikegami, P.R. Prucnal, and L. Thylen (Guest Editors). Special issue on photonic packet switching technologies, techniques, and systems. *IEEE Journal of Lightwave Technology*, 16(12):2065–2327, December 1998.

[34] S. Yao, B. Mukherjee, and S. Dixit. Advances in photonic packet switching: An overview. *IEEE Communications Magazine*, 38(2):84–94, February 2000.

[35] D. K. Hunter and I. Andonovic. Approaches to optical internet packet switching. *IEEE Communications Magazine*, 38(9):116–122, September 2000.

[36] P. E. Green. Misunderstood issues in lightwave networking. In *Conference Digest of the LEOS 1992 Summer Topical Meeting on Optical Multiple Access Networks*, pages 47–48. IEEE LEOS, IEEE, August 1992.

[37] J. M. Senior, J. M. McVeigh, and S. D. Cusworth. Multichannel slot reservation protocol for use on WDM optical fibre LAN. *Electronics Letters*, 27(20):1875–1877, September 1991.

[38] R. Ramaswami and K. Lui. Analysis of effective power budget in optical bus and star networks using erbium-doped fiber amplifiers. *Journal of Lightwave Technology*, 11(11):1863–1871, November 1993.

[39] N. Kashima. *Passive Optical Components for Optical Fiber Transmission*. Artech House, 1995.

[40] D. B. Mortimore. Low-loss 8×8 single-mode star coupler. *Electronics Letters*, 21(11):502–504, May 1985.

[41] L. P. Barry, P. Guignard, J. Debeau, R. Boittin, and M. Bernard. A high-speed optical star network using TDMA and all-optical demultiplexing techniques. *IEEE Journal on Selected Areas in Communications*, 14(5):1030–1038, June 1996.

[42] Z. Cao, J. Guo, L. Li, and P. Ye. Bidirectional active bus and its applications in fiber networks. *Journal of Optical Communications*, 17(3):106–108, August 1996.

[43] C. W. Barnard, J. Chrostowski, and M. Kavehrad. Bidirectional fiber amplifiers. *Photonics Technology Letters*, 4(8):911–913, August 1992.

[44] Ivan P. Kaminov. Photonic local networks. In S. E. Miller and I. P. Kaminov, editors, *Optical Fiber Telecommunications II*, chapter 26, pages 933–972. Academic Press, Inc., 24-28 Oval Road, London NW1 7DX, 1988.

[45] H Hodara and E Miles. High-speed local area networks. *Fiber and Integrated Optics*, 11(3):253–276, July-September 1992.

[46] K. W. Cheung. Design and implementation considerations for wavelength-division multiplexed (WDM) photonic dual bus. In *Proceedings of IEEE SUPERCOMM/ICC'92*, pages 848–854. IEEE, IEEE, May 1992.

[47] Nen-Fu Huang and Shiann-Tsong Sheu. DTCAP – a distributed tunable-channel access protocol for multi-channel photonic dual bus networks. In *INFOCOM '95. Fourteenth Annual Joint Conference of the IEEE Computer and Communications Societies. 'Bringing Information to People', Proceeding.*, pages 908–915 vol.2. IEEE, 1995.

[48] Chin-Chou Chen, Lon A. Wang, and Sy-Yen Kuo. A wavelength encoded multichannel optical bus for local area networks. *Journal of Lightwave Technology*, 14(3):315–323, March 1996.

[49] E. Goldstein. Optical ring networks with distributed amplification. *IEEE Photonics Technology Letters*, 3(4):390–393, April 1991.

[50] M. J. Karol. Exploiting the attenuation of fiber-opic passive taps to create large high-capacity LANs and MANs. *Journal of Lightwave Technology*, 9(3):400–408, March 1991.

[51] M. A. Santoro and M. J. Karol. Experimental and theoretical performance of ring shaped passive-bus optical networks. *IEEE Photonics Technology Letters*, 3(5):490–492, May 1991.

[52] A. S. Tannenbaum. *Computer Networks*. Prentice-Hall, 2nd edition, 1989.

[53] S. S. Wagner. Optical amplifier applications in fiber optic local networks. *IEEE Transactions on Communication*, 35(4):419–426, April 1987.

[54] D. A. Chapman. Erbium-doped fibre amplifiers: the latest revolution in optical communications. *Electronics and Communications Engineering Journal*, 6(2):59–67, April 1994.

[55] K. Lui and R. Ramaswami. Analysis of optical bus networks using doped fiber amplifiers. In *Summer Topical Meeting on Optical Multiple Access Networks, Conference Digest Paper OMTh12*. IEEE, July 1990.

[56] K. T. Koai and R. Olshansky. Nonregenerative photonic dual bus with optical amplifiers. *IEEE Photonics Technology Letters*, 5(4):482–485, April 1993.

[57] R. A. Barry and 14 others. All-optical network consortium–ultrafast TDM networks. *Journal on Selected Areas in Communications*, 14(5):999–1013, June 1996.

[58] K. L. Hall. Progress in high-speed TDMA communications. In *Proceedings of the IEEE Lasers and Electro-Optics Society 12th Annual Meeting, Volume*, volume 2, pages 535–536. IEEE, IEEE, 1999.

[59] D. A. Chapman. Extending the SLIM bus with wavelength division multiplexing. Department of Telematics, Report No.12., October 2002. The Open University, Milton Keynes MK7 6AA, UK.

[60] T. E. Darcie. Subcarrier multiplexing for multiple access lightwave networks. *Journal of Lightwave Technology*, 5(8):1103–1110, August 1987.

[61] W. Domon, Shibutani M., and Emura K. SCM optical multiple access network with cascaded optical modulators. *IEEE Photonics Technology Letters*, 5(9):1107–1108, September 1993.

[62] L. J. Cimini. Optical phase division multiplexing for local communications applications. *IEEE Transactions on Communications*, 37(12):1282–1292, December 1989.

[63] K. Kiasaleh. Performance of packet-switched fiber optic frequency hopping multiple access networks. *IEEE Transactions on Communications*, 43(7), July 1995.

[64] N. Karafolas and D. Uttamchandani. Optical fiber code division multiple access networks: a review. *Optical Fiber Technology*, 2:149–168, 1996. A comprehensive review with useful classification. 160 references, but note that from number 75 onwards all the references are offset by one.

[65] L.T. Blair and S.A. Cassidy. Impact of new optical technology on spectrally sliced access and data networks. *BT Technology Journal*, 11(2):46–55, 1993.

[66] J. L. Brooks, R. H. Wentworth, M. Tur R. C. Youngquis and, B. Y. Kim, and H. J. Shaw. Coherence multiplexing of fiber optic interferometric sensors. *IEEE Journal of Lightwave Technology*, 3(5):1062–1072, May 1985.

[67] G. C. Gupta, P. J. Legg, D. Uttamchandani, and I. Andonovic. Capacity bounding of coherence multiplexed local area networks due to interferometoric noise. *IEE Proceedings, Optoelectronics*, 144(2):69–74, April 1997.

[68] G. J. Pendock and D. D. Sampson. Capacity of coherence-multiplexed CDMA networks. *Optics Communications*, 143(1-3):109–117, November 1997.

[69] R. H. Wentworth. Theoretical noise performance of coherence-multiplexed interferometric sensors. *IEEE Journal of Lightwave Technology*, 7(6):941–956, June 1989.

[70] B. Wacogne and D. A. Jackson. Security vulnerability in coherence modulation comunication systems. *IEEE Photonics Technology Letters*, 8(3):470–472, March 1996.

[71] S. Benedetto, R. Gaudino, and P. Poggiolini. Direct detection of optical digital transmission based on polarisation shift keying modulation. *J. SEL*, 13(3):531–542, April 1995.

[72] S. Betti, G. De Marchis, E. Iannone, M. Marcelli, and F. Matera. Optical code division multiple access techniques based on polarisation modulated coherent systems. *Journal of Optical Communications*, 14(5):183–188, 1993.

[73] K. Iversen and D. Junghanns. On the combination of optical CDMA and POLSK. *Journal of Optical Communications*, 16(4):126–130, August 1995.

[74] M.C. Cardakli, S. Lee, A.E. Willner, V. Grubsky, D. Starodubov, and J. Feinberg. Reconfigurable optical packet header recognition and routing using time-to-wavelength mapping and tunable fiber bragg gratings for correlation decoding. *Photonics Technology Letters*, 12(5):552–554, May 2000.

[75] M. S. Borella and B. Mukherjee. Efficient scheduling of nonuniform packet traffic in a WDM/TDM local lightwave network with arbitrary transceiver tuning

latencies. *IEEE Journal on Selected Areas in Communications*, 14(5):923–934, June 1996.

[76] E. Hall, J. Kravitz, R. Ramaswami, M. Halvorson, S. Tenbrink, and R. Thomsen. The Rainbow-II gigabit optical network. *Journal on Selected Areas in Communications*, 14(5):814–823, June 1996.

[77] H. Kobrinski, R. M. Bulley, M. S. Goodman, M. P. Vecchi, C. A. Brackett, Curtis L., and J. L. Gimlett. Demonstration of high capacity in the LAMBDANET architecture: A multiwavelength optical network. *Electronics Letters*, 23(16):824–826, July 1987.

[78] T-K. Chiang, S. K. Agrawal, D. T. Mayweather, D. Sadot, C. F. Barry, M. Hickey, and L. G. Kazovsky. Implementation of STARNET: A WDM computer communications network. *IEEE Journal on Selected Areas in Communications*, 14(5):824–839, June 1996.

[79] I. P. Kaminov and 19 others. A wideband all-optical WDM network. *Journal on Selected Areas in Communications*, 14(5):780–799, June 1996.

[80] B. Mukherjee. WDM-based local lightwave networks. part I: Single-hop systems. *IEEE Network*, 6:12–27, May 1992.

[81] V. W. S. Chan, K. L. Hall, E. Modiano, and K. A. Rauschenbach. Architectures and technologies for high-speed optical data networks. *IEEE Journal of Lightwave Technology*, 16(12):2146–2168, December 1998.

[82] M. Lopez-Amo, L. T. Blair, and Urquhart P. Wavelength-division-multiplexed distributed optical fiber amplifier bus network for data and sensors. *Optics Letters*, 18(14):1159–1161, July 1993.

[83] C. K. Chan, L. K. Chen, and K. W. Cheung. A fast channel-tunable optical transmitter for ultrahigh-speed all-optical time-division multiaccess networks. *IEEE Journal on Selected Areas in Communications*, 14(5):1052–1056, June 1996.

[84] R. Pickholtz, D. Schilling, and L. Milstein. Theory of spread-spectrum communications – a tutorial. *IEEE Transactions on Communications*, 30(5):855–867, May 1982.

[85] L. G. Kazovsky, T. Fong, and T. Hofmeister. Optical local area network technologies. *IEEE communications magazine*, 32(12):50–54, December 1994.

[86] W. C. Kwong and P. R. Prucnal. 'synchronous' CDMA demonstration for fibre-optic networks with optical processing. *Electronic Letters*, 26(24):1990–1992, November 1990.

[87] W. C. Kwong, P. A. Perrier, and P. R. Prucnal. Performance companion of asynchronous and synchronous code-division multiple access technique for fiber-optic local area networks. *IEEE Transactions on Communications*, 39(11):1625–34, November 1991.

[88] Z. Kostic, E. Titlebaum, and S. V. Maric. The design of new optical codes and time-hopping patterns for synchronous spread-spectrum code division multiple access communication systems. In *International conference on communications*, pages 585–589, June 23-26 1991.

[89] A. Rawlings. *Networks*, volume 10 of *T322: Digital Telecommunications*. The Open University, 1989.

[90] R. Jones, C. C. Bissell, and D. J. Reed. *Communication Architectures*. T822 Multi-Service Networks: Structures. The Open University, 2002. Block 2 of T822.

[91] K. Iversen and D. Hampicke. Comparison and classification of all-optical CDMA systems for future telecommunication networks. In *All-Optical Communication Systems: Architecture, Control and Network Issues. SPIE proceedings 2614*, pages 110–121. SPIE, SPIE, October 1995.

[92] M. J. Parham, C. Smythe, and B. L. Weiss. Code-division multiple-access techniques for use in optical fibre local area networks. *Electronics and Communications Engineering Journal*, 4(4):203–212, August 1992.

[93] D. D. Sampson, G. J. Pendock, and R. A. Griffin. Photonic code-division multiple-access communications. *Fibre and Integrated Optics*, 16(2):129–157, 1997.

[94] J. A. Salehi. Emerging optical code division multiple access communication systems. *IEEE Network*, 3(2):31–39, March 1989.

[95] M. A. Santoro and P. R. Prucnal. Asynchronous fiber optic local area network using CDMA and optical processing. *IEEE Proceedings*, 75(9):1336–1338, September 1987.

[96] R. Gold. Optimal binary sequences for spread spectrum multiplexing. *IEEE Transactions on Information Theory*, pages 619–621, October 1967.

[97] D. A. Chapman. *Channel Coding*. T305 Digital Communications. The Open University, 1999. Block 5, Part 1 of T305.

[98] F. R. K. Chung, J. A. Salehi, and V. K. Wei. Optical orthogonal codes: Design, analysis and applications. *IEEE Transactions on Information Theory*, 35(3):595–604, May 1989.

[99] Y. L. Chang and M. E. Marhic. 2^n codes for optical CDMA and associated networks. In *Conference Digest, LEOS Summer Topical on Optical Multiple Access Networks*, pages 49–50, July 25-27 1990.

[100] A. S. Holmes and R. R. A Syms. All-optical CDMA using quasi-prime codes. *Journal of Lightwave Technology*, 1995.

[101] M. E. Marhic and Y. L. Chang. Pulse coding and coherent decoding in fibre-optic ladder networks. *Electronic Letters*, 25(22):1538–1546, October 1989.

[102] Guu-Chang Yang and W. C. Kwong. On the construction of 2^n codes for optical code-division multiple-access. *IEEE Trans. Commun*, 43(2–4):495–502, February-April 1995.

[103] W.C. Kwong, G.C. Yang, and J.G. Zhang. 2^n prime sequence codes and their optical CDMA coding architecture. In *Proceedings of the IEEE International Conference on Communications.*, volume 3, pages 1317–1321. IEEE, IEEE, 1995.

[104] L. Tančevski and I. Andonovic. Block multiplexing codes for incoherent asynchronous all-optical CDMA using ladder network correlators. *IEE Proceedings-Optoelectronics*, 142(3):125–131, June 1995.

[105] A. A. Shaar and P. A. Davies. Prime sequences: Quasi-optimal sequences for OR channel code division multiplexing. *Electronics Letters*, 19(21):888–890, October 1983.

[106] L. Tančevski, L. Bazgaloski, I. Andonovic, and J. Budin. Incoherent asynchronous optical CDMA using gold codes. *Electronics Letters*, 30(9):721–723, April 1994.

[107] T. O'Farrell and S. Lochmann. Performance analysis of an optical correlator receiver for SIK DS-CDMA communication systems. *Electronics Letters*, 30(1):63–65, January 1994.

[108] D. Zaccarin and M. Kavehrad. New architecture for incoherent optical CDMA to achieve bipolar capacity. *Electronics Letters*, 30(3):258–259, February 1994.

[109] L. Nguyen, B. Aazhang, and J. F. Young. All-optical CDMA with bipolar codes. *Electronics Letters*, 31(6):469–470, March 1995.

[110] S. C. Chang and J. K. Wolf. On the T-users M-frequency noiseless multiple access channel with and without intensity information. *IEEE Transactions on Information Theory*, 27(1):41–48, 1981.

[111] P. A. Davies and A. A. Shaar. Asynchronous multiplexing for optical-fibre local-area network. *Electronics Letters*, 19(10):390–392, May 1983.

[112] F. Khansefid, R. Gagliardi, and H. Taylor. Performance analysis of code division multiple access techniques in fibre optics with on-off and ppm pulsed signalling. In *Milcom 90: A new era. 1990 IEEE Military Communications Conference*, pages 909–915, September 30 - October 3 1990.

[113] H. M. H. Shalaby. A performance analysis of optical overlapping PPM-CDMA communication systems. *Journal of Lightwave Technology*, 17(3):426–433, March 1999.

[114] J. M. H. Elmirghani and R. A. Cryan. New PPM-CDMA hybrid for indoor diffuse infrared channels. *Electronics Letters*, 30(20):1646–1647, September 1994.

[115] H. H. Chan, J. M. H. Elmirghani, and R. A. Cryan. Optical wireless PPM CDMA networks employing OC and PC signature codes. *Journal of Optical Communications*, 20(3):92–97, June 1999.

[116] H. M. H. Shalaby. Performance analysis of optical synchronous CDMA communication systems with PPM signaling. *IEEE Transactions on Communications*, 43(2-4):624–634, February-April 1995.

[117] J. M. H. Elmirghani, H. H. Chan, and R. A. Cryan. Sensitivity evaluation of optical wireless PPM systems utilising PIN-BJT receivers. *IEE Proceedings, Part J.*, 143(6):355–359, 1996.

[118] J. M. H. Elmirghani and R. A. Cryan. Hybrid PPM CDMA systems utilizing optical orthogonal codes for indoor wireless infrared communication. *Microwave and Optical Technology Letters*, 8(1):44–47, January 1995.

[119] Y. L. Chang and M. E. Marhic. Fiber-optic ladder networks for inverse decoding coherent CDMA. *IEEE Journal of Lightwave Technology*, 10(12):1952–1962, December 1992.

[120] R.A. Griffin, D.D. Sampson, and D.A. Jackson. Demonstration of data transmission using coherent correlation to reconstruct a coded pulse sequence. *IEEE Photonics Technology Letters*, 4(5):513–515, May 1992.

[121] R. A. Griffin. *Coherent Optical Matched Filtering for Application in Photonic Code-Division Multiple Access Networks*. PhD thesis, Department of Physics, University of Kent, 1994.

[122] J. A. Salehi, A. W. Weiner, and J. P. Heritage. Coherent ultrashort light pulse code-division multiple access communication systems. *Journal of Lightwave Technology*, 8(3), March 1990.

[123] C. C. Chang, H. P. Sardesai, and A. M. Weiner. Code-division multiple-access encoding and decoding of femtosecond optical pulses over 2.5 km fiber link. *PTL*, 10(1):171–173, January 1998.

[124] M. Kavehrad and D. Zaccarin. Optical code division multiplexed systems based on spectral encoding of noncoherent sources. *Journal of Lightwave Technology*, 13(3):534–545, March 1995.

[125] E.D.J. Smith, P.T. Gough, and D.P. Taylor. Noise limits of optical spectral encoding CDMA systems. *Electronics Letters*, 31(17):1469–1470, August 1995.

[126] R. A. Griffin, D. D. Sampson, and D. A. Jackson. Modification of optical coherence using spectral phase coding for use in photonic code-division multiple access systems. *Electronics Letters*, 29(25):2214–2216, December 1993.

[127] L Tan□evski, I Andonovic, M. Tur, and J. Budin. Hybrid wavelength hopping time spreading code division multiple access systems. *IEE Proceedings-Optoelectronics*, 143(3):161–166, 1996.

[128] L. Tan□evski, I. Andonovic, and J. Budin. Secure optical network architectures utilizing wavelength hopping time spreading codes. *IEEE Photonics Technology Letters*, 7(5):573–575, 1995.

[129] H. Fathallah, L. A. Rusch, and S. LaRochelle. Passive optical fast frequency-hop CDMA communication system. *Journal of Lightwave Technology*, 17(3):397–405, March 1999.

[130] K. Kiasaleh. Fiber optic frequency hopping multiple access communication systems. *IEEE Photonics Technology Letters*, 3(2):173, 1991.

[131] D. A. Chapman. *Modulation*. T305 Digital Communications. The Open University, 1999. Block 5, Part 2 of T305.

[132] G. J. Foschini and G. Vannucci. Using spread spectrum in a high capacity fiber optic local network. *Journal of Lightwave Technology*, 6(3):370–379, 1988.

[133] S. Benedetto and G. Olmo. Performance evaluation of coherent optical code division multiple access. *Electronic Letters*, 27(22):2000–2002, October 1991.

[134] N. Karafolas and D. Uttamchandani. Self homodyne code division multiple access technique for fiber optic local area networks. *IEEE Photonics Technology Letters*, 6(7):880–883, 1994.

[135] N. Karafolas and D. Uttamchandani. Fiber optic spread spectrum system based on PSK spreading and self homodyne despreading of the optical spectrum. *Optics Communications*, 111:238–244, April 1994.

[136] N. Karafolas and D. Uttamchandani. Erratum: Fiber optic spread spectrum system based on PSK spreading and self homodyne despreading of the optical spectrum. *Optics Communications*, 112:350, 1994.

[137] D. Zaccarin and M. Kavehrad. Performance evaluation of optical CDMA systems using non coherent detection and bipolar codes. *Journal of Lightwave Technology*, 12(1):96–105, January 1994.

[138] N. Karafolas and D. Uttamchandani. Optical CDMA system using bipolar codes and based on narrow passband optical filtering and direct detection. *IEEE Photonics Technology Letters*, 7(9):1072–1074, September 1995.

[139] N. A. Ismail. Comparison of sequences for local area networks using spread spectrum multiple access. *Proceedings of the IEEE*, 76(1):87–88, January 1988.

[140] J. A. Salehi. Code division multiple access techniques in optical fiber networks (Part 1). *IEEE Trans Commun*, 37(8):824–833, August 1989.

[141] A. A. Shaar and P. A. Davies. Erratum. *Electronics Letters*, 19(24):1057, November 1983.

[142] G-C. Yang and W. C. Kwong. *Prime Codes with Applications to CDMA Optical and Wireless Networks*. Number 7 in Artech House Mobile Communications Series. Artech House, March 2002.

[143] G.C. Yang and T.E. Fuja. Optical orthogonal codes with unequal auto and cross correlation constraints. *IEEE Transactions on Information Theory*, 41(1):96–106, January 1995.

[144] S. M. Johnson. A new upper bound for error-correcting codes. *IRE Transactions on Information Theory*, 8, April 1962.

[145] F. R. K. Chung, J. A. Salehi, and V. K. Wei. Correction to "optical orthogonal codes: Design, analysis and applications". *IEEE Transactions on Information Theory*, 38(4):1429, July 1992.

[146] S. V. Marić. New family of algebraically designed optical orthogonal codes for use in CDMA fibre-optic networks. *Electronics Letters*, 29(6):538–539, March 1993.

[147] R. Petrovic and S. Holmes. Orthogonal codes for CDMA optical fibre LANs with varable bit interval. *Electronic Letters*, 26(10):662–663, May 1990.

[148] M.R. Dale and R.M. Gagliardi. Channel coding for asynchronous fiberoptic CDMA communications. *IEEE Transactions on Communications*, 43(9):2485–2492, 1995.

[149] J. H. Wu, J. Wu, and C. N. Tsai. Synchoronous fiber-optical code divison multiple access network with error control coding. *Electronic Letters*, 28(23):2118–2120, November 1992.

[150] J. G. Zhang and G. Picchi. Forward error-correction codes in incoherent optical fibre CDMA networks. *Electronics Letters*, 29(16):1460–1462, August 1993.

[151] J.G. Zhang. Improvement in bandwidth efficiency of asynchronous prime code CDMA networks by error correction coding. *Electronics Letters*, 30(6):514–515, March 1994.

[152] Z. Kostic and E. L. Titlebaum. The design and performance analysis for several new classes of codes for optical synchronous CDMA and for arbitrary-medium time-hopping synchronous CDMA communication systems. *IEEE Transactions on Communications*, 42(8):2608–2617, August 1994.

[153] P. R. Prucnal, M. A. Santoro, and S. K. Sehgal. Ultrafast all-optical synchronous multiple access fiber networks. *IEEE Journal on Selected Areas in Communications*, 4(9):1484–1493, December 1986.

[154] I. Vajda. Comments on code-division multiple access techniques in optical fibre networks – part II: Systems performance analysis. *IEEE Transactions on Communications*, 39(2):196, February 1991.

[155] R. Petrovic. Synchronous CDMA technique for fiber-optic lans with folded dual bus topology. In *Proceedings Southeastcon '92 Volume 1*, pages 006–009. IEEE, April 12-15 1992.

[156] J. A. Salehi and C. A. Brackett. Code division multiple access techniques in optical fiber networks (Part 2). *IEEE Transactions on Communications*, 37(8):824–842, August 1989.

[157] T. Ohtsuki. Performance analysis of direct-detection optical asynchronous CDMA systems with double optical hard limiters. *Journal of Lightwave Technology*, 15(3), March 1997.

[158] T. Ohtsuki, K. Sato, I. Sasase, and S. Mori. Direct-detection optical synchronous CDMA systems with double optical hard limiters using modified prime sequence codes. *IEEE Journal on Selected Areas in Communications*, 14(9):1879–1887, December 1996.

[159] H. M. H. Shalaby. Direct detection optical overlapping PPM-CDMA communication systems with double optical hard limiters. *Journal of Lightwave Technology*, 17(7):1158–1165, July 1999.

[160] C. C. Bissell and D. A. Chapman. *Digital Signal Transmission*. Cambridge University Press, 1992.

[161] R. Loudon. *The Quantum Theory of Light*. Oxford University Press, 2nd edition, 1983.

[162] C. Desem. Optical interference in lightwave subcarrier multiplexing systems employing multiple optical carriers. *Electronics Letters*, 24(1):50–51, January 1988.

[163] Q. Jiang and M. Kavehrad. An optical multiaccess star network using subcarrier multiplexing. *IEEE Photonics Technology Letters*, 4(10):1163–1165, October 1992.

[164] R. H. Wentworth. *Optical Noise in Interferometric Systems Containing Strongly Unbalanced Paths*. PhD thesis, Applied Physics, Stanford University, December 1988.

[165] L. Kazovsky, S. Benedetto, and A. Willner. *Optical Fiber Communication Systems*. Artech House, Boston and London, 1996 edition, 1996.

[166] P. Lorrain and D. Corson. *Electromagnetic Fields and Waves*. W. H. Freeman and Company, San Francisco, 2nd edition, 1970.

[167] W. B. Jones. *Optical Fiber Communication Systems*. Holt, Rinehart and Winston, 1987.

[168] R. J. Glauber. Optical coherence and photon statistics. In C. DeWitt, editor, *Quantum Optics and Electronics*, pages 63–186. Gordon and Breach Science Publishers, Inc., 150 Fifth Avenue, New York, 1965.

[169] M. C. Teich. Quantum theory of heterodyne detection. In E. M. Pell, editor, *Proceedings of the Third Photoconductivity Conference*, pages 1–5, Oxford, August 1969. International Union of Pure and Applied Physics, Pergamon.

[170] J. W. Goodman. *Statistical optics*. Wiley Series in Pure and Applied Optics. Wiley, 1985.

[171] A Yariv. *Optical Electronics*. Holt, Rinehart and Winston, 3rd edition, 1985.

[172] W. D. Cornwell. *On the Characterisation of Interferometric Noise in Optical Networks*. PhD thesis, University of Strathclyde. Dept. of Electronic and Electrical Engineering., 1998. Strathclyde Class number T9272.

[173] R. A. Linke and A. H. Gnauck. High-capacity coherent lightwave systems. *IEEE Journal of Lightwave Technology*, 6(11):1750–1769, November 1988.

[174] M. Nazarathy, W. V. Sorin, D. M. Baney, and S. A. Newton. Spectral analysis of optical mixing measurements. *IEEE Journal of Lightwave Technology*, 7(7):1083–1096, July 1989.

[175] P. J. Legg. *The Impact of Interferometric Noise on the Performance of Optical Communication Methods*. PhD thesis, University of Strathclyde. Dept. of Electronic and Electrical Engineering., 1995. Strathclyde class number T8471.

[176] H. Hodara. Statistics of thermal and laser radiation. *Proceedings of the IEEE*, pages 696–704, July 1965.

[177] N. A. Olsson. Lightwave systems with optical amplifiers. *Journal of Lightwave Technology*, 7(7):1071–1082, July 1989.

[178] G. R. Cooper and C. D. McGillem. *Probabilistic Methods of Signal and System Analysis*. CBS Publishing Japan Ltd., 2nd edition, 1986.

[179] M. Norgia, G. Giulian, and S. Donati. Noise evolution along optically amplified links in presence of nonlinear parametric gain. *Journal of Lighwave Technology*, 17(10):1750 – 1757, October 1999.

[180] J. Walker D. Halliday, R. Resnick. *Fundamentals of Physics*. Wiley, 6th edition, 1999.

[181] R. P. Feynman, R. B. Leighton, and M Sands. *The Feynman Lectures on Physics*, volume 3. Addison Wesley, 1963.

[182] J. O. Limb. Fiber optic taps for local area networks. In *Conf. Record, IEEE Intern. Commun. Conf. Vol.*, volume 3, pages 1130–1136. IEEE, 1984.

[183] R. Ramaswami and K. Lui. Analysis of optical bus networks using doped fiber amplifiers. *IBM internal report no. 18491*, November 1992.

[184] D. A. Chapman. Comment on 'using spread spectrum in a high capacity fiber-optic local network'. *Journal of Lightwave Technology*, 7:747, April 1989.

[185] A. E. Kamal and B. W. Abeysundra. Hybrid medium access protocols for high-speed dual-bus fiber-optic local area networks. *Computer Networks and ISDN Systems*, 26(5):563–584, January 1994.

[186] M. Fuller. Specialized optical amplifiers no longer mere laboratory curiosities. *Lightwave*, 18(2):203–204, 206, 208, 210, 212, 218, February 2001.

[187] K Wilner and A. P. Van Den Heuvel. Fiber-optic delay lines for microwave signal processing. *Proceedings of the IEEE*, 64(5):805–807, May 1976.

[188] K. C. Kao and G. A. Hockham. Dielectric-fibre surface waveguides for optical frequencies. *Proceedings of the IEE*, 113:1151–1158, July 1966. Reprinted in 1986, IEE Proceedings-J Vol 133 Part 3 pp191-198.

[189] B. Moslehi, J. W. Goodman, M. Tur, and H. Shaw. Fiber-optic lattice signal processing. *Proceedings of the IEEE*, 72(7):909–930, July 1984.

[190] K. P. Jackson. Optical fiber delay-line signal processing. *IEEE Transactions on Microwave Theory and Technology*, 33:193–209, March 1985.

[191] E. Marom. Optical delay line matched filters. *IEEE Transactions on Circuits and Systems*, 25(6):360–364, June 1978.

[192] R. L. Ohlhaber and K. Wilner. Fiber optic delay lines for pulse coding. *Electro-optic systems design*, 9(2):33–35, February 1977.

[193] D. D. Sampson. *High Bandwidth Temporal Correlators using Optical Fibre Networks*. PhD thesis, Department of Physics, University of Kent at Canterbury, 1992.

[194] W. Zhang, J. A. R. Williams, and I. Bennion. Optical fibre delay line filter free of limitation imposed by optical coherence. *Electronics Letters*, 35(24):2133–2134, November 1999.

[195] V. Krishnamurthy, M. C. Hargis, and M. R. Melloch. A 4-GHz large-area (160 000 μm^2) MSM-PD on ITG-GaAs. *Photonics Technology Letters*, 12(1):71–73, January 2000.

[196] A. Bandyopadhyay and M. J. Deen. Metal-semiconductor-metal photodetectors. In H. S. Nalwa, editor, *Photodetectors and Fiber Optics*, chapter 5, pages 328–333. Academic Press, 2001.

[197] M. Schwartz. *Information Transmission, Modulation, and Noise*. McGraw-Hill Series in Electrical Engineering. McGraw-Hill, 3rd edition, 1981.

[198] E. G. Neumann. *Single-Mode Fibers*. Springer Series in Optical Sciences. Springer-Verlag, 1988.

[199] P. Di Vita and U. Rossi. Evaluation of coupling efficiency in joints between optical fibres. *Alta Frequenza*, 477(5):414–423, May 1978. Also appeared in CSELT Technical Reports (*Rapporti Technici*) V.5 n.5 Dec. 77 pp157-167.

[200] M. S. Whalen and T. H. Wood. Effectively nonreciprocal evanescent-wave optical-fibre directional coupler. *Electronics Letters*, 21(5):175–176, February 1985.

[201] R. Griffin, J. D. Love, P. R. A. Lyons, D. A. Thorncraft, and S. C. Rashleigh. Asymmetric multimode couplers. *Journal of Lightwave Technology*, 9(11):1508–1517, November 1991.

[202] R. J. Boughton, M. Farhadiroushan, D. Kreit, R. C. Youngquist, and I. P. Giles. Optical-fiber systems with nonreciprocal couplers. *Optics Letters*, 12(3):205–207, March 1987.

[203] D. Yui, E. Sasaoka, T. Hattori, C. Hirose, H Hatayama, and N. Akasaka. SM-MM conversion 16×1 PLC optical coupler module. In *Proceedings of NOC 98*, pages 147–150, 1998.

[204] R. März. *Integrated Optics*. Artech House, 1995.

[205] R. P. Feynman, R. B. Leighton, and M Sands. *The Feynman Lectures on Physics*, volume I. Addison Wesley, 1963.

[206] OzOptics fiber optic component catalogue, 2000. www.ozoptics.com.

[207] H. S. M. Coxeter. *Introduction to Geometry*. Wiley, 1961.

[208] S. D. Personick. *Optical Fiber Transmission Systems*. Applications of Communications Theory. Plenum Press, New York, 1981.

[209] R. Guenther. *Modern Optics*. Wiley, 1990.

[210] D. Gloge. Weakly guiding fibers. *Applied Optics*, 10(10):2252–2258, October 1971.

[211] J. E. Midwinter and Y. L. Guo. *Optoelectronics and Lightwave Technology*. Wiley, 1992.

[212] Jong-Hoi Kim, Kwang-Ryong Oh, Hyun-Soo Kim, and Kyuman Cho. All-optical switching by counterpropagating operation in cascaded semiconductor optical amplifiers. *IEEE Photonics Technology Letters*, 12(5):513–515, May 2000.

[213] H. Kobayashi, R. Takahashi, Y. Matsuoka, and H. Iwamura. 1 Tbit/s demultiplexing using low temperature grown InGsAs/InAlAs multiple quantum wells. *Electronics Letters*, 34(9):908–910, April 1998.

[214] J. A. Salehi and C. A. Brackett. Code division multiple access techniques in optical fiber networks (Part 2). *IEEE Transactions on Communications*, 37(8):824–842, August 1989.

[215] M. Azizo glu, J. A. Salehi, and Y. Li. Optical CDMA via temporal codes. *IEEE Transactions on Commununications*, 40(7):1162–1170, July 1992.

[216] H.M. Kwon. Optical orthogonal code division multiple access system – Part I APD noise and thermal noise. *IEEE Transactions on Communications*, 42(7):2470–2479, 1994.

[217] H. B. Enderton. *Elements of Set Theory*. Academic Press, 1977.

[218] M. Nakazawa. Toward Terabit/s single-channel transmission. In *Optical Fiber Communication Conference, 1999, and the International Conference on Integrated Optics and Optical Fiber Communication, OFC/IOOC '99. Technical Digest, Vol.*, pages 132–134. IEEE, 1999.

[219] M. Saruwatari. Al-optical signal processing for Terabit/Second optical transmission. *IEEE Journal on Selected Topics in Quantum Electronics*, 6(6):1363–1374, November/December 2000.

[220] J. M. Senior. *Optical Fiber Communications : Principles and Practice*. Prentice Hall, 1985.

[221] Kyle Siegrist. Virtual laboratories in probability and statistics. http://www.math.uah.edu/stat/index.html, 2000.

Appendix A

Acronyms and abbreviations

ARPA Advanced Research Projects Agency

AS Amplified Source

ASE Amplified Spontaneous Emission

ASK Amplitude Shift Keying

BPM Beam Propagation Method

CDMA Code Division Multiple Access

CSMA/CD Carrier Sense Multiple Access with Collision Detection

DQDB Distributed Queue Dual Bus

DTCAP Distributed Tunable-Channel Access Protocol

DUT Device Under Test

DVM Digital Volt Meter

DWDM Dense Wavelength Division Multiplexing

EDFA Erbium Doped Fibre Amplifier

EQC Extended Quadratic Codes

FC Ferrule Connector

FDDI Fiber-Distributed Data Interface

FWHM Full-Width at Half Maximum

GRIN GRaded INdex

HLAN Helical-LAN

LAN Local Area Network

LED Light Emitting Diode

LP Linear Polarisation

MAI Multiple Access Interference

MEMS Micro Electro-Magnetic System

MSM Metal-Semiconductor-Metal

NOC Networks and Optical Communications (conference)

OCDMA Optical Code Division Multiple Access

OOC Optical Orthogonal Code

OOK On-Off Keying

PBX Private Branch eXchange

PIN Positive-Intrinsic-Negative

PINAMP PIN-AMPlifier

POLSK Polarisation Shift Keying

PPM Pulse Position Modulation

PSK Phase Shift Keying

QPSK Quadrature Phase Shift Keying

SCDMA Synchronous Code Division Multiple Access

SLIM Single Light-source with In-line Modulation

SNR Signal to Noise Ratio

SOA Semiconductor Optical Amplifier

SONET Synchronous Optical NETwork

SpE Spontaneous Emissions

TDMA Time Division Multiple Access

UKC University of Kent at Canterbury

WAN Wide Area Network

WDM Wavelength Division Multiplexing

WDMA Wavelength Division Multiple Access

WEMCOB Wavelength Encoded Multichannel Optical Bus

Appendix B

The analytic field of a chaotic source

This section summarises results for a field $\mathbf{E}(t) = \sqrt{P}\mathbf{u}(t)\, e^{-i\omega t}$ from a chaotic (thermal-like) optical source modelled by power spectral density $\frac{P}{2B}$ between $-\left(f_0 + \frac{B}{2}\right)$ and $-\left(f_0 - \frac{B}{2}\right)$ and between $f_0 - \frac{B}{2}$ and $f_0 + \frac{B}{2}$. From Goodman [170], both $\mathbf{E}(t)$ and $\mathbf{u}(t)$ may be modelled as *circular complex Gaussian random processes.*

Use is made of two results for circular complex Gaussian random processes:

□ Goodman Equation 3.9-2:

$$\overline{\mathbf{u}^*(t_1)\,\mathbf{u}^*(t_2)\,\mathbf{u}(t_3)\,\mathbf{u}(t_4)} = \overline{\mathbf{u}(t_3)\,\mathbf{u}^*(t_1)}\;\overline{\mathbf{u}(t_4)\,\mathbf{u}^*(t_2)} + \overline{\mathbf{u}(t_3)\,\mathbf{u}^*(t_2)}\;\overline{\mathbf{u}(t_4)\,\mathbf{u}^*(t_1)} \tag{B.1}$$

□ and Goodman Equation 3.9-3:

$$\overline{|\mathbf{u}(t_1)|^2\,|\mathbf{u}(t_2)|^2} = \overline{|\mathbf{u}(t_1)|^2}\;\overline{|\mathbf{u}(t_2)|^2} + \left|\overline{\mathbf{u}(t_1)\,\mathbf{u}^*(t_2)}\right|^2 \tag{B.2}$$

B.1 Results

The optical field has zero mean, so:

$$\overline{\mathbf{E}(t)} = \overline{\mathbf{E}(t+\tau)} = 0 \tag{B.3}$$

The power of the field is P, and directly from the definition $\mathbf{E}(t) = \sqrt{P}\mathbf{u}(t)\, e^{-i\omega t}$:

$$\overline{|\mathbf{E}(t)|^2} = \overline{|\mathbf{E}(t+\tau)|^2} = 2P \tag{B.4}$$

The self-coherence function of $\mathbf{E}(t)$ is defined by $\Gamma_E(\tau) = \overline{\mathbf{E}^*(t)\,\mathbf{E}(t+\tau)}$, and, using (Goodman Eqn. 5.1-14),

$$\Gamma_E(\tau) = \int_0^\infty 4G(f)\, e^{-i2\pi f\tau} df$$

where $G(f)$ is the power spectral density of $\mathbf{E}(t)$. So:

$$\begin{aligned}\overline{\mathbf{E}^*(t)\,\mathbf{E}(t+\tau)} &= \int_0^\infty 4G(f)\,e^{-i2\pi f\tau}df \\ &= \frac{2P}{B_s}\int_{f_0-\frac{B}{2}}^{f_0+\frac{B}{2}} e^{-i2\pi f\tau}df \\ &= 2Pe^{-i2\pi f_0\tau}\frac{\sin(\pi\tau B)}{\pi\tau B} \end{aligned} \tag{B.5a}$$

Similarly

$$\overline{\mathbf{E}(t)\,\mathbf{E}^*(t+\tau)} = \Gamma_E^*(\tau) = 2Pe^{i2\pi f_0\tau}\frac{\sin(\pi\tau B)}{B\pi\tau} \tag{B.6}$$

Also from Goodman:

$$\begin{aligned} & \overline{\mathbf{E}(t)\,\mathbf{E}(t+\tau)} \\ = & \overline{\left(E^{(r)}(t)+iE^{(i)}(t)\right)\left(E^{(r)}(t+\tau)+iE^{(i)}(t+\tau)\right)} \\ = & \overline{E^{(r)}(t)\,E^{(r)}(t+\tau)-E^{(i)}(t)\,E^{(i)}(t+\tau)+i\left(E^{(r)}(t)\,E^{(i)}(t+\tau)+E^{(i)}(t)\,E^{(r)}(t+\tau)\right)} \\ = & \ 0, \text{ using the results of Goodman 3.9-1} \end{aligned} \tag{B.7}$$

($E^{(r)}$ & $E^{(i)}$ are the real and imaginary components of E respectively)

Similarly

$$\overline{\mathbf{E}^*(t)\,\mathbf{E}^*(t+\tau)} = 0 \tag{B.8}$$

Using equations B.4 and B.6:

$$\begin{aligned}\overline{|\mathbf{E}(t)|^2\,|\mathbf{E}(t+\tau)|^2} &= \overline{|\mathbf{E}(t)|^2}\,\overline{|\mathbf{E}(t+\tau)|^2} + \left|\overline{\mathbf{E}(t)\,\mathbf{E}^*(t+\tau)}\right|^2 \\ &= 4P^2 + |\Gamma_E(\tau)|^2 \\ &= 4P^2 + 4P^2\left(\frac{\sin(\pi\tau B)}{B\pi\tau}\right)^2 \end{aligned} \tag{B.9}$$

B.2 Some transform pairs

Starting with [197]:

$$\begin{aligned} H(\tau) &= A\frac{\sin(\pi\tau B)}{\pi\tau B} \\ G(f) &= \begin{cases} \frac{A}{B} & \text{for } -B/2 < f < B/2 \\ 0 & \text{otherwise} \end{cases} \\ H(\tau) &\leftrightarrow G(f) \end{aligned}$$

Using frequency-domain convolution (all spectra are zero outside the domain spec-

ified):

$$(H(\tau))^2 = A^2 \left(\frac{\sin(\pi\tau B)}{\pi\tau B} \right)^2$$

$$\leftrightarrow$$

$$G(f) * G(f) = \begin{cases} \left(\frac{A}{B}\right)^2 (B - f) & \text{for } 0 < f < B \\ \left(\frac{A}{B}\right)^2 (B + f) & \text{for } -B < f < 0 \end{cases}$$

For two different bandwidths ($B_2 > B_1$):

$$H_1(\tau) = A_1 \frac{\sin(\pi\tau B_1)}{\pi\tau B_1} \text{ and } H_2(\tau) = A_2 \frac{\sin(\pi\tau B_2)}{\pi\tau B_2}$$

$$H_1(\tau) H_2(\tau) = A_1 A_2 \frac{\sin(\pi\tau B_1)}{\pi\tau B_1} \frac{\sin(\pi\tau B_2)}{\pi\tau B_2}$$

$$\leftrightarrow$$

$$G_1(f) * G_2(f) = \begin{cases} \left(\frac{A_1}{B_1}\right)\left(\frac{A_2}{B_2}\right)((B_2 + B_1) - f) & \text{for } B_2 - B_1 < f < B_2 + B_1 \\ 2\left(\frac{A_1}{B_1}\right)\left(\frac{A_2}{B_2}\right) B_1 & \text{for } -(B_2 - B_1) \le f \le B_2 - B_1 \\ \left(\frac{A_1}{B_1}\right)\left(\frac{A_2}{B_2}\right)((B_2 + B_1) + f) & \text{for } -(B_2 + B_1) < f < -(B_2 - B_1) \end{cases}$$

In single-sided form:

$$A \frac{\sin(\pi\tau B)}{\pi\tau B} \quad \leftrightarrow \quad 2\frac{A}{B} \quad \text{for } 0 < f < B/2$$

$$A^2 \left(\frac{\sin(\pi\tau B)}{\pi\tau B} \right)^2 \quad \leftrightarrow \quad 2\left(\frac{A}{B}\right)^2 (B - f) \quad \text{for } 0 < f < B$$

$$A_1 A_2 \frac{\sin(\pi\tau B_1)}{\pi\tau B_1} \frac{\sin(\pi\tau B_2)}{\pi\tau B_2} \quad \leftrightarrow \quad \begin{cases} 2\left(\frac{A_1}{B_1}\right)\left(\frac{A_2}{B_2}\right)((B_2 + B_1) - f) & \text{for } B_2 - B_1 < f < B_2 + B_1 \\ 4\left(\frac{A_1}{B_1}\right)\left(\frac{A_2}{B_2}\right) B_1 & \text{for } 0 \le f \le B_2 - B_1 \end{cases}$$

Appendix C

Gaussian models

The Gaussian beam is widely-used as a model of the field distribution of light emerging from a single mode fibre [209, 198]. This appendix describes the model (Section C.1) and a method of analysing the propagation of Gaussian beams through lenses (Section C.2).

The Gaussian beam model was used in Chapter 6 for modelling the coupling efficiency between single and multimode fibres in a hybrid coupler, and section C.3 of this appendix extends the modelling of Chapter 6 to take account of the finite size of the output fibre core (Section C.3.1) and lateral offsets (Section C.3.2).

Section C.4 contains a note on the definition of the spot size of a Gaussian beam and Section C.5 is brief introduction to the Gaussian approximation of the guided modes of optical fibre.

C.1 Gaussian beam model

Following Neumann [198], assuming the wave to be linearly polarised in the x-direction, the field of a Gaussian beam is described by [1]:

$$\underline{E}_x(r,z) = \underline{E}_x(0,0)\,\frac{\omega_0}{\omega(z)}\exp\left[\frac{-r^2}{\omega^2(z)}\right]\exp\left[-jnkz + j\Theta(z) - \frac{jnkr^2}{2R(z)}\right] \tag{C.1}$$

making the intensity a Gaussian function of radius[2] (Figure C.1(a)):

$$I(z,r) = I_o\frac{\omega_o^2}{\omega^2(z)}\exp\left(\frac{-2r^2}{\omega^2(z)}\right)$$

$\omega(z)$ is the *spot size*, which defines the radius at which the beam intensity has dropped to $1/e^2$ (but see discussion of spot size in Section C.4 below). $\Theta(z)$ is given

[1] Neumann [198] equation 4.1. The material in this appendix is all based upon Neumann Chapter 4.

[2] See equation 4.3 in Neumann [198]. Note that the $1/\omega^2(z)$ multiplier conserves the total power with z.

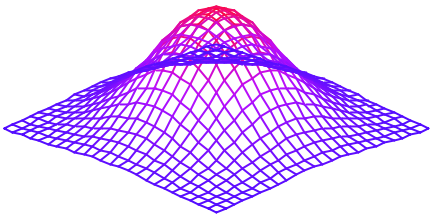

(a) Intensity profile

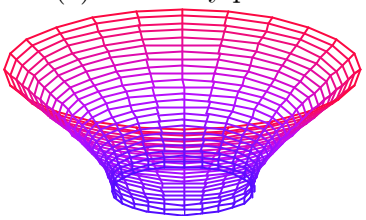

(b) Beam divergence

Figure C.1: Gaussian beam

by $\tan^{-1}\frac{z}{z_R}$ and $R(z)$ is the radius of curvature of the wavefront as a function of z, and is given by:

$$R(z) = \frac{z^2 + z_R^2}{z} = z\left(1 + \frac{z_R^2}{z^2}\right)$$

The beam divergence is modelled by expressing the spot size, $\omega(z)$, as a function of the distance, z, from the beam waist according to:

$$\omega(z) = \omega_0\sqrt{1 + (z/z_R)^2} \tag{C.2}$$

(see Figure C.1(b)) where ω_0 is the spot size at the beam waist and z_R is the *Rayleigh range* which determines the boundary between the near- and far-fields. z_R is given by:

$$z_R = \frac{n_r \pi \omega_0^2}{\lambda}$$

(where λ is the free-space wavelength and n_r the refractive index of the medium).

In the far field, where $z \gg z_R$, the spot size increases linearly as $\omega_0 z/z_R$, i.e. with gradient (tangent of the divergence angle) $\omega_0/z_R = \lambda/n_r\pi\omega_0$. For small values the angle is approximated by its tangent (paraxial assumption), giving, for the divergence angle:

$$\theta_D = \lambda/n_r\pi\omega_0 \tag{C.3}$$

C.2 The ABCD formulation of an optical system

A system element is modelled by the *ABCD* matrix of 'Gaussian constants'[209, 171]:

$$\begin{pmatrix} A & B \\ C & D \end{pmatrix}$$

Using this matrix, a paraxial ray at a distance r from the axis and an angle $r' = \frac{dr}{dz}$ to the axis is transformed by the system according to

$$\begin{pmatrix} r_o \\ r'_o \end{pmatrix} = \begin{pmatrix} A & B \\ C & D \end{pmatrix} \begin{pmatrix} r_i \\ r'_i \end{pmatrix}$$

(where the subscript i is for the input parameters and o for the output parameters).

The model of combined system of elements $1, 2, ...n$ can be determined by matrix multiplication:

$$\begin{pmatrix} A_s & B_s \\ C_s & D_s \end{pmatrix} = \begin{pmatrix} A_n & B_n \\ C_n & D_n \end{pmatrix} ... \begin{pmatrix} A_2 & B_2 \\ C_2 & D_2 \end{pmatrix} \begin{pmatrix} A_1 & B_1 \\ C_1 & D_1 \end{pmatrix}$$

The '*ABCD* law' formulation can also be used to analyse the propagation of an on-axis Gaussian beam through an optical system through the use of the q parameter:

$$q(z) = z + iz_R$$

which can be written:

$$\frac{1}{q(z)} = \frac{1}{R(z)} + i\frac{\lambda}{\pi n \omega^2(z)}$$

The q parameters of the input and output beams are then related by:

$$q_o = \frac{A_s q_i + B_s}{C_s q_i + D_s}$$

C.3 Refinements to the Gaussian beam model for coupling in a hybrid coupler.

C.3.1 Effect of the finite core size of the output fibre.

The light on the output fibre end-face has a Gaussian radial intensity profile with spot size $\omega(z)$ given by equation 6.12. On the ray model, the light within this will be coupled into the output fibre provided it is within the output fibre core. If the beam is assumed to be centred on the output fibre axis (no lateral offset), then for an output fibre core radius of r_o the coupling efficiency is given by:

$$\eta = \zeta \frac{\int_0^{r_o} I(r)\, 2\pi r dr}{\int_0^{\infty} I(r)\, 2\pi r dr} \tag{C.4}$$

where $I(r)$ is the radial intensity profile of the beam on the fibre end face and ζ accounts for the loss due to Fresnel reflection ($\zeta \approx 96\%$, assuming no anti-reflection coating on the fibre end-face).

$I(r)$ is given by (assuming a Gaussian beam)

$$I(r) = I_o \exp\left(\frac{-2r^2}{\omega^2(z)}\right)$$

For the configuration of Fig. 6.7 and from Eqn. 6.12 $\omega(z) = \omega_0 f_2/f_1$:

$$I(r) = I_o \exp\left(\frac{-2f_1^2 r^2}{f_2^2 \omega_0^2}\right)$$

Where ω_0 is the spot size of the input fibre, and $f_1$and f_2 are the collimating and focusing lens focal lengths respectively, as before.

Then

$$\begin{aligned}
\eta &= \zeta \frac{\int_0^{r_o} r \exp\left(\frac{-2f_1^2 r^2}{f_2^2 \omega_0^2}\right) dr}{\int_0^{\infty} r \exp\left(\frac{-2f_1^2 r^2}{f_2^2 \omega_0^2}\right) dr} \\
&= \zeta\left(1 - \exp\left(-2\frac{r_o^2}{\omega_0^2}\frac{f_1^2}{f_2^2}\right)\right) \\
&= \zeta\left(1 - \exp\left(-2\frac{r_o^2}{\omega_0^2}\right)\right) \qquad \text{(C.5)}
\end{aligned}$$

So, for example, with f_1 and f_2 chosen so that $r_o f_1/(\omega_0 f_2) = 1$ (the spot size of the image is equal to the output fibre core radius, effectively the basis of the calculation in Section 6.2, see Eqn. 6.8), then $\eta = 0.865\zeta = 0.830$ (for $\zeta = 0.96$), a loss of about 0.81 dB.

C.3.2 Imperfect lateral alignment

Eqn. C.5 assumes that the optics centres the image from the input fibres on the centre of the output fibre, and this section explores the consequences of this not being done. A closely related calculation has been done for fibre-to-fibre coupling [199] and for laser-to-fibre coupling [4].

The circular symmetry of the perfectly aligned coupling is lost, and in general an algebraic solution is unavailable, but numerical calculations can be used to illustrate the sensitivity of typical configurations to alignment errors.

The incident light intensity is assumed to have a Gaussian intensity distribution described by:

$$I(r) = I_o \exp\left(\frac{-2r^2}{\omega_g^2}\right)$$

(where ω_g is the spot size and I_o is the intensity at the centre of the beam). As before, it is assumed that all light incident upon the output fibre core is collected by the output fibre. The problem then becomes that of integrating the power in the Gaussian beam over a circular area of radius g (the radius of the output fibre core) offset from the centre of the Gaussian beam by a distance r_0 (the direction of the offset is arbitrary, since the Gaussian beam is circularly symmetrical). The geometry is analysed separately for the two cases $r_0 \geq g$ and $r_0 < g$ (i.e. whether or not the centre of the Gaussian beam is within the core of the output fibre, see Figure C.2).

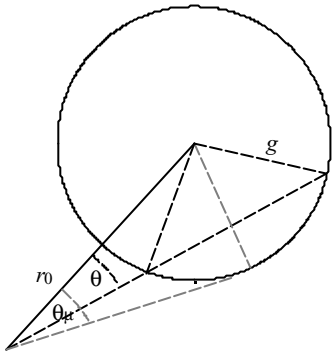

(a) $r_0 \geq g$

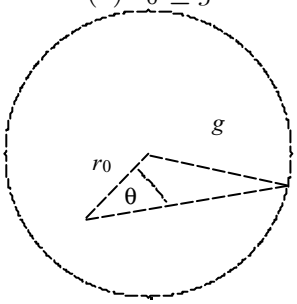

(b) $r_0 < g$

Figure C.2: Lateral offset between the Gaussian beam and the output fibre

The case $r_0 \geq g$

The geometry is shown in Figure C.2(a). Polar coordinates r, θ are used and the reference axis ($\theta = 0$) is taken as the line through the centre of the output fibre. By symmetry, the contributions from positive and negative θ are equal, and from the geometry the maximum value of θ is given by $\theta_m = \sin^{-1}(g/r_0)$. The limits on r are also found by geometry, and are given by[3]:

$$r_0\left(\cos(\theta) - \sqrt{\frac{g^2}{r_0^2} - \sin^2(\theta)}\right) \leq r \leq r_0\left(\cos(\theta) + \sqrt{\frac{g^2}{r_0^2} - \sin^2(\theta)}\right) \text{ for } 0 \leq \theta \leq \theta_m$$

This gives the total power collected by the fibre:

[3] The steps of the calculation:

$$p = 2\int_0^{\sin^{-1}\left(\frac{g}{r_0}\right)} \int_{r_0\left(\cos(\theta)-\sqrt{\frac{g^2}{r_0^2}-\sin^2(\theta)}\right)}^{r_0\left(\cos(\theta)+\sqrt{\frac{g^2}{r_0^2}-\sin^2(\theta)}\right)} I(r)\, r dr d\theta$$

The case $r_0 < g$

The geometry for this case is shown in Figure C.2(b)

Taking θ from 0 to π, with the limits of r running from 0 to $r_0\left(\cos(\theta) + \sqrt{\frac{g^2}{r_0^2} - \sin^2(\theta)}\right)$, (where the upper limit on r is derived as before) leads to:

$$p = 2\int_0^{\pi} \int_0^{r_0\left(\cos(\theta)+\sqrt{\frac{g^2}{r_0^2}-\sin^2(\theta)}\right)} I(r)\, r dr d\theta$$

Gaussian input beam coupling efficiency

For a Gaussian beam, $I(r) = I_o \exp\left(-2r^2/\omega_g^2\right)$ and the total power in the input beam is $(\pi/2) I_o \omega_g^2$, so the coupling efficiency is:

$$\xi_{off} = \frac{p}{(\pi/2) I_o \omega_g^2} = \begin{cases} \frac{4}{\pi\omega_g^2} \int_0^{\sin^{-1}\left(\frac{g}{r_0}\right)} \int_{r_0\left(\cos(\theta)-\sqrt{\frac{g^2}{r_0^2}-\sin^2(\theta)}\right)}^{r_0\left(\cos(\theta)+\sqrt{\frac{g^2}{r_0^2}-\sin^2(\theta)}\right)} \exp\left(\frac{-2r^2}{\omega_g^2}\right) r dr d\theta & \text{for } r_0 \geq g \\ \frac{4}{\pi\omega_g^2} \int_0^{\pi} \int_0^{r_0\left(\cos(\theta)+\sqrt{\frac{g^2}{r_0^2}-\sin^2(\theta)}\right)} \exp\left(\frac{-2r^2}{\omega_g^2}\right) r dr d\theta & \text{for } r_0 < g \end{cases}$$

The integral over r can be done algebraically (since it is of the form $r\exp\left(-kr^2\right)$), but the result in rather lengthy, and there is no simple algebraic solution to the subsequent integral over θ. Insight into the significance of a lateral offset can be derived, however, from a numerical calculation.

Figure C.3 for example, shows the coupling efficiency as a function of offset.

$$\begin{aligned} r_0 \sin\theta &= g \sin\phi \\ r &= r_0 \cos\theta + g\cos\phi \\ &= r_0 \cos\theta + g\sqrt{1-\sin^2\phi} \\ &= r_0 \cos\theta + g\sqrt{1 - \frac{r_0^2}{g^2}\sin^2\theta} \\ &= r_0\left(\cos(\theta) + \sqrt{\frac{g^2}{r_0^2} - \sin^2(\theta)}\right) \end{aligned}$$

The minimum value of r corresponds to taking the negative square root, and the maximum value to taking the positive square root.

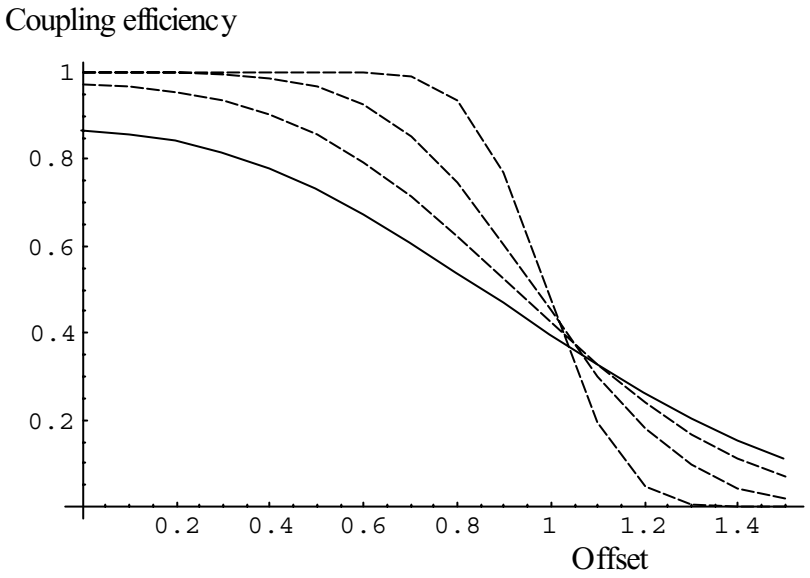

Figure C.3: The coupling efficiency, ξ_{off}, from a Gaussian beam to a step index fibre as function of relative offset (as a fraction of the output fibre radius, r_0/g) with Gaussian spot size as a parameter. Curves are for spot size/fibre radius of 1 (smallest dashes), 3/4, 1/2 and 1/4 (continuous curve).

C.4 Definition of spot size

Neumann [198] (see page 48 and 74ff) defines the spot size of a Gaussian beam by the *field radius* ω_G:

$$E(r) = E_0 \exp[-(\frac{r}{\omega_G})^2]$$

Snyder and Love [5] define the spot size by the *intensity radius* r_0:

$$E(r) = E_0 \exp[-\frac{1}{2}(\frac{r}{r_0})^2]$$
$$E^2(r) = E_0^2 \exp[-(\frac{r}{r_0})^2]$$

Both call it the spot size, but clearly $2r_0^2 = \omega_G^2$, so $\omega_G = \sqrt{2}r_0$.

Using the Gaussian approximation (Snyder and Love, Section 15.1) of a step index fibre with core radius a, the spot size of the fundamental mode is:

$$\frac{r_0}{a} = \frac{1}{\sqrt{2\ln V}} \quad \text{(C.6)}$$

$$\frac{\omega_G}{a} = \frac{1}{\sqrt{\ln V}} \quad \text{(C.7)}$$

Where V is the fibre normalised frequency, given by

$$V = \frac{2\pi a}{\lambda}\sqrt{n_{co}^2 - n_{cl}^2} = \frac{2\pi a}{\lambda} n_{co}\sqrt{2\Delta} \tag{C.8}$$

and

$$\Delta = \frac{n_{co}^2 - n_{cl}^2}{2n_{co}} \approx \frac{n_{co} - n_{cl}}{n_{co}}$$

C.5 Gaussian approximation of fibre modes

For a circular fibre with an infinite parabolic refractive index profile, Maxwell's equations may be solved to give explicit forms for the mode field distribution in terms of Laguerre polynomials [5]. Specifically, in circular coordinates, the field distribution of the l, m mode is described by:

$$E_{lm}(\rho, \phi) = \left(\frac{\sqrt{2}\rho}{\omega_g}\right) \exp\left[\frac{\rho^2}{\omega_g^2}\right] L_{m-1}^1\left(\frac{2\rho^2}{\omega_g^2}\right) \cos(l\phi)$$

Where ω_g is the spot size of the fundamental mode of the fibre. The principle of the Gaussian approximation [6] is that the mode field distribution of a fibre with some other refractive index profile (which does not have simple, explicit, solutions to Maxwell's equations) may be approximated by the field distribution of an equivalent parabolic fibre. A parabolic fibre is specified by the single parameter ω_g, so the approximation requires that ω_g of the equivalent parabolic fibre be calculated. This must be done *for each mode*, and Love and Hussey [6] have used a variational method and given a formula (see Figure D.7) which allows the calculation of ω_g for approximating the fields of a step-index fibre.

Appendix D

Mathematica programs

The main tool used for the simulations and analysis was *Mathematica*. This appendix briefly summarises the main *Mathematica* notebooks and packages written for this research, and includes a few general notes on the methodology and structures.

D.1 Methodology

Mathematica consists of two components: the *Kernel* and the *Front-End*. *Mathematica* code is written in *Notebooks* (*.nb files) using the Front-End, then the code is evaluated by the Kernel. In addition, a Notebook can be converted to a *Package* (*.m file) which can be read into another Notebook. A general methodology used for the work of this thesis was to define functions in code that was converted to packages, then the top-level Notebook read-in the required packages for use in the simulations.

D.2 Power levels in conventional and dark-signalling busses (Chapter 4)

The model tracks power levels along the bus with a list of four parameters, `sAndnList = {s0,s1,n0,n1}`, where s0,s1,n0,n1 represent the signal and noise during data 1s and 0s. Functions applied to `sAndnList` simulate the actions of optical components – fibre attenuation, optical amplifier, and modulator. The notebooks and packages are as follows.

D.2.1 Bus simulation packages

BusFunctions.m (Figure D.1) contains the functions used to simulate optical components. Each function is developed in a separate section, and Figure D.1 is printed with most of the sections closed, so that only the section title is displayed. The function `meanpower` which is used to calculate the mean signal power from the set of `sAndnList`parameters is shown in full. `meanpower` is a simple function which is

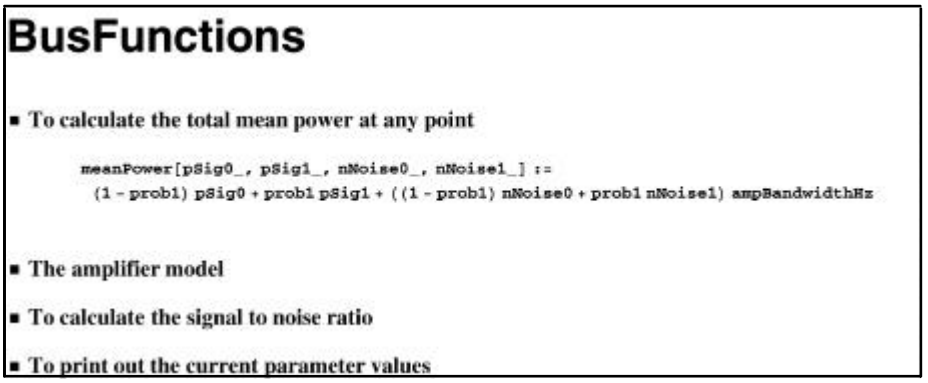

Figure D.1: The package "BusFunctions.m", used for the simulation of an optical fibre bus. The contents of all sections except the first have been collapsed to display only the headings.

fully defined in a single statement, but others functions are more complicated and use several stages. The amplifier model, for example, contains several stages including the calculation of gain and ASE (both of which depend upon input power).

`BusDefaults.m` is a package that contains the default values of the parameters (optical bandwidth, fibre losses, number of nodes, amplifier parameters etc.). Loading of `BusDefaults` is used to reset parameters to the default values before any simulations.

D.2.2 Bus simulation notebook

`BusSims.nb` (Figure D.2) is the notebook that runs specific simulations and displays the results. `BusFunctions.m` and `BusDefaults.m` are called from the notebook and read-in prior to running the simulations. Separate simulations (separate sections of the notebook, which may be run separately) are used to generate plots of the signal and noise power evolution along the bus, find the maximum tolerable bus length, determine the signal to noise ratio and signal power at the end of the bus as a function of various parameters (such as amplifier gain) and explore the trade-of between the signalling rate and the bus length. For each of the simulations results are plotted as graphs which are saved and used in reports.

D.3 Overlap integral calculations (Chapter 6)

There were two parts to this calculation: derivation of the fibre mode distributions (done by the notebook `fibreModes.nb)`, then overlap integral calculations themselves (done by the notebook `couplingCircle.nb`). A single package (`fibreFormulae.m`) contains all the functions used by both notebooks.

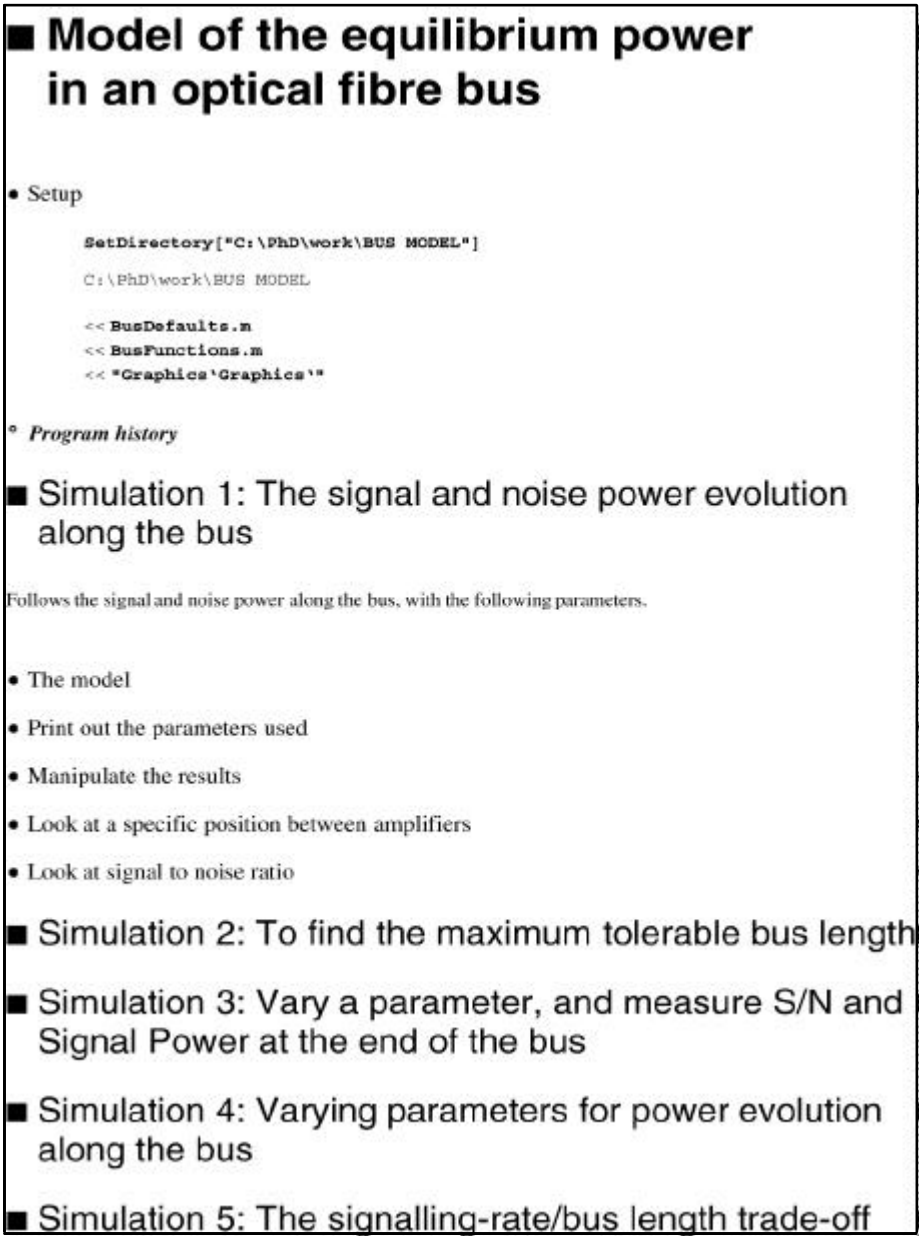

Figure D.2: The headings of the *mathematica* package used for simulating optical fibre busses. (The image is printed from an outline view of the notebook, by collapsing the contents of the 'Simulation' sections.)

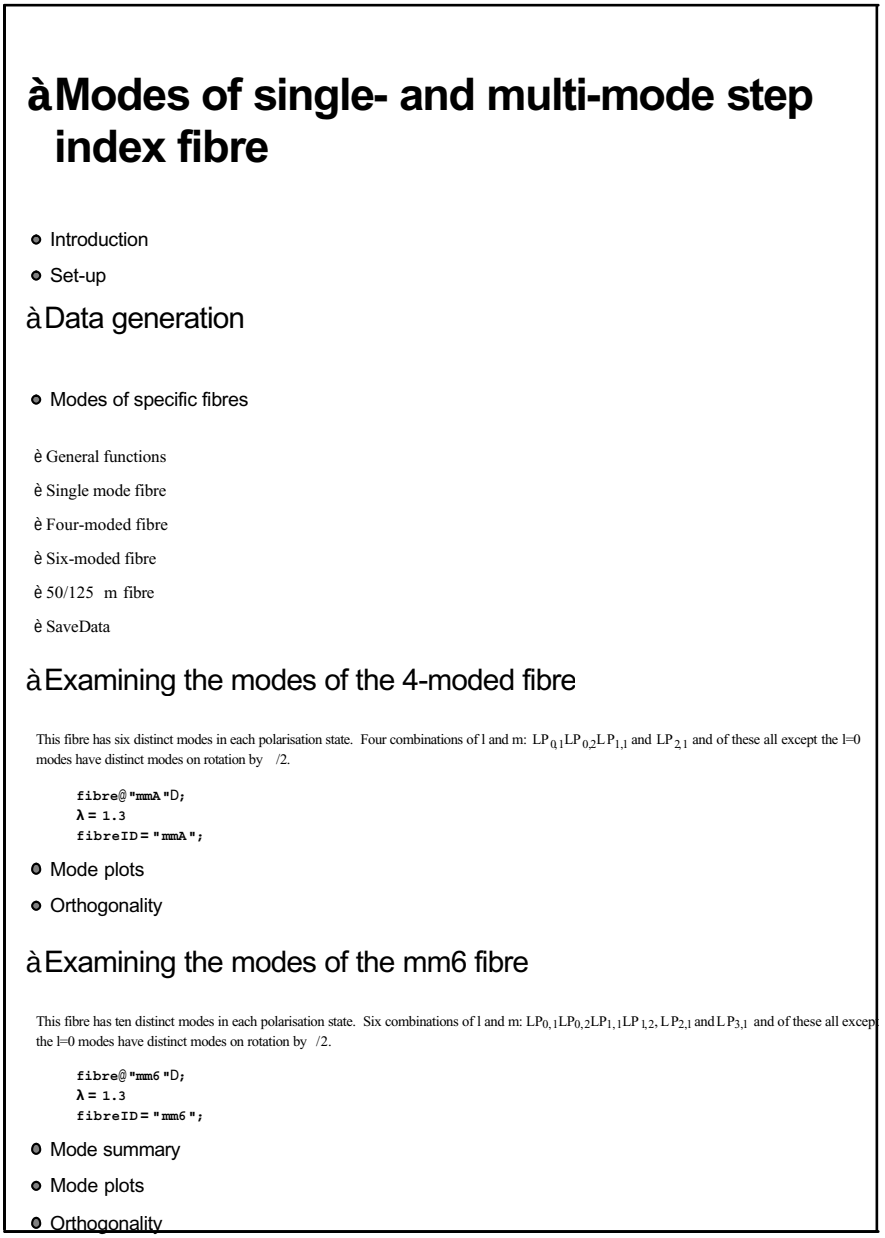

Figure D.3: Outline view of the `fibremodes` notebook.

D.3.1 Derivation of the fibres modes (*Mathematica* notebook `FibreModes.nb`)

Figure D.3 shows the outline of the `fibreModes.nb` notebook, which derives the parameters of the guided LP modes (all guided modes for the few-moded fibres, selected modes only of the 50/125 μm fibre) for several different sizes of step-index fibre (single mode, two 'few-moded' fibres, and 50/125 μm fibre). For each mode, the best Gaussian approximation is derived, and the radial dependence of the exact LP mode (separate Bessel functions for the core and cladding) is compared with the Gaussian approximation (a single Laguerre polynomial for both the core and cladding) in order to verify the accuracy of the approximation The calculated parameters of the modes are stored in a data file (`fibreModesData.txt`) for use in the overlap integral calculations.

The fields were derived as follows:

1. Solve the scalar wave equation for the step-index fibre by solving the characteristic equation that satisfies the boundary condition at the core-cladding interface. (See extracts from the *Mathematica* implementations in Figures D.4 and D.5.) The resulting mode propagation constant can be used with the appropriate Bessel functions for the mode field distribution (Figure D.6.)

2. Calculate the equivalent parabolic fibre approximation (the 'Gaussian approximation': see Section C.5). The *Mathematica* code to do this is shown in Figure D.7. The appropriate parabolic fibre mode is then used as the approximate mode distribution (Figure D.8).

3. To verify the Gaussian approximation, the radial distributions of the core and cladding step index fields were, for each mode, plotted together with the Gaussian approximation (Figure D.9). (The azimuthal distributions are identical for the two distributions, being simply given by $\cos(l\phi)$ or $\sin(l\phi)$, where l is the azimuthal mode number.)

D.3.2 Overlap calculations (*Mathematica* notebook `couplingCircle.nb`)

Figure D.10 shows the outline of the notebook `couplingCircle.nb`, used to calculate the overlap integral for the hybrid coupler. As explained above, the basic formulae are contained in `fibreFormulae.m` and the parameters of the fibre modes that were calculated in the `fibreModes.nb` notebook are contained in the data file `fibreModesData.txt`, so the 'setup' section of `couplingCircle.nb` includes loading of these two files. ('Calculus'VectorAnalysis' and 'Graphics', also shown being loaded in the Setup section of `couplingCircle.nb`, are standard packages – supplied as part of *Mathematica* – which add functionality to *Mathematica*.)

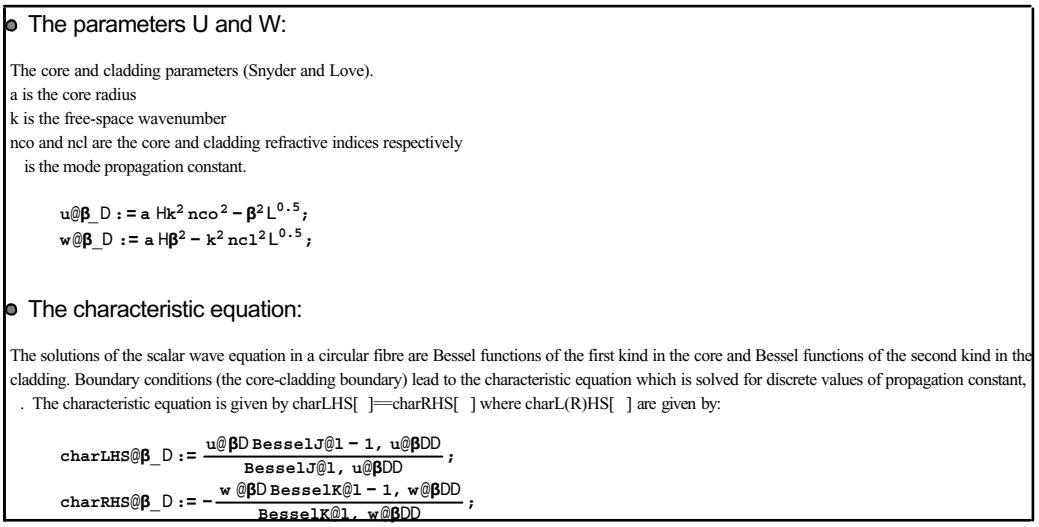

The parameters U and W:

The core and cladding parameters (Snyder and Love).
a is the core radius
k is the free-space wavenumber
nco and ncl are the core and cladding refractive indices respectively
is the mode propagation constant.

```
u@β_D := a Hk^2 nco^2 - β^2 L^0.5;
w@β_D := a Hβ^2 - k^2 ncl^2 L^0.5;
```

The characteristic equation:

The solutions of the scalar wave equation in a circular fibre are Bessel functions of the first kind in the core and Bessel functions of the second kind in the cladding. Boundary conditions (the core-cladding boundary) lead to the characteristic equation which is solved for discrete values of propagation constant, . The characteristic equation is given by charLHS[ ]==charRHS[ ] where charL(R)HS[ ] are given by:

$$\text{charLHS}[\beta\_D] := \frac{u[\beta D\,\text{BesselJ}[1-1, u[\beta D D}{\text{BesselJ}[1, u[\beta D D};$$

$$\text{charRHS}[\beta\_D] := -\frac{w[\beta D\,\text{BesselK}[1-1, w[\beta D D}{\text{BesselK}[1, w[\beta D D};$$

Figure D.4: Extract from *Mathematica* program `FibreFormulae#.nb`: formulae for the Characteristic Equation. ("Snyder and Love" is Reference [5].)

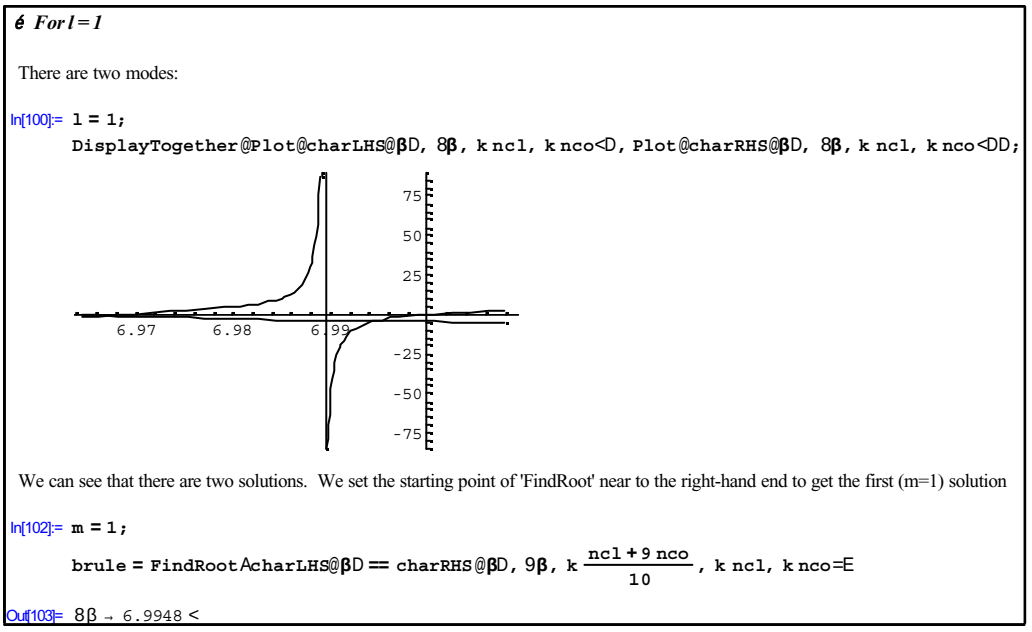

For l = 1

There are two modes:

```
In[100]:= l = 1;
          DisplayTogether@Plot@charLHS@βD, 8β, k ncl, k nco<D, Plot@charRHS@βD, 8β, k ncl, k nco<DD;
```


We can see that there are two solutions. We set the starting point of 'FindRoot' near to the right-hand end to get the first (m=1) solution

```
In[102]:= m = 1;
          brule = FindRootAcharLHS@βD == charRHS@βD, 9β, k (ncl + 9 nco)/10, k ncl, k nco=E
Out[103]= 8β → 6.9948 <
```

Figure D.5: Extract from *Mathematica* program `FibreModes#.nb` showing the solution of the Characteristic Equation for azimuthal mode number, $l = 1$ (for the "mm6" fibre).

```
coreField@l_D@β_D@r_, φ_D := BesselJAl, u@βD r/a E / BesselJ@l, u@βDD Cos@l φD;

claddingField@l_D@β_D@r_, φ_D := BesselKAl, w@βD r/a E / BesselK@l, w@βDD Cos@l φD
```

Figure D.6: Extract from *Mathematica* program `FibreFormulae#.nb`. The formulae for the core and cladding fields of a step index fibre in circular coordinates, with azimuthal mode number l and wave parameter β.

To get the best Gaussian fibre approximation we need to calculate the optimum value of g, which is given by solving the equation $\frac{(2m+l-1)!(l+m-1)!}{v^2 (m-1)!} = \frac{1}{r0^{2l}}$ LaguerreL $(m-1, l, \frac{1}{r0^2} EM^2)$ Exp $(-\frac{1}{r0^2}E)$, where r0 $\frac{g}{a\sqrt{2}}$ (the $\sqrt{2}$ is because of the different definitions of spot size between my use (which follows Neumann) and that of Snyder and Love).

(See Love and Hussey, Equation 19)

```
In[105]:= DisplayTogether[Plot[1/r0^(2 l) JLaguerreL[m - 1, l, 1/r0^2 EN^2] Exp[-1/r0^2 E], {r0, 0, 2}],
            Plot[(2 m + l - 1)! (l + m - 1)! / (v^2 (m - 1)!), {r0, 0, 2}]];
```

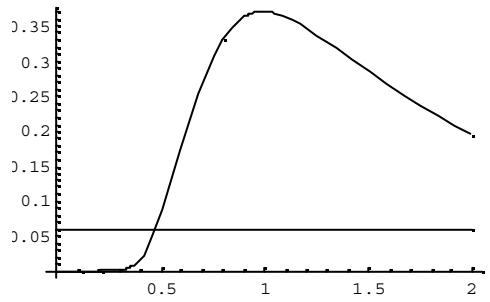


```
In[106]:= r0rule = FindRoot[(2 m + l - 1)! (l + m - 1)! / (v^2 (m - 1)!) == 1/r0^(2 l) JLaguerreL[m - 1, l, 1/r0^2 FN^2] Exp[-1/r0^2 F], {r0, 0.5, 0, 2}]

Out[106]= {r0 → 0.482435}

In[107]:= lagR@fibreID, mode_D = a Sqrt[2] r0 /. r0rule

Out[107]= 5.117
```

Figure D.7: Extract from *Mathematica* program `FibreModes#.nb` showing the derivation of the mode radius of the equivalent Gaussian fibre. See Reference [6] for details of this analysis.

Cylindrical coordinates

Equation 9 from Snyder and Hussey gives the field distribution of the LP_{1m} mode as a function of radius, ρ, azimuth, φ, and propagation along the fibre, z for the parabolic fibre.

In *Mathematica*, this is (where g is the spot size of the fundamental mode **of this parabolic fibre** Note that g will in general be different from ***each*** mode.):

é Radial distribution;

```
lagRadial@ωg_D@l_, m_D@ρ_D := Ê2 ρ/ωg Ù^l LaguerreLAHm - 1L, l, 2 ρ^2/ωg^2 ÙE ExpA-ρ^2/ωg^2 E
```

é Full description

NB: pattern matching with ensure that the correct version of the function is used by any given call

```
lagCylinder@ωg_D@8l_, m_, rot_<D@z_D@8ρ_, φ_<D := lagRadial@ωgD@l, mD@ρD Cos@l φ + rotD Exp@-I β zD;
```

é Shortened description

In the model of interest, z=0 and g will be determined by the fibre type (which will have been set as a (local) constant with the name of `fibreID') and the mode numbers, so it will make for more concise algebra using:

```
lagRadial@8l_, m_, rot_<D@ρ_D := lagRadial@lagR@fibreID, 8l, m, rot<DD@l, mD@ρD
lagCylinder@8l_, m_, rot_<D@8ρ_, φ_<D :=
 lagCylinder@lagR@fibreID, 8l, m, rot<DD@8l, m, rot<D@0D@8ρ, φ<D
```

Figure D.8: Extract from *Mathematica* program `FibreFormulae#.nb`. The formulae for the fields of a parabolic index-profile fibre (the "Gaussian Approximation") in cylindrical coordinates.

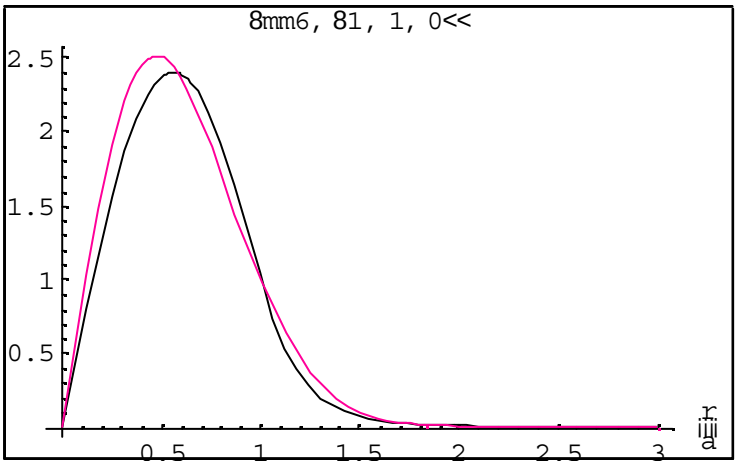

Figure D.9: Extract from *Mathematica* program `FibreFormulae#.nb`, showing the comparison between the radial field distribution of the step index fibre (black curve) and the Gaussian approximation (red curve).

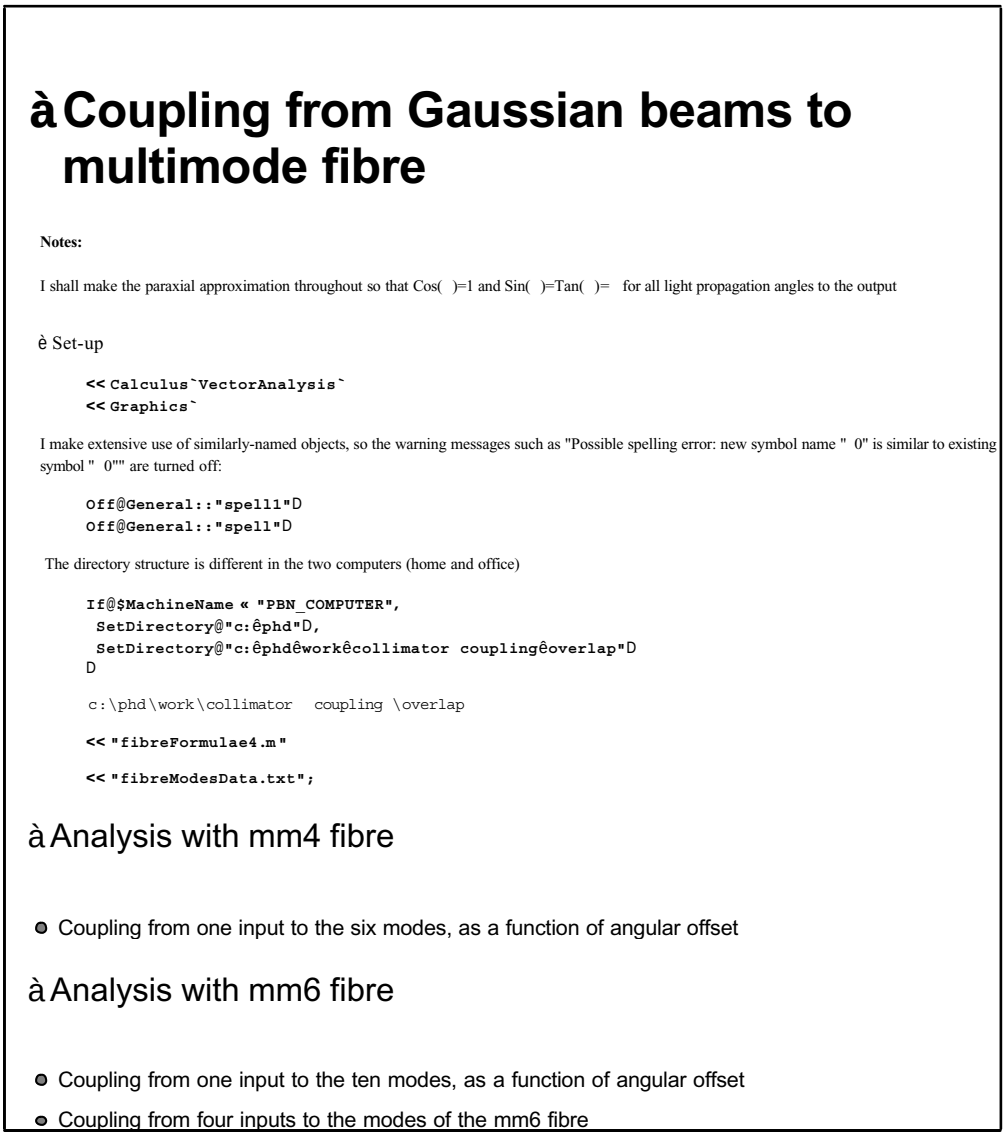

à Coupling from Gaussian beams to multimode fibre

Notes:

I shall make the paraxial approximation throughout so that Cos( )=1 and Sin( )=Tan( )= for all light propagation angles to the output

è Set-up

```
<< Calculus`VectorAnalysis`
<< Graphics`
```

I make extensive use of similarly-named objects, so the warning messages such as "Possible spelling error: new symbol name " 0" is similar to existing symbol " 0"" are turned off:

```
Off@General::"spell1"D
Off@General::"spell"D
```

The directory structure is different in the two computers (home and office)

```
If@$MachineName « "PBN_COMPUTER",
 SetDirectory@"c:êphd"D,
 SetDirectory@"c:êphdêworkêcollimator couplingêoverlap"D
D
```

```
c:\phd\work\collimator  coupling \overlap
```

```
<< "fibreFormulae4.m"
```

```
<< "fibreModesData.txt";
```

à Analysis with mm4 fibre

- Coupling from one input to the six modes, as a function of angular offset

à Analysis with mm6 fibre

- Coupling from one input to the ten modes, as a function of angular offset
- Coupling from four inputs to the modes of the mm6 fibre

Figure D.10: Outline of the notebook `CouplingCircle.nb`, used to calculate the overlap integrals for the hybrid coupler.

For each of the multimode fibres (mm4 and mm6), the coupling efficiency to each mode of the output fibre is derived for a single input as a function of angular offset, then for the mm6 fibre only the coupling between four inputs and one output was explored.

A single input at an angle ϕ to the output fibre axis.

Algebraic solutions with ϕ as a variable were derived and the solution saved as a text file. For example, the coupling to the ten modes of the mm6 fibre is given by the list `angleFuncs6`, which is stored in the data file `angleFuncs6.txt`:

```
<< "angleFuncs6.txt"

{1. e^(-186.019 ϕ^2), 8650.74 e^(-186.019 ϕ^2) (-1.9364963210993617×10^-9 + ϕ) ϕ^3, 0,
 182.486 e^(-167.849 ϕ^2) ϕ^2 Sign[ϕ]^4, 0, 4 e^(-167.849 ϕ^2) π^2 Abs[ϕ (0.296994 - 140.05 ϕ^2) Sign[ϕ]^2]^2,
 7960.35 e^(-155.259 ϕ^2) ϕ^4, 0, 0, 223245. e^(-146.633 ϕ^2) ϕ^6 Sign[ϕ]^2}
```

The ordering of the modes is fixed by the definition of `modeList`:

`modeList[''mm6'']` = {{0, 1, 0}, {0, 2, 0}, {1, 1, 0}, {1, 1, Pi/2}, {1, 2, 0}, {1, 2, Pi/2}, {2, 1, 0}, {2, 1, Pi/2}, {3, 1, 0}, {3, 1, Pi/2}}

The triplets identify the mode by {l, m, orientation}, as explained in Section 6.4.

The final output used in Chapter 6 was a plot of the coupling to each mode, as a function of angle, for each of the fibres (see Figures 6.15 and 6.16).

Four inputs with the optical phase origin of each as parameters, $\psi 1, \psi 2, \psi 3, \psi 4$.

Again coupling to the ten modes is determined and the solution saved in a text file. In order to be able to derive algebaic solutions of the overlap integrals it was found necessary to instruct *Mathematica* to follow a specific sequence of expansion and simplification of the integrands, using forms such as '`Simplify[ComplexExpand[`*integrand*`, TargetFunctions->{Re, Im}]]`' which instructs *Mathematica* first to expand the algebra *integrand* in terms of real and imaginary components, then to simplify the answer. The successful sequence – which allowed *Mathematica* to find a solution in a reasonable time – was found by 'directed trial and error'. Having derived the formulae for the coupling to each mode as a function of the four phase parameters $\psi 1, \psi 2, \psi 3, \psi 4$ (which is reproduced in as Figure 6.19 in Chapter 6), curves were plotted with three of the parameters fixed and one as the independent variable (see Figures 6.21, 6.22 and 6.23, on page 115ff).

D.4 Simulation of the performance of OCDMA in a SLIM bus (Chapter 8)

To simulate the performance of OCDMA in a SLIM bus, the model (described in Chapter 8) was implemented in a set of packages, then performance analysed through the use of several notebooks.

D.4.1 Packages used in the simulation of OCDMA in a SLIM bus

Packages used in the simulation of OCDMA in a SLIM bus are as follows:

SLIM-SimFuncs.m Contains the main functions of the model. Draws upon functions defined in `SLIM-GenFunc`, and uses parameters which are given default values in `SLIMPars`.

SLIM-GenFunc.m More functions used by the model, but of a more general nature than contained in `SLIM-SimFuncs`. For example, it has the Q function and functions for finding the minimum of a function in a range. It also contains the combinatoric functions used by the model.

SLIM-Manip.m Functions which manipulate the output of the model. For example, the main simulation gives the error probability given with the decision threshold level as a parameter. `getLowest` in `SLIM-Manip` finds the lowest error probability as a function of threshold level.

SLIM-Symbols.m By default, *Mathematica* treats subscripted symbols as functions with the subscript as a parameter (so, for example, n_t is taken to mean the function $n(t)$). To use subscripted variables as single symbols it is necessary to load a standard package (`Notation`) and `Symbolize` variable individually:

```
<< Utilities`Notation`;
Symbolize@n_tD;
```

Extensive use was made of subscripted variables in the simulations of this chapter, to make the code more readable, and all the `Symbolize` instructions were gathered together in the `SLIM-Symbols.m` package.

SLIMPars.m Sets-up default values for the parameters of the simulation. The default values are over-written if they are subsequently given a new value, but revert to the default if `SLIMPars` is reloaded. By reloading `SLIMPars` before each new simulation, therefore, the environment is set to a known state (the instruction `<<SLIMPars.m` in Figure D.11).

Fine structure steps

Another departure from the steps described above comes from the fact that the signal on the channel is not purely binary - it is not an 'OR' channel. In particular, the signal power is attenuated by $\frac{1}{M^r}$ where M is the modulator extinction, and r is the number of simultaneous pulses. The effect of this 'fine structure' is made more apparent in the following example by making the exctinction artificially low (3) and suppressing the 'smoothing' by reducing all the other sources of noise (increasing L_R to reduce thermal noise, reducing n_{Sp} to reduce intermodulation noise and reducing B_{elect} to reduce shot noise).

```
<< SLIMPars.m;
correlator= multiple;
L_R = 100000;
n_Sp = 0.01;
Mx = 3;
B_elect = 1 10^6;
muThresTable3 = Table@8x, pETscaled@x, 100D<, 8x, -10, 110, 0.25<D;
Save@"exploreResults", muThresTable3D;

multPlot = LogListPlot@muThresTable3, PlotJoined → True, AxesLabel → labsD;
```

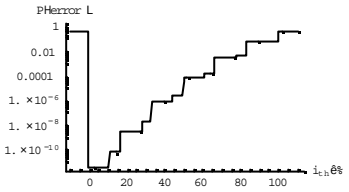

To look more closely at the structure the following plot expands the vertical scale:

```
LogListPlot@muThresTable3, PlotJoined → True, PlotRange → 81 10^-7, 1<, AxesLabel → labsD
```

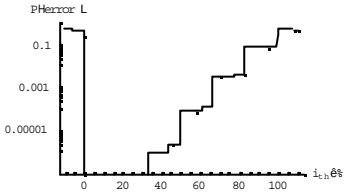


```
¦ Graphics ¦
```

Figure D.11: Extract from the Mathematica notebook `SLIMThresholdSim.nb`. pETScaled[x,N] is a function, defined in `SLIM-Manip.m`, which calculates the probability of error as a function of normalised threshold. '`correlator=multiple`' sets the simulations to run on the model of the hybrid correlator. (In the simulations the hybrid correlator was described as a 'multiple paths' correlator.)

OCDMAformulae.m Contains *Mathematica* implementations of Eqns.8.1 and 8.2 (see page 140).

D.4.2 Notebooks used in the simulation of OCDMA in a SLIM bus

Several notebooks (such as `SLIMThresholdSim.nb` and `SLIMSimulDimensions.nb`) were written to generate results that explore different aspects of the bus.

`SLIMThresholdSim.nb`, (Figure D.11) for example, looks at the error probability as a function of decision threshold to generate plots such as Figure 8.5 (on page 149). The results were saved in data files (the table `muThresTable3` is saved in the file `exploreResults` in the extract shown in Figure D.11) so that further plots could be generated at a later date without having to re-run the simulations.

```
In[1]:= <<DiscreteMath`Combinatorica`

In[2]:= Partitions@4D

Out[2]= 884<, 83, 1<, 82, 2<, 82, 1, 1<, 81, 1, 1, 1<<

In[3]:= partspadded@numI_Integer, lengthW_IntegerD :=
        partspadded@numI, lengthWD = Map@PadRight@#, lengthWD &, Select@Partitions@numID, Length@#D § lengthW &D,
          1D

In[4]:= partspadded@4, 3D

Out[4]= 884, 0, 0<, 83, 1, 0<, 82, 2, 0<, 82, 1, 1<<
```

Figure D.12: Calculation of a list of representative vectors.

D.4.3 Further details on the *Mathematica* implementation

In implementing the model used to simulate OCDMA in a SLIM bus it was possible to make use of some interesting features of *Mathematica*. Specifically, the combinatoric calculations were able to use the standard *Mathematica* package 'combinatorica', and the list-processing features of *Mathematica* were used to good effect in a number of ways, one of which is explained below.

Combinatoric calculations and the representative vectors, $\mathbf{k_r}$ (Section 8.2.5)

The function `Partitions`$[i]$ is supplied in the *Mathematica* standard package `DiscreteMath‘Combinatorica’` and generates a list of all partitions of i. The function `partspadded[numI, lengthW]` was written to manipulate partitions in order to generate a list of representative vectors for a given `numI` (the number of pulses hitting the correlator, j_u) and `numW` (the number of taps in the correlator, W). It does this by discarding all partitions that are longer than W and padding all partitions that are shorter than W with 0s. The coding of `partspadded` together with the calculation for the case of $j_u = 4$. $W = 3$ is shown in Figure D.12.

To calculate the probability of each representative vector (Eqn. 8.18) the multinomial function is also available in the `DiscreteMath‘Combinatorica’` package of *Mathematica* and the repetitions are derived by explicitly counting. This is illustrated in Figure D.13, again for the case of $j_u = 4$. $W = 3$. The final list of probabilities may be interpreted as saying that given that four pulses have 'hit' three taps, the probability that all four are in the same tap (without distinguishing which it is) is 1/27, the probability that three are in one tap and one in another is 8/27 etc. All possibilities are covered, so the probabilities must add to 1, as they do.

Calculation of P(error|$\mathbf{k}_r$) and the total error probability, P_{error}

For each representative vector, the associated probability of error is calculated using functions written to implement the equations of Section 8.2.4. Separate functions are,

```
In[26]:= vec = 884, 0, 0<, 83, 1, 0<, 82, 2, 0<, 82, 1, 1<<;
         reps = Map@Table@Count@#, iD, 8i, 0, Max@vecD<D &, vecD

Out[27]= 882, 0, 0, 0, 1<, 81, 1, 0, 1, 0<, 81, 0, 2, 0, 0<, 80, 2, 1, 0, 0<<

In[34]:= probs = Apply@Multinomial, vec, 81<D Apply@Multinomial, reps, 81<D ê 3^4

Out[34]= :1/27, 8/27, 2/9, 4/9>
```

Figure D.13: Multinomial function and generation of repetitions

$$\left(\sum_{i=0}^{\text{Min[30,Nusers-1]}} \text{PA}_{\text{error}}[i_{\text{thresh}}, i]\ \text{probju[i]}\right) + \left(\sum_{i=31}^{\text{Nusers-1}} 0.5\ \text{probju[i]}\right)$$

Figure D.14: Mathematica implementation of the total error probability. probju and PA_{error} are functions defined elsewhere in the simulation.

of course, needed for each of the three correlators.

Mathematica allows functions to be mapped over lists, so it was possible to write $\text{P}(\text{error}|\mathbf{k}_r)$ as a function of $\mathbf{k}_r$ and apply it to the list of $\mathbf{k}_r$ that was generated by `partspadded`, giving a list of error probabilities.

Multiplication by $\sum_{\mathbf{k}\in[\mathbf{k_r}]_{\text{rearrangement}}} P(\mathbf{k}|j_u)$ (which is also generated as a list, see Figure D.13) and summation over all $\mathbf{k}_r$ was then achieved in one step by a scalar product. In effect, the calculation was done as:

$$\text{P}(\text{error}|j_u) = \text{P}(\text{error}|\mathbf{k}_r)\left[\{\mathbf{k}_r\}_{j_u}\right] \cdot \text{P}(\mathbf{k}_r|j_u)\left[\{\mathbf{k}_r\}_{j_u}\right]$$

Where $\{\mathbf{k}_r\}_{j_u}$ is the list of representative vectors of weight j_u and the notation $\text{P}(\mathbf{k}_r|j_u)\left[\{\mathbf{k}_r\}_{j_u}\right]$ indicates that the function for calculating the probability of $\mathbf{k}_r$ given j_u is applied separately to all of members of $\{\mathbf{k}_r\}_{j_u}$.

Having calculated $\text{P}(\text{error}|j_u)$, the total error probability is calculated by summing over all j_u, weighted by $\text{P}(j_u)$ (Eqn. 8.17).

As noted in Section 8.3.4, a very substantial time saving for large numbers of simultaneous users was possible by the approximation that $\text{P}(\text{error}|j_u) \approx 0.5$. This approximation was built in to the calculation of total error probability by writing the final summation as:

$$\text{P}_{\text{error}} = \sum_{j_u=0}^{\min[30,N-1]} \text{P}(\text{error}|j_u)\text{P}(j_u) + \sum_{j_u=31}^{N-1} 0.5\text{P}(j_u)$$

Coded in *Mathematica*, this appeared as shown in Figure D.14.

As a test, sample calculations were done with this approximation and with the full calculation. No differences were seen to more than 10 significant figures. (This accuracy vastly exceeds the level required, suggesting that it would have been possible

to implement the approximation for j_u less than 30. There was no need to shorten the calculation time further, however, so it was left at 30.)

Appendix E

Measurement details

In the experiments described in Chapter 7, 'signal' power was measured by the dc current from a photodiode, measured with a digital voltmeter (DVM) and noise power measured with a digital oscilloscope. This appendix contains further details of both of these measurements.

E.1 DC signal measurements PINAMP

The received signal was measured using a PINAMP from LDI (Laser Diode Incorporated), part no. LPA0622PTA-FC (622 Mbit/s PINAMP with 50/125 fibre pigtail), serial no. 11534. This is an integrated transimpedance receiver [220] and was assembled according to the data sheet to give low-pass filtering with a cut-off of nominally 450 MHz. The PINAMP output impedance is 50- designed for a 50- terminated load, and has a $0.1\,\mu$F capacitor in-line with the output connector resulting in high-pass filtering with cut-off at $1/2\pi RC = 1/(2\pi 50\text{-}\ 0.1\,\mu\text{F}) = 32\,\text{kHz}$.

For simultaneous high-sensitivity ac measurements and dc measurements, a high-impedance tap was taken from before the output capacitor and the dc voltage measured with a digital voltmeter (DVM, Thurlby 1503, 10 M- input resistance). The tap was configured as in Figure E.1, giving a 9% measurement of the output. (Resistance values were chosen as high enough to have negligible loading on the PINAMP output (100 k- in parallel with 50- , is equivalent to $\frac{50\times 100000}{50+100000} = 49.975\text{-}$). The 4.7 nF capacitor provides low-pass filtering on the measurements of $1/(2\pi 10\,\text{k-}\ 4.7\,\text{nF}) = 3.4\,\text{kHz}$

The PINAMP response was calibrated by measuring the voltage on the tap as a function of input optical power (measured with an optical power meter, HP 8153A).

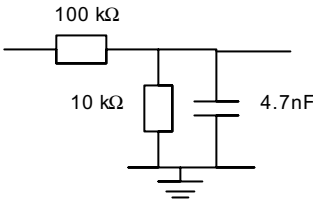

Figure E.1: PINAMP output tap for dc measurements

E.2 Statistics of the measurement of noise with the LeCroy digital oscilloscope

The measurements required for comparison with theory required the ac noise power, given by the variance of the output voltage[1]. The LeCroy oscilloscope has a built-in facility to report the standard deviation of the samples in a sweep, but not (directly) the variance. The variance is given simply by squaring the standard deviation, but complications arise when analysing the statistics of multiple sweeps.

One sweep of the oscilloscope takes a set of n voltage samples $\{s_1, s_2, ...s_n\}$. The variance of this set, $\mathrm{var}\left[\{s_1, s_2, ...s_n\}\right]$, is the mean power (voltage-squared) during that sweep, in a frequency range between a low limit determined by the sweep duration and a high limit determined by the input filtering.

For each sweep, the LeCroy oscilloscope measures the standard deviation of the samples:

$$x = \sqrt{\frac{\sum_{i=1}^{n}(s_i - \overline{s})^2}{n}}$$

In the terminology of statistics [221], one sweep counts as a random experiment which returns a value for the random variable x.

Writing $y = x^2 = \frac{\sum_{n=1}^{N}(s_n - \overline{s})^2}{N}$ for the variance of the samples in a given sweep, the desired parameter is $\mathrm{E}\left[y\right]$.

From a single sweep, the best estimate of $\mathrm{E}\left[y\right]$ is given by x^2.

For m sweeps the LeCroy calculates the mean and standard deviation of x:

$$\begin{aligned} \overline{x} &= \frac{1}{m}\sum_{j=1}^{m} x_j \\ x_{sd} &= \sqrt{\frac{\sum_{j=1}^{m}(x_j - \overline{x})^2}{m}} \end{aligned} \tag{E.1}$$

The best estimate of $\mathrm{E}\left[y\right]$ is given by:

$$\overline{y} = \frac{1}{m}\sum_{j=1}^{m} y_j = \frac{1}{m}\sum_{j=1}^{m} x_j^2 = x_{rms}^2$$

Using the standard result [160] that

[1] Using voltage-squared as a measure of power.

$$\text{mean square} = \text{square of mean} + \text{variance}$$

gives:

$$\overline{y} = x_{rms}^2 = x_{sd}^2 + \overline{x}^2$$

To determine the accuracy of the estimate of $\mathrm{E}[y]$ an estimate of $\mathrm{var}[y]$ is required, but the parameters available from the LeCroy do not allow the direct calculation of the standard deviation of y:

$$\begin{aligned}\mathrm{var}[y] &= \frac{1}{M}\left(\sum_{m=1}^{M} y_m^2 + \sum_{m=1}^{M}\overline{y}^2 - \sum_{m=1}^{M} 2y_m\overline{y}\right)\\ &= \overline{y^2} - \overline{y}^2\end{aligned}$$

This needs $\overline{y^2}$, which is not known.

If, however, the voltage samples are normally distributed, then it can be shown that [221]

$$\mathrm{var}[y] = 2\left(\mathrm{E}[y]\right)^2/(n-1)$$

Using $\overline{y}$ for $\mathrm{E}[y]$ gives

$$\mathrm{var}[y] = 2\left(x_{sd}^2 + \overline{x}^2\right)^2/(n-1)$$

If $\mathrm{E}[y]$ has been calculated from m sweeps, then the estimate for $\mathrm{E}[y]$ will be distributed normally with variance $\mathrm{var}[y]/m$.

In summary, the LeCroy oscilloscope returns the parameters $\overline{x}$ and x_{sd}. From these are calculated:

$$\begin{aligned}\widehat{\mathrm{E}[y]} &= x_{sd}^2 + \overline{x}^2\\ \widehat{\mathrm{var}[\mathrm{E}[y]]} &= \frac{2\left(x_{sd}^2 + \overline{x}^2\right)^2}{nm}\end{aligned}$$

Where the carat indicates an estimated parameter, and n is used instead of $n-1$ because n is large (1000).

The normalised standard deviation is simply:

$$\sqrt{\frac{2\left(x_{sd}^2 + \overline{x}^2\right)^2}{nm}}\Big/\left(x_{sd}^2 + \overline{x}^2\right) = \sqrt{\frac{2}{nm}}$$

Appendix F

Quadratic model of noise measurements

In the experiments described in Chapter 7, measurements are taken from a photodiode detecting light originating from a multimode laser diode, which may have reached the detector by more than one path. It is claimed that the measured noise power (voltage-squared) on the output of a photodetector is expected to be a quadratic function of the mean received signal (voltage):

$$\left\langle v_{noise}^2 \right\rangle = v_{fixed}^2 + c_{lin} v_{dc} + c_{quad} \alpha_1 \alpha_2 v_{dc}^2$$

where the fixed term is thermal noise and other noise originating in the receiver, the linear term is shot noise and the quadratic noise is optical beating

This appendix derives this formula and calculates expected values for v_{fixed}^2, c_{lin} and c_{quad}, for the experimental configuration used for this thesis.

In addition, Section F.2 presents a simple analysis of the situation in which there are more than two fields beating.

F.1 Quadratic form

Suppose two fields interfere, P_1 and P_2. The total power is $P_o = P_1 + P_2$ and the ratios are given by α_1 and α_2 such that $P_1 = \alpha_1 P_o$ and $P_2 = \alpha_2 P_o$, $(\alpha_1 + \alpha_2 = 1)$.

Then the output noise power due to beating (cf. Eqn. 5.5) between the two fields is given by

$$\begin{aligned} \sigma_{beat}^2 &= \frac{1}{\pi} \mathcal{R}^2 P_1 P_2 \tan^{-1}\left(B_e/\nu_1\right) \sum_{i=1}^{n} r_i^2 \\ &= \left(\frac{1}{\pi} \mathcal{R}^2 \alpha_1 \alpha_2 \tan^{-1}\left(B_e/\nu_1\right) \sum_{i=1}^{n} r_i^2 \right) P_o^2 \end{aligned}$$

In general, the total noise power is given by,

$$\sigma^2_{noise} = \sigma^2_{fixed} + 2e\mathcal{R}B_eP_o + \left(\frac{1}{\pi}\mathcal{R}^2\tan^{-1}\left(B_e/\nu_1\right)\sum_{i=1}^{n} r_i^2\right)\alpha_1\alpha_2P_o^2$$

With transimpedance R_t, noise on the output voltage is given by $R_t^2\sigma^2_{noise}$. Added to this is the thermal noise on the 50 Ω termination resistor and any noise on the oscilloscope input. These latter will, for the present, be combined with $R_t^2\sigma^2_{fixed}$ in a single revised term for the □xed noise, designated by v^2_{fixed}. As a function of optical power, therefore, the noise voltage measured on the output should be given by:

$$\begin{aligned}\left\langle v^2_{noise}\right\rangle &= R_t^2\sigma^2_{noise} + (\text{additional □xed noise})\\ &= v^2_{fixed} + 2R_t^2e\mathcal{R}B_eP_o + \left(\frac{1}{\pi}\mathcal{R}^2\tan^{-1}\left(B_e/\nu_1\right)\sum_{i=1}^{n} r_i^2\right)R_t^2\alpha_1\alpha_2P_o^2\end{aligned}$$

As a function of the dc voltage measured on the resistive tap $v_{pd} = \gamma P_o$ (from above, $\gamma = \left(\frac{9\times10^{-3}}{11}\,\mathrm{V}/\,\mu\mathrm{W}\right)$):

$$\begin{aligned}\left\langle v^2_{noise}\right\rangle &= v^2_{fixed} + 2R_t^2e\mathcal{R}B_e\frac{v_{dc}}{\gamma} + \left(\frac{1}{\pi}\mathcal{R}^2\tan^{-1}\left(B_e/\nu_1\right)\sum_{i=1}^{n} r_i^2\right)R_t^2\alpha_1\alpha_2\left(\frac{v_{dc}}{\gamma}\right)^2\\ &= v^2_{fixed} + c_{lin}v_{dc} + c_{quad}\alpha_1\alpha_2v^2_{dc} \qquad \text{(F.1)}\end{aligned}$$

The constant of proportionality for the linear term, $c_{lin} = 2R_t^2e\mathcal{R}B_e/\gamma$, is determined entirely by characteristics of the receiver, while the multiplier for the quadratic term has been split into two parts: $c_{quad} = \left(\frac{1}{\pi}\mathcal{R}^2\tan^{-1}\left(B_e/\nu_1\right)\sum_{i=1}^{n} r_i^2\right)R_t^2/\gamma^2$ which is determined by the characteristics of the light source and the receiver, and $\alpha_1\alpha_2$ which is a function of the split of the light between the two interfering components.

F.1.1 Estimates of the constants: v^2_{fixed}, c_{lin} and c_{quad}

For the given experimental con□guration estimates of the constants are possible. The various parameters needed for the estimates are as follows:

1. Transimpedance: R_t is the transimpedance of the photodiode in the PINAMP, which was not given in the component datasheet. The transfer gain was measured to be $4100\,\mathrm{V\,W^{-1}}$, however, and the data sheet gives the responsivity as $0.85\,\mathrm{A\,W^{-1}}$ (typical). This leads to an approximate value for the transimpedance of $\left(4100\,\mathrm{V\,W^{-1}}\right)/\left(0.85\,\mathrm{A\,W^{-1}}\right) = 4800\,\Omega$.

2. Electrical bandwidth: B_e From Section 7.4 the electrical bandwidth of the detection system is $20\,\mathrm{MHz} - 50\,\mathrm{kHz} \approx 20\,\mathrm{MHz}$

3. Noise-equivalent resistance in the photodiode: R_L. For the transimpedance design, this is given by the parallel combination of the actual load resistance and

the feedback resistance [160]. This information is not available, but an upper bound (which gives a lower bound on the noise) is given by the transimpedance of the circuit, R_t.

4. Mode width, ν_1, and mode distribution, $\sum_{i=1}^{n} r_i^2$, of the multimode laser. Neither of these are known (see Section 5.4.2), but an upper bound is given by assuming $B_e \gg \nu_1$ (so that $\tan^{-1}(B_e/\nu_1) = \pi/2$) and $\sum_{i=1}^{n} r_i^2 = 1$ (treating the multimode laser as single mode).

Using these parameters, estimates for v_{fixed}^2, c_{lin} and c_{quad} are obtained as follows.

Fixed term, v_{fixed}^2

A lower bound on v_{fixed}^2 is given by the thermal noise: $R_t^2 \frac{4kTB_e}{R_L}$. Thus

$$\begin{aligned} v_{fixed}^2 &\geq R_t^2 \frac{4kTB_e}{R_L} \\ &\geq R_t^2 \frac{4kTB_e}{R_t} = R_t 4kTB_e \\ &= (4800\text{-}\,)\,4\left(1.38\times10^{-23}\,\mathrm{J\,K^{-1}}\right)(293\,\mathrm{K})\,(20\,\mathrm{MHz}) \\ &= 1.6\times10^{-9}\,\mathrm{V}^2 \end{aligned}$$

Constant of proportionality for the linear term, c_{lin}

$$\begin{aligned} c_{lin} &= 2eR_t^2\mathcal{R}B_e/\gamma \\ &= 2\left(1.6\times10^{-19}\,\mathrm{C}\right)(4800\text{-}\,)^2\left(0.85\,\mathrm{A\,W^{-1}}\right)(20\,\mathrm{MHz}) \,/\left(\frac{9\times10^{-3}}{11}\,\mathrm{V}/\mu\mathrm{W}\right) \\ &= 1.5\times10^{-7}\,\mathrm{V} \end{aligned}$$

Constant of proportionality for the quadratic term, c_{quad}

As noted above, an upper bound on c_{quad} is given by $\tan^{-1}(B_e/\nu_1) = \pi/2$ and $\sum_{i=1}^{n} r_i^2 = 1$:

$$\begin{aligned} c_{quad} &= \left(\frac{1}{\pi}\mathcal{R}^2\tan^{-1}(B_e/\nu_1)\sum_{i=1}^{n} r_i^2\right) R_t^2/\gamma^2 \\ &\approx \left(\frac{1}{\pi}\left(0.85\,\mathrm{A\,W^{-1}}\right)^2\frac{\pi}{2}\right)(4800\text{-}\,)^2 \,/\left(\frac{9\times10^{-3}}{11}\,\mathrm{V}/\mu\mathrm{W}\right)^2 \\ &\approx 12 \end{aligned}$$

F.2 Multiple beam beating

Suppose that

$$P_o = \sum_{i=1}^{k} P_i$$

$$P_i = \alpha_i P_o \text{ with} \sum_{i=1}^{k} \alpha_i = 1$$

Assume that the components all originate from the same optical source – due to multiple paths – but that the path length difference between any two components is greater than the coherence length of the source. The beating between any two will therefore be similar, and the quadratic term of the noise will be weighted by a factor from a sum of all the cross terms:

$$\frac{1}{2}\sum_{i=1}^{k}\sum_{j=1,\, i\neq j}^{k} P_i P_j = \frac{P_o^2}{2}\sum_{i=1}^{k}\sum_{j=1,\, i\neq j}^{k} \alpha_i \alpha_j$$

It is relevant to explore whether splitting the power between more beams increases or decreases the beating power. Assume initially equal splitting between the beams, so that $\alpha_i = 1/k$ for all i. Then the weighting factor is

$$\begin{aligned}\frac{P_o^2}{2}\sum_{i=1}^{k}\sum_{j=1,\, i\neq j}^{k} \alpha_i \alpha_j &= \frac{P_o^2}{2k^2}\sum_{i=1}^{k}\sum_{j=1,\, i\neq j}^{k} 1 \\ &= \frac{P_o^2}{2k^2}\left(k^2 - k\right) \\ &= \frac{P_o^2}{2}\left(1 - \frac{1}{k}\right)\end{aligned}$$

Showing that the beating increases with increasing k, towards an asymptote of weight $P_o^2/2$.

Of particular relevance here is the case when the split is asymmetric, with one large component and several small components (due to small reflections). Assuming now that the total contribution from the small components combined is fixed and that the distribution among the components is (approximately) equal, then the more small components there are, the larger will be the beating.

For example, comparing a $(0.9, 0.05, 0.05)$ split with a $\left(0.9, \frac{0.1}{3}, \frac{0.1}{3}, \frac{0.1}{3}\right)$ split:

- The cross terms in $(0.9, 0.05, 0.05)$ give: $2 \times 0.9 \times 0.05 + 0.05^2 = .0925$
- The cross terms in $\left(0.9, \frac{0.1}{3}, \frac{0.1}{3}, \frac{0.1}{3}\right)$ give: $3 \times 0.9 \times \frac{0.1}{3} + 3 \times \frac{0.1}{3} \times \frac{0.1}{3} = 0.0933$

Appendix G

Angular dependence of Fresnel reflection

For perpendicular polarisation (**E** parallel to the fibre end-face), the amplitude reflection coefficient is given by [209]:

$$r = \frac{-\sin(\theta_i - \theta_t)}{\sin(\theta_i + \theta_t)}$$

where θ_i is the angle of incidence (to the normal to the end-face) and θ_t is the angle of transmission. From Snell's law, $n_i \sin(\theta_i) = n_t \sin(\theta_t)$.

For air/fibre interface, $\frac{n_t}{n_i} \approx 1.5$ and for θ_i between 0 and 10^o Snell's law gives θ_i varying between 0 and 6.6^o and r varies between 0.2 and 0.204. The fractional power reflected varies from $0.2^2 = .0\,4$ to $0.204^2 = 0.042$, and the fraction transmission varies between 0.96 and 0.958, a variation of about 0.2%.

For parallel polarisation the amplitude reflection coefficient is given by [209]:

$$r = \frac{\tan(\theta_i - \theta_t)}{\tan(\theta_i + \theta_t)}$$

Again using $\frac{n_t}{n_i} \approx 1.5$ and θ_i between 0 and 10^o, θ_r between 0 and 6.6^o, gives r between 0.2 and 0.199.The fractional power reflected varies from $0.2^2 = .0\,4$ to $0.199^2 = 0.0396$, and the fractional transmission varies from 0.96 to 0.9604, a variation of about 0.04%.